Development and characterization of laser chemical processes for high efficiency silicon solar cells

Dissertation

zur Erlangung des Doktorgrades

der Technischen Fakultät

der Albert-Ludwigs-Universität Freiburg im Breisgau

vorgelegt von

Sven Kluska

Fraunhofer Institut für Solare Energiesysteme (ISE)

Freiburg im Breisgau

2013

Datum der Einreichung: 20. Dezember 2013

Dekan: Prof. Dr. Yiannos Manoli
Hauptreferent: Prof. Dr. Eicke R. Weber
Koreferent: Prof. Dr. Leonhard M. Reindl

Datum der Prüfung: 07. Mai 2014

Für meine Eltern

Table of Contents

1 Introduction

1.1 Motivation and aim of this work

The rising worldwide energy consumption increases the demand for the replacement of fossil based energy sources by equivalent renewable energy sources such as wind energy, hydro power, geothermic, biomass or photovoltaic (PV). However, these sustainable energy sources have to fulfill equivalent criteria in terms of capacity, electricity costs and security of supply. These criteria set in the beginning challenging requirements on the different technologies. However, the establishment of foreseeing political frameworks, such as the “Erneuerbare Energiengesetz (EEG)” in Germany, triggered the development of new technologies and processes for the cost competitive energy production by renewable energy sources. These developments are for PV clearly visible in the price learning curve, which reveals a price decline of about 20% for every doubling of the cumulative production volume in the last decades [1]. The technological induced price declines combined with a considerable oversupply lead in the field of crystalline silicon PV to module costs down to 0.5-0.8 €/W_{peak} in the first quarter of 2013 [1]. Furthermore, the increasing installation of renewable energy sources in combination with significant technological improvements results for example in Germany in a share of about 25.8% for renewable energy sources (including 5.3% for PV) in the national wide electricity consumption [2]. This illustrates the significance of technological developments for the transformation to a sustainable energy system. Within this work the scientific point of view is focused on technological developments for PV.

The idea of PV is the conversion of light such as sun light into electricity by using the photovoltaic effect. A conventional silicon PV module is built from strings of several solar cells, which convert the incoming illumination in an electrical current flow. The conversion efficiency of the PV module is a function of different module parameters and the cell efficiency of each solar cell. The conversion efficiency is a crucial parameter of the system because it determines the maximum power output per installed system, as well as the electricity production cost per system. Therefore, the increase of the solar cell efficiency due to technological improvements not only increases the productivity of the system but also decreases the electricity production costs.

The improvement of the solar cell efficiency can be realized by a reduction of the local power losses due to resistive, optical and recombination effects. The decrease of these

loss mechanisms can be realized in improved solar cell designs by optimizations of each solar cell component or region. The local optimization of each solar cell region requires in many cases local structuring and doping process technologies. However, the integration of new process technologies cannot only be evaluated in terms of cell efficiency improvements but must be evaluated in terms of increasing fabrication costs, too. In fact the scientific challenge is the development of improved cell designs with increased solar cell efficiencies under the constraints of industrial feasibility and low processing costs in order to achieve low electricity production costs. Therefore, the aim of this work is the development and characterization of industrially feasible low-cost local structuring and doping processes for high efficiency silicon solar cells designs. In this context two main application areas are investigated:

1. Boron local back surface field structures (LBSF) by laser chemical processing (LCP) for p-type silicon solar cells

2. Local phosphorus doped structures by LCP for selective emitter designs with plated metal contacts

The development of LCP boron doped LBSF structures allows the fabrication of optimized solar cell designs with partial rear contacts and passivated rear sides. These solar cell designs show decreased recombination induced power losses and increased optical performance compared to state-of-the-art industrial solar cell designs.

The development of LCP selective emitter structures can result in several improvements. The selective emitter design optimizes the emitter doping in different cell regions, which results in lower recombination and series resistance losses and therefore, in higher cell efficiencies. Furthermore, this work shows that the applied LCP process can be combined with Ni-Cu plated front side metal contacts, which is a low cost alternative to state-of-the-art screen printed Ag contacts. The integration of plated Ni-Cu contacts brings in this case not only cell efficiency benefits but also allows the replacement of cost-intensive Ag for front side contacting.

1.2 Thesis outline

The presented thesis is structured in 7 chapters. Chapter 2 summarizes the theoretical background of important solar cell physics for this work and the relevant processing and characterization techniques.

Chapter 3 focusses on the development of a LCP based local boron laser doping process for the application as local back surface field (LBSF) in p-type passivated emitter and rear locally diffused (PERL) solar cells. The chapter is structured in five parts addressing alternative state-of-the-art local p-type doping processes (section 3.1),

the evaluation of suitable boron doping sources and the development of a LCP boron laser doping process (section 3.2), the first proof of concept of this process as LBSF in p-type PERL solar cells (section 3.3) and a detailed loss analysis of the application as LBSF with focus on the correlation of the base resistivity and the losses at the laser processed LBSF structures (section 3.4 & 3.5).

Chapter 4 aims to analyze the different impacts of selective emitter designs on the electrical performance of silicon solar cells by calculating and simulating the benefits of a highly doped region underneath the metal contacts on the contact resistance and contact recombination losses. Both loss mechanisms are discussed from a general point of view in section 4.1 and 4.2. The impact of both loss mechanisms on the electrical performance in different solar cell designs (Al-BSF, PERC, PERL) is discussed in section 4.3. Furthermore, section 4.3 and 4.4 analyze the correlation of different solar cell design features (selective emitter process – metallization scheme – homogenous emitter design) and how their interaction defines the possible cell efficiency benefit of a selective emitter design.

Chapter 5 analyzes the benefits of different cell design improvements on the electrical performance of Al-BSF solar cells. The fabricated solar cells described in section 5.1 feature a lightly doped thermally diffused emitter, plated Ni-Ag or Ni-Cu-Ag front side contacts and partly a selective emitter design by additional highly doped front side contact openings by LCP-SE. The presented solar cell results of section 0 are discussed in more detail in a loss analysis in section 5.3. The main findings of this loss analysis are summarized in the conclusion of section 5.4.

Chapter 6 analyzes the fabricated solar cells of chapter 5 in terms of annealing induced shunting effects. The analysis of the change in the global electrical characteristic due to contact annealing is discussed in section 6.1. The findings of chapter 5 and section 6.1 led to the formulation of a hypothesis about the physical origin of the annealing induced shunting effect in section 6.2. The stated hypothesis is experimentally investigated on the macro scale by local imaging characterization in section 6.3 and in the following section 6.4 by µ-imaging methods and electron imaging methods on the micro scale. Furthermore, the main design parameters of the highly doped contact openings in order to prevent annealing induced shunting are discussed in section 6.5, which allows further optimization routes for future process developments. Section 6.6 summarizes the characterization results of this chapter and evaluates the stated hypotheses.

Chapter 7 summarizes the results of chapter 3-6 and gives an outlook for further developments based on the findings of this work.

2 Fundamentals

2.1 Physics of silicon solar cells

2.1.1 Working principle & basic equations

Silicon solar cells convert incoming light into electricity. There are two main components of silicon solar cells. The first component is the band gap of silicon between the valence and conduction band with a band gap energy of 1.107 eV. Incoming light with photon energies larger than the band gap energy (such as visible light) is absorbed leading to free electron (e^-) and holes (h^+) in the conduction and valence band, respectively. Depending on the doping type of the silicon the minority charge carriers are electrons or holes for p- or n-type Si, respectively. Fig. 1 illustrates the energy band diagrams of an illuminated solar cell with highly doped layers at the two metal contacts (Met1, Met2). After carrier generation the silicon Fermi level is split into two quasi Fermi-levels (electron and hole quasi Fermi-level) and each charge carrier type has to be extracted at one of the contacts. The current extraction either requires selective metal contacts or charge separating regions between the contacts. State-of-the-art silicon solar cells use pn-junctions in order to separate the generated charge carriers. Assuming a p-type Si bulk material, the n^+ doped layer in Fig. 1 represents an n-type emitter doping. The space charge region of the pn-junction creates an energy barrier for the majority carriers of the bulk (h^+) and transfers the minority charge carriers of the bulk (e^-) into the emitter region, where they become majority carriers. The generated minority charge carriers diffuse in each region with a characteristic diffusion length, which is a function of the local lifetime distribution in the surrounding regions. The energy barriers of the doped layers at each contact prevent the diffusion of majority carriers and minority carriers form the bulk to the emitter and base contact, respectively. Thus, the recombination at the opposing metal contact can be significantly reduced. However, minority charge carriers generated within the doped regions or majority charge carriers overcoming the barrier (becoming minority charge carriers) can still recombine at the opposing metal contact. The transfer of electrons and holes in their respective metal contact is influenced by different aspects (i.e. work function difference between the metal and Si) and is discussed in more detail in section 2.3.

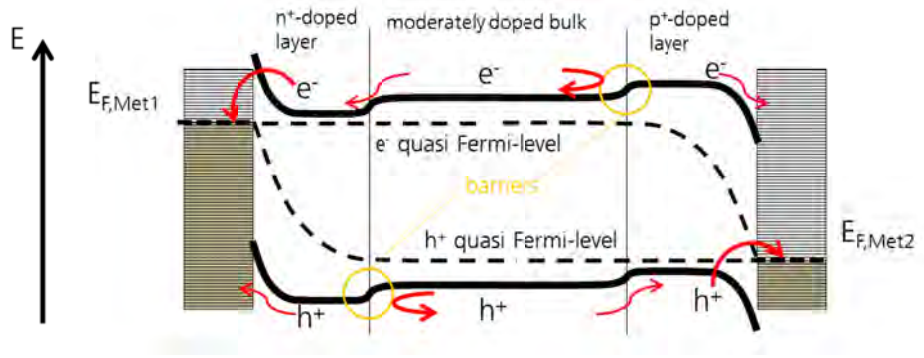

Fig. 1
Energy band diagram of an illuminated solar cell with highly doped layers

In principle the majority of silicon solar cell concepts is based on illuminated pn-junction diodes. Therefore, their electrical characteristic can be described by one- or multi-diode models. In the dark the electrical characteristic can be described by a sum of multiple diodes with different saturation current densities J_{0i}, ideality factors n_i, the Boltzmann constant k_B, the temperature T, the series resistance R_s and a linear term accounting for ohmic shunting currents over the parallel resistance R_p.

$$J(V) = \frac{V - J(V)R_s}{R_p} + \sum_i J_{0i}\left(e^{\frac{q(V-J(V)R_s)}{n_i k_B T}} - 1\right) \qquad (1)$$

The conventional form of Eq. (1) is a two diode equation, which accounts for recombination currents within the emitter and bulk in the first diode with $n_1 = 1$ and recombination currents within the space charge region usually described by a diode with ideality[1] $n_2 = 2$.

If the solar cell is not dominantly limited by series resistance effects, is operated in low level injection conditions and the photo-generation within the space charge region is negligible small, the differential equations governing the operation of the cell satisfy the principle of superposition [3, 4]. This allows the definition of the light JV curve as a dark JV curve shifted by the short circuit current density J_{sc}. The short circuit current density equals the current density due to light absorption within the solar cell reduced by the recombination current at $V = 0$.

[1] The value 2 results from the assumption that the energy level of the recombination center is located in the middle of the energy band gap in Si. In actual solar cells the energy levels of usual defect or impurity related recombination centers differ from that assumption. Therefore, the second ideality factor can differ from the value 2 in dark IV measurements of defect rich solar cells.

$$J(V) = J_{01}\left(e^{\frac{q(V-J(V)R_S)}{k_BT}} - 1\right) + J_{02}\left(e^{\frac{q(V-J(V)R_S)}{2k_BT}} - 1\right) + \frac{V - J(V)R_S}{R_p} - J_{sc} \quad (2)$$

Eq. (2) shows the 2-diode version of a light JV-characteristic of a pn-junction silicon solar cell. The 2-diode approach describes the main aspects of most pn-junction silicon solar cells and is the common model for solar cell characterization. Multi-diode models are usually only applied for advanced loss analysis [5]. The plots in Fig. 2 show an exemplary a) dark and b) light JV curve of a pn-junction silicon solar cell. The models in Eq. (1) and (2) allow to distinguish between the different components of the JV curve. The curves in Fig. 2 demonstrate that the JV curves are dominated by different parameters in each voltage regime. The linear term of the ohmic shunt R_p dominates for low voltages the dark JV curve. The same is true for the light JV curve; however, also the series resistance R_s becomes relevant in this voltage regime. In the mid-voltage regime the diode recombination according to an ideality of $n_2 = 2$ become dominant in the dark JV as well as in the light JV curve. For higher voltages the dark IV curve is dominated in the beginning by the first diode with an ideality of $n_1 = 1$ and later on by the series resistance R_s. The light JV curve is dominated for high voltages by the first diode. The opposing impact regimes of the series resistance in the light and dark JV curve can be explained by the fact that the impact of R_s becomes more and more relevant for increasing current densities. Therefore, R_s becomes relevant in the dark JV for high voltages and in the light JV curve in the low-mid voltage regime.

The performance of a solar cell is evaluated by different parameters of the light JV curve. The voltage point where the recombination currents completely compensate the generated short circuit current density J_{sc} is called open circuit voltage V_{oc}. The light JV plot in Fig. 2 b) shows that in most solar cells the first diode is the most dominating limitation on V_{oc}. The most efficient operating point for a solar cell is the maximum power point (MPP) at V_{mpp} with a current density J_{mpp}. The ratio of the maximum power output P_{mpp} of the solar cell and the incoming illumination power P_{in} defines the cell efficiency η shown in Eq. (3). Furthermore, Eq. (3) can be expressed using the fill factor *FF*, which is defined by Eq. (4). The fill factor gives the ratio of the MPP of the actual device and the theoretical maximum output power defined as the product of J_{sc} and V_{oc}.

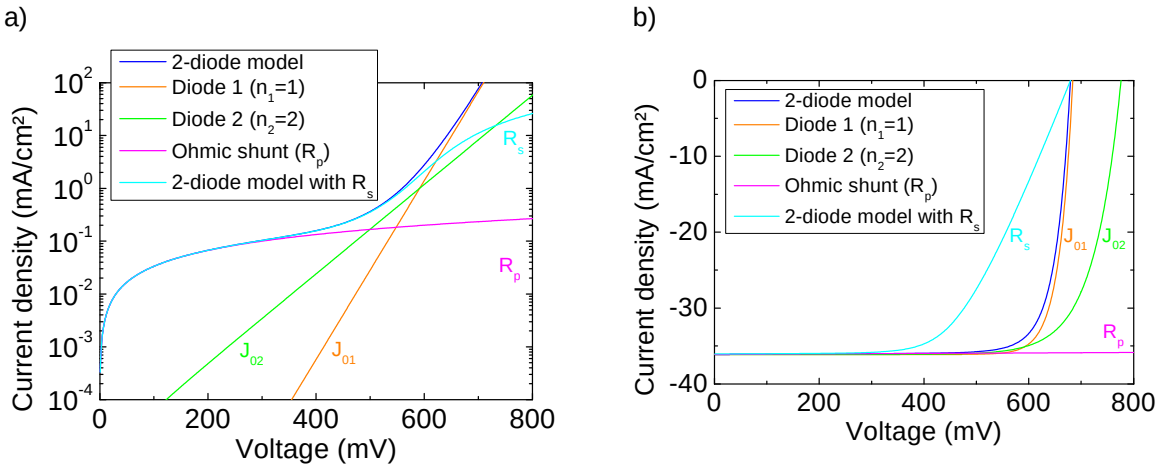

Fig. 2
Illustration of the different contributions to the dark IV a) and light IV b) characteristic of a pn-junction silicon solar cell assuming J_{01} = 100 fA/cm², J_{02} = 10 nA/cm², R_p = 3000 Ωcm² (for the blue, magenta and cyan line) or 10^{10} Ωcm² (else) and R_s = 5 Ωcm².

The interaction of J_{sc}, V_{oc} and FF results in different solar cell efficiencies. In Fig. 3 different combinations are illustrated for value ranges of each parameter comparable to state-of-the-art industrial and high efficiency lab-type one-sun silicon solar cells.

$$\eta = \frac{P_{mpp}}{P_{in}} \quad (3)$$

$$FF = \frac{P_{mpp}}{J_{sc}\, V_{oc}} \quad (4)$$

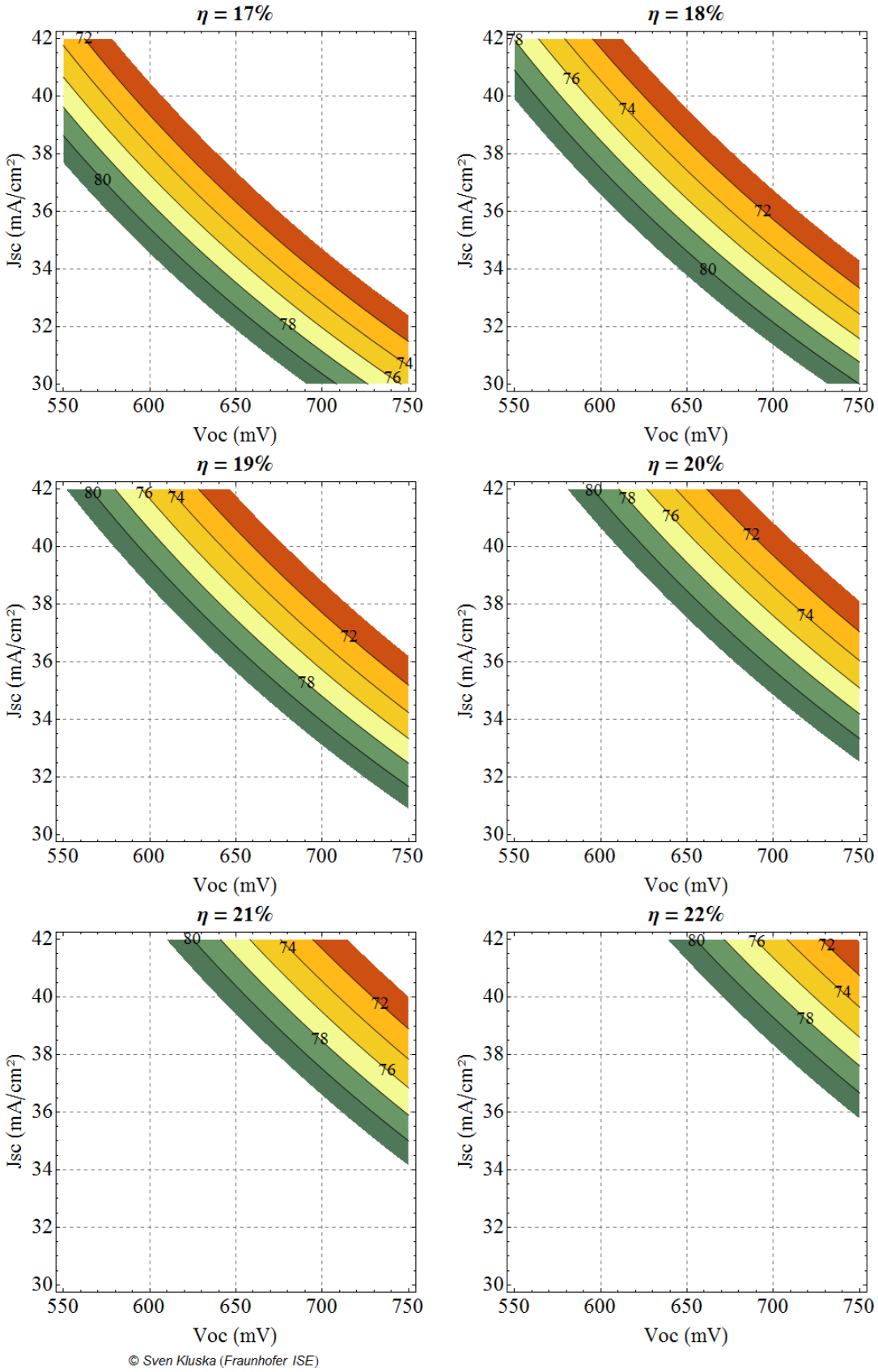

Fig. 3
J_{sc}, V_{oc} and FF (contour lines) combinations in order to reach different cell efficiencies η.

2.1.2 Al-BSF solar cell design

Within this work different kind of solar cell designs will become relevant. One of the most relevant solar cell designs in terms of industrial applicability and industrial market share is the aluminum back surface field (Al-BSF) solar cell. Fig. 4 shows the schematic design of screen printed Al-BSF silicon solar cells. The silicon substrate of an industrial Al-BSF solar cell is a p-type mono crystalline Czochralski grown (Cz), multi crystalline (mc) or casted quasi-mono silicon wafer with a thickness of 150-250 µm. The front side of the solar cells is textured with random pyramids fabricated by an alkaline etching process for Cz-solar cells or random valley structures (iso-texture) by an acidic etching process for mc-solar cells After texturing the pn-junction is formed using a thermal $POCl_3$ diffusion in order to create an n-type doped layer with pn-junction depths of about 200-350 nm and surface doping concentrations $N_D > 10^{20}$ cm^{-3}. After pn-junction formation the front side is coated with a dielectric in order to reduce the front side reflection and to electrically passivated the front side i.e. to reduce minority charge carrier recombination at the surface. In state-of-the-art Al-BSF solar cell designs this dielectric layer is usually a non-stoichiometric silicon nitride (SiN_x) fabricated in a plasma-enhanced chemical vapor deposition (PECVD) process. After deposition of the front side SiN_x layer the local front side metallization and the full area rear side metallization is applied by screen printing. The front side contact is realized by printing of silver paste and the rear side contact by printing of aluminum paste. After screen printing the contact formation is finalized in a short high temperature process (FFO) with peak temperatures between 750-950°C and process times of several minutes. Within the FFO process the solvents of the screen printing pastes are burned and the front side contact is etching through the SiN_x layer in order to realize a contact to the emitter. At the same time the rear side Al-paste forms an alloy with the silicon resulting in a highly aluminum doped layer with a thickness of about 5-15 µm and doping concentrations of about $N_A \sim 10^{19}$ cm^{-3}. This highly doped p-type layer is called back surface field [6] and acts as barrier for the minority charge carriers to the metalized surface, which reduces the recombination losses at the rear side.

The simple design and low processing effort has made the Al-BSF solar cell design to the dominating design in the silicon PV market at this moment. The constant effort in process optimization has led to high cell efficiencies of up to 19.9% [7]. However, different design aspects limit the maximum cell efficiency of the Al-BSF design. Especially the full area metallization and the full area Al-BSF doping of the rear side lead to enhanced recombination and optical losses.

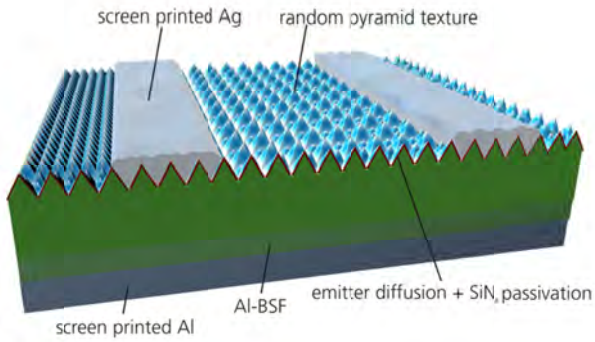

Fig. 4
Schematic Al-BSF solar cell design

2.1.3 PERC / PERL solar cell design

There are several high efficiency silicon solar cell designs, which enable higher maximum cell efficiencies in comparison to the Al-BSF design such as passivated emitter and rear cells (PERC) [8], passivated emitter and rear locally diffused (PERL) cells [9], back contact back junction solar (BC BJ) cells [10, 11] or hetero emitter solar cells. However, each of these concepts comes along with higher fabrication effort due to local doping structures (PERL, BC BJ), local metallization structures (PERC, PERL, BC BJ) or high requirements on pre-cleaning and deposition homogeneity (hetero emitter). Therefore, a main topic in the applied PV research is the development of industrially feasible local doping, structuring or metallization processes.

Within this work local structuring and doping processes will be developed for PERC and PERL solar cell designs. The main difference of these two concepts compared to the Al-BSF design is the replacement of the full area metallization on the rear side by a locally structured and metalized passivation layer. Fig. 5 shows an example of a PERL solar cell with rear side passivation layer and line shaped local back surface field structures. The PERC solar cell design has basically the same features as the PERL design but no local back surface field (LBSF) doping underneath the rear side contacts.

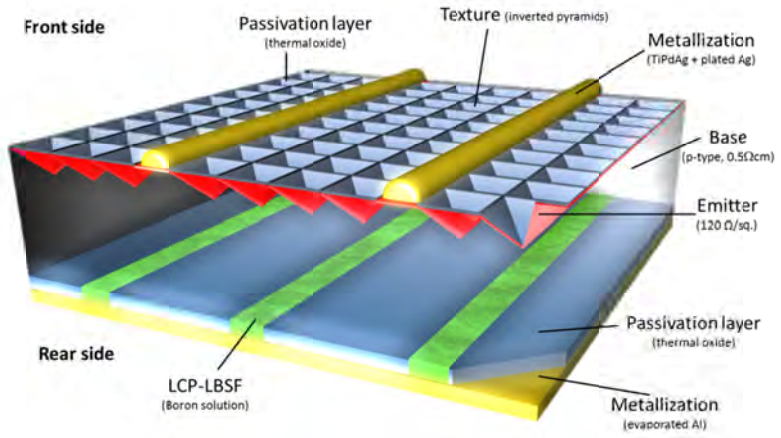

Fig. 5
Schematic of a PERL solar cell design with LBSF line contact design on the rear side. The PERC solar cell design has the same structure only the doping underneath the rear side contacts is missing.

2.2 Electrical characterization of silicon solar cells

The most common electrical characterization technique for silicon solar cells is the measurement of the current density-voltage (JV) characteristic under illumination (light JV) and in the dark (dark JV). The physical interpretation of both measurements is discussed in section 2.1.1. However, both techniques are strongly affected by series resistance effects, which lead to significant differences of the IV curves in early processing stages (without metal contacts) and the final solar cell. Therefore, the application of both methods is usually applied on the finished solar cell.

2.2.1 SunsV_{oc}

The SunsV_{oc} method developed by Sinton et al. [12] is widely used to perform electrical characterizations of solar cells even in early processing stages. The method aims to recreate series resistance free dark JV curve, which equals in first approximation the J_{sc}-V_{oc} curve for varying illumination intensities Ψ. The main assumption of SunsV_{oc} measurements is a linear dependency of the short circuit current density J_{sc} on the illumination intensity. This allows the recreation of the J_{sc}-V_{oc} curve by only measuring the V_{oc} of the solar cell and the simultaneous measurement of the illumination intensity Ψ by a calibrated reference solar cell. The measured illumination intensity can be multiplied by an estimation of the later J_{sc} at one sun of the solar cell resulting in a J_{sc}-V_{oc} curve. The influence of the error of the estimated J_{sc} on the resulting J_{sc}-V_{oc} curve is small and only leads to a shift in the currents of the pseudo J_{sc}-V_{oc} curve but leads to no variation in the shape. If the J_{sc} measurement is not limited by high series resistances, the J_{sc}-V_{oc} curve equals a series resistance free dark JV curve. Therefore, the measured pseudo J_{sc}-V_{oc} curve is also a series resistance free pseudo dark JV curve of the measured solar cell.

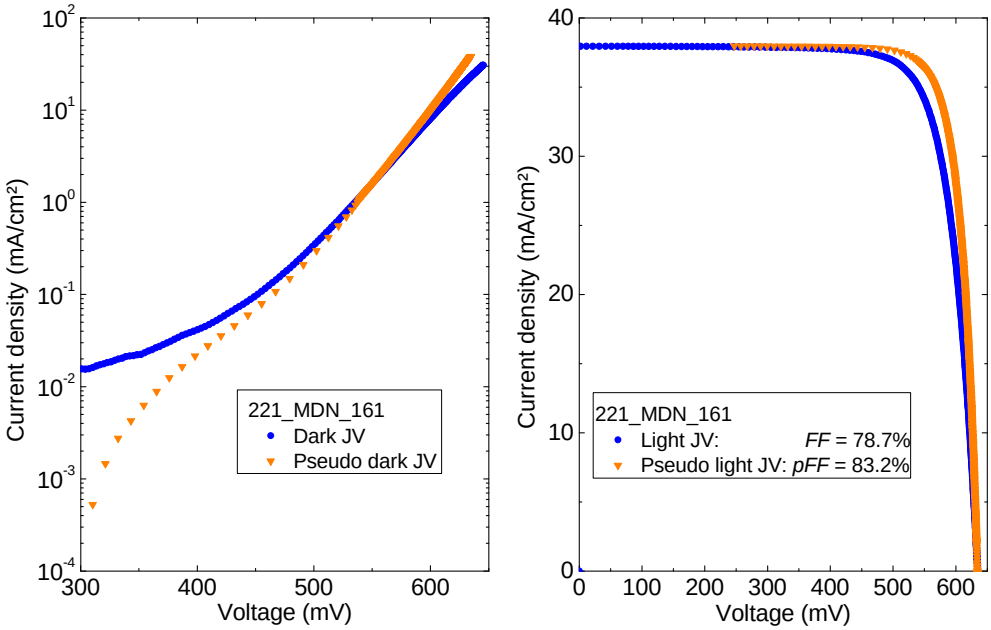

Fig. 6
Comparison of measured dark/light JV curves with the measured pseudo dark/light JV curve by SunsV_{oc}. The current density scale of the pseudo dark JV curve is equivalent to an illumination intensity scale multiplied by the solar cells J_{sc} = 38.0 mA/cm². Both measurements were performed in a Xenon flasher class AAA (25°C, measurement time 25 ms).

The main advantage of the SunsV_{oc} method is the fact that there is no direct current measurement at all, which means that there is in first approximation no net current flowing out of the cell. The only current extraction is the negligible measurement current of the voltmeter determined by its internal resistance. Thus, series resistance effects such as contact resistances[2] [12] or the series resistance of the metallization do not significantly affect the measured SunsV_{oc} curve.

In conclusion the SunsV_{oc} method measures a series resistance free dark JV curve (pseudo dark JV), which can be shifted by an estimated J_{sc} to a series resistance free light JV curve (pseudo light JV). The SunsV_{oc} light JV curve allows the determination of the series resistance free fill factor of the solar cells called pseudo-fill factor (*pFF*). The *pFF* is only influenced by recombination and shunting effects and is a useful parameter in order to evaluate the non-series resistance related limitations of a solar cells fill factor. In the following chapters it will be used in order to evaluate recombination related losses in the fabricated solar cells.

[2] The contact resistance only becomes significant if it is either larger than the internal resistance of the voltmeter or if it is not an ohmic but a Schottky diode contact (see section 2.3.2).

Fig. 6 illustrates the differences of the dark/light JV characteristics (blue data in Fig. 6) compared to the pseudo dark/light JV characteristics (orange data in Fig. 6) measured by the SunsV_{oc} method. The difference of the *FF* and *pFF* can be attributed to series resistance losses, which are also visible in the shallower slope of the dark JV curve (blue data in left plot in Fig. 6) for high currents (see influence of R_s on dark and light JV characteristics in Fig. 2). The difference in the lower voltage or current density (illumination intensity) regime can be attributed to junction capacitance effects [13], which will be discussed in the next section. The J_{sc} estimation for the SunsV_{oc} measurements in Fig. 6 equals the measured J_{sc}.

2.2.2 SunsV_{oc} measurement artifacts

SunsV_{oc} measurements can be used to detect and characterize processing faults such as Schottky contacts during solar cell fabrication. However, the SunsV_{oc} method features for specific sample designs measurement artifacts, which lead to an error in the measured pseudo dark/light curves. These artifacts lead to an over- or underestimation in the determined *pFF* and V_{oc}. Different physical reasons of measurement artifacts of SunsV_{oc} measurements are known from the literature. Examples are junction capacitances [13], high contact resistances [14, 15], shading effects of the contacting probe and/or high sheet resistances of the sample [16] and illumination inhomogeneities, spectral mismatches and height differences [17] or combinations of all of them. Table I summarizes different artifact features and shows exemplary data from the literature.

The presence of a junction capacitance is visible in Table I a) in the lower illumination intensity region and leads to an underestimation of the SunsV_{oc} curve compared to the dark IV curve. In the higher voltage (carrier density) region this effect becomes negligible and the SunsV_{oc} curve converges to the dark IV curve taking into account the series resistance related difference. The physical reason is explained in more detail in [13].

Contact resistance induced features in SunsV_{oc} measurements (see Table I b) have to be divided in two categories. The first one is correlated to Schottky contact induced V_{oc} losses that will be discussed in section 2.3.2 or in Bivour et al. [18]. These losses lead to a difference of the dark IV and pseudo dark IV curve. However, this effect cannot be designated as measurement artifact because this V_{oc} loss effect is also visible in the light IV curve. Therefore, the SunsV_{oc} method measures the real V_{oc} potential in the illuminated state but disagrees with the dark IV curve. In contrast to this the other category of contact resistance induced features in SunsV_{oc} measurements is correlated

to large ohmic contact resistances and leads for increasing contact resistances to a slightly shift of the SunsV_{oc} curve to higher voltages and similar to the Schottky feature to an inflection point in the SunsV_{oc} curve at high illumination intensities. This leads to an artificial overestimation of the measured *pFF*.

Harder et al. [16] analyzed the influence of shading effects of the probing tip and high emitter sheet resistances of the solar cell on SunsV_{oc} measurements (see Table I c). They discovered that in both cases the SunsV_{oc} measurements are shifted for high illumination intensities to lower voltages, which leads not only to lower V_{oc} values but also to an overestimation of the *pFF*. However, the simulations of Harder et al. also showed that the effect of probe contact shading only becomes relevant in the presence of high sheet resistances in the MΩ/sq. regime as in the case of some thin film solar cell applications. In conclusion they stated that for conventional c-Si solar cell designs with emitter sheet resistances below 200 Ω/sq. and voltage probe diameters below 1 mm, the V_{oc} deviation will be below 5 mV.

Roth et al. [17] discovered that setup related problems can lead to small differences in the one digit area between of the V_{oc} measured by SunsV_{oc} and calibrated light IV measurements (see Table I d-f). Examples are spatial illumination inhomogeneities within the measurement area, a spectral mismatch of the SunsV_{oc} flash spectrum and the AM1.5G spectrum and height differences of the reference solar cell and the solar cell sample.

Table I: Summary of measurement artifacts of the SunsV_{oc} method. The shown data are taken form the given references. The simulation cases (i)-(iii) in c) are described in more detail in [16] and represent the case of increasing sheet resistances ($R_{sh,emi}$ = 1.2-750 MΩ/sq., shading radius 50 µm) or increasing shading radius (10-250 µm, $R_{sh,emi}$ = 30 MΩ/sq.), which leads in both cases to the same plot.

	Estimated SunsV_{oc} influence	Dominant region	Ref.
a) Junction capacitance 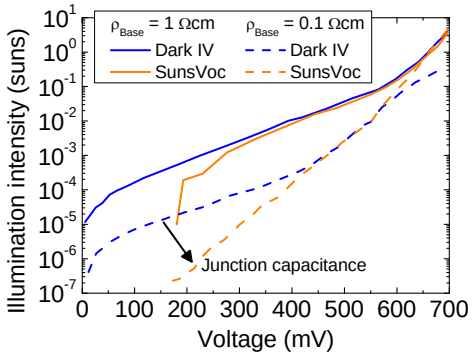	Negligible for Ψ = 1 sun $\|\Delta V_{oc}\|$ < 100 mV if Ψ<10^{-3} suns	Low ρ_{Base} Low Ψ regime	[13]
b) High R_{cont} 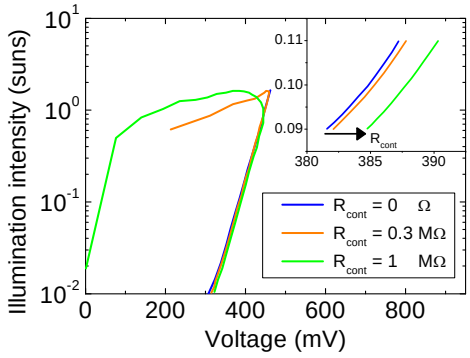	$\|\Delta V_{oc}\|$ < 10 mV if R_c<1 MΩ *pFF* overestimation if bending takes place	Parallel shift to better V_{oc} for all Ψ and inflection point for large Ψ	[14, 15]
c) Probe shading and high $R_{sh,emi}$ 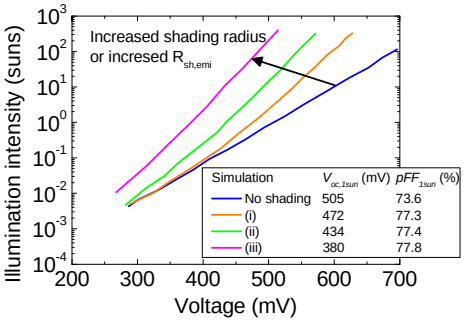	if: R_{sh} < 200 Ω/sq. & d_{probe} < 1 mm then: $\|\Delta V_{oc}\|$ < 5 mV else: $\|\Delta V_{oc}\|$ >> 5 mV, $\|\Delta pFF\|$ < 1%	high illumination intensities	[16]
d) Illumination inhomogeneities	$\|\Delta V_{oc}\|$ < 0.75 mV (metalized) $\|\Delta V_{oc}\|$ < 2 mV (non-metalized)	Large cells	[17]
e) Spectral mismatch	$\|\Delta V_{oc}\|$ < 5.5 mV	Large mismatch monitor cell-sample	[17]
f) Height difference	$\|\Delta V_{oc}\|$ < 0.7 mV/cm	Height difference monitor cell-sample	[17]

2.3 Schottky contacts

2.3.1 Schottky theory

The formation of a metal-semiconductor interface leads to modifications of the energy bands within the semiconductor. The energy band deformation is a result of a work function difference between the metal and the semiconductor. The work function defines the energy difference of the Fermi level E_F and the vacuum energy level E_{vac}. The work function mismatch at the metal-semiconductor interface leads to the formation of an energy barrier schematically shown in Fig. 7.

Depletion
p-type: $\phi_{f,m} < \phi_{f,Si}$
n-type: $\phi_{f,m} > \phi_{f,Si}$

Accumulation
p-type: $\phi_{f,m} > \phi_{f,Si}$
n-type: $\phi_{f,m} < \phi_{f,Si}$

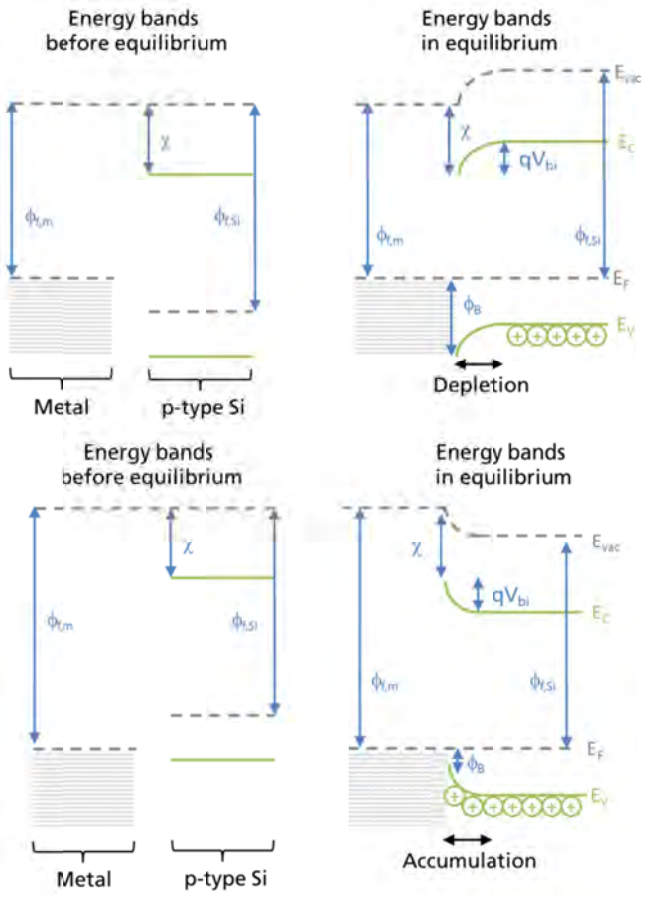

Fig. 7
Energy band diagrams of a metal-semiconductor contact (p-type Si) before and after equilibrium for two types of work function differences.

The characteristic of the band bending at the interface strongly depends on the work functions of the metal $\phi_{f,m}$ and the semiconductor $\phi_{f,Si}$. In equilibrium the Fermi level E_F in both materials is the same and the conduction and valence band E_C and E_V show a bending, which is determined by the work function difference or so called built-in voltage $qV_{bi} = \phi_{f,m}-\phi_{f,Si}$. This system can also be described by the barrier height ϕ_B, shown in Eq. (5). ϕ_B is defined as the difference of the metal work function and the

electron affinity χ of the semiconductor and depends on the doping type of the semiconductor. The sum of $\phi_{B,n}$ and $\phi_{B,p}$ gives the band gap energy E_g (see Eq. (6)).

n-type Si: $\phi_{B,n} = \phi_{f,m} - \chi$
p-type Si: $\phi_{B,p} = E_g - (\phi_{f,m} - \chi)$ (5)

$$E_g = \phi_{B,p} + \phi_{B,n} \quad (6)$$

The band bending leads either to an accumulation or depletion at the contact interface illustrated in Fig. 7. In the case of accumulation the contact shows ohmic behavior and for the case of depletion rectifying so called Schottky diode behavior. The current flow is hindered by the Schottky barrier and can only be realized by thermionic emission, thermionic field emission or field emission tunneling. The probability of each mechanism strongly depends on the barrier height and width, which can also be influenced by additional doping at the contacts. Fig. 8 shows the three current transport mechanisms at the interface of Schottky contacts.

For undoped contacts as in the case of rear side contacts of some PERC solar cell designs, the transport is limited to thermionic emission. If that is the case the Schottky contact can be described by a Schottky diode equation with an ideality n_s shown in Eq. (7) [19, 20]. The ideality of most Schottky diodes is $n_S \approx 1$.

$$J(V) = J_{01,S}\left(e^{\frac{qV}{n_S k_B T}} - 1\right) \quad (7)$$

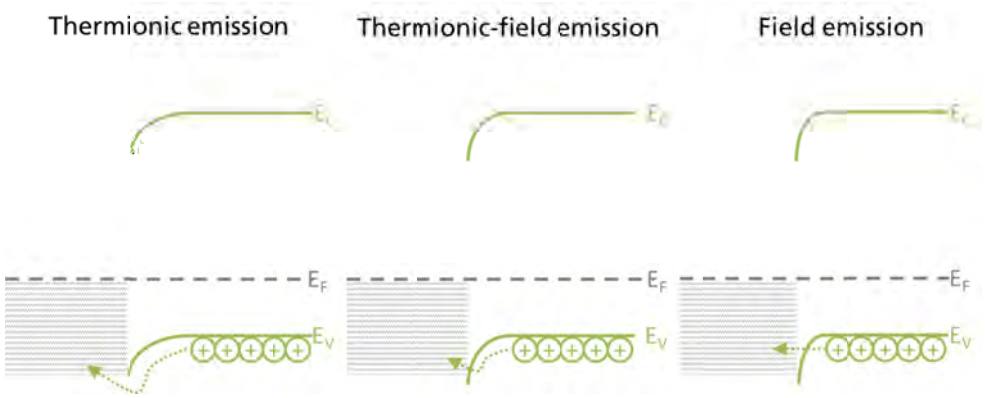

Fig. 8
Current transport mechanisms at a metal semiconductor (p-type) interface.

The saturation current density $J_{01,S}$ of the Schottky diode is given by Eq. (8) [19]. A_x^* is the Richardson constant (p-type Si: (32 ± 2) $Acm^{-2}K^2$ [21], n-type Si: (112 ± 6) $Acm^{-2}K^2$ [21]).

$$J_{01,S} = A_x^* T^2 e^{-\frac{q\phi_B}{k_B T}} \quad (8)$$

The barrier height depends on the silicon dopant species and the applied metal. Table II shows measured barrier heights from the literature for different contact types on n- and p-type Si.

Table II: Barrier heights on n-type ($\phi_{B,n}$), p-type Si ($\phi_{B,p}$) and work functions ϕ_f of various metals [19, 22-24] measured at 300 K.

Element	$\phi_{B,n}$ (eV)	$\phi_{B,p}$ (eV)	ϕ_f (eV)
Ag	0.78	0.54	4.26 - 4.74
Al	0.45 - 0.72	0.4 - 0.75	4.06 - 4.26
Au	0.8	0.34	5.1 - 5.47
Cu	0.58	0.46	4.53 - 5.1
Ni	0.61 - 0.66	0.51	5.04 - 5.35
NiSi	0.65 - 0.78	-	4.82
Ni_2Si	0.66 - 0.75	-	4.94 - 4.96
$NiSi_2$	0.63 - 0.79	-	5.03
Pd	0.81	-	5.22 - 5.6
Pt	0.9	-	5.12 - 5.93
Si	-	-	4.05 + ΔE_F
Ti	0.5	0.61	4.33
W	0.67	0.45	4.32-5.22

The barrier height depends not only on the work function difference between metal and semiconductor but also on the surface condition at the interface. Therefore, the measured values in Table II show a wide spreading. The data of Card [25] in Fig. 9 show exemplarily for the case of Al that oxide layers at the interface of Al-Schottky contacts on p- and n-type Si have a significant impact on the measured barrier heights. These thin oxide layers can be formed due to native oxide growth and before the metallization or even after metallization. Furthermore, Card [25] showed that thermal treatments significantly change the measured barrier heights.

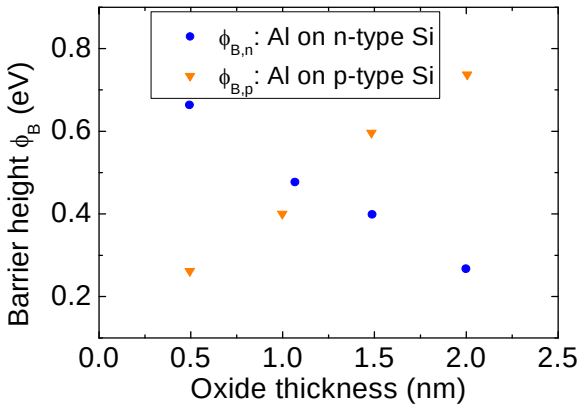

Fig. 9
Barrier height dependence of Al on p- and n-type Si on the oxide thickness at the interface (data from [25])

As shown in Fig. 8 the current transport at the Schottky contact is dominated by three transport mechanisms: thermionic emission, thermionic field emission and field emission. The probability of each mechanism is a function of the surface doping concentration at the metal-semiconductor interface and the Schottky barrier height. Therefore, the contact resistance is limited by the resistance of the dominating transport mechanism. Models for the contact resistivity for each mechanism are published in [19, 26, 27]:

Thermionic emission (TE):

$$\rho_{c,TE}(N_x,\ \phi_B) = \frac{k_B}{qA_x^*T} e^{\frac{q(\phi_B - \Delta\phi(N_x))}{k_B T}} \tag{9}$$

Thermionic field emission (TFE):

$$\rho_{c,TFE}(N_x,\ \phi_B) = \frac{k_B}{qA_x^*T} C_1(N_x,\ \phi_B) e^{\frac{2\sqrt{K_S\varepsilon_0 m_T^*}(\phi_B - \Delta\phi(N_x))}{q\hbar\sqrt{N_x}\coth\frac{E_{oo}(N_x)}{k_B T}}} \tag{10}$$

Field emission (FE):

$$\rho_{c,FE}(N_x,\ \phi_B) = \frac{k_B}{qA_x^*T} C_2(N_x,\ \phi_B) e^{\frac{2\sqrt{K_S\varepsilon_0 m_T^*}(\phi_B - \Delta\phi(N_x))}{q\hbar\sqrt{N_x}}} \tag{11}$$

Parameters:

$$\Delta\phi(N_x) = \frac{q^3 N_x (V_{Bi} - k_B T/q)}{8\pi^2 K_S \varepsilon_0^3} \tag{12}$$

$$C_1(N_x,\ \phi_B) = \frac{k_B T \cosh\left(\frac{E_{oo}(N_x)}{k_B T}\right)\sqrt{\coth\left(\frac{E_{oo}(N_x)}{k_B T}\right)}}{\sqrt{\pi q\left(\phi_B + \Delta E_{F,x}(N_x)\right)E_{oo}(N_x)}} e^{\frac{q\Delta E_{F,x}(N_x)}{E_{oo}(N_x)\coth\left(\frac{E_{oo}(N_x)}{k_B T}\right)} - \frac{q\Delta E_{F,x}(N_x)}{k_B T}} \tag{13}$$

$$E_{oo}(N_x) = \frac{q\hbar}{2}\sqrt{\frac{N_x}{m_T^* K_S \varepsilon_0}} \tag{14}$$

$$C_2(N_x,\,\phi_B\,) = \left(\frac{\pi}{\sin\left(\frac{\pi k_B T \ln\left(\frac{-4\,\phi_B}{\Delta E_{F,x}(N_x)}\right)}{2E_{oo}(N_x)} \right)} - \frac{2E_{oo}(N_x)}{k_B T \ln\left(\frac{-4\,\phi_B}{\Delta E_{F,x}(N_x)}\right)} e^{\frac{-q\Delta E_F \ln\left(\frac{-4\,\phi_B}{\Delta E_{F,x}(N_x)}\right)}{2E_{oo}(N_x)}} \right)^{-1} \quad (15)$$

Eqs. (9) - (15) fully describe the contact resistivity for each transport mechanism. The contact resistivity models depend on the dielectric constant of Si K_S = 11.9 [24], the vacuum permittivity $\varepsilon_0 \approx 8.8542 \cdot 10^{-12}\,\frac{A\,s}{V\,m}$, the effective mass of the tunneling electron $m_T^* = 0.3\,m_e$ [28] with the electron elementary mass m_e, the reduced Planck constant $\hbar$ and the difference $\Delta E_{F,n}$ or $\Delta E_{F,p}$ of the majority energy band E_C or E_V and the Fermi energy level E_F:

$$\Delta E_{F,n}(N_D) = E_{C,n}(N_D) - E_{F,n}(N_D) \quad (16)$$
$$\Delta E_{F,p}(N_A) = E_{F,p}(N_A) - E_{V,p}(N_A) \quad (17)$$

Fig. 11 shows the modeled effective contact resistivity and measured values by Schroder [29] for varying surface doping concentrations on p-type Si. It can be seen that for low doping densities the experimental contact resistivities are significantly lower than the modeled values for aluminum ($\phi_B = 0.4 - 0.75$ eV) on p-type Si. The reason for this is assumed to be caused by an alloying of the Al and the Si, which increases the effective interface doping density for lowly doped or undoped surfaces.

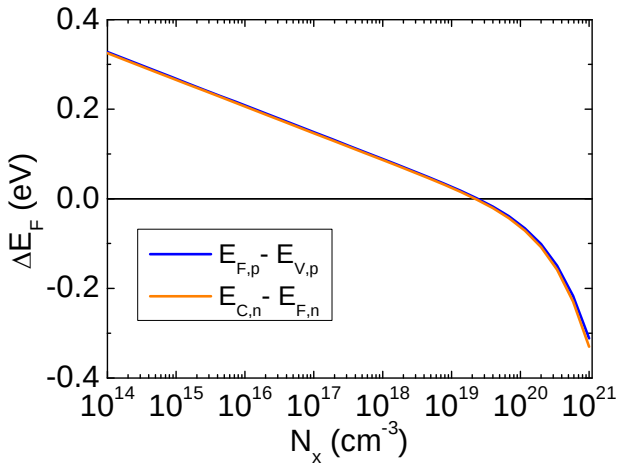

Fig. 10
Difference $\Delta E_{F,p}$ and $\Delta E_{F,n}$ of the majority energy band E_C or E_V and the Fermi energy level E_F at 300 K, calculated with the PV Lighthouse [30] band gap calculator taking into account band gap narrowing by Schenk [31] and assuming Fermi-Dirac statistics and complete dopant ionization.

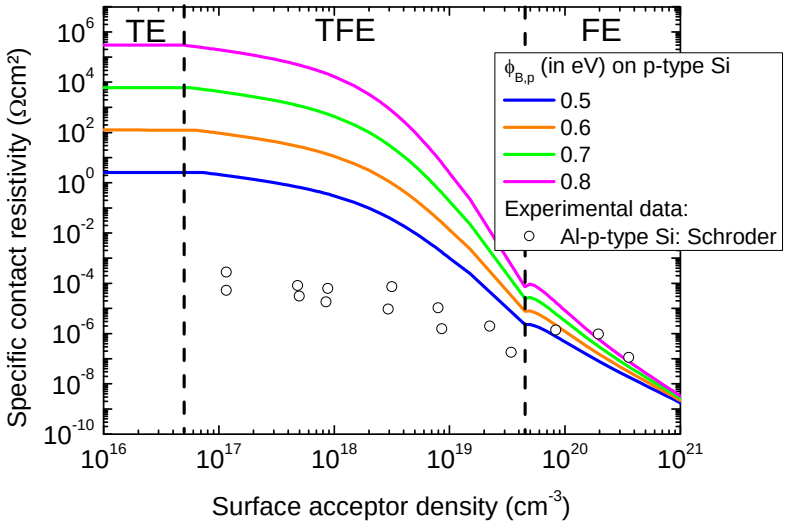

Fig. 11
Modeled and measured [29] contact resistivities for aluminum on p-type Si.

The appearance of Schottky barriers at the front or rear side contact of solar cells has a detrimental influence on the solar cell performance. Depending on the location of the Schottky contact and the orientation of the Schottky diode, the open circuit voltage can be decreased and the series resistance can be increased leading to a decrease in solar cell efficiency. The following will analyze the impact of Schottky contacts on the electrical characteristics of silicon solar cell.

2.3.2 Electrical characteristics of Schottky contacts in solar cells

Locally contacted solar cell designs such as PERC or PERL solar cells sometimes suffer under the detrimental consequences of rear side Schottky contacts. Especially for low base resistivities the work function mismatch can lead to increased barrier heights, which create a Schottky diode in reverse to the pn-junction diode on the front side. Fig. 12 shows a schematic of the equivalent circuit of this system.

The system in Fig. 12 is divided in two parts which describe the recombination and generation currents in in the pn-junction solar cell (J_{01}, J_{02}, J_{Auger}) and the Schottky diode (J_S, $R_{p,S}$). The Schottky diode can be described by Eq. (7) and creates a recombination current source in series to the pn-junction diode system. Furthermore, the Schottky diode has a shunt resistance in parallel, which correlates to the rear contact resistance.

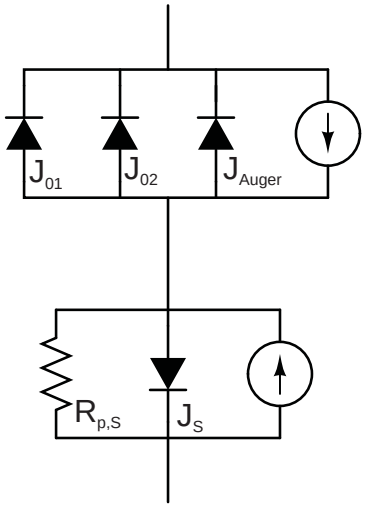

Fig. 12
Equivalent circuit of a solar cell with front or rear side Schottky contact.

Electrical characteristic of Schottky contacts in SunsV_{oc} measurements

The electrical characteristic of a pn-Schottky diode system can be experimentally characterized by SunsV_{oc} measurements [32]. SunsV_{oc} measurements (see section 2.2.1) are an easy and common way to measure the open circuit voltage and a series resistance free pseudo-light-IV curve of the cell. In open circuit conditions the generated current $I_{gen} = \Psi I_{sc}$ is compensated by the recombination currents at the Schottky diode I_s and the pn-junction diode I_{pn}. (see Eq. (18)). As shown in Fig. 12 the pn-Schottky diode system can be described by two recombination current sources, which are connected in series. Therefore, the voltages in the subsystems are defined by Eq. (19).

$$\Psi I_{sc} = I_S(V_S) + I_{pn}(V_{pn}) \quad (18)$$

$$V_{oc,ext} = V_{pn} - V_S \quad (19)$$

The external voltage V_{ext} of the system is the difference of the subsystem voltages[3]. The whole system equals a modified Ebers-Moll equivalent circuit as described by Sproul et al. [33], where the ratio of the two recombination currents I_S and I_{pn} is expressed by the factors $\alpha_S + \alpha_{pn} = 1$. Each recombination current can be expressed in Eqs. (21) and (20) using α_S and α_{pn}, which are influenced by the generation profile, the diffusion lengths in the solar cell and the solar cell geometry. In the following the factors are set to $\alpha_S = 0.5$ and $\alpha_{pn} = 0.5$, which represents the case of a homogenous generation profile in the sample and equally distributed recombination

[3] Please note that the different algebraic signs of V_s and V_{pn} are a consequence of the different diode orientations in Fig. 12.

currents at the pn-junction and Schottky diode. This case is representative for the effect of Schottky diodes in SunsV$_{oc}$ measurements. If $\alpha_S < 0.5$ the effects shown in the following are weakened and the systems acts more and more like a conventional pn-junction diode and vice versa for $\alpha_S > 0.5$.

$$I_{pn}(V_{pn}) = \alpha_{pn}\,\Psi I_{sc} \quad (20)$$

$$I_S(V_S) = \alpha_S\,\Psi I_{sc} \quad (21)$$

The recombination current in each subsystem can be described by its equivalent circuit models shown in Eq. (22) and (23).

$$I_{pn}(V_{pn}) = A_{cell}\left(J_{01}\left(e^{\frac{qV_{pn}}{kT}}-1\right)+J_{02}\left(e^{\frac{qV_{pn}}{2kT}}-1\right)+qWC_An_i(T)^3\left(e^{\frac{3qV_{pn}}{2kT}}-1\right)+\frac{V_{pn}}{R_{p,pn}}\right) \quad (22)$$

$$I_S(V_S) = A_S\,A^*T^2e^{-\frac{q\phi_B}{kT}}\left(e^{\frac{qV_S}{n_SkT}}-1\right)+\frac{A_{cell}V_S}{R_{p,S}} \quad (23)$$

The pn-junction current I_{pn} is described by an enhanced two diode model including the saturation current densities J_{01} and J_{02}, the elementary charge q, the Boltzmann constant k, the temperature T, the active cell area A_{cell}, the wafer thickness W, a parallel resistance $R_{p,pn}$, the temperature dependent ambipolar Auger coefficient $C_A(T) = \frac{1.1\cdot10^{-28}}{T-193} + 2.1\cdot10^{-33}T$ [34] and the temperature dependent intrinsic carrier density $n_i(T) = 1.64\cdot10^{13}T^{1.706}e^{-\frac{qE_g}{2kT}}$ in cm^{-3} [33] with the band gap energy E_g in eV. In Eq. (22) the conventional 2 diode model is enhanced with an additional Auger recombination part, which becomes important for high injection scenarios which are relevant for SunsV$_{oc}$ measurements. The current in the Schottky subsystem is described in Eq. (23) by the Schottky diode equation shown in Eq. (7). Schottky contacts in solar cells are usually a result of process inhomogeneities or processing faults. Therefore, they usually appear not as homogenous contact but as inhomogeneous distribution of Schottky and ohmic contacted regions. This is taken into account in Eq. (23) by an additional parallel resistance $R_{p,S}$, which reduces the recombination current at the Schottky diode. Eqs. (19) - (23) can be used to model a SunsV$_{oc}$ measurement of a solar cell with a rear side Schottky contact. The solutions V_{pn} and V_S of Eqs. (19) - (23) are the voltages of each subsystem and their difference gives the externally measurable open circuit voltage for each illumination intensity.

Table III: Simulation parameters for the Schottky contact simulations.

Parameter		Unit
J_{01}	$50 \cdot 10^{-15}$	A/cm²
J_{02}	$5 \cdot 10^{-9}$	A/cm²
ϕ_B	0.5	eV
n_S	1	
A_{cell}	4	cm²
A_S	0.2	cm²
I_{sc}	0.156	A
T	298.15	K
W	0.02	cm
$R_{p,pn}$	10^5	Ωcm²
$R_{p,S}$	2	Ωcm²
α_S	0.5	
α_{pn}	0.5	

Using numerical solvers Eqs. (19) - (23) were solved in this work for a typical intensity illumination range of a SunsV_{oc} measurement: $\Psi = 0.01 - 1000$ suns. In order to examine the relevant influence parameters on the V_{pn} and V_S results, a representative set of solar cell parameters of a high efficiency solar cell is defined and shown in Table III. The parameter list includes a rear side Schottky diode defined by ϕ_B, $R_{p,S}$ and A_S. The parameter set is similar to the high efficiency PERL and PERC solar cell design used in chapter 3.

Fig. 13 shows the simulated voltages at the pn-diode, the rear side Schottky diode and the simulated external voltage of a SunsV_{oc} measurement. As shown in Eq (19) the external voltage is defined as difference of the pn- and Schottky-diode voltage. The simulated curve in Fig. 13 illustrates that for low illumination intensities the measured external voltage V_{ext} during the SunsV_{oc} measurement is completely dominated by the pn-junction diode and only for high illumination intensities the impact of the rear side Schottky diode becomes relevant.

The numerical solutions of Eqs. (19) - (23) can also be used to identify the characteristic influence of the different Schottky diode parameters on the SunsV_{oc} curve. Fig. 14 illustrates the impact of different barrier heights (top left plot), Schottky shunt resistances (top right plot), Schottky ideality factors (center left plot), Recombination current ratio factor α_s (center right plot) and the pn-junction saturation current densities (bottom left and right plot) on the SunsV_{oc} curve.

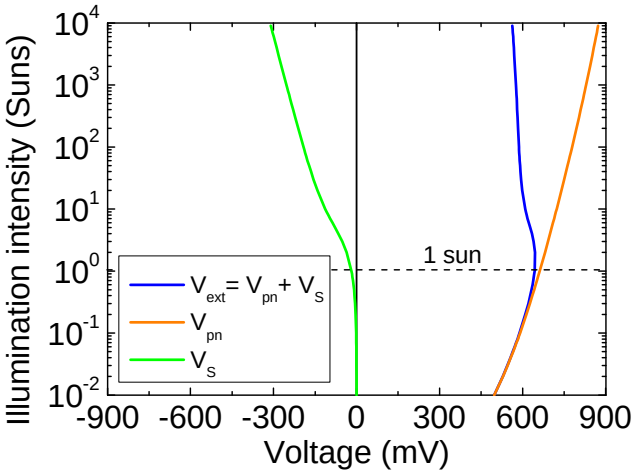

Fig. 13
Simulated SunsV_{oc} measurement of the external voltage (V_{ext}, blue line) of a pn-junction solar cell (V_{pn}, orange line) with additional rear side Schottky contact (V_S, green line) by numerical solution of Eqs. (19) - (23) using the simulation parameters in Table III.

An increase of the barrier height (top left plot) results in a shift of the SunsV_{oc} curve in the high illumination range to lower voltages. This shift equals the voltage difference of the according barrier heights.

The variation of the Schottky shunt resistance (top right plot) demonstrates that the parallel resistance to the Schottky diode determines the lowest illumination intensity level at which the bending of the SunsV_{oc} curve starts.

In general the ideality factor of the Schottky diode is assumed to be unity. However, several publications [35-38] show that interfacial insulating layers, doped layers, rough or damaged semiconductor surface, silicide formation or an image force effect at the barrier can cause non-idealities, which usually slightly increase the ideality factor Schottky diodes in reality. The variation of the ideality factor of the Schottky diode in Fig. 14 (center left plot) determines the slope of the SunsV_{oc} curve in the high illumination range. As shown by Glunz et al. [32] the external voltage is proportional to: $\lim_{\psi\to\infty} V_{ext} \sim (n_{Auger} - n_S)$, with $n_{Auger} = \frac{2}{3}$.

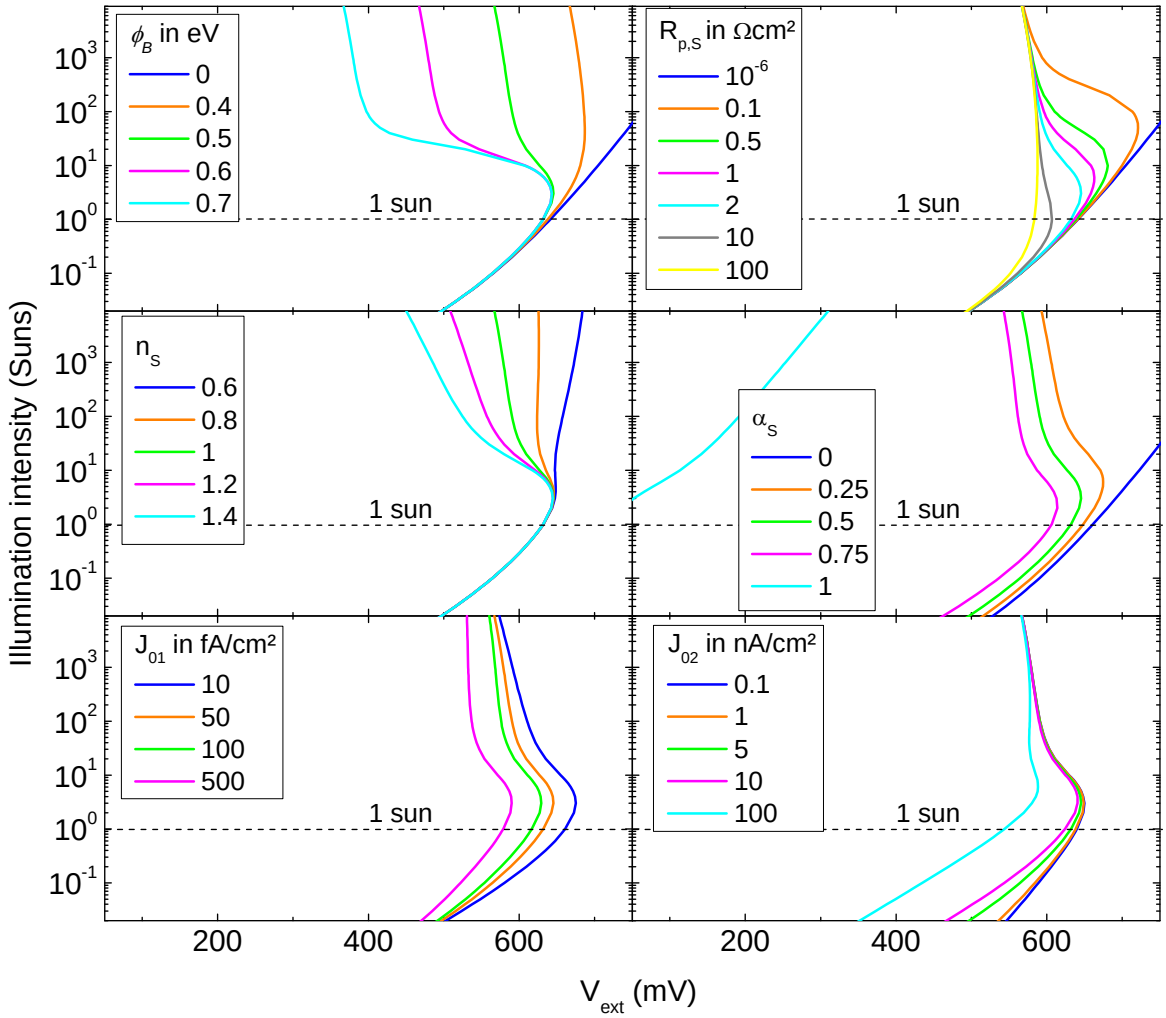

Fig. 14
Simulated SunsV_{oc} curves of a solar cell with rear side Schottky contact obtained by numerical solution of Eqs. (19) - (23) using the simulation parameters given in Table III and varying Schottky barrier height ϕ_B, parallel resistance to the Schottky diode $R_{p,S}$, the area of the Schottky diode A_S, saturation current density J_{01} and J_{02} of the pn-junction and the ideality factor n_S of the Schottky diode. Please note that for α_s = 1in the center right plot the voltages of the cyan curve are multiplied by -1 for better comparability. The cyan curve is completely dominated by the Schottky diode, which would lead to negative external voltages.

The recombination current ratio factor (center right plot) displays the dominant recombination region in the solar cell. If the generated minority charge carriers recombine dominantly at the Schottky diode ($0.5 < \alpha_S \leq 1$) the SunsV_{oc} curve is less and less dominated by the pn-junction diode behavior. The low recombination current at the pn-junction leads to a low pn-junction voltage, which shifts the SunsV_{oc} curve to lower voltages for increasing α_s. Furthermore, the negative slope of the Schottky diode behavior leads to lower inflection voltages of the SunsV_{oc} curve for increasing α_s.

The pn-diode parameters J_{01} and J_{02} also influence the SunsV_{oc} curve (bottom left and right plot). The increase of J_{02} results in a shift of the curve in the low illumination intensities to lower voltages. Furthermore, the increase of J_{01} causes a shift of the curve in the whole illumination intensity range to lower voltages.

Fig. 13 and Fig. 14 demonstrate that a rear side Schottky contact limits the open circuit voltage of a solar cell. Depending on the barrier height and the availability of alternative current paths by a parallel resistance $R_{p,S}$, the impact of the Schottky contact on the open circuit voltage can be already visible at one sun and therefore, be visible in a light IV-curve and the cell efficiency.

For solar cells with ohmic contacts the SunsV_{oc} measurement of the illumination intensity – open circuit voltage curve equals the series resistance free dark IV-curve of the solar cell and is usually called pseudo dark-IV curve. The difference of the short circuit current density and the pseudo dark-IV allows the determination of a series resistance free pseudo light-IV. In the presence of a rear side Schottky contact the determination of a pseudo dark IV by SunsV_{oc} is not valid anymore. The Schottky induced bending of the SunsV_{oc} curve is not present in a dark IV-measurement of a Schottky limited solar cell and can lead even to pseudo fill factors above unity for the pseudo light IV curve.

Electrical characteristic of Schottky contacts in dark IV measurements

The impact of a rear side Schottky contact on the dark IV curve is not as significant as for SunsV_{oc} or light IV measurements. The dark IV measurement represents the resulting recombination current in forward bias of the pn-junction diode. According to Eq. (18) and (19) this leads to the same current at the pn-diode and the Schottky diode. However, the opposite direction of the pn- and Schottky-diode leads to an opposite algebraic sign of I_{pn} and I_S. Including a parallel resistance to the rear side Schottky contact the dark IV measurement is defined by Eq. (24).

$$I_{pn}(V_{ext} + V_S) + I_S(V_S) + A_{cell}\frac{V_S}{R_{p,S}} = 0 \qquad (24)$$

For a sweep of the applied external voltage Eq. (24) can be solved numerically using the definitions of I_{pn} and I_S in Eq. (22) and (23). The solution gives a simulated dark IV curve[4] of a solar cell with a rear side Schottky contact.

[4] The series resistance R_s of the pn-junction diode is not taken into account in this simulation.

a) b)

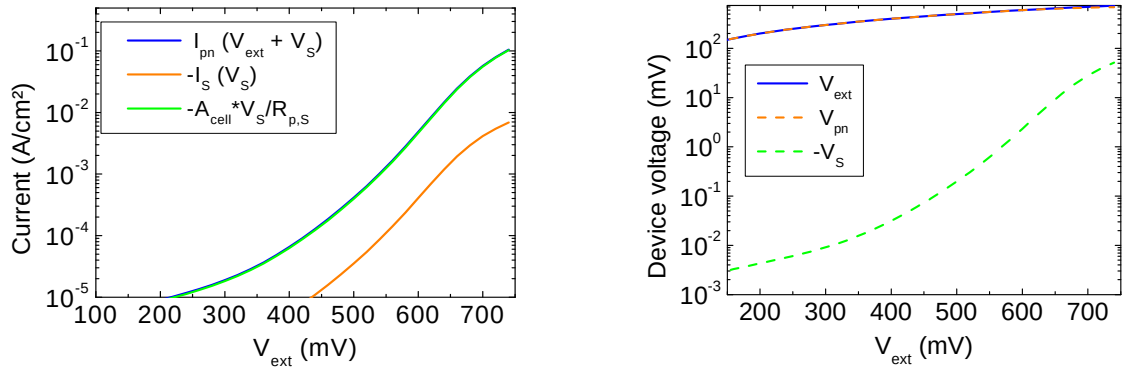

Fig. 15
Simulated dark IV measurement and the according device voltages at the pn- and Schottky diode as function of the external voltage of a solar cell with rear side Schottky contact by numerical solution of Eq. (24) using the simulation parameters in Table III.

Using the simulation parameters shown in Table III the numerical solutions of Eq. (24) gives an understanding why the Schottky contact is not dominating the dark IV curve. The simulated currents in Fig. 15 a) illustrate that for the assumed value of the parallel resistance $R_{p,S}$, the current path along the parallel resistance is the dominant one on the rear side for the whole external voltage range. Therefore, the dark IV measurement significantly differs from the pseudo dark IV from the SunsV_{oc} measurement. Fig. 15 b) shows the according voltages at the front and rear side for the applied external voltage range.

Although the impact of the Schottky diode on the dark IV curve is not as dominant as in the SunsV_{oc} curve, there is an influence in the higher voltage range. Fig. 16 illustrates the influence of different barrier heights (top left plot), Schottky shunt resistances (top right plot), Schottky ideality factors (center left plot), Schottky contact areas (center right plot) and both saturation current densities (bottom left and right plot) on the dark IV curve. Despite the known behavior of J_{01} and J_{02} in the low and mid-voltage regime of the dark IV curve (bottom left and right plot), there is an impact of the Schottky barrier height ϕ_B (top left plot) and the Schottky shunt resistance $R_{p,S}$ (top right plot) in the higher voltage regime. For high barrier heights or high parallel resistances the Schottky diode influences the dark IV curve similar to the impact of high series resistances on the solar cell dark IV characteristic. The Schottky ideality factor (center left plot) and the Schottky area (center right plot) have no significant influence on the dark IV curve.

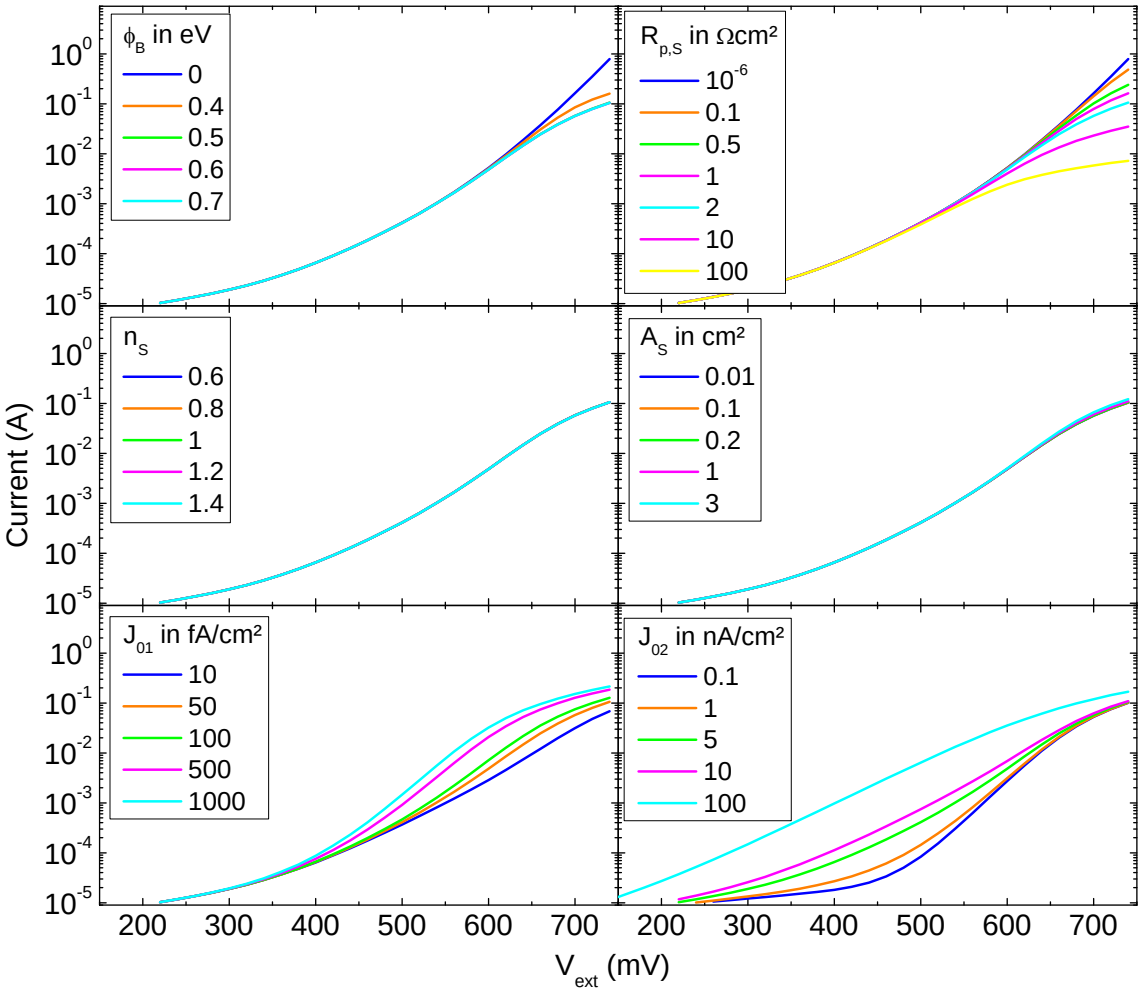

Fig. 16
Simulated dark IV measurement of a solar cell with rear side Schottky contact by numerical solution of Eq. (24) using the simulation parameters in Table III and varying Schottky barrier height ϕ_B, parallel resistance to the Schottky diode $R_{p,S}$, the area of the Schottky diode A_S, saturation current density J_{01} and J_{02} of the pn-junction and the ideality factor n_S of the Schottky diode.

In conclusion the simulation results in Fig. 14 and Fig. 16 show that a rear side Schottky contact leads to a characteristic inflection in the SunsV_{oc} measurement of the pseudo dark IV curve but has only a small impact on the dark IV measurement. In the dark IV case Schottky contacts induce to decreased slopes in the higher voltage regime similar to the impact of high series resistances.

Further discussion on the influence of Schottky contacts on the electrical performance of silicon solar cells are shown in chapter 3. The experimental data in section 3.5 will demonstrate even though the Schottky contacts are not directly visible in the dark IV

curve, the Schottky induced losses can dominate the characteristic of the light IV curve and limit the solar cells *FF* and V_{oc}.

2.4 Process technologies for industrially feasible silicon solar cell designs

Advanced solar cell designs such as PERL (see section 2.1.3) usually feature local doping and passivation structures in combination with narrow metal contact structures. The conventional processing schemes in a lab-type environment are based on photolithographic (PL) mask and etch processes and PL structured evaporation of suited metals such as Al, Ti, Pd and/or Ag. These processes are with state-of-the-art technology not transferable to mass production due to low throughput and high processing costs, though. Therefore, alternative processing routes have to be found in order to realize similar cell designs with industrially feasible processing technologies. The following sections will give an overview of state-of-the-art processes for industrially feasible high efficiency silicon solar cell designs. The focus of the discussed processes is on laser based process technologies, which allow a simultaneously processing of local doping structures and local contact openings of the passivation layer.

2.4.1 Industrially feasible selective emitter technologies

There are a variety of processing technologies to create industrially feasible n-type selective emitter (SE) structures for silicon solar cells, which have their specific pros and cons depending on the aimed cell design and their interaction with other process technologies within the processing chain. Therefore, a substantiated evaluation of suitable SE technologies is only possible within the complete processing chain. Hahn [39] gives an overview of state-of-the-art SE processes including silicon ink printing [40], ion implantation [41], etch-back technology [42], oxide mask diffusion [43], PSG laser doping [44-46], laser doped selective emitter (LDSE, see section 2.4.3) [47-50] and laser chemical processing (LCP, see section 2.4.4). The non-laser based technologies in this list and PSG laser doping are located in the process chain at some point before the passivation layer formation. Therefore, the processes only create a highly doped region in the later metalized regions or -as in the case of the etch-back process- decreases the doping concentration in the later non-metalized regions. The application of these processes requires an alignment procedure [51] for the following metallization process and is mostly combined with screen printed contacts.

LDSE and LCP offer the possibility to combine a local highly doped region with a self-aligned passivation layer opening. The local passivation opening allows the

application of self-aligned plating of the metal contacts. The introduction of plated metal contacts can give an additional benefit in terms of cell efficiency and processing costs due to a lower sensitivity of the contact resistivity on the surface doping concentration, narrow contact widths and the replacement of Ag as contact material with low cost alternatives such as a stack of plated Ni-Cu.

2.4.2 Industrially feasible local back surface field technologies

Many of the SE processes presented in section 2.4.1 could in principle be used for the formation of n- or p-type local back surface field structures (LBSF). Generally, processes such as ion implantation or laser doping from a spin-on dopant could be easily adapted for the formation of LBSF structures. However, for p-type LBSF doping structures two laser based local Al doping processes have become the most popular technology for industrial applications. The first technology is the laser fired contact process (LFC, see section 2.4.3) developed by Schneiderlöchner et al. [52] by using an evaporated or screen printed Al layer on top of the rear side passivation as laser doping source and as rear metal contact. The alternative process developed by Agostinelli et al. [53] uses laser structuring to create local rear side passivation layer openings and a subsequently Al screen printing and Al-Si alloying process in a conveyor belt furnace (firing) in order to create local p-type doped rear contact regions.

The main developments of industrially feasible n-type LBSF structures are also mostly based on laser doping processes. The main difference of the developed laser doping processes is the used doping source. The PasDop process developed by Suwito et al. [54] uses the rear side passivation layer as phosphorus doping source by applying a PECVD deposition of phosphorus rich $Si_{1-x}C_x$, SiN_xO_y or SiN_x [55] layers and subsequently perform a laser process in order to get locally doped contact openings. Other processes use liquid doping sources such as phosphoric acid applied by either spin/spray-on processes [56] or by using LCP [57].

2.4.3 Local doping and passivation structuring

Wet film laser doping (WFLD)

The term wet film laser doping (WFLD) will be used in this work for the description of different laser doping processes, which have in common that they use a galvanometric scanner system in order to guide the laser spot over the sample and that they use a wet film on top of the sample as doping source. The most popular WFLD process is an n-type laser doping process called laser doped selective emitter (LDSE) developed by the University of New South Wales in Sydney. The laser doped selective

emitter (LDSE) process [2, 58] is a method to locally structure a passivation layer and simultaneously create a highly n-type doping profile within the opening. The LDSE process uses a liquid dopant source, which is applied on top of the passivation layer, using spin-on or spray-on techniques. After an optional baking step of the liquid the passivation layer is locally patterned by a focused laser spot guided over the sample by using a galvanometric scanner system. LDSE is mostly used in combination with a plated metallization scheme, such as Ni-Ag or Ni-Cu plating, which enables a self-alignment due to the locally passivation layer pattern. Fig. 17 shows a schematic of the LDSE process in order to form a local highly doped region for a selective emitter design. Recent publications showed very high cell efficiencies with LDSE and plated front side contacts for Al-BSF solar cells [48, 49] and PERL solar cells [50] with cell efficiencies of up to 19.8% and 20.3%, respectively.

The application of different liquid layers for WFLD allows either n-type or p-type doping structures by using phosphoric acid or commercially available boron spin-on dopants, respectively. The application of highly focused laser beams allows the formation of narrow structuring widths down to 5-10 µm, which is perfectly suited in combination with fine line metallization processes such as metal plating. The WFLD process used in section 6.5 in this work was developed by Christian Geisler using a continuous wave laser system with a wavelength of 532 nm and a spun-on 30% H_3PO_4 layer as phosphorus doping source.

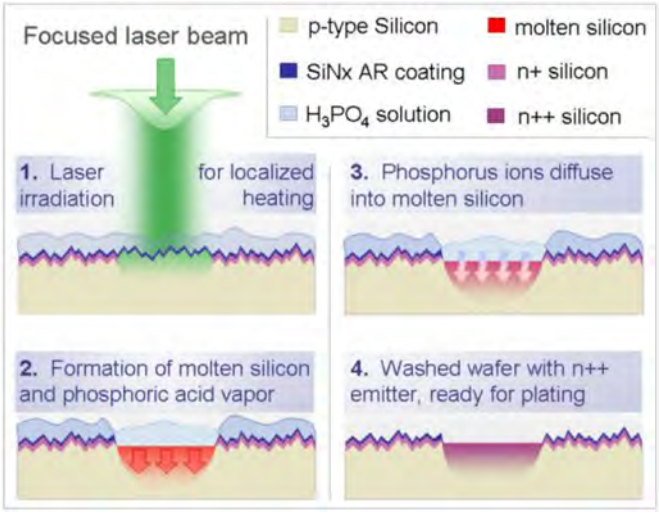

Fig. 17
Schematic of the LDSE passivation layer patterning and local n-type doping process (from [59]).

Local Aluminum doping structures

The full area back surface field doping of conventional p-type BSF-solar cell designs is based on alloyed p-type doping profiles using screen printed Al-pastes. However, advanced solar cell designs such as PERL solar cells require locally doped contact structures. One approach to form locally p-type doped structures is the use of Al metal layers as doping source and local structuring processes of passivation layers as local contact pattern. Within the last decade two laser based approaches proved to be suitable to create industrially feasible Al-local back surface fields. The first approach is the laser fried contact process (LFC) proposed by Schneiderlöchner et al. [52] and further developed by Jan Nekarda [60] by laser process optimization and the introduction of alternative Al doping sources such as screen printed Al and Al-foils. The process scheme is presented in Fig. 18. The starting point is a wafer with a fully passivated rear side and an Al layer on top of the passivation. At this point the rear side metal layer is not in direct contact with the silicon. The contact formation is realized by using a pulsed laser system in order to locally structure the passivation layer and simultaneously create a local p-type doping within the contact structure using the Al layer as doping source.

An alternative approach for the fabrication of Al-LBSF structures was suggested by Agostinelli et al. [53] under the name i-PERC. The i-PERC process sequence starts with a local structuring process such as local laser ablation for local contact opening formation of the rear side passivation layer. After the rear side contact opening formation the rear side metallization is performed by full area Al screen printing and a subsequent contact firing process in a conveyor belt furnace. The passivation layer pattern acts during the firing process as diffusion or alloying barrier resulting in Al-alloyed LBSF structures within the laser ablated areas.

Within this work an optimized LFC process by Jan Nekarda [60] and colleagues was used in chapter 3 in order to form p-type LBSF structures for PERL solar cell designs.

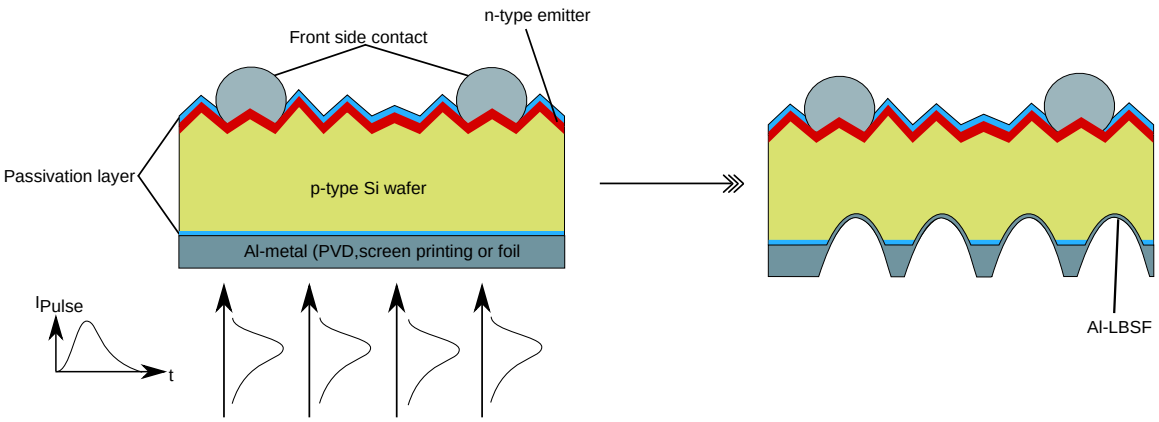

Fig. 18
Process scheme of Al-LBSF formation using the laser fired contact (LFC) process. The image is based on a graphic from [61].

2.4.4 Laser chemical processing (LCP)

Laser chemical processing (LCP) is based on the idea of combining a laser structuring process with a liquid jet in order to enhance the laser structuring process by chemical reactions or simultaneously induce physical transport phenomena by the liquid jet such as removal of the laser induced melt or diffusion of liquid jet constituents into the laser induced melt. LCP is a further development of the LaserMicroJet (LMJ) technology of the company Synova, which uses a laser spot coupled into a laminar water jet. LMJ was developed by Richerzhagen [62] and is mainly used to microstructure different materials without the drawback of a limitation of the process working distance due to the constant focus length of conventional laser systems. In the LMJ system the laser spot coupled into the liquid jet is guided onto the sample by total internal reflection at the liquid jet-atmosphere interfaces. Therefore, the maximum spatial distribution of the laser spot is limited by the diameter of the liquid jet, which allows a focused laser processing independently of the working distance to the sample. The working distance has not to be modified during processing in order to assure a focused laser spot as long as the laminar flow of the liquid jet can be assured. However, the liquid jet itself acts as multi-mode waveguide, which induces a distance dependent inhomogeneous spatial laser intensity profile within the liquid jet [63, 64].

Willeke et al. [65] and Kray et al. [66] further developed the LMJ system by replacing the water jet with a liquid jet using various chemicals in order to induce further chemical reactions or locally diffuse the chemical components into the laser structured area. The further development of the LMJ process by using a non-water based liquid jet is called laser chemical processing (LCP).

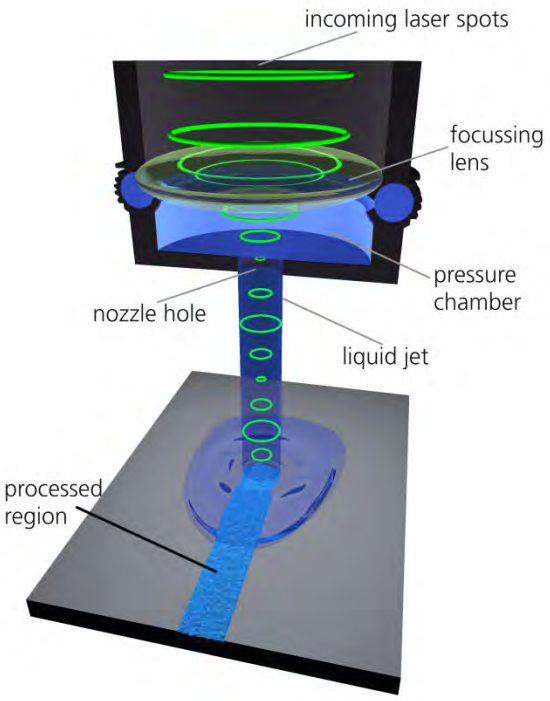

Fig. 19
Working principle of LMJ and LCP.

The working principle of LMJ and LCP is shown in Fig. 19. The laminar liquid jet is created by using a high pressure pump system pumping the liquid into the nozzle head with pressures between 100-200 bar. The nozzle can have opening diameters between 30 and 200 µm and is located in a high pressure chamber with a glass window on the top surface above the nozzle position. The laminar liquid jet leaving the nozzle has a diameter of approximately the nozzle diameter and is surrounded by a sheath gas for an increased laminar length. The sheath gas used in this work was N_2 for the experiments of chapter 5 and He for the experiments in chapter 3.

The laser emission in the conventional LMJ or LCP system is guided through an optical fiber from the laser to the high pressure chamber (coupling unit). An alternative approach co-developed in this work is a direct guidance of the laser spot from the laser to the coupling unit by using a system of mirrors and an optical beam expander. This system showed in experiments a reduction of the spatial laser inhomogeneities on the sample and significantly smaller structure widths than the liquid jet diameter. The fiber coupling system was in this work only used in chapter 3 and the direct coupling system was used for the experiments in chapter 5-6. The guided laser spot is focused on the nozzle entrance in the coupling unit and enters the high pressure chamber

through a window. After coupling the laser spot into the liquid jet, it is guided onto the sample and can be used for locally melting of the sample or locally ablation of either a volume of the substrate material or thin layers on top of the sample. The processed sample is moving on an x-y-axis system below the liquid jet. The relevant processing parameters of the LCP technology are a combination of laser system parameters (wavelength, laser pulse energy, laser pulse duration, etc.), liquid jet parameters (jet diameter, optical absorption, liquid jet pressure, etc.), sample movement parameters (spatial laser pulse distance) and the surface properties of the processed sample (antireflection layers, topography, etc.). This work used an R&D LCP system of the company Synova in combination with q-switched frequency doubled (green: 532 nm) diode-pumped solid state nanosecond pulsed laser systems. The laser system used in chapter 3 and 5-6 was a Hippo 532QW from Spectra Physics and a Nanio 532-20-V from Innolas Laser, respectively.

The application areas of LCP so far were local micro structuring of silicon and other materials [66-68], wafering of silicon [68, 69] and local doping for silicon and thin film solar cell applications [49, 59, 61, 70-78]. Within this work LCP is primarily used for simultaneously micro structuring of passivation layers and local doping of the silicon substrate within the opening structure. LCP has many advantages for this purpose. On the one hand the application of different laser systems allows precisely controlled local silicon melting in combination with self-aligned passivation layer openings. On the other hand the application of various chemicals allows either n-type or p-type doping in silicon. Therefore, LCP is perfectly suited in order to create local highly doped structures in high efficiency solar cells such as local back surface fields or the highly doped contact opening for selective emitter designs.

2.4.5 Light induced plating

Conventionally, the front side metal contacts in silicon solar cells are fabricated by Ag screen printing, which has proven to be a reliable and high throughput metallization process. However, limitations of the minimum printing width, high contact resistivities on lowly doped surfaces and increasing Ag costs make it interesting to develop new metallization schemes to overcome these limitations. Light induced plating (LIP) of Ni, Cu, Ag or Sn is an alternative approach for structured metal deposition in solar cell fabrication. LIP is based on the idea of using the photovoltaic effect of a semiconductor device in order to realize controlled metal deposition from an electrolyte onto the semiconductor surfaces by regulating the electrochemical potential of the system [79-83].

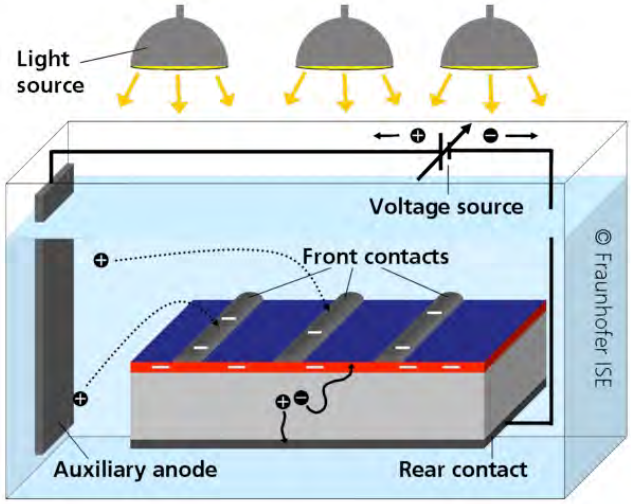

Fig. 20
Schematic setup of a light induced plating (LIP) process for the fabrication of front side metal contact for p-type silicon solar cells [84].

Fig. 20 shows the schematic LIP setup for the deposition of local metal contacts. LIP can be used in order to plate metals such as Ni, Cu or Ag in locally patterned passivation openings of n-type emitter regions. The solar cell precursor is in a process stadium where all other processes (emitter diffusion, front side passivation, rear side metallization) are completed and the passivation layer on the front side of the solar cell is locally removed in the pattern of the desired metal grid. The passivation patterning can be realized by laser structuring or mask and etch approaches. In order to deposit the front side metal contacts by LIP, the solar cell precursor is immersed into an electrolyte and illuminated on the front side. The rear side contact is connected to a voltage source applying a bias voltage between the rear contact and an auxiliary anode also immersed into the electrolyte. The illuminated pn junction of the solar cell induces a potential difference between the local front side contact openings and the rear side metal contact. The n-type emitter acts in this situation as electron source leading to a reduction process at the contact opening pattern, and therefore, to a metal deposition from the electrolyte solution. The corresponding oxidation process at the auxiliary anode leads to a dissolution of metal ions into the electrolyte, thus replenishing it. The deposition rate of the system can be controlled by the applied bias voltage between the auxiliary anode and the rear metal contact of the solar cell. Furthermore, the illumination intensity of the front side pn-junction is an additional parameter to control the deposition. By applying an optimized voltage bias between the auxiliary anode and the rear metal contact of the solar cell in combination with the illumination induced pn-junction voltage, the reduction and oxidation of the rear side metal contact can be held at the same rate. This results in no net dissolution or plating

on the rear side metal contact, while at the same time deposition at the front side occurs. The deposited metals for solar cell fabrication are at first Ni in order to achieve an interface contact layer with low contact resistivity, a diffusion barrier between the silicon and the subsequently plated Cu and after an annealing induced silicidation process a sufficient adhesion for the later module production. Subsequently, plated Cu or Ag layers build the main body of the front side contact grid. Cu plating offers the opportunity to replace cost intensive Ag on the front side with the advantage of low material costs and similar metal finger conductivity. The more interested reader is referred to the publications of Bartsch [84-88] and Mette [89] about plating processes in solar fabrication.

2.5 Nickel-copper metallization for silicon solar cells

The replacement of screen printed Ag front side contacts by using plated Ni-Cu stacks involves the danger of increased recombination losses due to copper or nickel diffusion into Si. Although Ni and Cu show similar recombination properties [90-92] and diffusivities at high temperatures ($T > 600°C$) in silicon [93, 94], only Cu diffuses significantly at low temperatures ($< 200°C$) and causes severe degradations in the electrical performance of p-type silicon solar cells [95]. Therefore, diffusion barriers are applied at the silicon-Cu interface in order to avoid Cu induced recombination centers in Si. In semiconductor applications typical diffusion barriers against Cu are TiN, TaN or Ta [96-98]. In PV applications Ni is usually applied as diffusion barrier against copper [95, 99].

The electrical and structural properties of silicon metal interfaces can be modified by silicidation processes. Silicidation describes the formation of a metal-silicon compound at the silicon interface. The required energy for the compound formation is usually supplied by heating the material. The compound formation at the interface can be used to improve the contact resistivity or the adhesion of the metal silicon interface [100]. Silicidation processes are typically used in semiconductor applications for different combinations of silicon with metals such as Ni, Ti, Co, W, Mo, Ta or Pt.

In this work plated Ni layers are used as emitter contact material, which enable low contact resistivities and provide a diffusion barrier against subsequently plated copper layers. In order to achieve sufficient contact adhesions, the Ni-Si interface is silicided in an annealing process. The silicidation process is a diffusion-driven reaction of Ni and Si and results in different silicide phases. The formed silicide phase depends on the applied thermal budget [101, 102] and the Ni/Si ratio [102]. In a medium temperature range of 200-500°C the most dominant silicide phases are Ni_2Si for

temperatures 200 < T < 350°C and NiSi for 350 < T < 550°C. These two phases are the most common for semiconductor or PV applications due to a low resistivity and high phase stability. Table IV gives an overview of the resistivity, the Si and Ni consumption for the silicide formation and the formation depth as function of the temperature *T* and the annealing time *t* of Ni_2Si and NiSi.

Table IV: Resistivity, Si and Ni consumption for the silicide formation and silicide formation depth of Ni_2Si and NiSi.

Phase	Resistivity (μΩcm)	$\frac{\text{Consumed Si (nm)}}{\text{Consumed Ni (nm)}}$	Silicide depth (cm)	
Ni	0.069	-		
Ni_2Si	33	0.91	$W_{Ni_2Si} = \sqrt{t\left(10^{-2}e^{-\frac{1.3\,q}{kT}}\right)}$	[101]
NiSi	16	1.83	$W_{Ni_2Si} = t\left(10^{3}e^{-\frac{1.4\,q}{kT}}\right)$	[101]

The parameterization of the silicidation depth of Ni_2Si and NiSi by Coe eta al. [101] in Table IV demonstrates that the phase formation strongly depends on the temperature and the annealing time. Coe demonstrated that each silicide phase shows a different dependence on the annealing time t, which implies different limitation in each phase formation processes. The formation of Ni_2Si ($W \sim \sqrt{t}$) demonstrates a diffusion rate limitation in the supply of material necessary for the growth of the phase. The formation of NiSi ($W \sim t$) increases linearly with time, which indicates that the growth of the phase is limited by the reaction rate at one or both layers of the interface.

The Ni silicide phase formation can be controlled by different annealing profile parameters such as the plateau time and plateau temperatures as well as the temperature ramps at the beginning and the end. Fig. 21 illustrates the consecutive formation of Ni_2Si and NiSi phases. In the beginning Ni diffuses into the silicon and creates Ni_2Si at the Ni interface and NiSi at the Si interface. Simulations of Christensen et al. [103] showed that the barrier for Si moving via vacancy mechanism inside the Ni bulk is 20 times higher than the diffusion barrier for Ni inside Si. “The simulations indicate that there is a thin layer of NiSi closest to the Si/silicide interface. In the presence of excess Si, there is a thermodynamic driving force to convert Ni_2Si into NiSi. This can occur in one of two ways which both involve diffusion through the NiSi layer. Si can diffuse from the silicon substrate through NiSi and react with Ni_2Si to form NiSi, via the reaction:

$$Si + Ni_2Si \rightarrow 2NiSi \qquad (25)$$

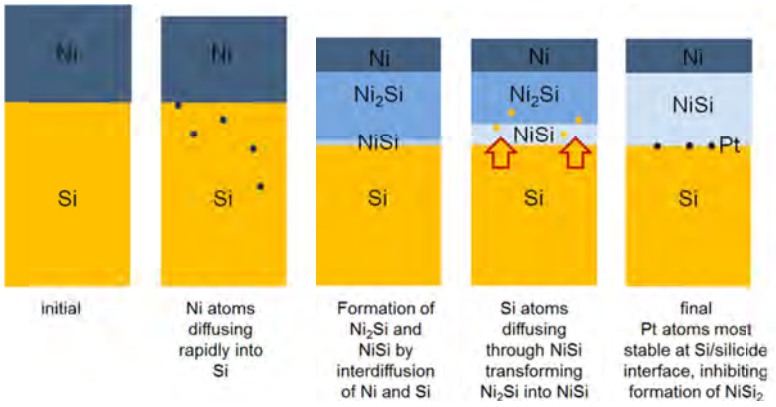

Fig. 21
Schematics of the key steps in the formation of Ni(Pt) silicides by Christensen et al. [103]

The energy gain is 47 kJ/mol. The other possibility is that Ni from either the metal overlayer or from Ni_2Si diffuses through NiSi to react with Si at the Si/NiSi interface. For Ni to react with Si:

$$Si + Ni \rightarrow NiSi \qquad (26)$$

the energy gain is 115 kJ/mol if Ni is taken from Ni bulk." [103] In semiconductor applications the Ni layer contains small amounts of Pt, which stabilizes the formation of NiSi by transforming silicon rich phases such as Ni_2Si in monosilicides in the form of $Pt_xNi_{1-x}Si$ [103]. The silicide growth of plated Ni contacts in laser patterned silicon solar cells can show significant deviations from the theoretical behavior. Different interface parameters such as interface oxides or inhomogeneous plating or laser patterning can result in inhomogeneous silicide growth or even prevention of silicide formation.

a) b)

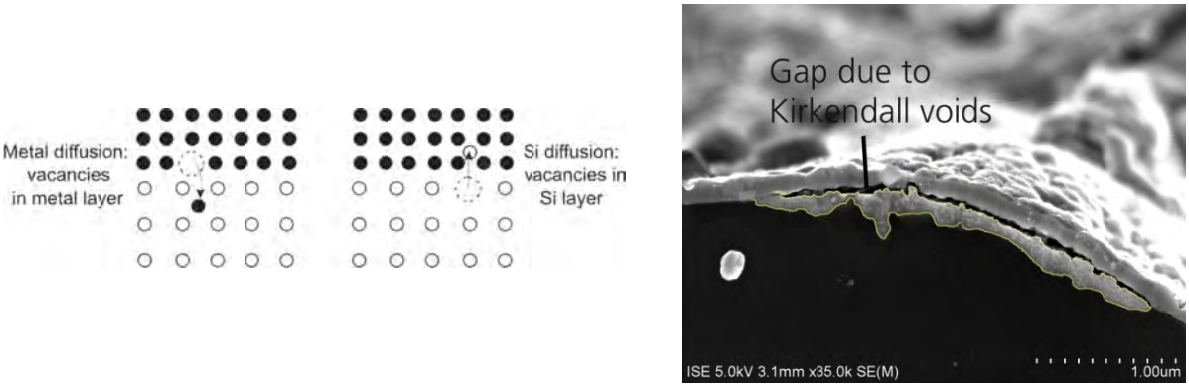

Fig. 22
a) Schematics of Kirkendall voiding [102] at the Ni interface and b) a resulting gap due to Kirkendall voiding between the Ni layer on top of a silicided (yellow contour lines) region.

Lee et al. showed that native oxides with a width of 2 nm can prevent any silicidation up to temperatures of 800°C [104]. Furthermore, the species diffusion can lead to vacancies at the interface (Kirkendall voids). This effect is shown in Fig. 22 a) and can lead to voids or gaps between the Ni and the silicide layer shown in Fig. 22 a).

2.6 Imaging characterization techniques

Imaging characterization techniques have proven to be a fast and reliable tool in order to characterize local electrical properties of silicon wafers or silicon solar cells. The interested reader is referred to the publications [105-113]. Within this work imaging characterization techniques are mainly used to locate non-linear shunting regions in order to determine the physical origin of annealing induced shunting of Ni plated solar cells in chapter 6. The two imaging techniques most suitable for this purpose are dark lock-in thermography (DLIT) [113] and reverse biased electroluminescence (ReB-EL) [114].

2.6.1 Dark lock-In thermography

DLIT [113] is a thermography imaging technique, which uses the lock-in method in order to measure small local temperature differences of the solar cell. The locally dissipated heat can be correlated to free carrier density variations, which enables information about local loss mechanisms in the solar cell. The local heat emission is detected by a charge-coupled device (CCD) camera in a wavelength range of 3-5 µm. The emitted spectrum relates to a black body emission spectrum according to Planck's law of radiation. The lock-in techniques allows the detection of small heat emission differences induced by a periodic variation of the applied bias voltage, and therefore, a periodic variation of the bias induced heat emission. The DLIT method can be used in the solar cell characterization for shunt imaging, series resistance imaging, the measurement of local IV curves, the detection of high recombinative areas and the detection of local breakdown spots (hot spots). A detailed summary of the application areas of DLIT for solar cell characterization can be found in [113].

As discussed in [109] the combination of the lock-in technique and thermography has different benefits such as the significant improvement of the signal to noise ratio, the reduction of blurring effects in the thermography image due to heat conduction and the direct proportionality of the measured DLIT signal to the dissipated power for optimized lock-in reference functions. The schematic measurement setup of DLIT is shown in Fig. 23.

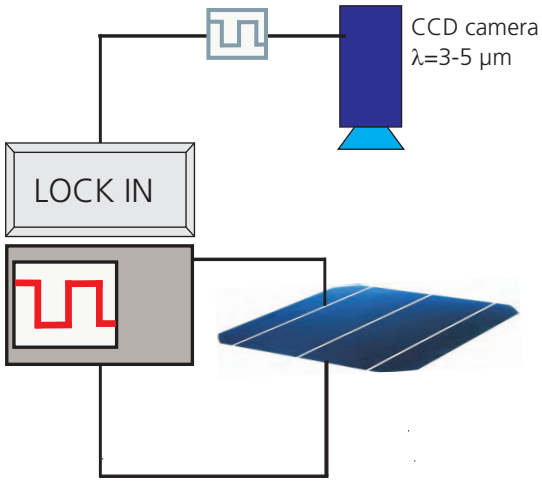

Fig. 23
DLIT measurement setup

The main drawback of DLIT is that the long wavelength detection regime comes along with a lower imaging resolution compared to imaging techniques in the lower wavelength regime (0.3-1.1 µm) such as photoluminescence (PL) or electroluminescence. The DLIT setup used in this work featured an imaging resolution of 256x256 pixels. By applying an illumination source (i.e. laser source) to the DLIT setup the measurement can be performed under real working conditions of the solar cells, which is then called illuminated lock-in thermography (ILIT).

2.6.2 Reverse biased electroluminescence

Kwapil [114], Bothe [115] and Kasemann [109] showed that local breakdown spots in solar cells can also be characterized by electroluminescence imaging in reverse bias (ReB-EL). The ReB-EL setup is illustrated in Fig. 24. The solar cell is operated at a fixed voltage in reverse bias and resulting emission in the visible and near infrared (λ = 0.3-1.1 µm) is detected by a Si CCD camera with an imaging resolution of 1024x1024 pixels. Under reverse bias the solar cell emits a broad spectrum, which is a combination of different breakdown mechanisms (Avalanche breakdown, internal field emission and thermal breakdown) [114, 115] and relates to different transitions such as indirect interband transition, direct interband transition and intraband transitions [116].

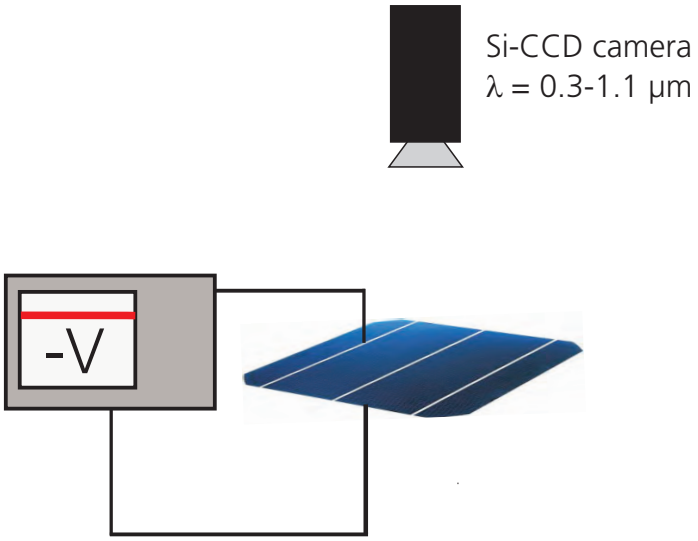

Fig. 24
ReB-EL measurement setup.

Kwapil [114] and Bothe [115] showed that in multi crystalline (mc) silicon solar cells the emission characteristics of different breakdown effects show similar trends in DLIT and ReB-EL measurements. They classified three different breakdown types with distinctive signal-voltage characteristics in DLIT and ReB-EL. Fig. 25 illustrates the different signal-voltage characteristics.

Type I breakdowns (early breakdowns) show in DLIT for low reverse voltages no emission signal and at reverse voltages of about $V \leq$ -12 V a linear signal-voltage characteristics. The same type shows in ReB-EL measurements a linear signal voltage characteristic from the beginning. This breakdown type was correlated to tunneling assisted breakdown processes (probably internal field emission) via energy states in the band gap or in the vicinity of conducting channels. The physical reason of type I breakdowns can be Al particles on the solar cell surface [114, 117] or local defect structures in the passivation layer and/or Si [114].

Type II breakdowns (soft breakdowns) show in DLIT and ReB-EL for low reverse voltages no emission signal and at reverse voltages of about $V \leq$-10 V a soft exponential signal-voltage characteristics. These breakdowns could be correlated to trap assisted tunneling (internal field emission) or trap-assisted Avalanche breakdowns, which are induced by defect rich areas with high recombination activity. Examples for type II breakdowns are cracks or metal precipitates affecting the space charge region of the emitter.

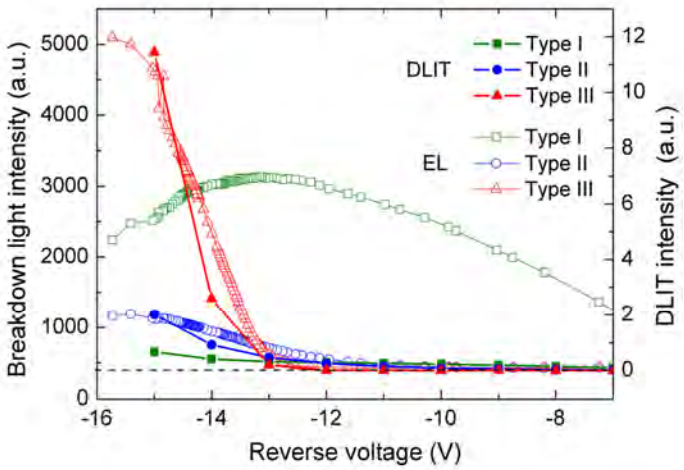

Fig. 25
Comparison of the breakdown light intensity measured via the ReB-EL setup (open symbols) and the DLIT setup (closed symbols) as function of the applied reverse voltage. The dashed line corresponds to the EL camera background noise. The image is taken from [114].

Type III breakdowns (hard breakdown) show in DLIT and ReB-EL also no emission signal for low reverse voltages and at reverse voltages of about $V < -15\,\mathrm{V}$ a hard exponential signal-voltage characteristics. This breakdown type could be correlated to Avalanche breakdowns due to high local electric fields due to topography related high voltage breakdown sites such as thin emitter structures or local etch pit structures.

3 LCP local boron doping process

The focus of this chapter is the development of a LCP based local boron laser doping process for the application as local back surface field (LBSF) in p-type PERL solar cells. The chapter is structured in five parts addressing alternative state-of-the-art local p-type doping processes (section 3.1), the evaluation of suitable boron doping sources and the development of a LCP boron laser doping process (section 3.2), the first proof of concept of this process as LBSF in p-type PERL solar cells (section 3.3) and a detailed loss analysis of the application as LBSF with focus on the correlation of the base resistivity and the losses at the laser processed LBSF structures (section 3.4 & 3.5).
The results shown in this chapter led to following publications [118-120].

3.1 State-of-the-art local p-type doping processes

Several high efficiency silicon solar cell concepts require local p-type doped structures in order to form local back surface fields (LBSF) or local emitter structures. The conventional lab type approach usually involves a variety of photolithographic structuring steps in order to from local p-type doped areas by thermal boron diffusion. This approach allows a high doping quality under the restraint of high processing cost and low processing capacity. Therefore, several processes were developed in order to allow an industrially feasible fabrication of local p-type doped structures in the past.

Currently, the industrially most relevant processes for the formation of p-type doped are laser based doping processes such as laser fired contacts [52, 60] or boron spin-on doping laser processes [50] or the formation of locally aluminum doped structures within a locally structured passivation layer mask [121, 122] or due to locally screen printed aluminum structures [123]. All these processes allow the formation of locally highly doped aluminum or boron doped structures in an industrial environment. A short summary of these processes is shown in Table V. The aluminum based doping processes rely on evaporated or screen printed aluminum layers, which act as Al doping source. Therefore, the metallization process is coupled to the local doping process and is limited on Al based metallization techniques. Furthermore, applications with a structured metallization on top of the locally doped areas, such as interdigitated doping structures [123] require highly precise alignment techniques between the different processing steps.

Table V: Industrially feasible local p-type doping processes

Process	Doping source	Contact metal	Possible Application
Laser fired contact / emitter (LFC / LFE)	Al	Al	LBSF [52] or local emitter [124]
Spin-on laser doping(SLD)	B	No limitation	LBSF [50] or local emitter
Al-screen printing	Al	Al	LBSF [121, 122] or local emitter [123]
Laser chemical processing (LCP)	Al or B	No limitation	LBSF [119] or local emitter

The decoupling of the contact metal process and the doping process comes along with a better flexibility in the choice of the contact metal layer and the choice of the doping elements. The application of the LCP boron doping process for the formation of locally p-type doped structures comes along with several processing related benefits. On the one hand the LCP process does not need an existing doping precursor on top of the sample as in the case of LFC. This allows the formation of interdigitated p- and n-type doped structures as in the case of back contact back junction solar cells [11, 125] and sets no limitation on the according contact metal. On the other hand the LCP process enables a simultaneously doping and local structuring of the passivation layer. This allows the application of self-aligned contacting schemes such as Ni-Ag or Ni-Cu plating as well as other metallization techniques such as evaporation or screen printing. Therefore, the development of a p-type doping LCP process can enable improved and industrially feasible processing schemes for different high efficiency solar cell designs.

3.2 Process development

In order to transfer high efficiency solar cell concepts such as PERL [126] in mass production, it is crucial to develop industrially feasible local structuring and local p- and n-type doping techniques. This chapter will focus on the fabrication of locally doped p-type structures. Fig. 26 shows possible elements in order to form shallow acceptor states within the silicon band gap. The most relevant elements in terms of thermalization energy and industrial applicability are boron and aluminum due to their acceptor levels close to the valence band of Si.

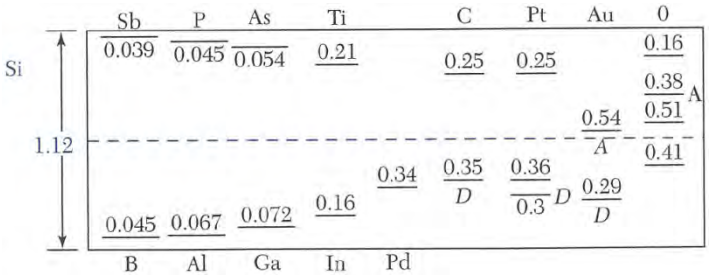

Fig. 26
Acceptor and donor energy levels in silicon [127]

Comparing both elements, boron shows intrinsic advantages for p-type doping in silicon solar cells. On the one hand, boron shows a higher solid solubility in silicon than aluminum [128], which is about one order of magnitude higher. On the other hand, not all of the introduced dopants are electrically active and boron has a higher ionization rate of electrically active acceptor states compared to aluminum overall, as shown in Fig. 27. Both effects enable an overall higher peak doping density for boron doping, which can give significant advantages for the application LBSF structures.

Therefore, most of the p-type doping structures in lab type high efficiency solar cells [9, 129] use local boron doping processes. However, it can be seen that aluminum p-type doped solar cells can also reach high cell efficiencies [52] i.e. by using screen printed and fired aluminum pastes [122, 123].

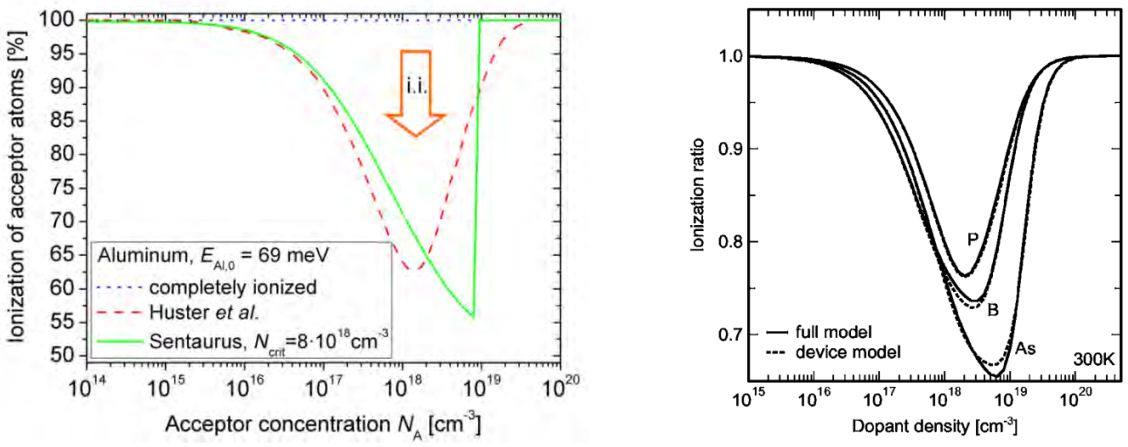

Fig. 27
Ionization ratio of Al (left graph [130]) and B, P and As (right graph [131]) in Si as function of the dopant density N_A.

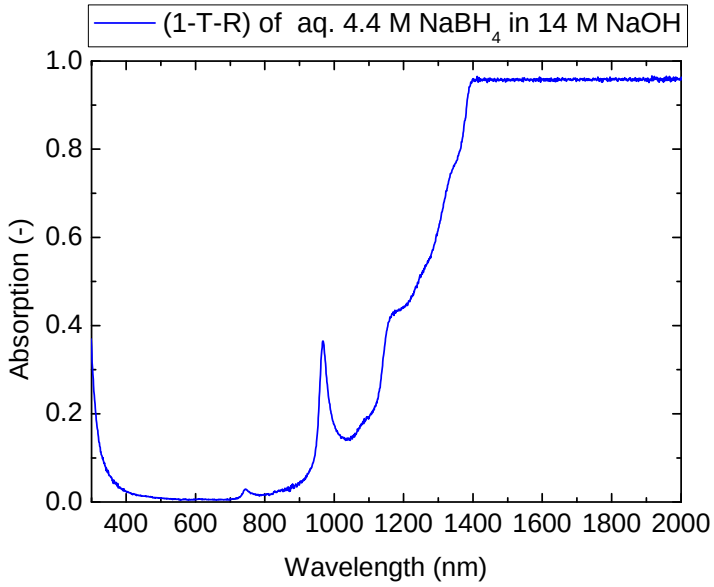

Fig. 28
Measured absorption spectra of 4.4 M aqueous $NaBH_4$ solution in 14 M NaOH.

Possible doping sources have to fulfill certain criteria in the case of LCP. The doping source has to be liquid under atmospheric conditions, it should be non-flammable, transparent for the applied laser wavelength, contain a large amount of boron or aluminum, should not contain large amounts of n-type dopants such as phosphorus or recombination active centers with energy levels in the middle of the band gap[5] and should offer a reasonable price in terms of cost per liter. These limitations reduce the list of possible p-type dopants for LCP significantly. Previously, different kinds of liquid boron sources were evaluated i.e. Rodofili et al. [71] showed already that boric acid does not provide a sufficient boron doping in the case of LCP. Therefore, other liquid boron sources were evaluated by fabricating laser doped lines or laser doped line fields on n-type silicon wafers in order to measure the doping of the fabricated LCP p-type doped structures by four point probe sheet resistance measurements and transmission line measurements.

One of the most promising boron sources was an aqueous solution of $NaBH_4$ due to the fact that it is transparent for wavelengths around 532 nm as shown in Fig. 28 and it is commercially available in large amounts. However, the solubility of $NaBH_4$ in water limits at some point the maximum boron concentration in the solution. The addition of sodium hydroxide can increase the maximum solubility of $NaBH_4$ in the solution. Therefore, a commercially available 4.4 M $NaBH_4$ aqueous solution in 14 M NaOH was chosen for the experiments in this chapter.

[5] The recombination rate decreases exponentially with the difference of the impurity energy level and the middle of the band gap energy.

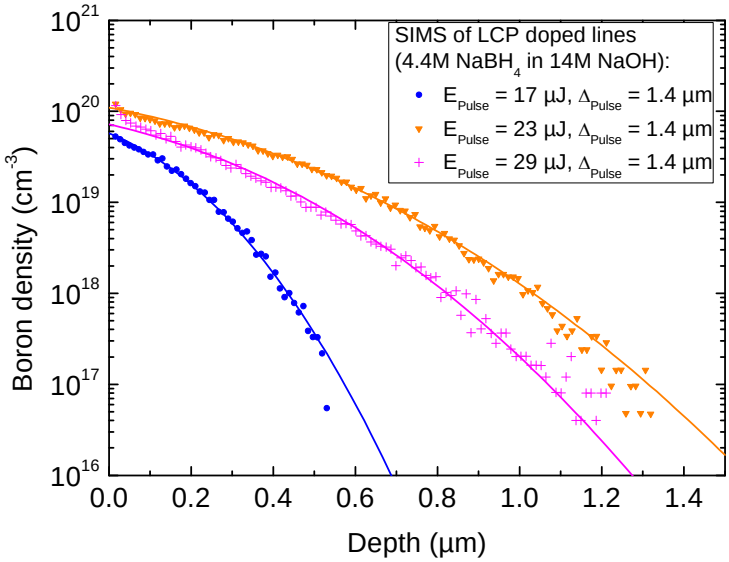

Fig. 29
Processed doping profile for different laser pulse energies measured by secondary ion mass spectroscopy (SIMS). The drawn lines are guides to the eye (graph from [132]).

In order to evaluate the suitability of this solution as p-type doping source in silicon, LCP doped line structures were processed on a silicon wafer using different laser pulse energies E_{Pulse} at a spatial laser pulse distance of Δ_p = 1.4 µm on the sample. The used laser for the experiments in this chapter was a frequency doubled 532 nm Nd:YAG laser with a laser pulse duration of about 10 ns. Fig. 29 shows the measured doping profiles of the processed test structures. The shown data are the mean doping concentrations in a circular SIMS measurement area with the diameter of about 10 µm in the center of a LCP line with a width of about 50 µm. All structures show surface doping concentrations of about $6 \cdot 10^{19} - 1 \cdot 10^{20}$ cm^{-3} and doping depths between 0.7-1.6 µm. The calculated sheet resistances and the simulated saturation current densities of the profiles in Fig. 29 are shown in Table VI. The saturation current density J_{01} was simulated using the freely available software EDNA [133]. The simulations assumed a physical surface recombination velocity of a metalized surface $S_0 = 10^7$ cm/s, Fermi-Dirac statistics and no additional Shockley-Read-Hall recombination within the doped area. The sheet resistance and the doping depth show a strong correlation to the applied pulse energy.

Table VI: Calculated sheet resistance and simulated saturation current density using EDNA [133] of the boron doping profiles shown in Fig. 29.

Pulse energy (µJ)	Pulse distance (µm)	Peak doping concentration (cm^{-3})	Doping depth: $N_A = 10^{16}\ cm^{-3}$ (µm)	Calc. sheet resistance (Ω)	Simulated[6] J_{01} (fA/cm^2)
17	1.4	6×10^{19}	0.7	122	1297
23	1.4	1×10^{20}	1.6	36	436
29	1.4	7×10^{19}	1.3	59	660

Fell [134] showed that the melting depth correlates with the applied pulse energy. The maximum doping depth can be achieved with optimum pulse energy. This limitation is caused by decrease of the melting depth for too low pulse energies and increasing evaporation for increasing pulse energies.Therefore, it is assumed that the slightly decrease of the melting depth and the sheet resistance for the highest pulse energy is caused by increasing evaporation.

All LCP boron doping profiles shown in Fig. 29 are suitable for the application as LBSF in high efficiency silicon solar cells. The high surface doping concentration should provide a good contact resistance and the low J_{01} level should provide high open circuit voltages and low recombination at the rear side contacts of the solar cell. The simulated J_{01} are a lower limit of the processed laser doped structure, though. Laser damage, doping inhomogeneities or lower doping densities at the edges of the laser structured area could result in an increase of J_{01}.

3.3 Proof of concept: LCP boron local back surface fields for Si solar cells

Solar cells with a PERL [126] design were fabricated using the developed p-type LCP boron doping process, where the rear side passivation layer is locally opened and LBSF doping is applied simultaneously. Fig. 30 shows a schematic of the fabricated LCP-PERL solar cells. The substrates were 0.5 Ωcm p-type FZ-Si wafers with a thickness of 250 µm. Each wafer featured 7 cells with cell sizes of 2x2 cm^2. The front side was textured with an inverted pyramid structure and has a 120 Ω/sq. deep diffused phosphorus diffusion as emitter[7]. The front and the rear side is passivated with 105 nm thermal SiO_2-layers, which act as passivation layer and antireflection coating for the front side. The front side metal contacts were processed with photolithography in combination with an evaporated stack of Ti-Pd-Ag that was thickened with Ag-plating. The photolithographic defined front side contact opening had an opening width of 5 µm and a front side finger pitch of 800 µm.

[6] S_0=10^7 cm/s

[7] Please note, that there is no additional selective emitter diffusion on the front side.

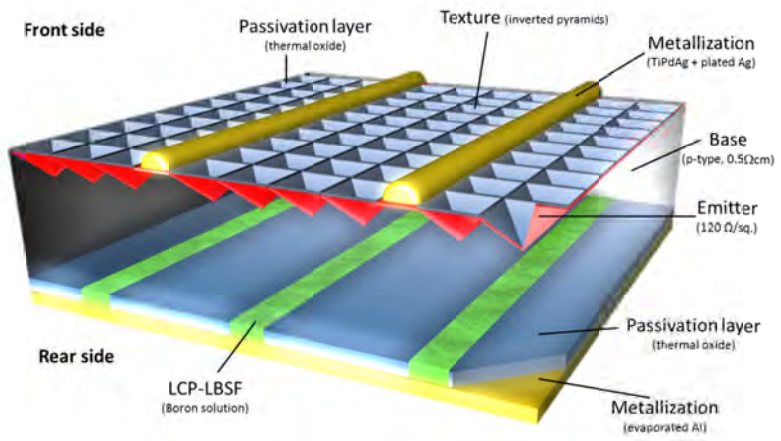

Fig. 30
Schematic of the processed LCP-PERL solar cells with line contact design on the rear side. The LCP-PERC cells have the same structure only the dopings underneath the rear side contacts are missing.

On the rear side the passivation layer was locally opened with LCP, which at the same time creates local boron doping in the opened area (see step 1 in Fig. 31). The LCP boron doped openings act as LBSF in this structure and were metalized with an evaporated aluminum layer of 2 µm thickness (see step 2 in Fig. 31). The applied contact design on the rear side was a line structure with a varying pitch in the range of 1000 – 2500 µm, a line length of 2 cm (equals cell length) and a line width of about 50 µm. The boron source for the LCP process was 4.4 M $NaBH_4$ aqueous solution in 14 M NaOH.

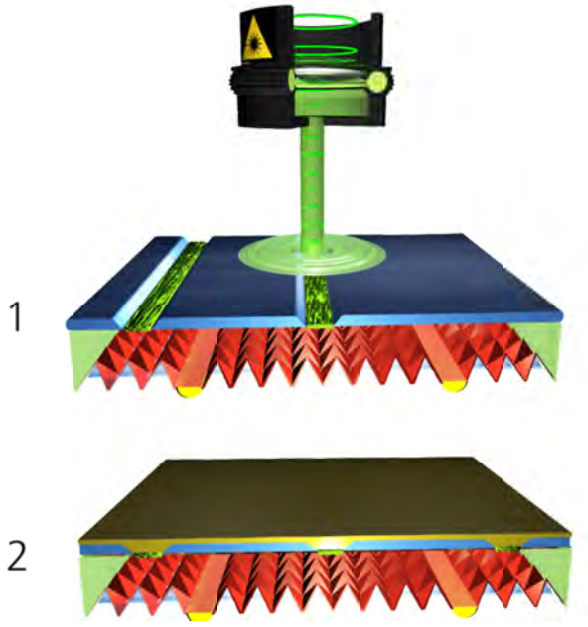

Fig. 31
Processing scheme of the LBSF formation by LCP

The line doping were processed with an overlap of single LCP laser pulses with a spatial laser pulse distance of 1.4 µm on the sample, a wavelength of 532 nm, a pulse energy (before the liquid jet) of 20 µJ and a laser pulse duration of about 10 ns.

In order to evaluate the quality of the LCP boron doping as LBSF, reference cells with no LCP boron doping on the rear side were processed. The solar cell design of the reference cells is the same as for the LCP-PERL solar cells, except that in the reference case, the rear side openings were processed with DI-water as LCP medium. This results in non-doped rear side openings, which means that the reference cells have a PERC solar cell design [8] without an LBSF doping on the rear side. This reference design was chosen because it assures the same rear side geometry for the processed PERL and PERC solar cells. This makes it easier to compare the processed cells and avoids any geometry-related influences on the cell parameters.

Table I shows the cell efficiency η, the fill factor *FF*, the short circuit current density J_{sc}, the open circuit voltage V_{oc}, the pseudo fill factor *PFF* (measured by SunsVoc [11]) and the measured series resistance R_s (measured by comparison of light I-V-curve with SunsVoc measurements [12]) of the best LCP-PERL and LCP-PERC solar cells. The best LCP-PERL solar cell shows a maximum cell efficiency of η = 20.9%. This cell shows a cell efficiency benefit of $\Delta\eta$ = 0.4%abs. to the reference cell with the same pitch and $\Delta\eta$ = 0.3%abs. to the best reference solar cell with a smaller rear side pitch of 1000 µm.

The solar cells results in Table VII show a proof of concept of the developed LCP boron doping process as local back surface field for p-type PERL silicon solar cell designs.

Table VII: Cell results of the best LCP-PERL and LCP-PERC solar cells for line contact LBSF design and a base resistivity of 0.5 Ωcm (p-type).

	LCP-PERL (best cell)	LCP-PERC (same pitch)	LCP-PERC (best cell)	LCP-PERL (same pitch)
η [%]	20.9	20.5	20.6	20.4
J_{sc} [mA/cm²]	38.7	38.7	38.7	38.0
V_{oc} [mV]	675	670	666	665
FF [%]	80.0	79.0	79.9	80.8
PFF [%]	82.9	83.0	82.7	82.8
R_s [Ωcm²]	0.49	0.63	0.50	0.33
Pitch [µm]	2500	2500	1000	1000
LCP- liquid	4.4 M $NaBH_4$ in 14 M NaOH	H_2O	H_2O	4.4 M $NaBH_4$ in 14 M NaOH

3.4 Impact of base resistivity on the quality of LCP boron local back surface fields

The two main functions of the LBSF doping are the lowering of the contact resistance and the screening of the minority charge carriers from the highly recombinative metal contacts. Both effects are strongly affected by the wafer substrate doping level. As shown by Glunz et al. [135] the impact on the cell performance of the existence or not of an LBSF doping and its quality increases significantly with increasing base resistivity. Therefore, the realization of the boron LCP LBSF process on varying base resistivities allows a deeper understanding of the limiting factors of the process, which directs to further optimization routes. There are several physical reasons, which cause this strong dependency on the base resistivity, which will be discussed in this section.

3.4.1 LCP boron local back surface fields for base resistivities of 0.5-9 Ωcm

The impact of the base resistivity on the LBSF quality of the processed LCP boron doping was analyzed by fabricating p-type PERL solar cells similar to the description in section 3.3 and shown in Fig. 30. However, the cells discussed in this section have one major change on the front side compared to the cells in Fig. 30. The front side contact opening was in this case 30 µm due to the fact that the front side metal contacts were fully evaporated Ti(50 nm)-Pd(50 nm)-Ag(2000 nm) without any plating step afterwards. This avoids any influence on the series resistance of the cells due to different plating results of cells with different cell efficiency potential. This was done due to a strong dependence of the plating results on the open circuit voltage of the solar cell. However, this led to a six times higher contact opening area fraction, which causes overall a lower open circuit voltage level due to an increased impact of the metalized emitter saturation current density $J_{01,cont}$ and lower short circuit current densities due to more contact finger shading. Therefore, the cell efficiency level in this section is in general lower than in section 3.3 and the open circuit voltage is about 20 mV lower for the cells with the same cell design as in section 3.3.

In order to evaluate the quality of the LCP boron doped LBSF in the LCP-PERL solar cell design two different reference groups were fabricated in parallel. The solar cells in the first reference group are LCP-PERC solar cells, which have rear side openings without additional doping processed by LCP using H_2O as liquid jet. The solar cells in the second reference group have aluminum doped local back surface fields fabricated by an established laser fired contact (LFC) process [52] in the Fraunhofer ISE PV-TEC. All groups were processed on FZ p-type wafers with four different base resistivities of ρ_{Base} = 0.5, 1, 4 and 9 Ωcm. Table VIII shows the rear side designs of the three different solar cell groups. In the LCP-PERC and PERL case the rear side

contact openings are line shaped and for the LFC case single points. The difference in the contact geometry has technological reasons. The LCP process has a moving linear stage were the sample moves. This setup causes a significantly reduced process time if using line geometries. Furthermore, the small opening width of less than 50 µm reduces the overall rear side contact fraction. The LFC process on the other hand uses a galvanometer scanner system, which allows a very fast movement of the laser spot over the sample. The fast processing time and the quite large opening diameter of 100 µm leads to a favoritism of a single point geometry. Furthermore, the LFC process at this time was fully optimized for point geometries [60].

Fig. 32 shows the measured light IV curve parameters of the processed LCP-PERL, LCP-PERC and LFC solar cells. The LCP cells in Fig. 32 all have rear side line contact pitch of 2000 µm. In the LFC case the rear side point contact pitch varies for the different base resistivities as shown in Table VIII. All three cell designs are differently influenced by increasing base resistivities of the Si wafer. The LCP-PERC solar cells (red boxplots in Fig. 32/Fig. 33) show a large decrease in all IV parameters for increasing base resistivity. This behavior is already known for this cell design [32, 135] and is mostly caused by the formation of a Schottky contact on the rear side contacts for high base resistivities. This effect will be further discussed in the next section. The LFC solar cells (blue boxplots in Fig. 32/Fig. 33) on the other hand perform almost stable for all base resistivities, which is mainly caused by the formation of a local Al back surface field and an optimized pitch for each base resistivity. The optimized LFC process allows in this experiment a high quality reference mainly limited by the front side recombination properties.

Table VIII: Rear side design of the three different solar cell groups fabricated on p-type FZ wafers with four different base resistivities of ρ_{Base} = 0.5, 1, 4 and 9 Ωcm.

	LCP-PERL	LCP-PERC	LFC
LBSF doping type	local LCP boron doping	no doping	local laser fired aluminum doping
Doping medium	4.4 M $NaBH_4$ in 14 M NaOH	H_2O	evaporated Al
LBSF geometry	lines	lines	single points
Contact opening width (µm)	line width = 50 µm	line width = 50 µm	diameter = 100 µm
Rear contact pitch (µm)	500 1000 2000 4000	500 1000 2000 4000	depending on ρ_{Base}: 0.5 Ωcm: 900 1 Ωcm: 700 4 Ωcm: 435 9 Ωcm: 343

The IV parameters of the LCP-PERL solar cells (green boxplots in Fig. 32/Fig. 33) with $\rho_{Base} \leq 1$ Ωcm are similar to the ones of the LFC solar cells. However, going to larger ρ_{Base} a significant *FF* and V_{oc} decrease becomes obvious. The FF decrease can mainly explained by increasing lateral series resistance losses in the base for increasing base resistivity. This explanation is supported by a comparison of the series resistance free pseudo-FF (*pFF*) and the calculation of the total series resistance R_s of the cells. Both parameters are shown in Fig. 33. The series resistance was determined by a comparison of the pseudo-IV curve measured by SunsV_{oc} [12] and the light IV curve. This series resistance determination method [136] showed a good reproducibility and is comparable to other determination methods [137]. The series resistance induced loss in the *FF* can be decreased by an optimized line pitch. However, a smaller pitch will further increase the V_{oc} losses of the LCP-PERL solar cells. Therefore, the most important question for further process optimizations of the LCP local boron doping process is the reason of the significant V_{oc} decrease for increasing base resistivity.

The next section will examine the limiting loss mechanisms in the fabricated solar cell designs in order to determine the process related limiting factors and enable alternatives for further process optimization.

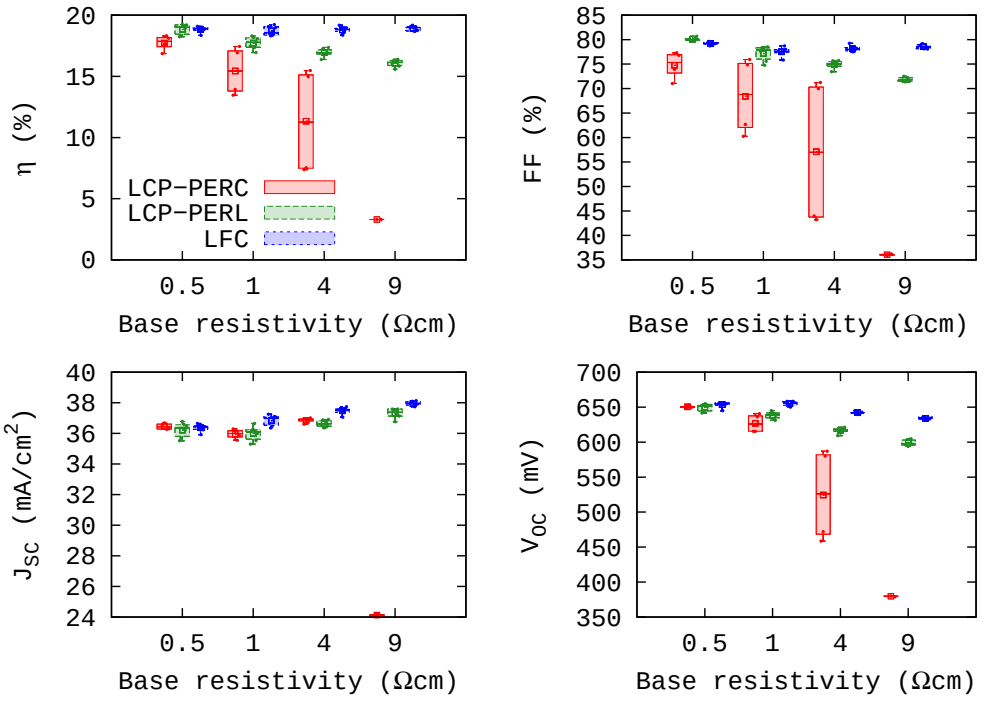

Fig. 32
Measured light IV-parameters of the LCP-PERC, LCP-PERL and LFC solar cells as function of the Si wafer base resistivity. The shown LCP PERC/PERC results are for a constant rear side line pitch of 2000 µm and the LFC results for a varying rear side point pitch shown in Table VIII. Please note the discrete x-scale.

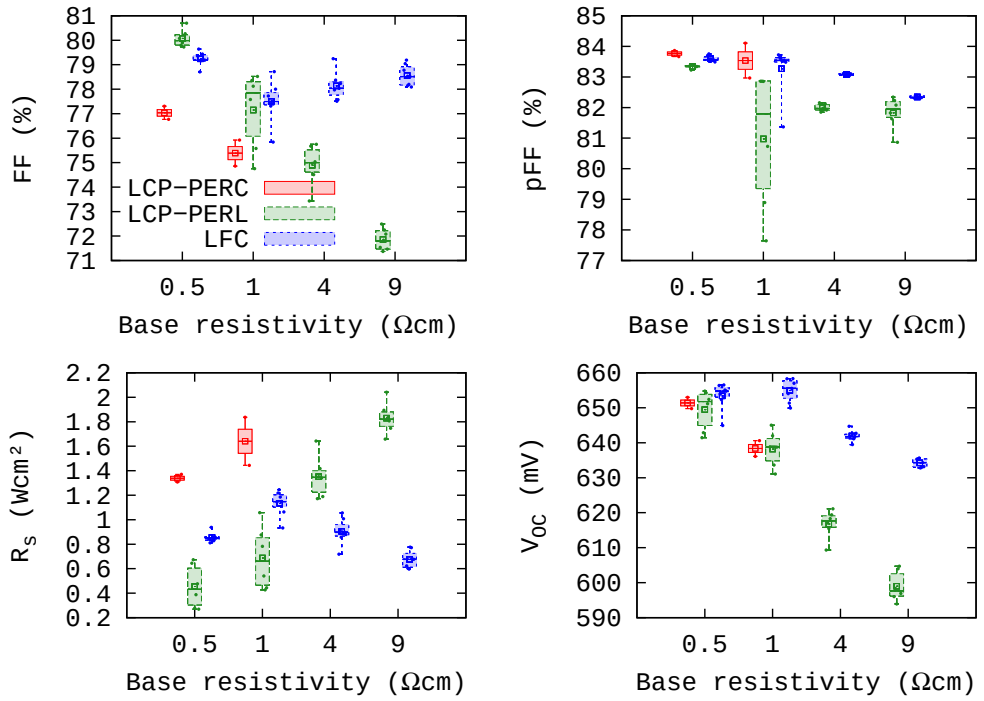

Fig. 33
Comparison of the *FF*, *pFF*, R_s and V_{oc} of the cells shown in Fig. 32. Please note the discrete x-scale.

3.5 Loss analysis of LCP local back surface field solar cells

Compared to the LFC reference, the LCP-PERC and LCP-PERL solar cells show significant lower *FF* and V_{oc} levels for higher values of base resistivity. In the following, the reasons for this base resistivity related degradation of the LCP-PERL and –PERC cells will be analyzed.

3.5.1 Contact geometry related losses

A direct comparison of the LCP-PERL and LFC cells in section 3.4 is difficult due to the fact that the rear contact geometry is different for each cell design. This section will discuss the intrinsic differences of the impact of the contact geometry for different base resistivities.

Fig. 34 shows the two types of rear contact designs of the LCP-PERL and LFC solar cells with line and point contacts, respectively. The influence of each geometry on the series resistance losses and the recombination losses has to be analyzed. The total series resistance of the solar cell $R_{s,total}$ is a superposition of different series resistance contributions.

$$R_{s,total} = R_{s,Emi} + R_{s,cont,Emi} + R_{s,metal} + R_{s,spread} + R_{s,cont,base} \quad (27)$$

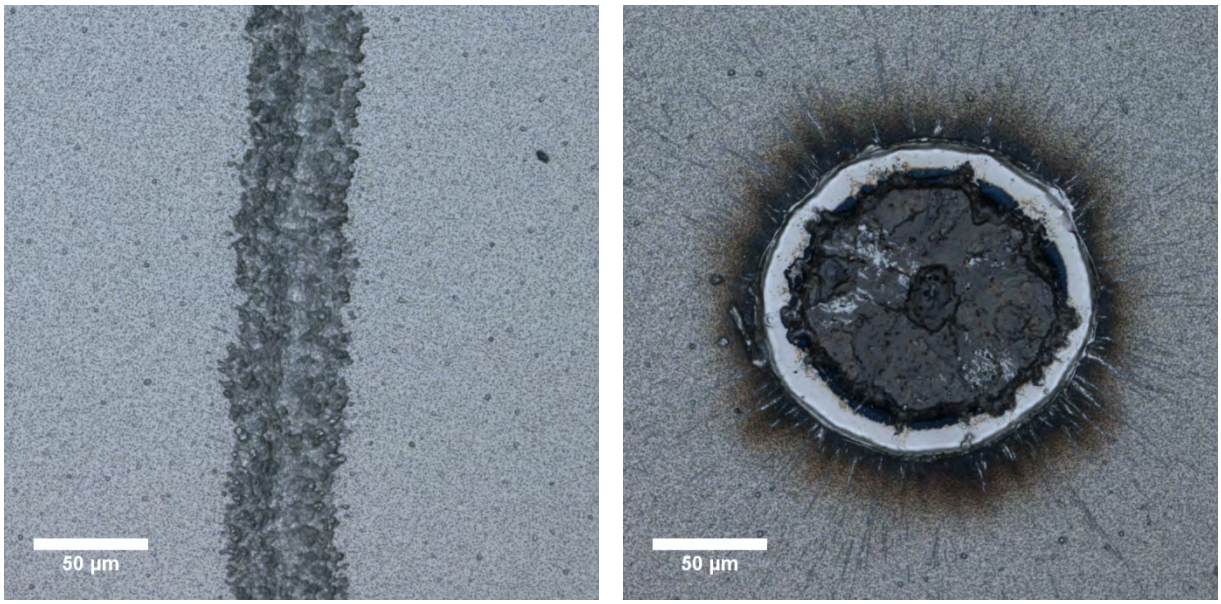

Fig. 34
Comparison of a LCP boron doped line contact (left image) and a LFC point contact (right image) both after metallization.

Eq. (27) shows the contributions to the total series resistance of a solar cell. The total series resistance is the sum of the emitter resistance $R_{s,Emi}$, the front side contact resistance $R_{scont,Emi,}$, the series resistance of the front and rear side metallization $R_{s,metal}$, the contact resistance of the rear side metal contact $R_{s,cont,base}$ and the spreading resistance within the base $R_{s,spread}$. The spreading resistance in the base is strongly influenced by the base resistivity and depends on the rear side geometry. Under the assumption of low contact resistivities at the doped LCP and LFC contacts, $R_{s,spread}$ becomes the limiting series resistance contribution for large base resistivities. In order to determine if the line contact design induces intrinsic disadvantages in the fabricated solar cells the spreading resistance was simulated for each case using a generalized model by Karmalkar et al. [138] shown in Eq. (28) in the generalized form suggested by Saint-Cast et al.[139].

$$R_{s,spread} = \frac{W\rho_{Base}}{f_{cont}}\left((1-\gamma)\left(1+\frac{\Delta_{cont}-x}{x}\right)^{\frac{\beta}{1-\gamma}}+\gamma\right) \qquad (28)$$

The spreading resistance in in Eq. (28) is in Ωcm² and is calculated using the wafer thickness W, the contact area fraction f_{cont}, the half contact pitch Δ_{cont} and the half line width or point radius x. The parameters γ and β are listed in Table IX for the according geometry.

Table IX: Parameters for the spreading resistance model shown in Eq. (28).

Line contact	Point contact (circular contact in a concentric circle)
$\beta = -1$	$\beta = -2$
$\gamma = \frac{x}{W \tan\alpha} \ln\left(1 + \frac{W \tan\alpha}{x}\right)$	$\gamma = \frac{1}{1 + \frac{1.13\,W}{x} \tan\alpha}$
$\propto \approx \frac{57°}{1 + \frac{0.35x}{W}}$	$\propto \approx \frac{50°}{1 + \frac{0.31x}{W}}$

Eq. (28) was used in order to calculate the spreading resistance for the LCP-PERL (line contact with line width $2x$ = 50 µm) and the LFC (point contact with diameter $2x$ = 100 µm). Fig. 35 shows the measured total series resistance $R_{s,total}$ of the LCP-PERL and LFC solar cells and the calculated spreading resistance part for a varying contact fraction and the four different base resistivities. It can be seen that the spreading resistance becomes dominating for the line contact design for small contact fractions (large pitch) and large base resistivities. For a base resistivity of 4 Ωcm the two smallest contact fractions (2.5% and 1.25% relating to a pitch of 2000 and 4000 µm, respectively) are dominated by the spreading resistance contribution. The spreading resistance part for 5% contact fraction (1000 µm) is still about 60% of the total resistance ($R_{s,spread,line}$ = 0.42 Ωcm², $R_{s,total}$ = 0.72 Ωcm²). However, the total series resistance of these cells is on a similar level compared to the point contact LFC design with an optimized pitch and the LCP-PERL cells with the largest contact fractions (10%, pitch of 500 µm). This indicates that even for the second largest contact fraction the total series resistance is already dominated by other contributions (see Eq. (27)).

The line contact design did not show any intrinsic disadvantage in terms of series resistance if the line pitch is reduced to reasonable values for large base resistivities. Although, the calculated spreading resistance of LCP-PERL solar cells shows for the given geometries an intrinsic disadvantage of about a factor of two (comparing the blue lines to the orange lines in Fig. 35), the contribution of it to the total series resistance is only limiting for large pitch (small contact fraction).

The fill factor characteristics in Fig. 36 show the inverse contact fraction dependence as the total series resistance in Fig. 35. Therefore, the contact geometry is again only limiting the fill factor of the fabricated LCP-PERL solar cells for large base resistivities and large pitch.

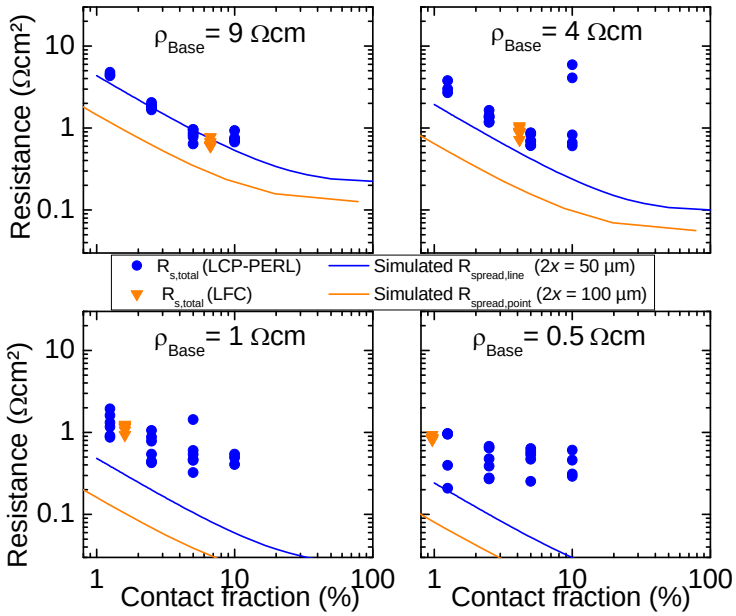

Fig. 35
Measured total resistance and calculated spreading resistance of the LCP-PERL and LFC solar cells.

The *pFF* of the LCP-PERL cells (blue open symbols in Fig. 36) decreases for large contact fractions. This is assumed to be a consequence of recombination related loss of the *pFF* due to increased recombination at the LCP LBSF structures. The pitch related decrease in the *pFF* is more pronounced for high base resistivities and is almost negligible for $\rho_{Base} < 1$ Ωcm. The increased recombination activity for the LCP LBSF structures for high base resistivities will be discussed in more detail in the next sections.

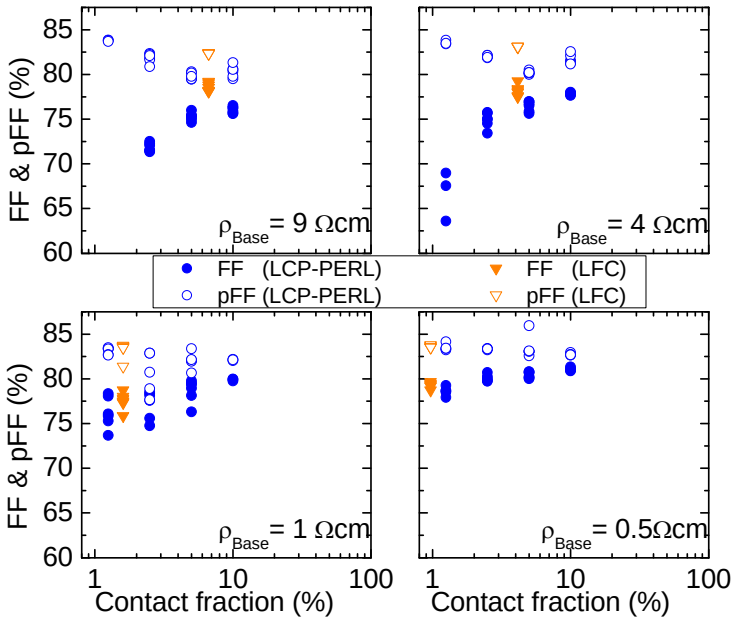

Fig. 36
Measured fill factor (FF) and pseudo-fill factor (pFF) of the LCP-PERL and LFC solar cells.

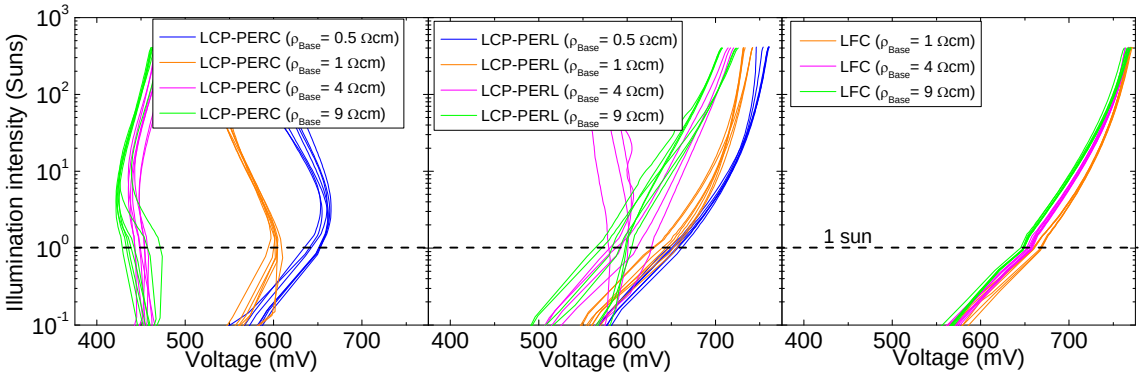

Fig. 37
SunsV$_{oc}$ measurement under high illumination intensities of LCP-PERC (left plot), LCP-PERL (center plot) and LFC (right plot) solar cells with varying base resistivity.

3.5.2 Local Schottky contact induced losses

As discussed in chapter 2.2 Schottky contacts in solar cells can induce a reverse diode to the pn-junction diode, which can decrease the open circuit voltage and the fill factor due to a reverse voltage and an increased contact resistance, respectively. Past publications [32, 136, 140] already showed that SunsV$_{oc}$ measurements can reveal if a Schottky diode limits the open circuit voltage of a solar cell. The reverse Schottky diode induces a reduced open circuit voltage for high illumination intensities and alters the slope of the measured illumination intensity – open circuit voltage curve to negative values.

Fig. 37 shows SunsV$_{oc}$ measurements for LCP-PERC, LCP-PERL and LFC solar cells with varying base resistivities without distinguishing the data for different rear side pitch. As expected, the LCP-PERC cells (left plot) show a V_{oc} limitation due to the missing doping at the contact and the resulting rear side Schottky diode. The Schottky diode induces a negative slope of the illumination intensity – voltage curve, which reduces the open circuit voltage of the cells. The limitation of the V_{oc} for 1 sun already appears for base resistivities $\rho_{Base} \geq 1$ Ωcm. For 4 and 9 Ωcm base resistivity the negative Schottky diode slope even dominates the measurement for low illumination intensities. This means that the significant V_{oc} decrease of the LCP-PERC cells with high base resistivities shown in Fig. 32 is mostly caused by a rear side Schottky contact. The appearance of the Schottky contact also explains the *FF* drop shown in Fig. 32 due to an increased contact resistance, which is mostly limited by a thermionic current transport over the Schottky barrier.

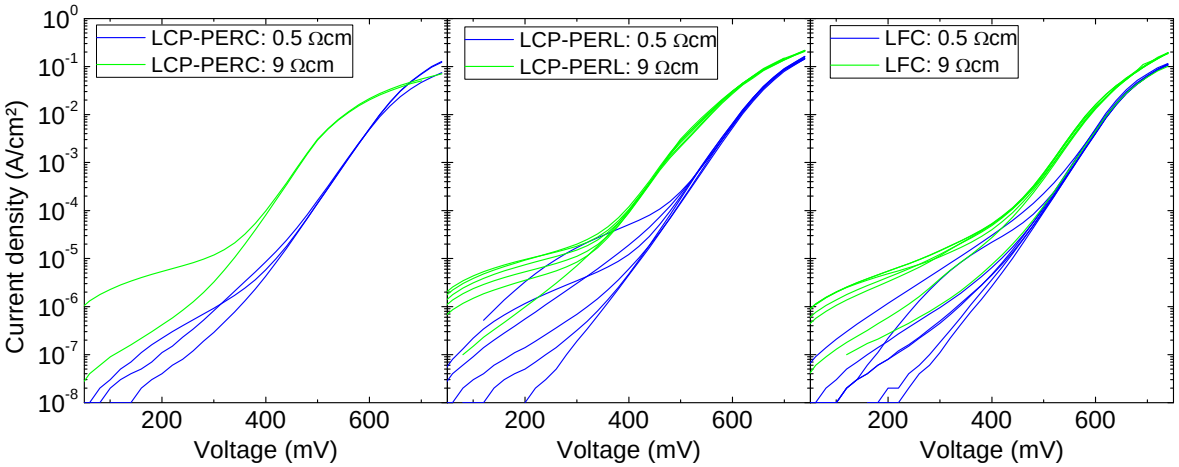

Fig. 38
Measured dark-IV curve of LCP-PERC (left plot), LCP-PERL (center plot) and LFC (right plot) solar cells with varying base resistivity (ρ_{Base} = 0.5 Ωcm (blue data) or 9 Ωcm (green data). The LCP-PERC and PERL cells have a constant line pitch of 1000 µm and the LFC solar cells have an optimized pitch of 343 µm and 900 µm for ρ_{Base} = 0.5 Ωcm and 9 Ωcm, respectively.

The Schottky contact limitation of the LCP-PERC solar cells only becomes obvious in the illuminated state, such as for SunsV_{oc} measurements or in the light IV curve. The dark-IV curve the LCP-PERC cells (left plot in Fig. 38) do not show any characteristic features compared to the LCP-PERL (center plot in Fig. 38) or LFC (right plot in Fig. 38) solar cells, which would give a hint to their significantly lower V_{oc} level. The only apparent feature of the LCP-PERC cells (9 Ωcm base resistivity) is the smaller slope of the current density curve in the high voltage regime (V > 600 mV). As discussed in section 2.3.2 the inflection of the SunsV_{oc} curve and the decreased slope in the high voltage region of the dark IV curve of the LCP-PERC solar cells are characteristic measurement features for rear side Schottky contacts.

The LFC solar cells show no significant Schottky diode behavior in the right graph in Fig. 37 for the measured illumination range. This shows that the performed LFC process formed a sufficient local Al back surface field doping, which enabled an ohmic contact at the rear side.

The LCP-PERL solar cells show an unexpected behavior in the center graph in Fig. 37. If the formation of the local boron back surface field was successful the SunsV_{oc} measurements of the cells in Fig. 37 should look similar to the LFC case. However, the curves of the LCP-PERL solar cells in Fig. 37 show a slight bending at high illumination intensities for 0.5 and 1 Ωcm base resistivity. This indicates that there might be a detrimental impact of a Schottky contact diode. Though, this alleged Schottky diode behavior of an inflection in the SunsV_{oc} curve is not more pronounced for 4 and 9 Ωcm base resistivity, as in the case of the LCP-PERC solar cells. For these

high base resistivities the illumination intensity – voltage curve seems to be shifted to a lower voltage regime and shows no inflection even for high illumination intensities[8]. This effect cannot be explained assuming a complete Schottky diode behavior along the whole LCP-PERL rear side openings. Furthermore, the low or similar series resistance level of the LCP-PERL solar cells compared to the LFC solar cells shown in Fig. 33 and Fig. 35 indicates that there is no Schottky contact limitation but that the dominant current path on the rear side is an ohmic contact.

Dopant contrast imaging measurements at cross sections of boron LCP LBSF structures were performed. An example of a representative area is shown in Fig. 39. The dopant contrast of the samples observable as gray contrast was quite low. However, the inhomogeneous appearance of the light grey contrast between the white Al-layer and the dark Si bulk in Fig. 39 indicates that the created boron doping in this area could result in a non-homogenously doped contact opening. This could lead to the formation of local Schottky contacts within an otherwise ohmic rear side opening. Furthermore, locally defected structures become obvious as void structures in the SEM image of the LBSF cross sections of the LCP-PERL solar cells.

The previous section showed that the pFF of the LCP-PERL solar cells was reduced for high base resistivities and high LBSF contact fractions, which is a hint for increased recombination in the LBSF regions due to a reduced lifetime in this area. However, the separation of local Schottky contact induced losses and the impact of a lifetime reduced regions around the LCP rear side opening is experimentally hard to distinguish.

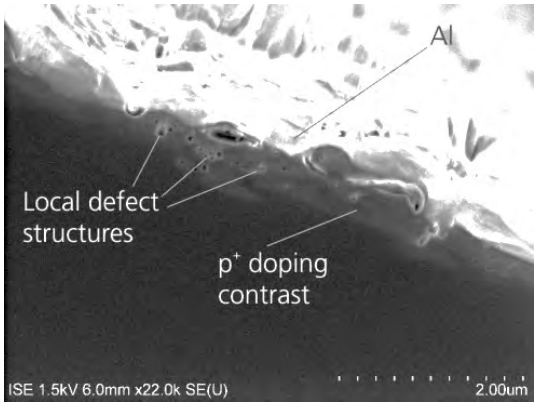

Fig. 39
SEM image of a cross section of a boron LCP LBSF contact after the Al metallization.

[8] The inflection points of the four LCP-PERL solar cells with a base resistivity of ρ_{Base} = 4 Ωcm in Fig. 37 are assumed to be caused by LCP processing errors leading to no sufficient openings of the passivation layer.

Therefore, simulations of the fabricated solar cells were performed. In order to take 2-d effects of the inhomogeneous doping quality into account, the following simulation results are based on 2-d simulations with the simulation software Sentaurus TCAD [141] and were performed by Heiko Steinkemper. The simulation setup was based on the solar cell design shown in Fig. 30 and Table VIII. In the simulations the illumination intensity was varied in the range of the measured SunsV_{oc} results and the according open-circuit voltage was determined. This allows a modeling of the measured SunsV_{oc} curves shown in Fig. 37. Furthermore, dark-IV curves of the different simulation scenarios were simulated.

The simulation analyzes three different scenarios. The first one is an incomplete doping along the contact. The rear side contact is in this case divided into two contact fractions. The first one is an ohmic contact assuming an Al metal contact on top of the 23 µJ boron doped LBSF shown in Fig. 29. The second part of the contact is a Schottky contact assuming the Al metallization directly on the p-type base. The simulations were performed for two different base resistivities (0.5 and 9 Ωcm) and different contact fractions. All simulations assume a rear side pitch of 1000 µm and a rear side contact width of 50 µm. Fig. 40 shows the simulated SunsV_{oc} measurements in comparison to the experimental curve of a LCP-PERL cell with the same cell design.Fig. 40 shows that the simulated SunsV_{oc} curves matches with the measured curves of the LCP-PERL solar cells for a Schottky fraction below 80% and 96% for ρ_{Base} = 0.5 and 9 Ωcm, respectively. This indicates that the boron LCP rear side openings show no large amount of local Schottky contact areas but seem to be dominated by ohmic LBSF doped areas.

Comparing both resistivities, the simulation shows that possible Schottky dominated areas - if existing - are limited to very low fractions within the local rear side contacts. In a next step the simulations took into account a laser damaged area by setting the lifetime to 10 ns in the complete region within a radius of 5 µm around the contact. Fig. 41 illustrates the simulation results of combinations of local Schottky contact ratios and a laser damaged zone LDZ). The simulated SunsV_{oc} measurements with a LDZ in Fig. 41 show a similar behavior as the simulation results without LDZ in Fig. 40 b). In the case of a LDZ the simulation of a solar cell without any Schottky fraction matches the best with the measurement. Furthermore, by a comparison of the simulated SunsV_{oc} curves of Fig. 41 and Fig. 40 b) it is visible that the implementation of a LDZ leads to a shift of the simulated SunsVoc curve to lower voltages.

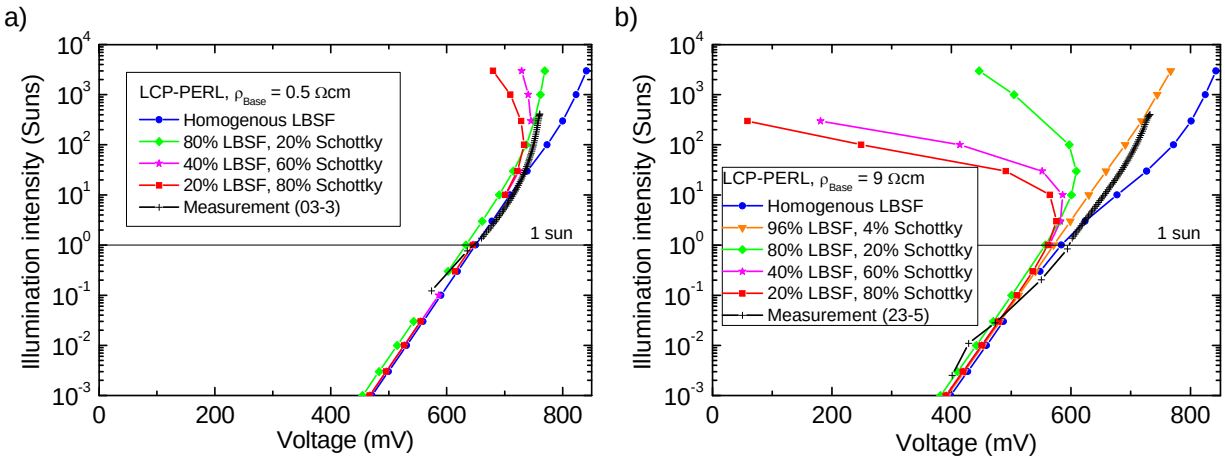

Fig. 40
Comparison of simulated and experimental SunsV_{oc} curves of LCP-PERL solar cells (rear side pitch: 1 mm) with line shaped rear side openings of partial Schottky and LBSF character, assuming different Schottky-LBSF contact ratios and two different base resistivities.

The same trend is visible for the LCP-PERL solar cells with increasing ρ_{Base} in the measured SunsV_{oc} of Fig. 37. This indicates that the shift to lower Voc values of the LCP-PERL solar cells might be a result of locally laser induced damage around the LCP LBSF structures. This assumption will be further discussed in the next section.

3.5.3 Local lifetime reduced regions

Internal quantum efficiency (IQE) measurements confirm that the local rear side contacts are regions of high recombination. Fig. 42 shows the measured IQE of a LFC solar cell (green filled squares) with a base resistivity of 9 Ωcm. The IQE curve of the LFC solar cell illustrates a current collection near unity for generation wavelengths up to almost 1000 nm.

In contrast to that the LCP-PERL solar cells (blue filled circles) show an earlier breakdown of the IQE curve at about 900 nm. The increasing absorption length in silicon for increasing wavelength in this regime allows depth dependent information of the local current collection. The wavelengths below 900 nm are mostly absorbed on the front side or the bulk of the solar cell, which leads to a correlation of front side or bulk recombination effects and the IQE in this regime. Larger wavelengths also reach the rear side of the solar cell and lead to a higher sensitivity of the IQE on rear side recombination effects in this regime.

Therefore, the decrease in the IQE for wavelengths larger than 900 nm of the LCP-PERL cells correlates with increased recombination on the rear side. Furthermore, the IQE decrease correlates with increasing rear side contact fraction when comparing the

blue filled circles (LCP-PERL solar cell, low contact fraction) to the orange filled triangle (LCP-PERL solar cell, large contact fraction). This correlation leads to the conclusion that local lifetime reduced areas are present around the LCP-LBSF regions. These lifetime reduced areas are the origin of increased recombination losses and therefore, the origin of the reduced open circuit-voltage compared to the LFC reference solar cells. The local lifetime reduced areas are most likely a consequence of laser induced damage, which is visible in Fig. 39 as local hole shaped defect structures within the laser processed area.

The comparison of the blue filled circles (LCP-PERL, large f_c) and the magenta filled stars (LCP-PERC, large f_c) in Fig. 42 shows the same level in the long wavelength IQE. The same IQE level for the LCP-PERL solar cells processed with a sodium containing liquid jet doping source and the H_2O liquid jet processed LCP-PERC solar cells leads to the conclusion that the increased rear side recombination is not a consequence of sodium induced recombination centers. However, despite laser induced damage structures, the introduction of additional impurities such as oxygen[9] during the laser doping process could also enhance the local recombination in these areas.

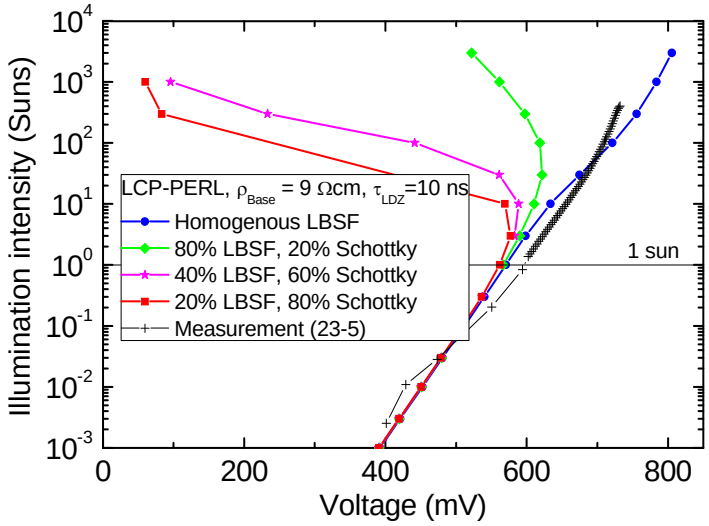

Fig. 41
Comparison of simulated and experimental SunsV_{oc} curves of LCP-PERL solar cells (rear side pitch: 1 mm) with line shaped rear side openings of partial Schottky and LBSF character, assuming different Schottky-LBSF contact ratios and a laser damaged zone with a reduced lifetime of 10 ns within a radius of 5 µm around the contact.

[9] SIMS measurements show a similar Oxygen concentration compared to the boron concentration using 4.4 M NaBH4 in 14 M NaOH as LCP doping source. Furthermore, the application of a H2O liquid jet for the LCP-PERC solar cell rear side contact openings leads also to an introduction of a similar non-electrically active oxygen profile in the processed area.

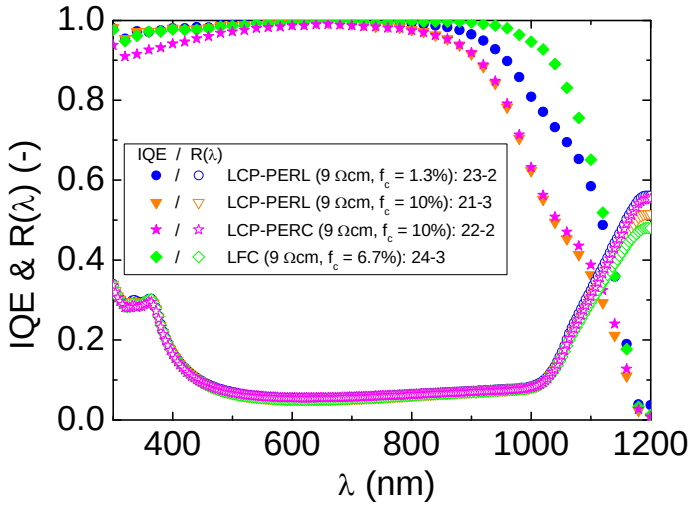

Fig. 42
Measured IQE and reflection spectra of two LCP-PERL solar cells with small (blue data) and large (orange data) rear side contact area fraction f_c, a LCP-PERC solar cell (magenta data) with large contact fraction and the according LFC reference (green data) with the same base resistivity.

3.6 Summary and further optimization routes

Chapter 3 summarizes the developments of a LCP based boron laser doping process in order to create local back surface fields for p-type PERL solar cells. After a screening of potential boron doping sources for LCP, the most promising candidate was an aqueous solution of 4.4 M $NaBH_4$ in 14 M NaOH. SIMS measurements validated a high amount of B with a surface doping concentration of up to 10^{20} cm^{-3}.

The first implementation of the boron LCP laser doping process as LBSF in p-type PERL solar cells showed a successful proof-of-concept and allowed the fabrication of solar cells with a maximum cell efficiency of 20.9%. The cells were fabricated on FZ-Si wafers with a base resistivity of 0.5 Ωcm.

After the successful proof-of-concept the boron LCP process was further evaluated by the application as LBSF for PERL solar cells with varying base resistivities and compared to a LCP process for PERC solar cells and an established LFC solar cell process. The increase of the base resistivity reveals doping or recombination related process problems, which have a stronger impact on high base resistivity material. On the one hand the appearance of Schottky contacts due to non- or low LBSF doping could be analyzed and on the other hand the influence of laser induced damage on the cell performance for LCP-PERL solar cells was shown. The p-type solar cells were fabricated on FZ-Si wafers with a base resistivity of 0.5, 1, 4 and 9 Ωcm and featured either non-additionally doped LCP line rear contact openings (LCP-PERC), LCP boron doped LBSF line structures (LCP-PERL) or point-shaped LFC LBSF structures

(LFC) on the rear side. The IV results of the different solar cell designs revealed a stable performance of the LFC reference cells, a significant decrease of the cell performance of the LCP-PERL solar cells with increasing base resistivity and a massive breakdown of the cell performance of the LCP-PERC solar cells for base resistivities larger than 1 Ωcm.

A loss analysis of the processed solar cells with varying base resistivity revealed a slight disadvantage of the line contact design of the LCP-PERL solar cells compared to the point contact design of the LFC reference solar cells, especially for high base resistivities, related to an increased spreading resistance of the line contact design for same contact fractions compared to the point contact design. However, the series resistance analysis showed that the LCP-PERL solar cells are not limited by an increased contact resistance as in the case of the LCP-PERC solar cells. The low series resistances of the LCP-PERL solar cells proofed that the formation of an ohmic rear side contact by the LCP boron doping was successful. In contrast to that the LCP-PERC solar cells showed a limitation due to the formation of a rear side Schottky contact. However, despite the good contacting behavior, the LCP-PERL solar cells showed a cell performance limitation due to a decrease in the open circuit voltage for increasing base resistivities. A combination of simulation results and measurement results could show that the V_{oc} limitation is not a consequence of local Schottky contacts due to non-homogenously doped contact openings but a result of local lifetime reduced areas around the LCP processed LBSF structures. The local lifetime reduction is most likely a consequence of laser induced damage during the laser doping process due to non-optimized processing parameters.

The performed experiments in this work showed that the application of the developed boron LCP laser doping process was mostly limited by the discussed laser damage related cell performance limitation for high base resistivities but also demonstrated several technological hurdles such as nozzle or pipe plugging of small precipitates of the liquid boron source during processing and handling challenges due to high etch rates of silicon caused by the NaOH containing boron source. These findings demonstrate that beside an optimization of the laser processing parameters also further evaluations of liquid boron doping sources (non-etching, high boron concentration, low chemical reactivity with water, low concentration of recombination active elements) would lead to significant technological improvements.

Further optimization routes for the LCP boron laser doping process should address a reduction of the introduced laser damage and possible alternative boron doping

sources with lower pH values. The impact of laser damage depends on the applied laser process, the passivation layer properties and the possibility of annealing steps after laser processing. The successfully optimized LFC process by Nekarda [60] and his co-workers shows that an enhanced laser parameter study with different laser pulse durations and/or wavelengths could significantly decrease the appearance of laser induced damage zones.

4 Theoretical considerations on selective emitter solar cells

The following chapter aims to analyze the different impacts of selective emitter designs on the electrical performance of silicon solar cells by calculating and simulating the benefits of a highly doped region underneath the metal contacts on the contact resistance and contact recombination losses. Both loss mechanisms are discussed from a general point of view in section 4.1 and 4.2. The impact of both loss mechanisms on the electrical performance in different solar cell designs (Al-BSF, PERC, PERL) is subsequently discussed in section 4.3. Furthermore, section 4.3 and 4.4 discuss the correlation of different solar cell design features (selective emitter process – metallization scheme – homogenous emitter design) and how their interaction defines the possible benefit of a selective emitter design.

There are several experimental [46] (see [39] for a review) or simulation [142] (see [143] for a review) based publications, discussing the impact of selective emitter designs on the cell performance of silicon solar cells. However, most of the works are either focusing on lab-type solar cell designs or industrially feasible solar cell designs with screen printed front side contacts. This work expands the discussion by including also plated contacts, which are a promising alternative for industrially feasible high efficiency silicon solar cell designs.

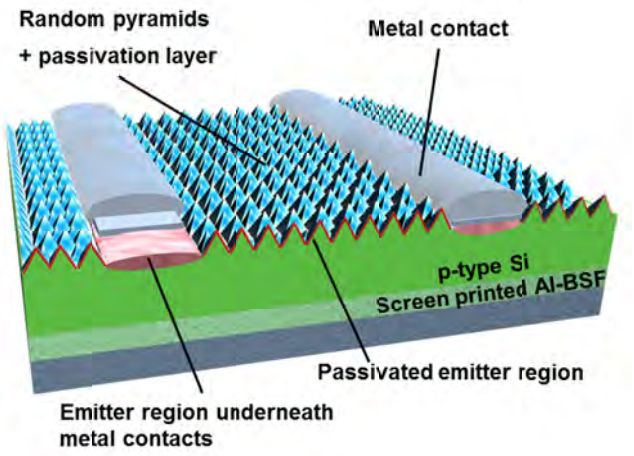

Fig. 43
Exemplary scheme of an Al-BSF solar cell design with a selective emitter (SE) on the front side. The selective emitter features differently doped emitter areas (red colored area) underneath the metal contacts and in the passivated region in between the contacted area. In consistency with the schemes of Al-BSF solar cells with SE in the following chapters, the shown solar cell features a 2-layer metal contact on the front side exemplary for Ni-Cu or Ni-Ag plated contacts.

The term “selective emitter” is used for a locally optimized emitter design with different emitter doping profiles underneath the metal contacts and in the passivated regions between the metal contacts. Fig. 43 shows an example for a selective emitter design of an Al-BSF solar cell. An emitter with the same doping profile underneath the metal contacts and in the passivated regions will be called in this work “homogenous emitter”. The beneficial impact of the selective emitter can be separated into two parts. On the one hand the passivated emitter region can be optimized in terms of low saturation current density and high quantum efficiency in order to reduce recombination related V_{oc} and J_{sc} losses, respectively. On the other hand the emitter region underneath the metal contacts can be optimized in terms of low saturation current density, low contact resistivity and high prevention against metallization induced shunts or spikes. The following sections will discuss the impact of state-of-the-art selective emitter designs in terms of optimizing the series resistance and recombination losses in the solar cell.

4.1 Emitter contact resistance losses

The emitter doping profile underneath the metal contacts and in the passivated regions has a strong impact on different series resistance components in the solar cells. An increased peak surface doping density underneath the metal contacts reduces the contact resistance due to the transition from thermionic or thermionic field emission current transport to a tunneling dominated current transport into the metal contact by field emission (see Fig. 8 in section 2.3.1). The tunneling dominated current transport comes along with low contact resistivities.

There are different techniques to form the emitter metal contacts for solar cells. Photolithography in combination with an evaporated or sputtered metal layer is the most common technique for high efficiency lab type solar cells. The application of Ti or Al layers allows good contact resistivities due to a low work function mismatch on n- and p-type Si, respectively. However, this technique includes high processing time and processing costs. Therefore, industrial solar cells mostly feature Ag screen printed contacts on the front side. Screen printing of metal pastes allows low processing time and processing costs. Depending on the application, Ag or Al pastes are used in order to contact n-type or p-type doped surfaces, respectively. The Ag-paste contains Ag crystallites, glass frit and organic solvents and is printed onto the emitter passivation layer (PECVD-SiN_x). During a subsequent firing process the organic solvents are burned and the silver/glass finger fires through the SiN_x and the contact is formed by local silver crystallites at the emitter surface. An industrially feasible alternative to Ag screen printing is Ni/Cu/Ag plating [50, 78, 144-146]. This technique forms a plated

Ni contact at the emitter surface, which is subsequently annealed at 250-450°C forming a Ni-silicide phase at the metal-silicon interface. The Ni and the Ni silicide layer provide low contact resistivities for n-type doped silicon surfaces and act as diffusion barrier against the subsequently plated Cu layer.

Fig. 44 shows a comparison of measured and modeled contact resistivities for screen printed Ag and plated Ni contacts. The experimental values of the plated contacts (blue, green and orange data) show that the application of Ni based contacts allows low contact resistivities even on low emitter surface doping densities. The experimental values of the Ag screen printed fingers (magenta data) show a large difference to the modeled values along the whole doping density range and for all barrier heights. This difference is caused by the fact that the contact formation for printed contacts is much more complex than for plating or evaporation, which causes a much smaller actual contact area in comparison to the printed area. There are different theories about the contact formation [147-149], which show that the current transport at the silicon-metal interface is dominated by silver crystallites at the interface. Therefore, the printed area, which is assumed for the calculation of the experimental contact resistivities, is larger than the contact area, which leads to larger experimental values compared to the theory.

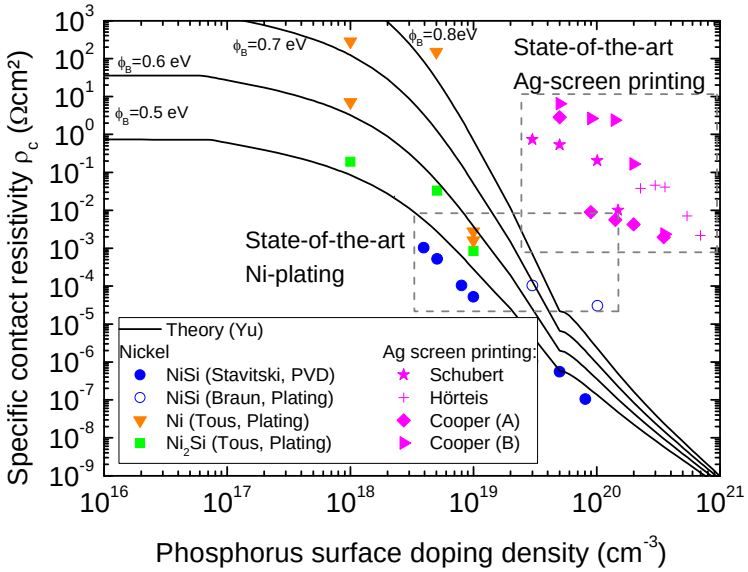

Fig. 44
Measured and modeled contact resistivities of plated Ni and screen printed Ag contacts on n-type doped surfaces with varying surface doping densities. The presented data are measurements of ρ_c of Ni, different Ni silicide phases and screen printed Ag contacts from Stavitski [150], Braun [151], Tous [152], Schubert [148], Hörteis [147] and Cooper [153]. The calculated contact resistivities are based on the model of Yu [27], which is further described in section 2.3.1.

The simulations (shown as black lines in Fig. 44 for different barrier heights) indicates that high emitter doping densities at the silicon metal interface lead to reduced contact resistances in the solar cell. However, not only the interface properties influence the contact resistance losses but also the current density flowing through the contact. Thus, the contact design also influences the contact resistance. The contact resistance R_{cont} (in Ωcm²) of the solar cell is linear in the contact resistivity, which is weighted by the ratio of the active cell area of the unit cell A_{unit} and the contact area A_{cont}. Assuming line shaped contacts the area ratio can be replaced by the ratio of the finger pitch x_{pitch} and the contact width w_{cont} as shown in Eq. (29).

$$R_{cont} = \frac{x_{pitch}}{w_{cont}} \rho_c \qquad (29)$$

Eq. (29) can be used to evaluate if the contact resistance will be a limiting series resistance contribution in a solar cell design. The total series resistance R_s of state-of-the-art non-concentrating silicon solar cells is usually in the range of 0.2-2 Ωcm². Assuming that the contact resistance contribution should not be larger than 0.05 Ωcm², which would be 25% for R_s = 0.2 or 2.5% for R_s = 2 Ωcm², Eq. (29) defines a maximum contact resistivity $\rho_{c,max}$. Fig. 45 shows the influence of the contact design on the maximum contact resistivity $\rho_{c,max}$.

The combination of Fig. 44 and Fig. 45 shows that for screen printed contacts the contact resistance becomes a limiting loss in the solar cell easily because ρ_c is larger than $\rho_{c,max}$ for emitter doping densities below 10^{20} cm^{-3}. However, in the case of plated Ni contacts ρ_c is below $\rho_{c,max}$ for emitter doping densities down to 10^{19} cm^{-3}. This shows that for screen printed metallization schemes on lowly doped emitters the implementation of a selective emitter design becomes more beneficial due to a higher sensitivity of the contact resistance on the surface doping concentration. On the other hand the contact resistance of plated Ni contacts is for surface doping densities above 10^{19} cm^{-3} mostly limited by the contact geometry, which reduces the impact of an additional highly doped area underneath the metal contacts.

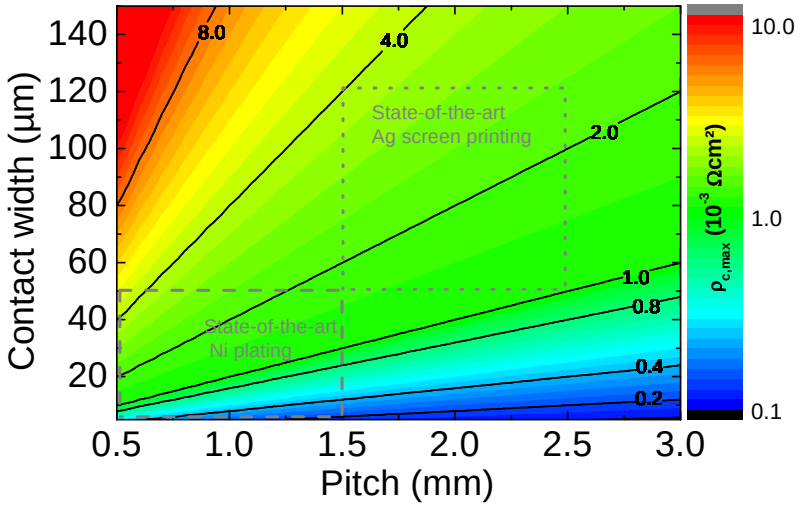

Fig. 45
Maximum contact resistivity[10] for a contact resistance R_{cont} < 0.05 Ωcm².

In conclusion the impact of a selective emitter only becomes significant for the series resistance losses of a solar cell if the surface doping density of the homogenous emitter is not sufficient to ensure $\rho_c < \rho_{c,max}$.

4.2 Emitter recombination losses

The impact of the emitter recombination losses on the solar cell efficiency is mostly caused by a reduction of the open circuit voltage and the short circuit current density. The most relevant parameter describing the open circuit voltage loss is the saturation current density J_{01} of the two diode equivalent circuit of the solar cell. The open circuit voltage shows a great sensitivity on this parameter, which describes Auger and Shockley-Read-Hall (SRH) related recombination currents in the solar cell. If the cell is not limited by series resistance effects, in low level injection conditions and if the photo-generation within the space charge region is negligible small [3, 4, 116] the differential equations describing the operation of the cell satisfy the principle of superposition. This allows the definition of the light J-V curve as a shifted dark J-V curve by the short circuit current density J_{sc}. Furthermore, the saturation current density J_{01} can be written in first approximation as area weighted sum of the recombination paths in each cell region as shown in Eq. (30) and (31).

$$J_{01} = J_{01,E} + J_{01,base} + J_{01,rear} \quad (30)$$

$$J_{01,E} = \frac{1}{A_{cell}}\left((A_{cell} - A_{cont})J_{01,pas} + A_{cont}J_{01,cont}\right) \quad (31)$$

[10] For a comparison of Fig. 44 and Fig. 45 the contact width equals for screen printed contacts the printed width.

The saturation current densities of the passivated emitter region $J_{01,pas}$, of the metalized emitter region $J_{01,cont}$, of the bulk $J_{01,base}$ and rear side $J_{01,rear}$ are weighted with their according area fractions. The metalized area A_{cont} is for state-of-the-art industrial solar cells in the range of 5-10% of the cell area A_{cell}.

EDNA [133] simulations were performed in order to estimate the impact of the emitter doping profile and possible improvements due to a selective emitter doping on the saturation current densities. The assumptions were a metalized surface[11] with $S_{0,cont} = 10^7$ cm/s [154, 155] for the contacted emitter regions and a passivated textured surface with a surface recombination velocity $S_{0,pas}$ for the passivated emitter regions. $S_{0,pas}$ was calculated using the parameterization of the data of Glunz et al. [156] by Altermatt et al. [157] shown in Eq. (32). This parameterization describes the surface recombination velocity at the interface of a textured surface passivated with a thermal silicon oxide as a function of the phosphorus surface doping density $N_{d,peak}$.

In contrast to state-of-the-art industrial silicon solar cells this parameterization assumes a thermal oxide instead of a PECVD SiN_x passivated textured surface. Although, there is a parameterization for PECVD SiN_x passivations [157] on planar surfaces the model in Eq. (32) was chosen due to the fact that $S_{0,pas}$ is much more influenced by a texture than by the difference of the passivation systems and there is no model available yet, which describes a PECVD SiN_x passivated textured surface. Therefore, the simulated results can also be used in order to show the dominant trends for SiN_x passivated emitters on textured surfaces.

$$S_{0,pas}(N_{D,peak}) = 1500\left(\frac{N_{D,peak}}{10^{19}\ \mathrm{cm^{-3}}}\right)^{0.3}\ \mathrm{cm/s} + 2000\left(\frac{N_{D,peak}}{10^{19}\ \mathrm{cm^{-3}}}\right)^{2.2}\ \mathrm{cm/s} \qquad (32)$$

The EDNA simulations assumed Fermi-Dirac statistics and n-type Gaussian doping profiles with depths of 0.2-1.5 µm, peak doping densities $N_{D,peak}$ of $5 \cdot 10^{18} - 3 \cdot 10^{20}$ cm^{-3} and a base doping density of 10^{16} cm^{-3}, which equals for p-type Si a base resistivity of about 1.5 Ωcm. This broad range of doping profile parameters can be used to estimate all kind of furnace diffused $POCl_3$ emitter doping, such as deep lab type emitter profiles as well as state-of-the-art industrially feasible shallow diffusion profiles. High efficiency solar cell designs usually feature lightly doped emitters with

[11] The surface recombination velocity is in the maximum limited by the thermal velocity of electrons or holes in silicon, which are depending on the temperature and the applied electric field in the regime of 10^7 cm/s. Therefore, metalized surface is defined as worst case assuming the maximum surface recombination velocity of 10^7 cm/s.

higher sheet resistances of 100-200 Ω/sq. in order to decrease the saturation current density $J_{01,pas}$ within the passivated emitter regions and recombination related J_{sc} losses. This can bring benefits in terms of open circuit voltage but also comes along with an increase of the saturation current density $J_{01,cont}$ in the metalized contact regions.

Fig. 46 shows the sheet resistances of the Gaussian diffusion profiles (lower left) and the according simulated saturation current densities for the passivated $J_{01,pas}$ (upper left) and metalized case $J_{01,cont}$ (upper right) and the ratio of both (lower right). Assuming a typical sheet resistance of thermally diffused emitters for lab type and industrial high efficiency solar cells of R_{sh} > 100-200 Ω/sq. the according $J_{01,cont}$ is in the region of 500-1000 fA/cm². Going to a selective emitter with a highly doped area beneath the contact, $J_{01,cont}$ can be reduced to a range of 100-500 fA/cm².

The results show the antilogy of the optimum doping profile aiming for low saturation current densities for the case of passivated and metalized surfaces. For the metalized case the doping profile acts as shielding, repelling the minority carriers from the high recombinative surface, which is more effective with higher surface doping concentrations and deeper doping depths. On the other hand the saturation current density decreases in the case of passivated surfaces with decreasing surface doping concentrations due to reduced Auger recombination and an improvement of the surface recombination velocity at the interface $S_{0,pas}$.

However, looking at the ratio of $J_{01,pas}$ and $J_{01,cont}$ in the lower right plot of Fig. 46 it becomes obvious that the introduction of a selective emitter becomes more and more important for low peak doping concentrations. Furthermore, $J_{01,cont}$ has to be weighted by the area fraction of the metalized emitter regions (~5-10%). The impact of a selective emitter can be described by replacing $J_{01,cont}$ in Eq. (31) as multiple of $J_{01,pas}$ by $\alpha = J_{01,pas}/J_{01,cont}$.

$$J_{01,E} = J_{01,pas}\left(1 + \frac{A_{cont}}{A_{cell}}(\alpha - 1)\right) \qquad (33)$$

The ratio α can be reduced by the implementation of a selective emitter. However, Eq. (33) and the plot of α in the lower right plot in Fig. 46 show that the impact of the metalized contact region on $J_{01,E}$ is below 10% for small area fractions of 5-10% and small values of α < 3 as in the case for high peak doping densities.

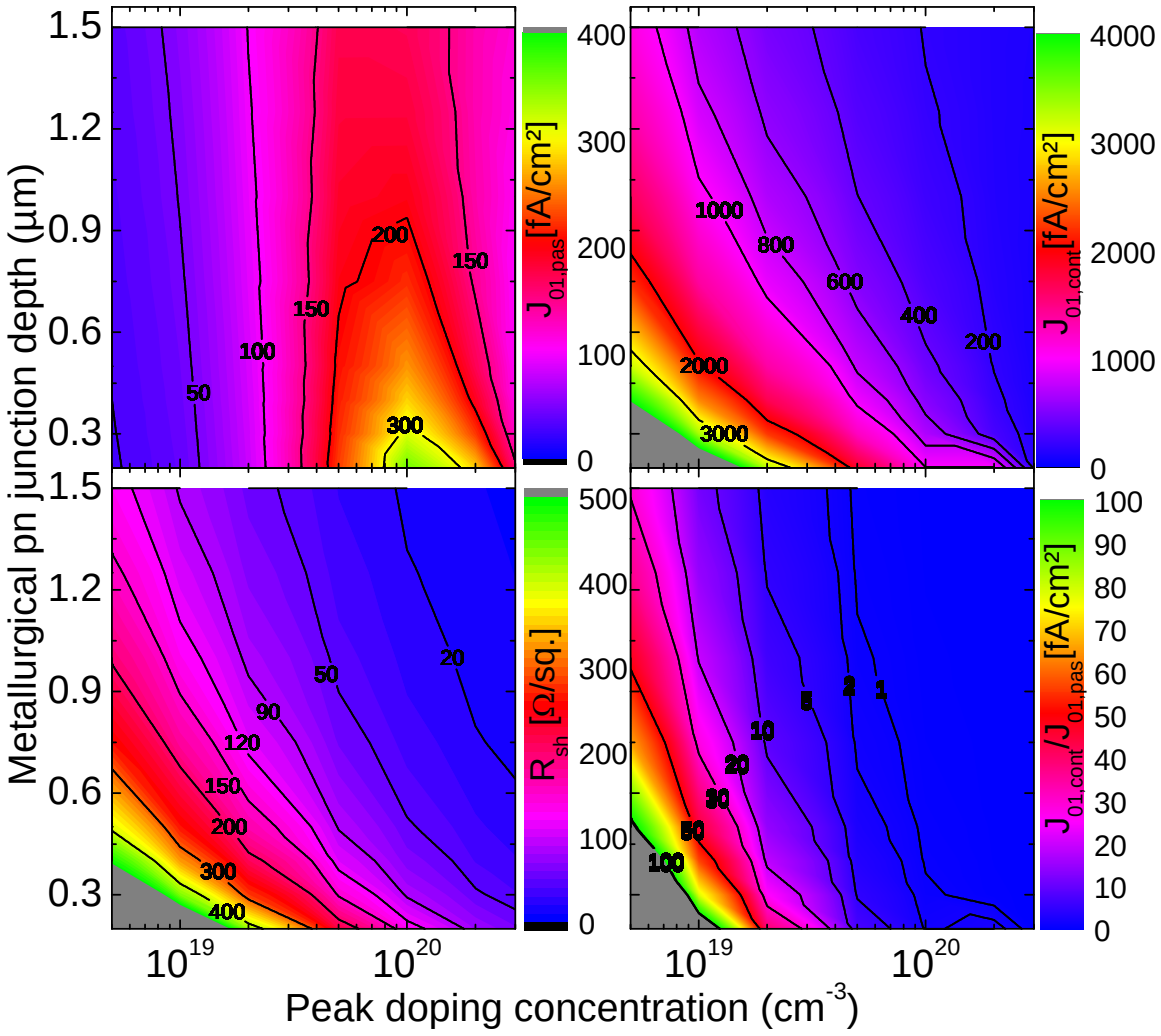

Fig. 46
Calculated sheet resistances (lower left) of the simulated doping profiles, a comparison of the saturation current densities assuming a metalized (upper right) and passivated surface (upper left) using EDNA [133] and the according ratio of $J_{01,cont}/J_{01,pas}$(lower right).

Therefore, the effect on the open circuit voltage of an additional highly doped area underneath the metal contacts in combination with rather high doping levels in the passivated region will be very small. The following simulations will show in which cell design the implementation of a selective emitter becomes beneficial and in which cell designs the cell performance is not limited by a homogenous emitter design.

4.3 Simulation of solar cells with and without selective emitter designs

The following simulations will demonstrate how different aspects of the solar cell design influence the solar cell performance. There is a discussion how the application of homogenous emitter and metallization schemes with a high sensitivity of the contact resistivity on the surface doping concentration will lead to resistance related

limitations of the cell performance for lowly doped emitter profiles. Additionally, the simulations will estimate the impact of reduced recombination effects due to highly doped regions underneath the emitter metal contacts. In the end the simulations will estimate possible benefits of the transformation of a homogenous emitter to a selective emitter design. In this context the correlation between the applied metallization scheme and the possibly resulting benefit of a selective emitter design will be discussed.

4.3.1 Simulation setup

The Quokka simulator [158] was used to perform 2d simulations of different solar cell designs in order to see the impact of improved front side contact saturation current densities $J_{01,cont}$ and contact resistivities ρ_{cont} due to a selective emitter doping or/and advanced metallization schemes such as Ni-Cu plating. This simulation tool features conductive boundary approximations at the interfaces using saturation current densities or surface recombination velocities for the description of local structures such as diffusions, passivated surfaces and contact openings. The Quokka simulator allows a fast simulation of the IV-curve parameters of a defined solar cell design, assuming a variety of cell design parameter sets. Table X and Table XI summarize the simulation parameters of the following Quokka simulations. Four different cell designs are analyzed. The Al-BSF design describes state-of-the-art industrial solar cells with screen printed Al contacts on the rear leading to a full area Al back surface field. The best solar cells with a similar design achieved maximum cell efficiencies of up to 19.9% [7]. The front side features a rather lowly doped emitter with a Gaussian profile with a peak doping density of 10^{20} cm^{-3} and a pn-junction depth of about 0.2 µm.

Table X: Quokka 2d simulation material parameters

Simulation parameters	
Geometrical dimensions	2d
Mobility model	Klaassen [159]
Temperature *T*	300 K
Bulk lifetime τ_B	500 µs
Cell thickness *W*	190 µm
Half front side pitch *x*	0.65 mm
Si material	p-type Si, 1.5 Ωcm

Table XI: Quokka 2d simulation cell design parameters

Simulation parameters				
Front side contact opening width: $2w_{SE}$	20 µm			
Front side metal contact width: $2w_c$	$2w_c = 2w_{SE}$ + 20 µm			
External series resistance in metallization $R_{s,m}$	0.16 Ωcm²			
External shunt resistance R_p	100 kΩcm²			
Cell design	**Al-BSF**	**PERC**	**PERC** (opt. emitter)	**PERL** (opt. emitter)
HE surface doping density	10^{20} cm^{-3}	10^{20} cm^{-3}	10^{19} cm^{-3}	10^{19} cm^{-3}
Metallurgical pn-junctiondepth	0.2 µm	0.2 µm	1 µm	1 µm
HE sheet resistance $R_{sh,HE}$	130 Ω/sq.	130 Ω/sq.	129 Ω/sq.	129 Ω/sq.
Passivated saturation current density $J_{01,pas}$	355 fA/cm²	355 fA/cm²	51 fA/cm²	51 fA/cm²
Passivated saturation current density $J_{02,pas}$	10 nA/cm²	10 nA/cm	5 nA/cm	5 nA/cm
Metalized saturation current density $J_{01,cont}$	1006 fA/cm²	1006 fA/cm²	1045 fA/cm²	1045 fA/cm²
Metalized saturation current density $J_{02,cont}$	30 nA/cm²	30 nA/cm²	20 nA/cm²	20 nA/cm²
Front side contact resistance ρ_c	1 mΩcm²	1 mΩcm²	1 mΩcm²	1 mΩcm²
BSF geometry	full area	lines	lines	lines
LBSF width w_{LBSF}	-	50 µm	50 µm	50 µm
Rear side pitch $2x_r$	-	1.3 mm	1.3 mm	1.3 mm
(L)BSF sheet resistance $R_{sh,BSF}$	20 Ω/sq.	20 Ω/sq.	20 Ω/sq.	20 Ω/sq.
Rear side contact resistance $r_{c,B}$	1 mΩcm²	1 mΩcm²	1 mΩcm²	1 mΩcm²
(L)BSF saturation current density $J_{01,BSF}$	250 fA/cm²	250 fA/cm²	250 fA/cm²	50 fA/cm²

The second design is a PERC solar cell with the same front side as the Al-BSF design but with a passivated rear side with line contacts. The line contact geometry is mostly attributed to the 2-d simulation geometry, which only describes 2-d symmetrical unit cells as in the case of lines. The line contacts have in the metalized regions the same $J_{01,rear}$ as the Al-BSF. The next design PERC (opt. emitter) is based on the PERC design but with a driven-in emitter on the front side with a peak doping density of

10^{19} cm^{-3} and a pn-junction depth of about 1 µm. The sheet resistance of both emitter profiles is about 130 Ω/sq.. Finally, the last design features not only the driven-in emitter on the front side but also a reduced $J_{01,rear}$ of the local metal contacted areas, as in the case of a diffused boron doped local back surface field. The values for $J_{01,cont}$ and $J_{01,pas}$ are calculated for the two different doping profiles using the EDNA [133]. The value of $J_{02,pas}$ and $J_{02,cont}$ are an educated guess based on the measured $J_{02,total}$ of solar cells from performed experiments such as the one shown in chapter 5.

4.3.2 Contact resistance limitations for homogenous emitter designs

The application of lowly doped emitter profiles is for Ag-screen printed front side contacts limited due to a high sensitivity of this metallization scheme on the surface doping concentration. As discussed in in section 4.1 and Fig. 44 the contact resistivity will dominate the series resistance losses of the solar cell and limit the overall solar cell efficiency.

Fig. 47 shows the simulated dependency of the solar cells fill factor on the front side contact width and front side contact resistivity for all cell designs. The simulation results show that high contact resistivities lead to a significant decrease of the *FF*. The *FF* decrease can be partially compensated by larger contact widths; however, the increased shading in turn decreases the solar cell efficiency. Fig. 48 illustrates the solar cell efficiency as a function of the front side contact width and front side contact resistivity for all cell designs. A typical solar cell would have a specific contact resistivity below 10^{-4} or 10^{-1} Ωcm² for plated Ni or screen printed Ag contacts at surface doping concentrations above 10^{20} cm^{-3} (see Fig. 44). However, the simulated and experimental contact resistivity range for screen printed and plated front side contacts in Fig. 44 shows that especially for the driven-in emitter the contact resistivity would become the limiting factor in the solar cell.

The experimental data of ρ_{cont} for Ag-screen printing on surface doping densities smaller than 10^{20} cm^{-3} are larger than 1 Ωcm², which is far outside the plotting range in Fig. 47 and would lead to very low fill factors and cell efficiencies. In the case of plated Ni contacts the silicide phase at the interface becomes relevant. Depending if it is Ni, NiSi or $NiSi_2$ ρ_{cont} can be above 10^{-3} Ωcm² for elemental Ni or below 10^{-3} Ωcm² for Ni silicide phases. This shows that the emitter design of homogenous emitter solar cells is at some point limited by the contact resistivity of the applied metallization scheme. The application of a selective emitter with a highly doped region underneath the metal contacts can decouple the contact resistance limitation and the emitter profile optimization in the passivated regions.

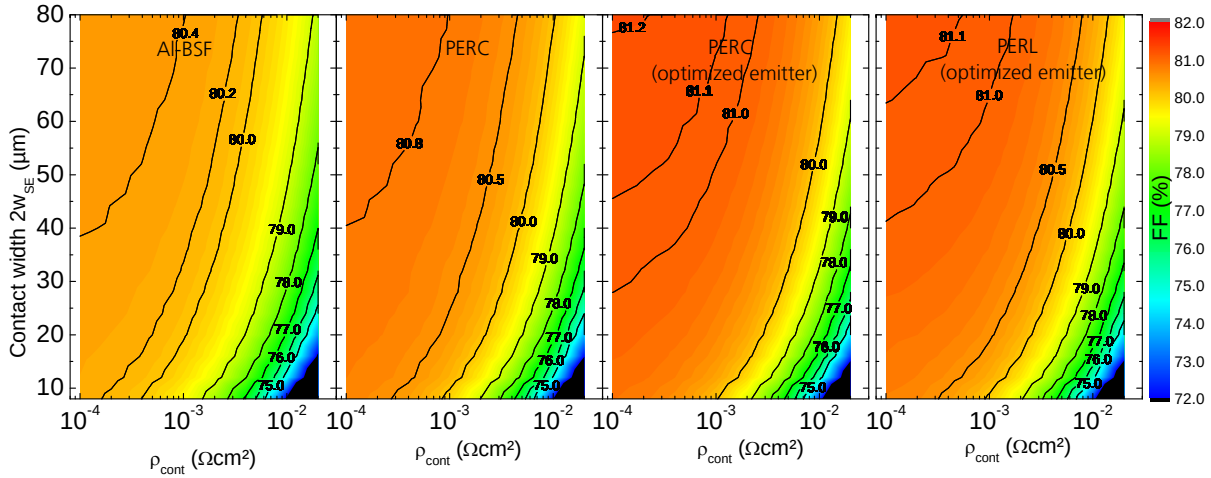

Fig. 47
Simulated fill factor *FF* of the four solar cell designs described in Table X and Table XI as a function of the front side contact width and the front side contact resistivity.

The simulations in this section show that the benefits of a selective emitter design in comparison to a homogenous emitter design in terms of contact resistance strongly depends on the interaction between the surface doping concentration of the homogenous emitter, the applied metallization scheme and the applied metal contact width. The selective emitter becomes more and more beneficial for lowly doped homogenous emitter profiles, metallization schemes with a high sensitivity on the doping concentration and small contact widths. However, the impact of the additional highly doped region of the selective emitter becomes almost negligible for high surface doping concentrations, metallization schemes with contact resistivities below 10^{-3} Ωcm² and large contact widths.

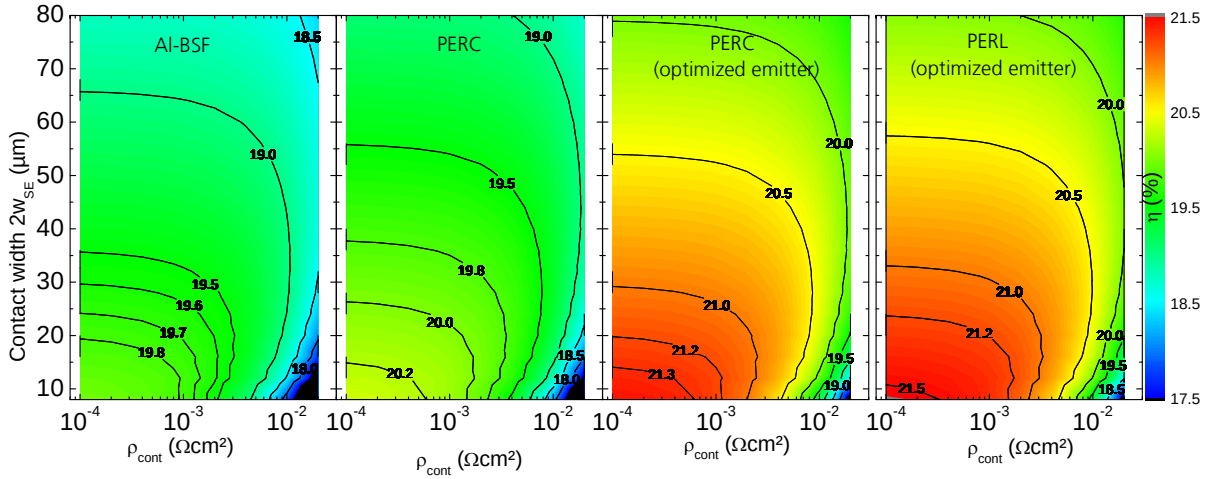

Fig. 48
Simulated solar cell efficiency η of the four solar cell designs described in Table X and Table XI as a function of the front side contact width and the front side contact resistivity.

4.3.3 Recombination benefits of highly doped contacts

The simulations of the saturation current densities in Fig. 46 shows that for lowly doped homogenous emitter profiles the saturation current density of the metalized areas $J_{01,cont}$ becomes large and eventually lead to a limitation of the open circuit voltage. Historically [8], the decoupling of the optimization of the saturation current densities in the passivated $J_{01,pas}$ and contacted areas $J_{01,cont}$ was one of the intentions for the selective emitter design.

Fig. 49 shows the simulated dependency of the solar cells open circuit voltage on the front side contact width and front side saturation current density in the contacted region. A decrease in both parameters leads to an increase in V_{oc}. The impact of both parameters correlates, which leads to a small impact of w_{SE} on V_{oc} for low $J_{01,cont}$ and a large impact of w_{SE} on V_{oc} for large $J_{01,cont}$. The simulated $J_{01,cont}$ of the homogenous emitter profiles in Table X is about 1000 fA/cm². The introduction of a selective emitter design with a highly doped area underneath the metal contacts could further reduce $J_{01,cont}$ below this value. However, depending on the contact width the reduction of $J_{01,cont}$ to values below 1000 fA/cm² leads in most cases only to a small increase in V_{oc}. The same trends are also visible in the solar cell efficiency in Fig. 50. This shows that the implementation of a selective emitter design is not necessarily significant for the open circuit voltage, especially, for small contact widths and $J_{01,cont}$ in the range of 1000 fA/cm² or less.

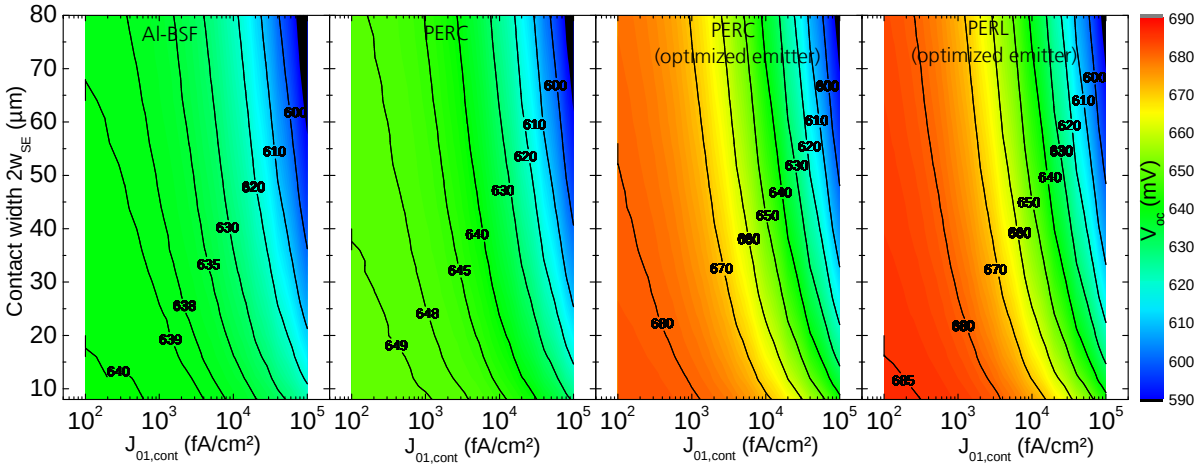

Fig. 49
Simulated solar cell open circuit voltage V_{oc} of the four solar cell designs described inTable X and Table XI as a function of the front side contact width and the saturation current density in the front side contact region.

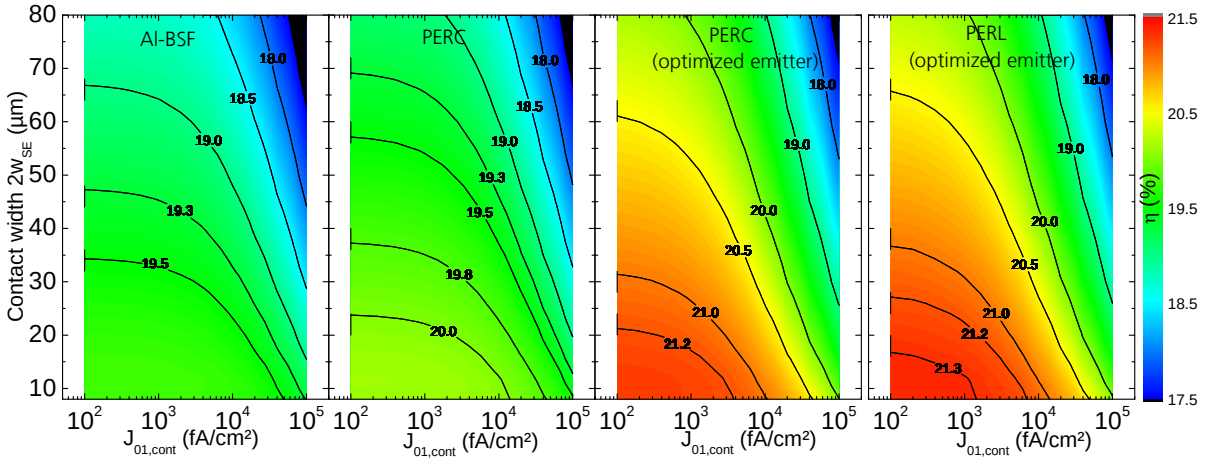

Fig. 50
Simulated solar cell efficiency η of the four solar cell designs described in Table X and Table XI as a function of the front side contact width and the saturation current density in the front side contact region.

In some cases $J_{01,cont}$ can become much larger either due to a "dead layer" of electrically inactive phosphorus precipitates in highly doped emitter profiles [160] or very lowly doped emitter profiles with peak doping densities below 10^{20} cm^{-3}. Nevertheless, both of these cases do not apply for the simulated driven-in emitter with a Gaussian profile and a surface doping density between 10^{19}-10^{20} cm^{-3}.The comparison of the simulated cell efficiencies of the different cell designs in Fig. 50 illustrates that the introduction of a selective emitter becomes more and more beneficial for high efficiency solar cell designs. Assuming a contact width of $2w_{SE}$ = 25 µm, the introduction of a selective emitter is for the Al-BSF solar cell design not significant. In fact, even an increase of $J_{01,cont}$ up to 10^4 fA/cm² would not significantly decrease the cell efficiency. For increased contact width the impact of $J_{01,cont}$ becomes more relevant, however, the Al-BSF solar cell efficiency is much more sensitive on the contact width than on the recombination properties of the contacted region. The PERC and PERL designs show similar trends and also a rather low sensitivity on $J_{01,cont}$ improvements below 1000 fA/cm².

4.3.4 Selective emitter vs. homogenous emitter design

In the previous two sections the contact resistance and contact recombination properties were analyzed separately. However, in actual solar cells both properties are correlated and depend on the diffusion profile, the contact opening process and the metallization scheme. Fig. 51 summarizes the simulated cell efficiency (subfigure a)), open circuit voltage (subfigure b)) and fill factor (subfigure c)) as a function of the front side contact resistivity and the front side contact saturation current density for all

cell designs. The simulations in Fig. 51 assume a contact opening width of 20 µm, which is typical for laser openings.

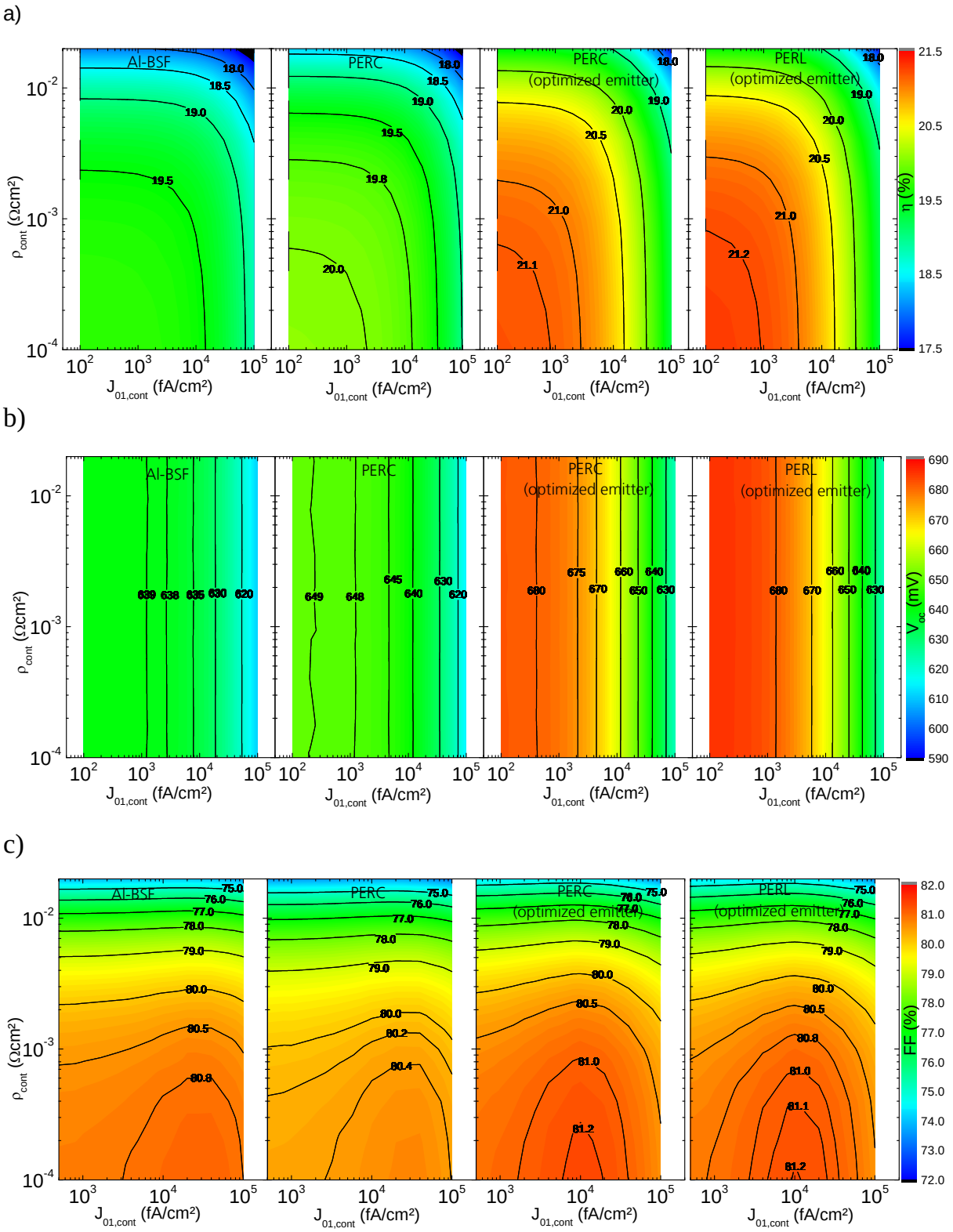

Fig. 51
Simulated a) solar cell efficiency η, b) open circuit voltage V_{oc} and c) fill factor *FF* of the four solar cell designs described in Table X and Table XI as a function of the front side contact resistivity and the saturation current density in the front side contact region.

The simulation results in Fig. 51 show similar trends as in the previous simulations. One new finding is the local maximum of the *FF* for saturation current densities around 10^4 fA/cm². The local maximum is a consequence of the fact that in this $J_{01,cont}$ regime the V_{oc} is already decreased but the increased contact recombination is under maximum power point (MPP) conditions not the limiting recombination path. Therefore, the reduction of the V_{oc} and the stability of the MPP lead to an increased *FF*. However, the cell efficiency is not significantly affected by this trend.

The comparison of the cell efficiency results in Fig. 51 a) gives important information about the relevant cell design improvements for industrially feasible high efficiency silicon solar cells. The simulations show that the introduction of a selective emitter for small contact openings only becomes beneficial if the contact resistivity is a limiting factor of the solar cell. If that is not the case the almost negligible contact recombination improvements does not necessarily justify the increased processing effort and processing cost of a selective emitter. However, the simulation results in Fig. 51 a) demonstrate that the reduction of the contact resistivity due to an additional highly doped contact region in combination with small contact openings can improve the cell efficiency even if the local doping would be connected to an increase of $J_{01,cont}$. This scenario is possible for laser induced damage due to the application of high laser pulse energies during the contact opening formation.

The comparison of the different cell designs shows that for the case of a metallization scheme with low contact resistivities even for small contact widths –as in the case of plated Ni-Cu or Ni-Ag contacts- the improvement of the emitter doping in the passivated regions and the introduction of a passivated rear side are much more beneficial than the introduction of a selective emitter doping. In fact the simulation predicts that the selective emitter becomes for this metallization scheme not relevant in terms of maximum cell efficiency for all cell designs. However, chapter 6 will discuss why the introduction of a selective emitter is still beneficial for this metallization scheme in terms of shunting prevention.

4.4 Conclusion

The performed calculations and simulations in this chapter aimed to analyze the two main aspects of the selective emitter doping: the influence of the doping concentration on the contact resistivity and the reduction of the saturation current density of highly doped regions. Furthermore, 2d simulations of four different solar cell designs revealed the impact of the front contact properties on the solar cell performance.

The experimental data from the literature and the calculated dependence of the contact resistivity and the surface doping concentration in Fig. 44 showed that beside the theoretical improvement of ρ_{cont} for high doping concentrations the metallization scheme itself strongly influences the contact resistance in the actual solar cell. Screen printed Ag contacts show in this context a significantly higher sensitivity on the doping concentration than plated Ni contacts. The solar cell simulations in Fig. 48 revealed that for $\rho_{cont} > 10^{-3}$ Ωcm² the cell efficiency decreases due to fill factor limitations of the contact resistance. The ρ_{cont} related fill factor losses can be reduced by larger contact widths; however, the simulations in Fig. 49 and Fig. 50 show that this leads to a cell efficiency limitation due to a decrease in the V_{oc} and J_{sc} due to increased contact recombination and shading, respectively. Furthermore, the results of Fig. 49 and Fig. 50 indicate that a decrease of $J_{01,cont}$ only becomes relevant in the presence of large contact widths or for cell designs aiming for cell efficiencies $\eta > 21\%$. Especially, the simulations of the Al-BSF cell design demonstrate that a decrease or increase of $J_{01,cont}$ for values below 10^4 fA/cm² has no significant impact on the resulting cell efficiency.

The discussed findings in this chapter can help in the process design for industrially feasible high efficiency silicon solar cells. They show that for technology related limitations such as the avoidance of non-mass production compatible processes the interaction between the cell design, the metallization scheme, the thermally diffused homogenous emitter and the applied selective emitter process decides whether or not the introduction of a selective emitter is beneficial in terms of maximum cell efficiency. Regarding state-of-the-art processing technologies, it is in most cases more beneficial to reduce the contact width and improve the homogenous emitter diffusion than introducing a selective emitter by highly doped regions underneath the contacts. The introduction of a selective emitter design is in industrially feasible cell designs mostly beneficial at the point when the applied metallization scheme limits the cell efficiency due to large ρ_{cont} or if the highly doped region prevents shunting related cell efficiency limitations. The latter will be discussed in the following two chapters.

5 LCP selective emitter doping for plated Si solar cells

The following chapter analyzes the benefits of different cell design improvements on the electrical performance of Al-BSF solar cells. The fabricated solar cells described in section 5.1 feature a lightly doped thermally diffused emitter, plated Ni-Ag or Ni-Cu-Ag front side contacts and partly a selective emitter design by additional highly doped front side contact openings by LCP-SE. The presented solar cell results of section 0 are analyzed in more detail in a loss analysis in section 5.3. The main findings of this loss analysis are summarized in the conclusion of section 5.4.

The results of the presented experiments in this chapter led to following publication [73].

The application of local phosphorus doping by LCP gives the opportunity of industrially feasible selective emitters (LCP SE) or local back surface fields in silicon solar cell designs. The two key aspects of this process within solar cell fabrication schemes are the local structuring of passivation layers or silicon and the creation of locally highly doped regions. Within this work the process development of the n-type LCP process focusses on the application of forming a highly doped contact opening for a selective emitter design (LCP SE) for p-type solar cells. The historical idea of selective emitter structures and local back surface fields is the reduction of local recombination and series resistance losses at the metal contacts [8]. However, the industrial approach of high efficiency solar cell designs [50] usually differs from the historical lab type approach [8, 9]. This is caused by process related design limitations for the emitter diffusions, the applied passivation layers and the metallization structures. Depending on the applied emitter and especially the metallization scheme the influence of the additional highly doped LCP SE structure underneath the metal contacts on the contact resistance and the total recombination losses can be highly significant or almost negligible (see chapter 4).

5.1 Solar cell fabrication

One evolutionary approach towards an industrially feasible high efficiency solar cell concept is the implementation of a selective emitter and plated Ni-Ag or Ni-Cu front side contacts in the conventional Al back surface field (Al-BSF) solar cell design. In comparison to solar cells with screen printed Ag front side contacts, the plated Al-BSF solar cells can bring cell efficiency benefits due to reduced shading of the narrow plated metal fingers, decreased recombination losses due to an optimized emitter profile in the passivated regions and good contact resistances of the Ni seed layer (see Fig. 44). The good contact resistivity of Ni even on lowly doped surfaces enables also the introduction of lightly doped emitters. One advantage to screen printed selective emitter solar cells is also the possibility of very narrow finger width in the range of 20-50 µm, which allows a small finger pitch on lightly doped emitters for an optimized trade-off between series resistance, recombination and optical losses.

The presented experiment in this section will evaluate the benefit of a lightly doped emitter and plated front side contacts for an Al-BSF solar cell design (see Fig. 52) compared to conventional fully screen printed solar cells. Furthermore, the influence of a selective emitter doping and the impact of different plating schemes will be discussed. Large area (156x156 mm²) Al-BSF silicon solar cells were fabricated in the High Eta lab and the PV technology evaluation center (PV-TEC) at Fraunhofer ISE using commercial grade 1-3 Ωcm p-type Cz-Si. The processing scheme is shown in Fig. 53.

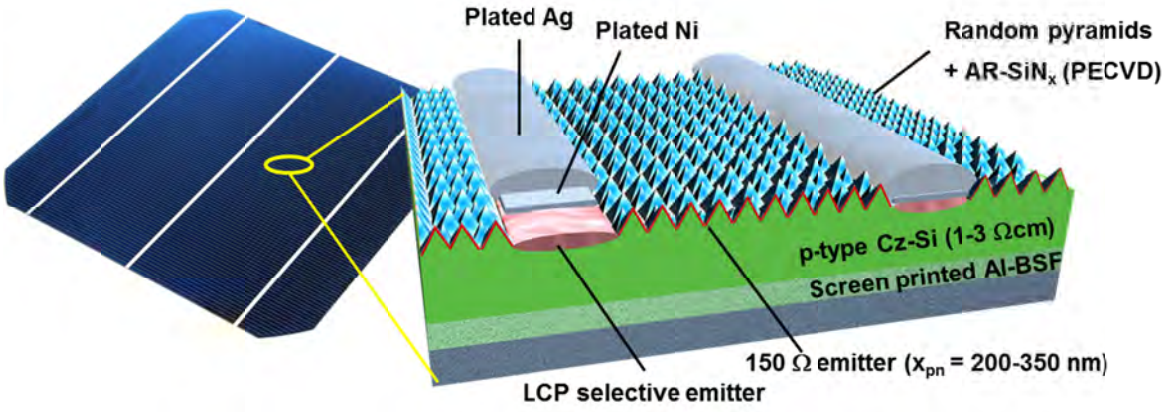

Fig. 52
Photography and schematic of the fabricated Al-BSF solar cells (156x156 mm²) with plated Ni-Ag front side contacts and LCP selective emitter doped openings of the SiN_x antireflection coating (AR-SiN_x). The UV laser ablated solar cells have the same design but without a selective emitter design with highly doped front side contact openings.

The textured Cz Si wafers were provided by SolarWorld Innovations GmbH. The thermal $POCl_3$ diffusion process was performed at Fraunhofer ISE. The applied diffusion process creates a homogenous emitter on the front side with a sheet resistance of about 150 Ω/sq. and an estimated pn-junction depth of 200-350 nm. The rear side was protected during the diffusion process with a 300 nm PECVD SiO_x diffusion barrier resulting in a single side pn junction formation. The diffusion barrier and the PSG layer of the diffusion process were removed afterwards in a PSG etch back process with extended etching time. The subsequent PECVD SiN_x passivation coating of the front side was performed at SolarWorld Innovations GmbH, which showed in pretests low pin hole densities in order to minimize parasitic plating. On the rear side of the cells a full area Al-screen printing process was performed with a subsequent fast firing process in a conveyor belt furnace (FFO) for the formation of the Al-BSF. Fig. 52 shows a schematic of the processed solar cells.

<table>
<tr><td colspan="2">Selective emitter</td><td colspan="2">Homogeneous emitter</td><td>Reference emitter</td></tr>
<tr><td>Ni-Ag</td><td>Ni-Cu-Ag</td><td>Ni-Ag</td><td>Ni-Cu-Ag</td><td>Ag screen printing</td></tr>
<tr><td>Group A</td><td>Group B</td><td>Group C</td><td>Group D</td><td>Group E</td></tr>
<tr><td colspan="5">1-3 Ωcm Cz-Si, 200 µm wafer thickness</td></tr>
<tr><td colspan="5">Alkaline random pyramid texture</td></tr>
<tr><td colspan="5">PECVD SiO_2 (300 nm rear side diffusion barrier)</td></tr>
<tr><td colspan="4">120 Ω/sq. $POCl_3$ diffusion</td><td>75 Ω/sq. $POCl_3$ diffusion</td></tr>
<tr><td colspan="5">PSG / diffusion barrier etch</td></tr>
<tr><td colspan="5">PECVD SiN_x (70 nm front side antireflection coating)</td></tr>
<tr><td colspan="2">LCP*</td><td colspan="3"></td></tr>
<tr><td colspan="4">Al screen printing (rear side)</td><td>Ag + Al screen printing
(front + rear side)</td></tr>
<tr><td colspan="5">FFO (Al-BSF firing)</td></tr>
<tr><td colspan="2">LCP*</td><td colspan="2">UV ablation</td><td></td></tr>
<tr><td colspan="4">Ni LIP</td><td></td></tr>
<tr><td>Ag LIP</td><td></td><td>Ag LIP</td><td></td><td></td></tr>
<tr><td colspan="4">Tempering</td><td></td></tr>
<tr><td></td><td>Ni etch back</td><td></td><td>Ni etch back</td><td></td></tr>
<tr><td></td><td>Ni LIP</td><td></td><td>Ni LIP</td><td></td></tr>
<tr><td></td><td>Cu LIP</td><td></td><td>Cu LIP</td><td></td></tr>
<tr><td></td><td>Ag LIP</td><td></td><td>Ag LIP</td><td></td></tr>
</table>

Fig. 53
Processing scheme of the fabricated Al-BSF solar with and without selective emitter and with plated front side contacts.
*The LCP process for the cells in group A/B was either performed before or after firing (FFO) in order to evaluate a possible laser damage annealing during the firing step.

Within this experiment the benefit of a selective emitter and plated front side contacts was evaluated. Therefore, two different laser structuring techniques were used in order to create a laser opening of the front side passivation layer for the following plating process. The contact opening formation of the front side SiN_x anti reflection coating was either performed by pulsed nanosecond (20 ns) UV laser ablation at the company Rena GmbH or a locally opening and doping process by laser chemical processing (LCP) [66] at Fraunhofer ISE. The UV laser ablation results in homogenous emitter solar cells and the LCP opening process creates a selective emitter solar cell with a lowly doped emitter in the passivated regions and a high laser doped region underneath the front side metal contacts. LCP enables a simultaneously SiN_x ablation and locally phosphorus doping of the silicon underneath. The LCP system focusses a pulsed laser spot (532 nm, 70 ns laser pulse duration) into a liquid jet of 85% H_3PO_4 by using a nozzle with a diameter of 50 µm. The n-type LCP process used in this work was performed on a system without any optical fibers in between the laser and the liquid jet. This setup showed in previous experiments the best homogeneity and enables a very well-focused laser spot with a spot size of about 5 µm at the nozzle entrance. Furthermore, high laser pulse repetition rates of 200 kHz were chosen allowing a spatial pulse distance of 0.5 µm on the sample. The LCP-SE SiN_x openings showed a mean line width of 20 ± 5 µm. However, due to non-optimal coupling of the laser spot into the liquid jet in some cases the SiN_x ablation was quite inhomogeneous and resulted in a large line width but a small opening fraction (see left microscope image in Fig. 54). This can lead to misinterpretation in the later loss analysis for area sensitive measurement results. Therefore, the effective line width $w_{eff,line}$ is introduced in Eq. (34); calculated by reducing the opened area A_{cont} of the laser structured line with the width[12] w_{line} and the length l_{line} to a homogenously opened line with the same opening area and a resulting effective line width $w_{eff,line}$.

$$w_{eff,line} = \frac{A_{cont}}{l_{line}} \qquad (34)$$

In Fig. 54 the dependency between the line width and the effective line width is displayed. It can be seen that for homogenously opened lines (left and middle microscope image in Fig. 54) there is a linear dependency between the two line parameters. All line width parameters are a result of process variations during the LCP processing and have been used for the subsequent plating. The few deviations from the

[12] The opening area and the line width is determined by a self-written image analyzing script, which determines the opened area by color information analyzing and the line width as maximum edge of the opened area.

linear dependency correlate with non-homogenously opened laser openings (right microscope image in Fig. 54) due to non-optimal processing settings.

The front side metallization processing was divided into three processing schemes. The reference group (group E) was not laser structured at all and the front side was metalized by fired Ag-screen printed contacts (3 busbar design, 100 µm finger width, 2.3 mm pitch). All other groups featured plated front side metal contacts by either Ni-Ag or a two-step Ni-Cu-Ag light induced plating process (LIP) also with a 3 busbar design with 97 fingers with 1.6 mm pitch. The laser structuring was either performed at Rena GmbH for undoped UV laser ablated contact openings or at Fraunhofer ISE for highly doped LCP-SE contact openings. The Ni-Ag plated solar cells (group A & C) were plated after the laser structuring by subsequent inline Ni and inline Ag LIP processes. After the plating[13] the cells were annealed in an inline furnace for 10 min. at 350°C in an N_2 atmosphere in order to form a Ni-silicide at the silicon metal interface for better adhesion and low contact resistivity. Fig. 55 shows the two different types of laser structured front sides before and after Ni-Ag plating. After the laser processing the opening width is about 20-30 µm for both laser processes, which results in approximately 40-60 µm metal fingers after Ni-Ag or Ni-Cu-Ag plating.

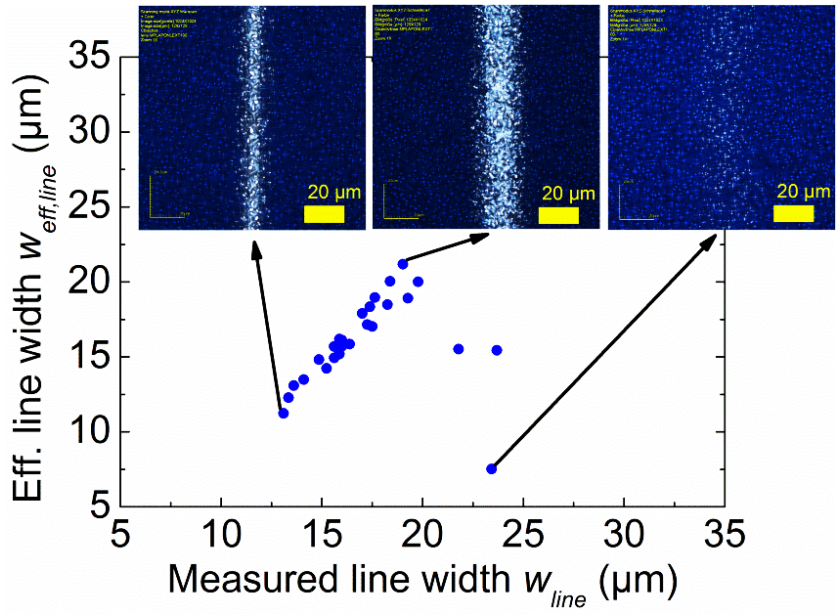

Fig. 54
Dependency between the line width and the effective line width introduced in Eq. (34). The inset images are microscope images of different doped LCP-SE laser openings (gray area) of fabricated solar cells with random pyramid texture and SiN_x passivation (blue area).

[13] The delay between plating and annealing was 2 days due to logistic reasons.

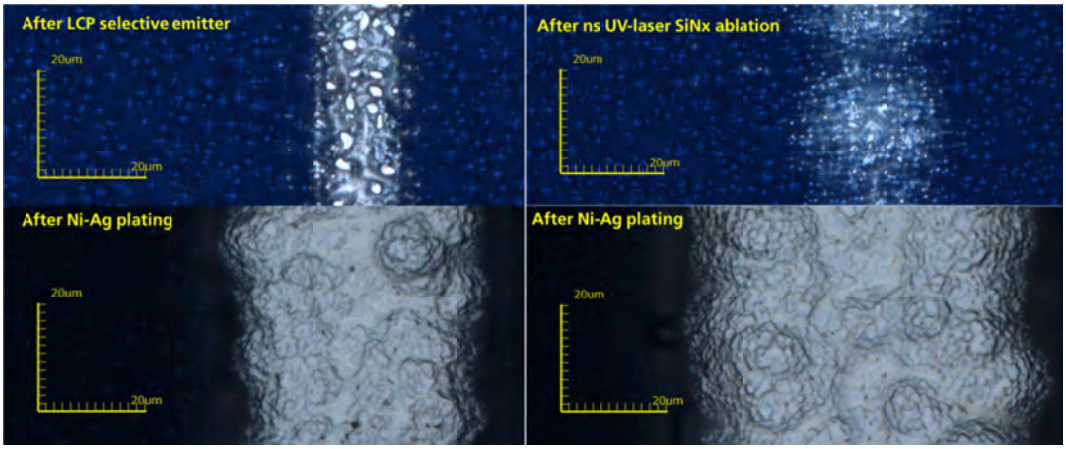

Fig. 55
Top view confocal microscope images before and after Ni-Ag plating of the LCP selective emitter laser opening process (left) and the nanosecond (ns) UV laser ablation (right) of the front side SiN_x

The Ni-Cu-Ag plated solar cells of group B & D were fabricated using a two-step plating process after the laser structuring, which achieved good adhesive contacts in recent experiments by Mondon et al. [100]. The laser structured wafers were inline Ni plated in an LIP process at Fraunhofer ISE with an applied bias voltage and subsequently[14] annealed for 2 min. at 275°C or 450°C in a forming gas atmosphere in order to form a Ni silicide layer. After the anneal the remaining Ni residues were etched back in a H_2O_2:H_2SO_4:H_20 (1:1:4) solution and the front metal grid was processed in subsequent inline Ni and Cu LIP processes under applied bias voltage and bias current, respectively. At the end the Ni-Cu metal grid was capped by a short inline Ag LIP layer in order to provide a good solderabilty and prevent the oxidation of the Cu layer. Fig. 56 shows the contact formation of the Ni-Cu-Ag metallization after different processing steps.

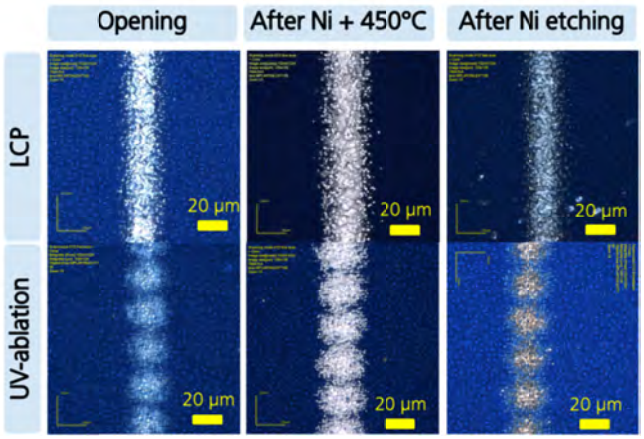

Fig. 56
Top view confocal microscope images before and after the initial Ni plating and after the Ni etching for the LCP selective emitter laser opening process and the ns UV ablation of the front side SiN_x

[14] The maximum delay between plating and annealing was about 10 min.

5.2 Solar cell results

In Table XII the cell results of the best solar cells of each processing group are summarized. The best solar cell of the fully screen printed reference group E reached a maximum cell efficiency of 18.2%.

Table XII: IV parameter results of the fabricated large area (156x156 mm²) Al-BSF solar cells with maximum cell efficiency of each group. The cells are measured under standard testing conditions (25°C, 1000 W/cm², AM1.5G) with a Xenon flasher class AAA (measurement time 25 ms).

Group	Emitter	Metallization	η (%)	*FF* (%)	*pFF* (%)	J_{sc} (mA/cm²)	V_{oc} (mV)
A	SE 150Ω/sq.	Ni-Ag	19.0	78.5	83.0	37.9	637
B	SE 150Ω/sq.	Ni-Cu-Ag	18.5	77.4	81.5	37.4	639
C	HE 150Ω/sq.	Ni-Ag	18.9	77.9	83.2	38.0	639
D	HE 150Ω/sq.	Ni-Cu-Ag	18.7	78.4	82.0	37.4	636
E	HE 75Ω/sq.	SP	18.2	78.7	82.8	36.7	631

The best solar cells of group A-D with lightly doped emitters and plated front side contacts showed maximum cell efficiencies of 18.5-19.0%. The champion cell of this experiment was in group A with a LCP selective emitter and Ni-Ag plated front side contacts and showed a maximum cell efficiency of 19.0%. The main benefits of the cells in group A-D compared to the fully screen printed reference solar cells in group E are higher short circuit current densities and higher open circuit voltages. However, comparing the selective (group A and B) and homogenous emitter solar cells (group C and D) for each plating scheme it becomes obvious that the selective emitter does not show any benefit in terms of maximum cell efficiency in this experiment. This finding is in agreement with the simulation results discussed in chapter 4.In Fig. 57 the IV parameter results for the best processing scheme of each processing group are plotted. Group A and C show the highest efficiency level of all processing groups. The processing groups B and D demonstrate a lower efficiency level than the groups A and C but still show higher maximum cell efficiencies than the reference group E. All laser processed and plated groups A-D display a larger spreading of the data than the reference group E. The following sections will discuss the influence of the lightly doped emitter, the plated front side contacts and the selective emitter on the cell efficiency benefit compared to the reference solar cells. Furthermore, the differences in the cell results between the processing groups will be discussed in a detailed loss analysis.

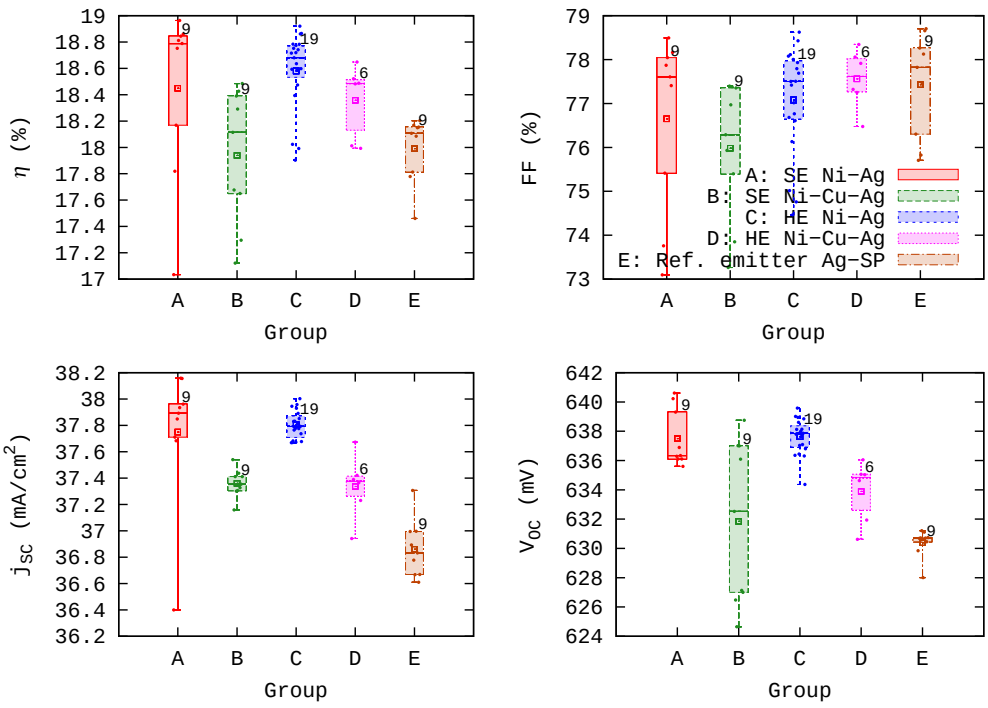

Fig. 57
IV parameter results of the best processing scheme[15] of each processing group.

5.3 Loss analysis

5.3.1 Short circuit current density analysis

Fig. 57 illustrates the higher J_{sc} level of about 38 mA/cm²of the plated solar cells with lightly doped emitter of group A-D compared to 37 mA/cm² of the to the screen printed reference cells with a more heavily doped emitter of group E. The reasons for the short circuit current density benefit of group A-D are lower recombination losses and less shading effects. Lower recombination losses can be achieved in group A-D by an improvement of the emitter diffusion profile. The lightly doped emitter has an overall lower doping density concentration compared to the more heavily doped emitter in group E. Thus, the Auger recombination current losses in the emitter region are lower. Furthermore, the lightly doped emitter shows a lower surface doping concentration of about $2 \cdot 10^{20}$ cm^{-3}, which reduces recombination losses due to dead layer effects of electrically inactive phosphorus precipitates in the surface region [160].

[15] Group A is limited to the solar cells with LCP after the FFO firing process and group B & D to the solar cells annealed at 275°C (2 min., FGA)

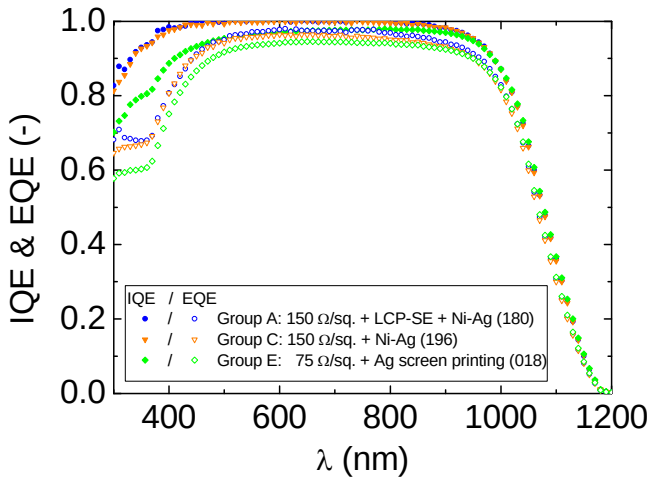

Fig. 58
Measured internal (closed symbols) and external (open symbols) quantum efficiency of solar cells with the homogenous 75 and 150 Ω/sq. emitter and a solar cell with a selective emitter (150 Ω/sq. + LCP-SE). The measurement spot size is about 20 mm² in a contact finger region and under a bias illumination of 0.3 suns.

The lower recombination losses of the lightly doped emitter can be seen in higher internal (IQE) and external quantum efficiencies (EQE) in the lower wavelength region in Fig. 58. Group A and C give an IQE value between 0.8-1.0 in the wavelength regime of 300-500 nm, while group E results in an IQE range of 0.7-0.95 in the same wavelength regime. The EQE gives the ratio of the measured short circuit current density and the incoming photon flux as a function of the wavelength λ. The IQE is similar to the EQE but only accounts for photons entering the solar cell. The short absorption length of silicon in the lower wavelength region leads to a high sensitivity of the IQE to front side recombination effects. The IQE analysis allows a direct comparison of the recombination losses in the lightly doped emitter of group A-D and the more heavily doped emitter in group E disregarding the different shading fractions of the plated and screen printed front side contacts. The theoretical short circuit current density benefit of the higher IQE can be calculated using Eq. (35).

$$J_{sc,IQE} = \frac{q}{hc} \int \lambda \cdot IQE(\lambda) \cdot I_{AM1.5G}(\lambda)\, d\lambda \qquad (35)$$

In Eq. (35) h is the Planck constant, c is the speed of light and $I_{AM1.5g}$ is the solar spectral irradiance AM1.5G in $Wm^{-2}nm^{-1}$. In Table XIII the IQE and EQE spectra of Fig. 58 are converted into the theoretical short circuit current density. The comparison of $J_{SC,IQE}$ of the lightly doped emitter and the more heavily doped emitter shows that the reduced recombination losses lead to a short circuit current density benefit of about

1 mA/cm². Furthermore, the impact of the selective emitter on the IQE is almost negligible. For the measured solar cells the maximum $J_{SC,IQE}$ benefit for the selective emitter is 0.1 mA/cm² compared to the lightly doped homogenous emitter. This indicates that the additional highly doped region under the plated contacts does not significantly change the recombination losses in the short circuit current density. Reasons for the small impact might be the high surface doping concentration of the homogenous emitter even without additional laser doping and the fact that the generation rate in the laser doped region is almost zero due to shading.

The cells with a lightly doped emitter with and without a selective emitter in Table XIII show a similar $J_{sc,IQE}$ level. However, the measured J_{sc} and $J_{sc,EQE}$ show a significant benefit of the cells with LCP doped contact openings. This J_{sc} improvement can be correlated to solar cells with smaller contact opening widths and therefore, more narrow plated finger widths shown in Fig. 59. The results in Fig. 59 illustrate that for the applied solar cell design and the applied thermally diffused emitter profile the impact of the contact opening width and the metallization width is much more important for the maximum short circuit current density than the impact of a selective emitter. The low amount of data in Fig. 59 does not allow a substantiated prediction of the functional dependency between the two measurement values but in first approximation the measured short circuit current density decreases linear with an increase of the shaded area due to the metal grid [161].

Table XIII: Comparison of the measured J_{sc} and the calculated $J_{sc,IQE/EQE}$ from the measured quantum efficiencies using Eq. (35).Within group A the cells marked with * are LCP processed before FFO (A*) and the others are LCP processed after FFO (A).

Emitter	Metallization	Group	Cell	$J_{sc,IQE}$ (mA/cm²)	$J_{sc,EQE}$ (mA/cm²)	$J_{sc,meas}$ (mA/cm²)
150Ω/sq. + LCP-SE	Ni-Ag	A	180	41.2	39.1	38.2 ± 1.1
			044	41.1	38.5	37.6 ± 1.1
		A*	170*	41.2	39.0	37.9 ± 1.1
			191*	41.2	39.1	38.1 ± 1.1
150Ω/sq.	Ni-Ag	C	196	41.1	38.6	37.7 ± 1.1
			168	41.1	38.8	37.8 ± 1.1
75Ω/sq.	Ag screen printing	E	018	40.0	37.9	36.7 ± 1.0
			007	40.0	37.9	36.8 ± 1.0

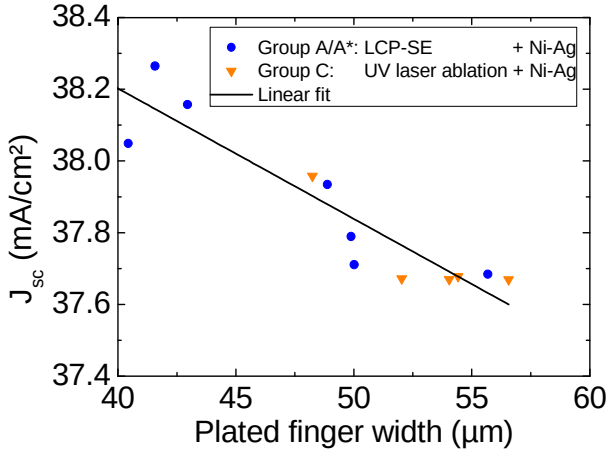

Fig. 59
Measured short circuit current density as function of the Ni-Ag plated finger width for exemplary cells of group A/A* and C with and without selective emitter, respectively. The data can be linearly fitted with the function: $J_{sc}(w_{plat}) = ((39.7\pm0.2) - (0.036\pm0.004)\ w_{plat})$ mA/cm².

The linear fit in Fig. 59 disregards J_{sc} limitations due to series resistance effects for low finger widths. However, the intercept should give the maximum J_{sc} without shading, which equals the definition of $J_{sc,IQE}$. The predicted maximum $J_{sc,max} = (39.7 \pm 0.2)$ mA/cm² from the linear fit and the measured $J_{sc,IQE} \approx 41$ mA/cm² differ about 1 mA/cm², which is the same difference between the measured J_{sc} of the solar cells and the measured $J_{sc,EQE}$ in Table XIII. The difference is assumed to be caused by spectral mismatch and measurement errors between the QE-measurement setup and the IV tester.

The solar cells with high J_{sc} of group A and C did not show significantly higher series resistances. This shows that a shorter plating step, which results in lower plated finger widths, would be beneficial for the fabricated solar cell design; until the plated finger width starts to significantly limit the cell efficiency due to increased grid and contact resistances.

5.3.2 Open circuit voltage and pseudo fill factor analysis

The V_{oc} results in Fig. 57 demonstrate a higher open circuit voltage level for the groups A-D with the lightly doped emitter and plated contacts compared to the reference group E with the more heavily doped emitter and screen printed contacts. The V_{oc} benefit of group A-D can be explained by a better saturation current density of the lightly doped emitter in the passivated regions and a smaller contact area fraction of the plated contacts compared to the screen printed contacts. In Fig. 60 the impact of the sheet resistance on the V_{oc} results is illustrated. The aimed sheet resistances of the applied thermal diffusion recipes were 120 Ω/sq. and 75 Ω/sq. for the groups A-D and

group E, respectively. The screen printed solar cells of group E (purple stars in Fig. 60) with a higher doped emitter show a V_{oc} of about 628-633 mV by maintaining a sheet resistance of about 65-75 Ω/sq.. The solar cells with a lower doped emitter show a V_{oc} range of about 635-642 mV for sheet resistances between 80-130 Ω/sq..

The applied diffusion recipe for the lowly doped emitter of group A-D showed in pretests of Ulrich Jäger very low saturation current densities. However, in the presented experiment this recipe lead to low sheet resistances in the end zones of the diffusion boat, which explains the partly low values. The weak dependency of the measured V_{oc} on the measured sheet resistance shows that the saturation current density in the passivated regions $J_{01,pas}$ is not the dominant parameter for the V_{oc} spreading within group A/A* and C. The following discussion will be focused on group A and C in order to evaluate the influence of the presence of a selective emitter, the influence of the contact geometry and the V_{oc} development along the processing chain. The found results can also be applied to the processing groups B and D, though.

In Fig. 61 the open circuit voltages of the finished solar cells are plotted as a function of the laser structuring process. In this graph group A is divided into two parts. The first part (LCP before FFO) includes only cells where the LCP process was performed before rear side screen printing and fast firing (FFO) of the Al-BSF and the second part (LCP after FFO) includes the cells where LCP-SE was performed after the Al-BSF firing as shown in Fig. 53.

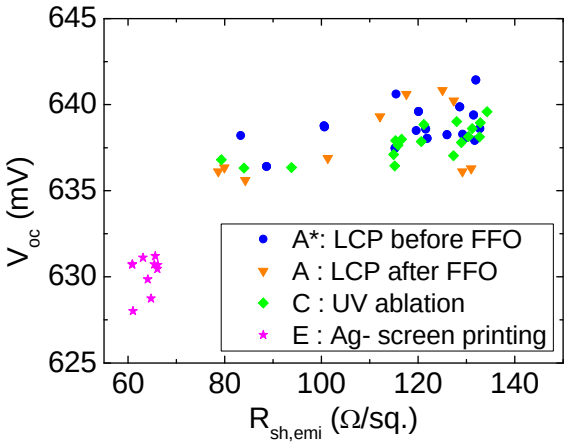

Fig. 60
Measured V_{oc} of the finished solar cells as a function of the sheet resistance $R_{sh,emi}$ of the thermally diffused emitter for the different processing groups. Please note that the shown $R_{sh,emi}$ was measured before PSG etch, which induces an offset to lower values compared to $R_{sh,emi}$ in the finished solar cells.

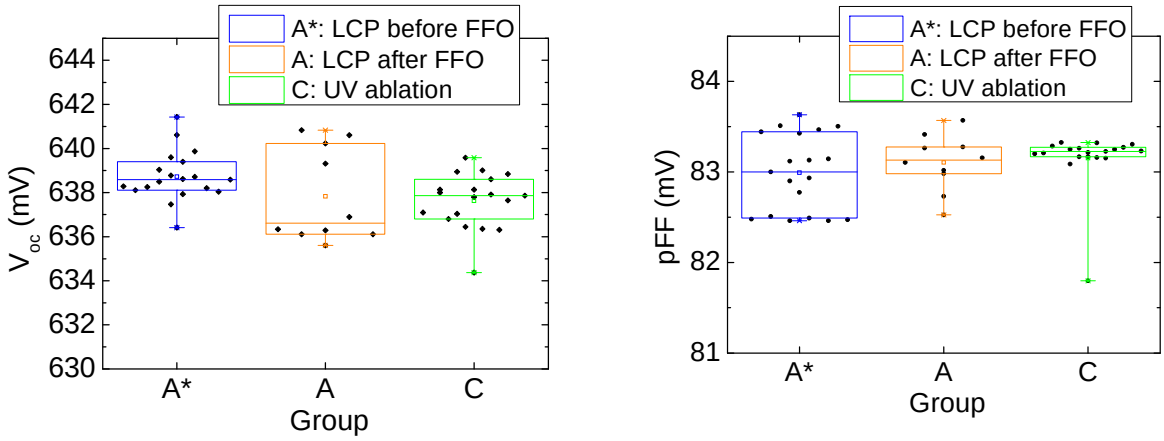

Fig. 61
V_{oc} and *pFF* distribution of the different laser processing groups.

The variation in the LCP process implementation was performed due to a recent work of Kyeong et al. [49], who published a positive annealing aspect of the firing process for LCP processed solar cells, which led to increased open circuit voltages.

On the first sight the maximum or mean V_{oc} and *pFF* results in Fig. 61 seem not to correlate with the process implementation of the LCP-SE process. However, both parameters are strongly influenced by the non-passivated area fraction of the SiN_x opening. Therefore, the data has to be first correlated to the effective opening width in order to distinguish between area related and process related influences on V_{oc} and *pFF*.

The results in Fig. 62 show the detrimental influence of increasing contact opening fractions on V_{oc} and *pFF*. The processing route in this experiment allowed only for the LCP processed solar cells optical characterization of the laser structured openings before plating. Therefore, the effective opening width of the UV results is the mean value measured for a control group with the same group size on the same material and is plotted against the mean cell results of the finished UV ablated solar cells. The V_{oc} results in Fig. 62 indicate that the implementation of the LCP process before FFO (A*) can bring a slightly V_{oc} benefit of 2-3 mV for larger effective opening widths in the range of 15-20 µm. However, this effect is not obvious in the *pFF* results. Furthermore, the presence of a selective emitter doping shows only small effects on the V_{oc} and *pFF* results. Comparing the V_{oc} of LCP before FFO (A*) and the mean UV results (C), there might be a slightly benefit of again 2-3 mV but this could also gain from a possible annealing effect of the FFO and not due to the selective emitter doping. This assumption is supported by the comparison of the V_{oc} results of the LCP

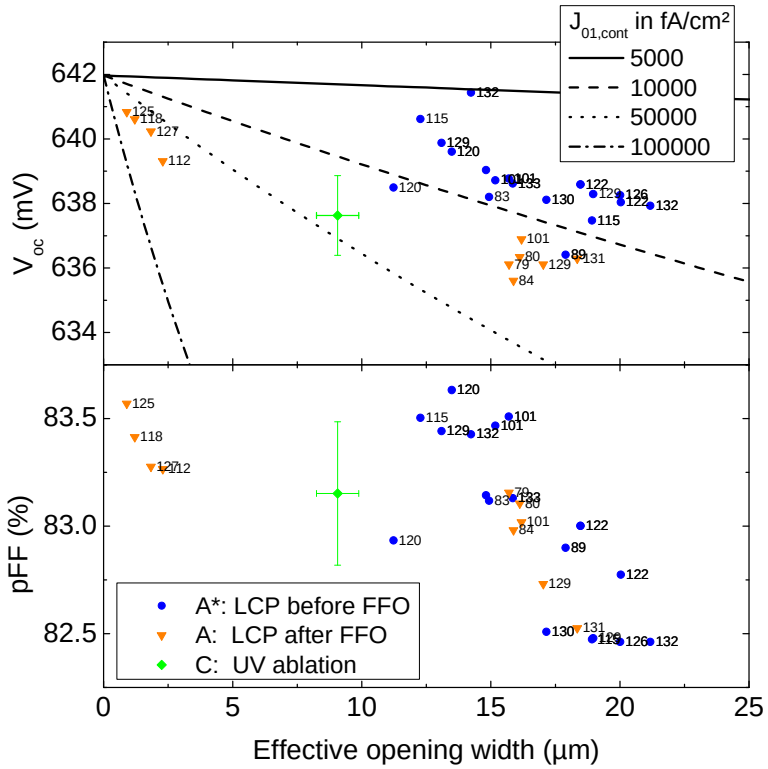

Fig. 62
V_{oc} and *pFF* of the finished solar cells as function of the effective opening width introduced in Eq. (34). The data labels represent $R_{sh,emi}$ before PSG etch and the lines in the V_{oc} plot are guides to the eye using Eq. (31) for the calculation[16] of $J_{01,E}$ and the one diode model for the calculation of the resulting V_{oc}.

after FFO (A) group and the UV ablated group (C), which show a similar V_{oc} level assuming a linear dependency on the effective opening width. The low impact of the selective emitter doping on the maximum open circuit voltage level is a consequence of the already highly doped homogenous emitter profile of the industrially like shallow emitter with rather high surface concentration. These results support the findings of chapter 4, which showed that the impact of a selective emitter only becomes significant for either larger contact opening fractions or significant lower and/or deeper thermally diffused emitter profiles.

5.3.3 Fill factor analysis

The previous section already showed that the fabricated solar cells demonstrate a high pseudo fill factor level at about 83%. The difference of the fill factor and the pseudo fill factor correlates with series resistance losses in the solar cell. Therefore, the fill factor is very sensitive to series resistance related parameters, such as the front side

[16] $J_{01,rear}$ and $J_{01,pas}$ were estimated to contribute in total 535 fA/cm² to achieve the maximum V_{oc} of about 642 mV

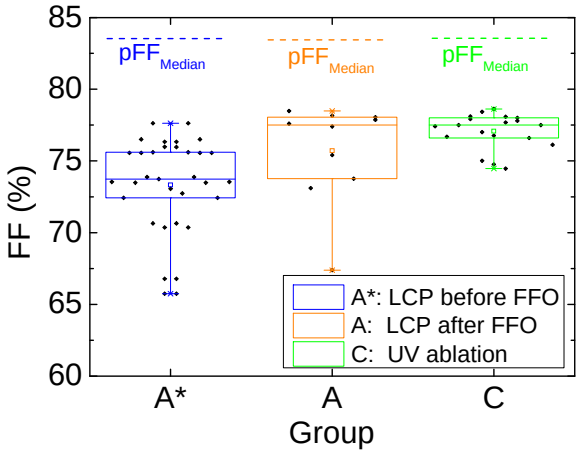

Fig. 63
Fill factor distribution of the finished solar cells of the different processing groups. As reference the median values of the *pFF* are shown as dashed lines for each group.

contact geometry. The following discussion will be reduced to group A/A* and C in order to evaluate the influence of the presence of a selective emitter, the influence of the contact geometry and the determination of the limiting series resistance contributions. The discussed findings are also representative for the groups B and C, though.

In Fig. 63 the fill factors of the different processing groups are compared. The LCP selective emitter group A* with the LCP process before Al-BSF firing (FFO) shows a reduced median FF compared to the other groups. The same *pFF* level of the processing groups in Fig. 61 in contrast to the FF variations in Fig. 63 indicate that the broader fill factor distribution of the fabricated solar cells is a consequence of a broader series resistance distribution. As discussed in section 3.5.1 different features in the solar cell contribute to the total series resistance loss. Some of these parts can be easily measured in the finished solar cells, such as the series resistance in the front and rear side metal contacts. Other ones like the contact resistance need special measurement structure designs but can be estimated for the fabricated solar cells by analytical models. The measured series resistance contribution of the front side metal grid is in the range of 0.1-0.3 Ωcm^2 and is not the limiting contribution for solar cells with low fill factors. In Fig. 64 the *FF* is plotted as function of the measured series resistance without the contribution of the front side metal grid. In this graph it becomes obvious that the low *FF* results of some solar cells are a consequence of semiconductor or contact resistance losses in the device. The full area BSF contact on the rear side leads to extremely low contributions of the rear side contact resistance,

the vertical base resistance and the series resistance within the Al metal rear side[17]. Therefore, the most relevant series resistance contributions are either the series resistance losses within the emitter or the contact resistance of the front side contact. In Fig. 64 the data points are labeled with the measured emitter sheet resistance right after diffusion $R_{sh,emi}$. The wafers of group A-D were randomly split in two batches for the diffusion process. Each diffusion process was performed with about 100 wafers leading to a mean $R_{sh,emi}$ of about 120 Ω/sq. after the diffusion. $R_{sh,emi}$ is inductively measured for all wafers at 72 positions showing a good homogeneity for each wafer with standard deviations of about 5%. However, the standard deviation of $R_{sh,emi}$ within one diffusion batch was about 6% leading to minimum values of about 80 Ω/sq. for one wafer and maximum values of about 140 Ω/sq. for another wafer. The subsequent PSG etching process removes some nanometers of the diffused emitter doping, which results in a higher sheet resistance after PSG etch with a mean value of about 150 Ω/sq. Due to lack of data for the sheet resistance after PSG etch the shown $R_{sh,emi}$ data equal the measurements right after diffusion, which however, monotonically correlate with $R_{sh,emi}$ of the finished solar cell.

The data in Fig. 64 show that the occurrence of high series resistances Rs- Rs,front grid does not correlate with high emitter sheet resistances. Therefore, the most likely explanation is a high front side contact resistance for solar cells with low fill factors. As shown in section 4.1 the contact resistance is a function of the contact resistivity and the contact area.

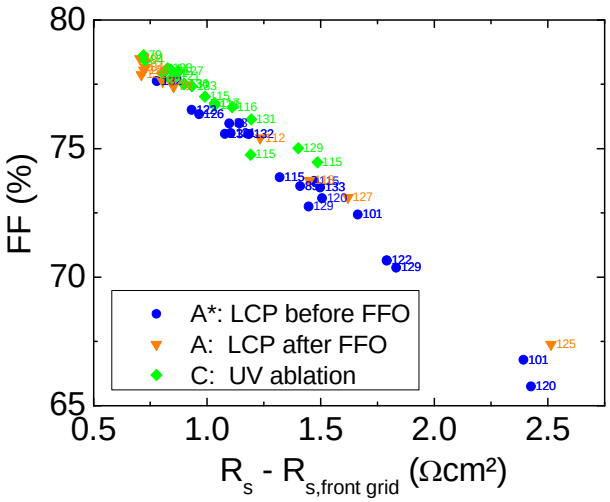

Fig. 64
Measured *FF* of the finished solar cells as function of measured series resistance R_S (without the influence of the front side metal grid $R_{s,front\ grid}$). The data labels represent $R_{sh,emi}$ before PSG etch.

[17] Measurements show a contribution of the rear side metal contact (without contact resistance) of about 0.02-0.03 Ωcm² for all solar cells.

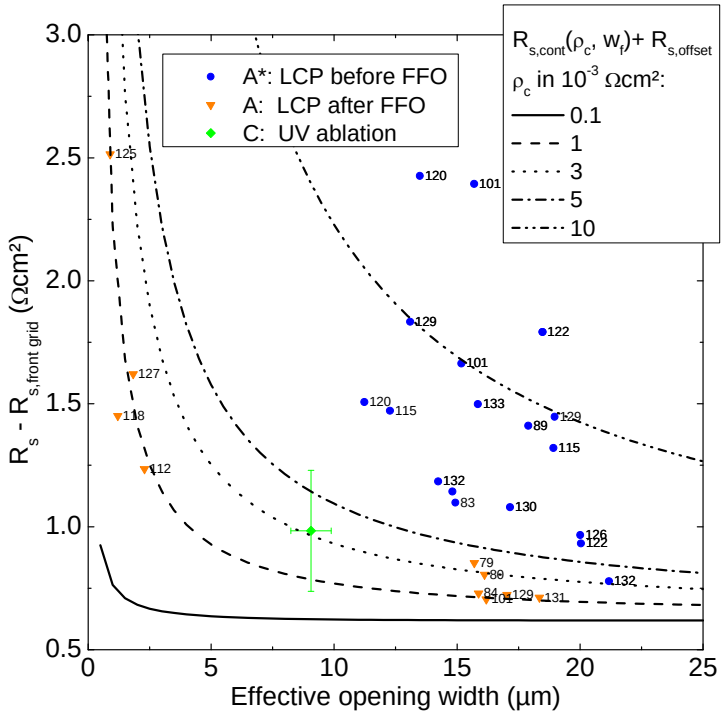

Fig. 65
Measured series resistance R_s (without the influence of the front side metal grid $R_{s,front\ grid}$) as function of the effective opening width introduced in Eq. (34). The data labels represent $R_{sh,emi}$ before PSG etch.

For plated contacts the contact area equals the effective opened area of the laser structured SiN_x layer (represented in this work by the effective opening width introduced in Eq. (34)). The contact resistivity depends on the exact metal-semiconductor interface conditions, such as surface doping concentration, possible Ni-silicide phases due to annealing steps or possible oxide layers between Ni and Si. However, knowing that the surface doping density is $N_{d,peak} \geq 10^{20}$ cm^{-3} for the applied diffusion recipe and has been shown in the same range for the LCP-SE doping, the results of Fig. 44 in section 4.1 indicate that the contact resistivity should be below 10^{-3} Ωcm² independently of the barrier height for the according Ni or Ni silicide phase. Therefore, the high contact resistances could either be a consequence of small front side contact area fractions or current transport limiting barriers such as interface oxides.

In Fig. 65 the measured R_s- $R_{s,front\ grid}$ is shown as a function of the measured effective opening width. As guide to the eye the theoretical geometrical dependence for a contact resistance limited solar cell are shown in the same plot. The theoretical series resistance lines in Fig. 65 are calculated by a sum of Eq. (36) and an offset resistance

of 0.6 Ωcm² referring to the contact resistance contribution and the other series resistance contributions, respectively.

$$R_{s,cont} = \frac{\rho_c}{\left(\left(l_f + \frac{1}{2}\left(\Delta_{Finger} - w_f\right)\right) L_T\right)} \coth\left(\frac{w_f}{2L_T}\right) A_{uc} \qquad (36)$$

The derivation of the contact resistance $R_{s,cont}$ (in Ωcm²) of a unit cell described in Eq. (36) can be found in the work of Mette [89]. $R_{s,cont}$ is a function of the contact resistivity ρ_c, the finger length l_f, the finger pitch Δ_{Finger}, the finger width w_f, the transfer length $L_T = \sqrt{\frac{\rho_c}{R_{sh,emi}}}$ and the unit cell area A_{uc}.

The opening width dependence of the "LCP after FFO" data (group A) in Fig. 65 shows a good agreement with the theoretical behavior of contact resistance dominated solar cells. The inference of the exact contact resistivity ρ_c is not possible from the data in Fig. 65 due to large errors resulting from the impact of the $R_{s,offset}$ assumption and the simplification of the geometry dependence by the introduction of the effective opening width. However, the similar data range and geometry dependence of the "LCP after FFO" (group A) and the "UV ablation" (group C) data in contrast to the "LCP before FFO" (group A*) data shows that group A and C are not limited by high contact resistivities but in some cases only by the contact geometry. On the other hand the significant difference in the data of group A* indicates either large contact resistivities or the inequality of the optical contact geometry and the electrical contact geometry. Both effects could be explained by the presence of interface oxides for this processing group. These thin insulating layers could be created during the FFO firing step, resulting in thicker oxide layers, as in the case of group A and C, where only thin native oxide layers are expected. Therefore, the oxide removing pretreatment before the Ni plating process could be sufficient for group A and C but too weak for the complete removal of the insulating layers of group A* build in the high temperature FFO firing step with a set-peak temperature of 900°C and a total processing time of about 1 min. under ambient air. The reduced contact area due to insulating interface layers of group A* could also be an explanation for the higher V_{oc} and *pFF* level, while accounting for the geometry dependence shown in Fig. 62. In this case the insulating layer would reduce or in the best case passivate some of the electrically active contact area and lead to a reduced contact recombination and, therefore, higher V_{oc}.

5.3.4 Impact of the metallization scheme

In the previous sections the discussion was limited to the groups A and C with plated Ni-Ag front side contacts. This section compares the impact of different plating processes and processing schemes on the solar cell performance. As discussed in section 5.1 group B and D were fabricated using a multiple step plating process: pretreat – Ni LIP – annealing – Ni etch back – pretreat – Ni LIP – Cu LIP – Ag LIP. The groups B/D were divided for the annealing process in two sub-groups, each seeing either 275°C (B/D) for 10 min. or 450°C (B'/D') for 10 min. under forming gas atmosphere. In order to ensure a complete removal of insulating oxide layers within the laser structured openings, group B/D had a pretreat of 60 s in 1% HF solution before the first Ni plating step and a pretreat of about 5 s in 1% HF solution before the second Ni plating step. The multiple pretreats lead to enhanced parasitic plating (ghost plating) for the groups B/D.

Fig. 66 shows the V_{oc}, J_{sc}, *pFF* and *FF* results as function of the plated front side metallization scheme. In this graph the data is not distinguished in the different laser structuring processes. It becomes obvious that the annealing process at 450°C (B'/D') results in a massive drop in the V_{oc} and *pFF* compared to the other groups. This annealing induced shunting will be discussed in more detail in the next section. Comparing the general performance of the different data distributions the main differences are a lower V_{oc}, J_{sc} and *pFF* distribution for the Ni-Cu groups (B/B'/D/D'). Furthermore, the distribution width of the V_{oc} and *pFF* results is larger for these groups.

The lower J_{sc} performance of the groups B/B'/D/D' (orange and green boxplots in Fig. 66) can be explained by a significant amount of parasitic plating outside the laser structured area for the Ni-Cu plated solar cells. The parasitic plated regions cause more shaded area and therefore, lower J_{sc} values. The increase in parasitic plating is a consequence of the multiple and enhanced pretreats, which also affect the unstructured areas of the SiN_x passivation layer and lead to parasitic plating in the etched SiN_x pin-holes.

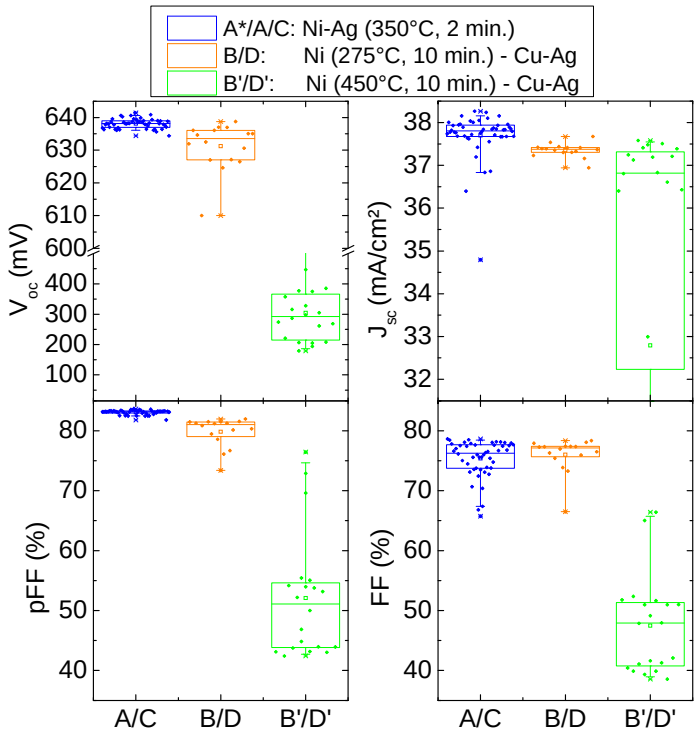

Fig. 66
Measured IV-parameters of the finished solar cells from group A-D.

Two different effects have to be separated in the analysis of the V_{oc} and *pFF* behavior. On the one hand the massive decrease of the high temperature Ni-Cu groups (B'/D', green boxplots in Fig. 66). This annealing induced shunting will be discussed in the next chapter. On the other hand the V_{oc} and *pFF* level is slightly lower for the low temperature Ni-Cu groups (B/D, orange boxplots in Fig. 66) compared to the Ni-Ag groups (A/C, blue boxplots in Fig. 66). The following discussion will be focused on the latter one.

In Fig. 67 the V_{oc} and *pFF* results of the Ni-Ag (A*-blue filled circles / A – orange filled triangles / C – green filled diamonds) and the low temperature Ni-Cu (B* - blue hollow circles / B – orange hollow triangles / D – green hollow diamonds) groups are presented as a function of the effective opening width. Both performance parameters show an offset to lower values for the Ni-Cu groups (hollow symbols). Furthermore, for the Ni-Cu groups the correlation of both parameters to the effective opening width is not clear due to a smaller amount of data. However, also in this case the lowest V_{oc} and *pFF* results correlate with the largest effective opening widths.

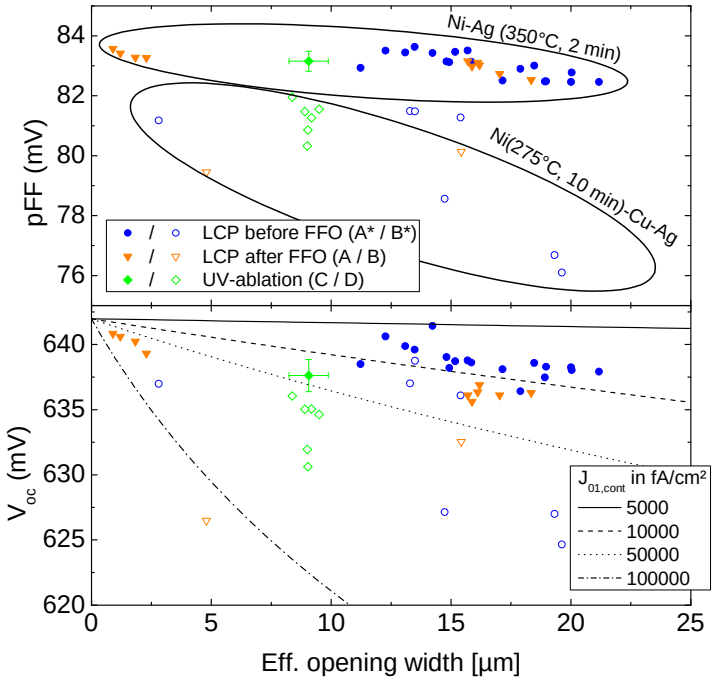

Fig. 67
Measured pFF and Voc of the finished solar cells of group A-D as a function of the effective opening width introduced in Eq. (34).

Reasons for the negative offset of the Ni-Cu groups could be the successful formation of a Ni silicide interface layer during annealing, which increases $J_{01,cont}$ for increasing silicidation depth. Fig. 68 shows an estimation of the influence of the silicidation depth on $J_{01,cont}$ for different exemplarily diffusion profiles. $J_{01,cont}$ in Fig. 68 was calculated using the simulation software EDNA [133] and successively cutting of the doping profile from the top in 50 nm steps. The simulations show that even silicidation depths far below the distance x_{SCR} of the space charge region (SCR) edge to the surface can lead to an open circuit voltage loss. Additionally, the Ni-Cu cells were annealed right after the plating process with a delay below 5 min. In contrast to that the Ni-Ag groups had a delay of 2 days in between the plating process and the annealing process, which may prevent a successful silicidation due to the creation of a native oxide layer at the Ni-Si interface. A variation in the silicidation depth due to inhomogeneous silicide growth as investigated by Rauer et al. [162] could also explain the broader distribution for the Ni-Cu groups in Fig. 67.

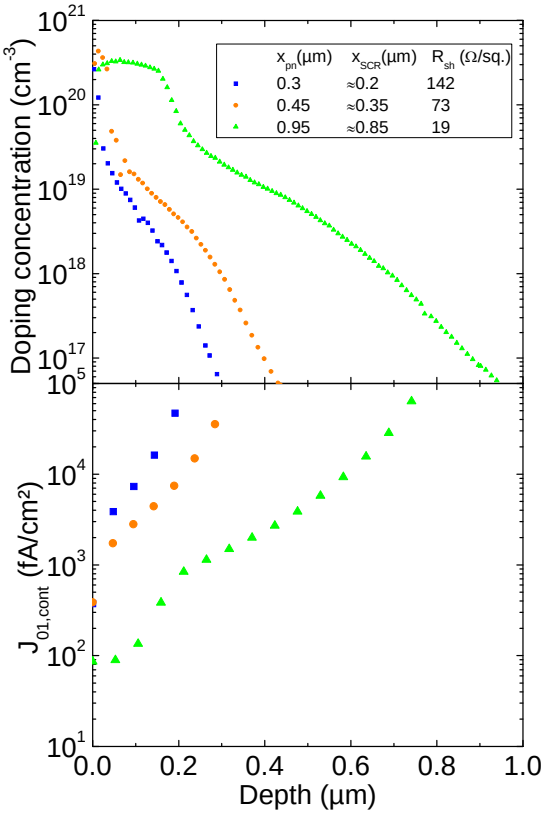

Fig. 68
Simulated influence of the silicidation depth on the saturation current density at the contact $J_{01,cont}$ for 3 exemplary diffusion profiles.

As presented in Fig. 44 Ni silicides show low contact resistivities on silicon. The contact resistance is investigated to corroborate the hypothesis that the lower V_{oc} and *pFF* level is a consequence of successful silicide formation in the Ni-Cu process groups and that the prevented silicide formation due to interface oxides is the reason for the better performance of the Ni-Ag process groups. The Ni-Cu groups should show lower contact resistances and the *pFF* decrease should correlate with lower contact resistances.

The used IV measurement cell tester allows a parallel measurement of the solar cells light and dark IV characteristic, SunsV_{oc} curve and the determination of different series resistance components. There are different methods to determine the total series resistance R_s of solar cells (see [137] for a review). In the following[18] R_s is determined by a comparison of the light IV curve and the series resistance free SunsV_{oc} curve suggested by Wolf and Rauschenbach [136] and evaluated by Pysch et al. [137] as robust method. In order to analyze differences in the contact resistance of the different

[18] Besides the light IV-SunsV_{oc} method the total R_s was additionally calculated by a comparison of light and dark IV curve. Both methods showed the same trends of the following discussion and only slightly differed by about 5-10%.

processing groups and to avoid any influence of metal grid inhomogeneities such as different plating geometries or metal finger interruptions, the total R_s was corrected with the measured metal grid resistance $R_{s,front}$. Therefore, the series resistance difference R_s-$R_{s,front}$ in the following graphs only correlate to series resistances in the silicon and contact resistances. The difference R_s-$R_{s,front}$ will be called internal series resistance in the following discussion.

Fig. 69 presents the total series resistance R_s and the front side metal grid resistance $R_{s,front}$ of the different processing groups. In this case the data is only distinguished by the different plating and annealing processes. The Ni-Ag solar cells show much higher internal series resistances R_s-$R_{s,front}$ as the Ni-Cu groups. Furthermore, the high temperature Ni-Cu group (B*'/ B'/ D') demonstrates a lower internal series resistance distribution than the low temperature Ni-Cu group (B*/ B/ D). As discussed in previous sections the main contribution of the internal series resistance is th front side contact ressitance. This finding supports the assumption that interface oxide layers may prevent the formation of Ni silicides, which lead on the one hand to higher V_{oc} and *pFF* levels but also to higher contact resistances for the Ni-Ag process group.

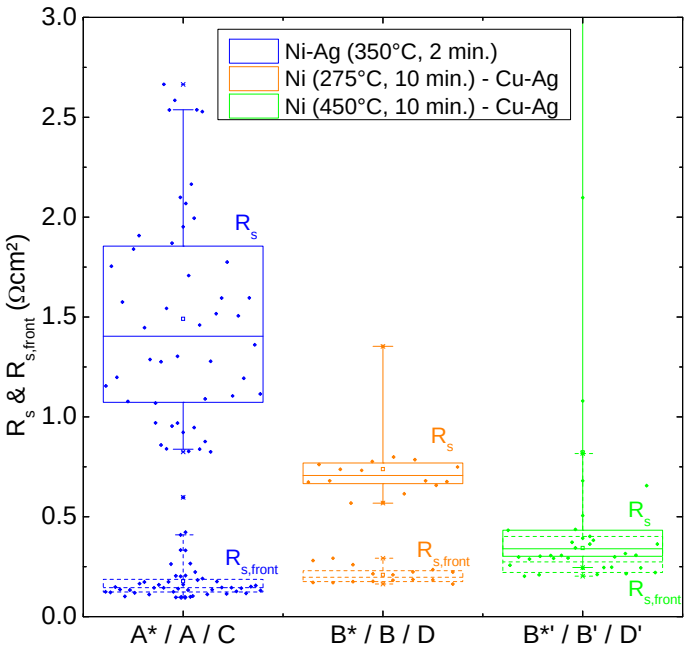

Fig. 69
Total series resistance R_s and the front side metal grid resistance $R_{s,front}$ of the different processing groups.

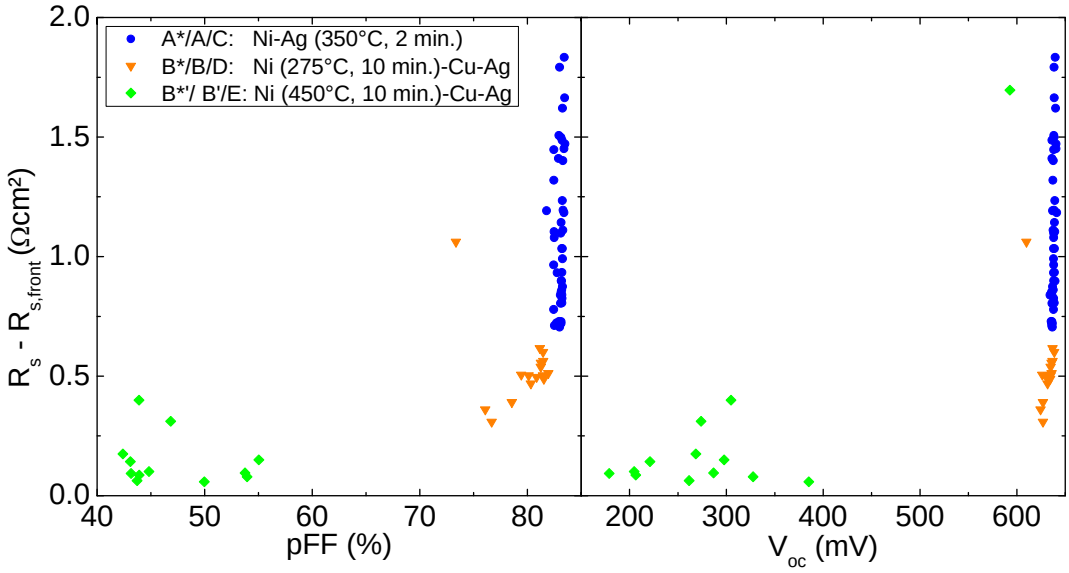

Fig. 70
Correlation of the internal series resistance R_s-$R_{s,front}$ and the *pFF* and V_{oc} from SunsV_{oc}.

Furthermore, Fig. 70 shows that there is a correlation between the *pFF* and the internal series resistance R_s-$R_{s,front}$ (left plot in Fig. 70), as well as the V_{oc} and R_s-$R_{s,front}$ (right plot in Fig. 70). Normally, a *pFF* correlation with the series resistance is not present due to the fact that the *pFF* results from voltage measurements under variable illumination intensity in V_{oc} conditions. Therefore, there is no current flowing in or out of the cell during the whole measurement, which makes it insensitive to contact resistance influences. As discussed in section 5.3.2 Schottky contacts or large sheet resistances can influence the SunsV_{oc} measurement. Both effects are not present in this processing stage. The correlation in this case demonstrates that the origin of the *pFF* decrease also affects the internal series resistance of the solar cell. The hypothesis of a *pFF* decrease due to the formation of Ni silicides agrees with this finding due to the reduced contact resistivity of Ni silicide layers at the Ni-Ni_xSi_y-Si interface in comparison to the Ni-Si interface. An increased recombination rate at the local silicides also explains a reduction in the V_{oc} with increasing fractions of silicided areas, which results in the reduction of the internal resistance, too. The discussions in the following chapter will examine why the *pFF* is much more sensitive on this effect than the V_{oc}.

5.4 Conclusion

The experiment described in this chapter aimed to develop an evolutionary improvement of the Al-BSF solar cell design. In this context three cell design improvements were analyzed: the introduction of a lowly doped thermally diffused emitter doping, narrow Ni-Ag or Ni-Cu-Ag plated front side contacts and the

introduction of a selective emitter design by an additional highly doped contact opening by LCP-SE. The solar cells were fabricated from commercial 156x156 mm² Cz-Si wafers, featured a three busbar design on the front side and a full area Al-BSF on the rear side. The reference solar cells were conventional fully screen printed (fired Ag front side contacts) Al-BSF solar cells with a 75 Ω/sq. emitter on the front. The other process groups featured a thermally diffused 150 Ω/sq. emitter with a pn-junction depth of about 200-300 nm and plated Ni-Ag or Ni-Cu-Ag front side contacts. The contact openings were either performed by a UV-laser ablation process or by a LCP-SE laser doping process, which introduces an additional highly doped area underneath the opening structure. The different contact opening techniques resulted either in a homogenous emitter design (HE) for the UV laser ablation or in a selective emitter design (SE) for the LCP-SE processed solar cells. The fabricated solar cells showed a significant cell efficiency benefit compared to the fully screen printed reference solar cells and reached maximum cell efficiencies of up to 19%.

The introduction of the lightly doped emitter proved to be beneficial in terms of the short circuit current density J_{sc} and the open circuit voltage V_{oc}. The J_{sc} improvement is caused by better quantum efficiencies in the lower wavelength regime due to decreased Auger recombination. Furthermore, the better recombination properties of the lightly doped emitter lead to a lower saturation current density in the passivated regions $J_{01,pas}$, resulting in a higher V_{oc}.

The introduction of Ni plated front side contacts allowed the introduction of the lightly doped emitter in the first place due to a low contact resistivity even for reduced surface doping densities. The *FF* analysis indicated that cells with low *FF* were mostly limited by contact resistance losses due to small contact opening widths or in the case of LCP-SE processed before the FFO firing process by interface insulating layers. The series resistance analysis also indicates that the contact resistance becomes very low in the case of successful silicidation of the Ni-Si interface during an annealing step. Furthermore, the narrow finger widths of the plated contacts result in an increased J_{sc} due to lower front side contact shading compared to the fabricated screen printed Ag contacts.

The introduction of the selective emitter did not show any significant improvement in terms of maximum cell efficiency. This finding is in agreement with the simulation results of the Al-BSF solar cell design with and without selective emitter discussed in chapter 4. The only significant improvements in V_{oc} or R_s of the LCP-SE solar cells could be explained by mostly geometry related effects. One main reason in this context

is on the one hand the low sensitivity of the Al-BSF design on contact recombination improvements and on the other hand that the applied thermally diffused emitter already had a rather high surface doping concentration of about $2 \cdot 10^{20}$ cm^{-3}. In contrast to screen printed contacts, which react very sensitive on surface doping reductions, plated Ni contacts are not limited by high contact resistivities in this regime. The contact resistivity becomes even less problematic after the silicidation of the Ni-Si interface.

The fabricated solar cells with plated Ni-Ag or Ni-Cu-Ag front side contacts showed a correlation between the measured pseudo fill factor *pFF* and the internal series resistance R_s-$R_{s,front}$. This finding supported the hypothesis that the contact interface features for some cells still insulating layers, which improves the V_{oc} and the *pFF* of the solar cell but also increases the contact resistance. However, the *pFF* improvement is in this context an indication that the silicidation of the Ni-Si interface was in this case not successful. The solar cells in this experiment faced the problem that the improvement of the contact resistance visible in the reduced internal series resistance came along with a reduced *pFF* most likely caused by silicidation induced shunting in the space charge region.

The origin of the *pFF* reduction especially for high annealing processes will be addressed in the next chapter.

6 Annealing induced non-linear shunting of Ni plated solar cells

The fabricated solar cells of the last chapter were further analyzed in this chapter in terms of annealing induced shunting effects. The analysis of the change in the global electrical characteristic due to the contact annealing discussed in section 6.1 led to the formulation of a hypothesis about the physical origin of the annealing induced shunting effect in section 6.2. The stated hypothesis is experimentally investigated on the macro scale by local imaging characterization in section 6.3 and in the following section 6.4 by µ-imaging methods and electron imaging methods on the micro scale. Furthermore, the main design parameters of the highly doped contact openings in order to prevent annealing induced shunting are discussed in section 6.5, which allows further optimization routes for future process developments. Section 6.6 summarizes the characterization results of this chapter and evaluates the stated hypothesis.

The experimentally results presented in section 6.1-6.3 and section 6.5 were generated in collaboration with a supervised diploma [97] and master thesis [96], respectively. Furthermore, the publication [73] of the author is partly based on the findings of this chapter.

The previous section discussed the strong correlation of the solar cell performance of plated solar cells and the applied metallization scheme. Especially, the Ni plating-annealing process sequence proves to be crucial for the solar cell performance. The annealing process is crucial for the formation of Ni silicide layers at the interface, which improve the contact resistivity but also are crucial for a good contact adhesion. Fig. 71 illustrates the peel force results of plated Ni-C front side contacts without annealing (blue line) resulting in insufficient adhesion. In contrast, the plated Ni-Cu contacts with an annealing induced silicidation (orange line) demonstrates a sufficient adhesion after soldering comparable to the reference Ag screen printed contact (green line). This section will show in which way the electrical performance of the solar cell is changed, where the origins of this shunt-like behavior are located and discuss the agreement of the hypothesis of Ni silicide induced shunting with the findings of the measurements.

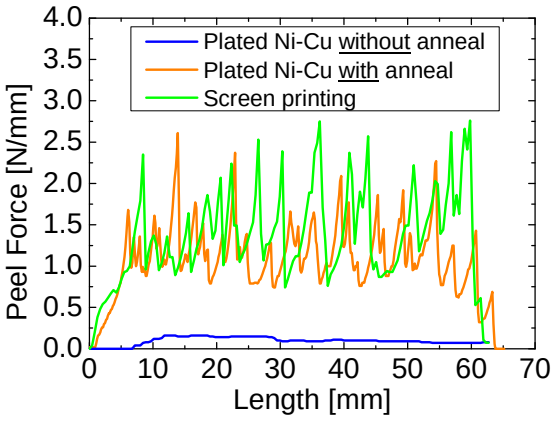

Fig. 71
Comparison of peel force tests of plated busbars with and without annealing and a screen printed reference. The shown plot is taken from [73], which is based on the data of Mondon et al. [163].

6.1 Global electrical shunting characteristic

In order to understand the dynamic of the annealing induced *pFF* breakdown, the Ni-Ag process groups of section 5.1 were consecutively annealed at different temperatures and characterized after each annealing step. Fig. 72 shows the measured *pFF* and SunsV_{oc} after different annealing steps for 2 min. in N_2 atmosphere.

The Ni-Ag plated solar cells show decreased *pFF* and V_{oc} for increasing temperatures. However, the design of this experiment does not allow any conclusion about the different influences of the total annealing time and the peak temperature. Nevertheless, the data show that the decrease in *pFF* and V_{oc} is a dynamic process, which continuously decreases the cell performance with each heat treatment. The performance distribution of the selective emitter solar cells seems to be slightly more robust against the heat treatment in comparison to the UV laser ablated solar cells. The comparison of cell tester measurements before and after the annealing row confirms also for the Ni-Ag plated solar cells the correlation of *pFF* reduction and internal series resistance improvement. Fig. 73 (right plot) demonstrates this finding for three exemplary Ni-Ag plated solar cell of the processing groups A* (blue circles), A (orange triangles) and C (green squares) from section 5.1 before (solid symbols) and after (open symbols) the consecutive annealing row. The series resistance plot in Fig. 73 (left plot) demonstrates that the series resistance improvement, which correlates with decreasing *pFF* values, is a result of decreasing internal series resistance and therefore, the contact resistance of the solar cell. A sufficiently deep doping underneath the plated contacts should avoid this correlation due to a movement of the space charge region away from the highly recombinative silicide layer. The similar trend in the *pFF*-internal resistance correlation for both laser opening schemes raises

the question where the reason of the performance breakdown is located and why the selective emitter doping cannot prevent it.

In order to choose suitable characterization methods the physics of the performance breakdown has to be analyzed. Fig. 74 shows four different IV characteristics of an exemplary Ni-Ag plated solar cell of the processing groups A* after the first annealing step (blue circles) at 350°C for 2 min and after the last annealing step (orange triangles) at 425°C for 2 min of the consecutive annealing row. After the first heat treatments of 350°C, the cell[19] shows high *pFF* and V_{oc} values of 83.6% and 637 mV, respectively. Furthermore, the dark IV curve in subplot b) in Fig. 74 shows a typical 2-diode like behavior (blue circles).

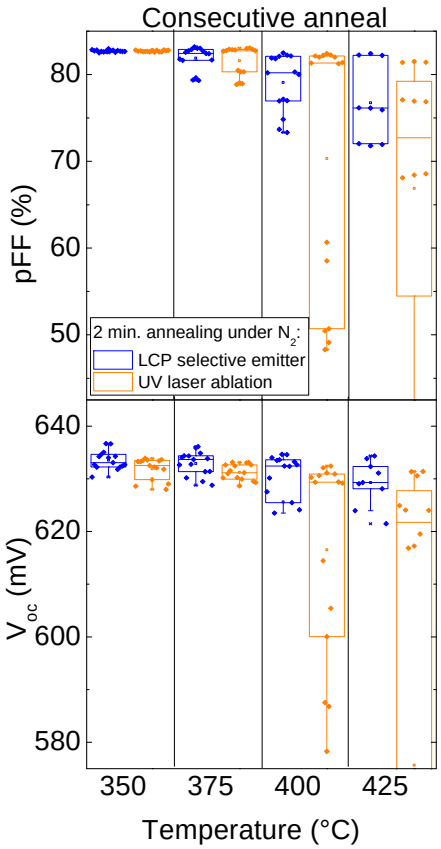

Fig. 72
Measured pseudo fill factor (*pFF*) and open circuit voltage (V_{oc}) measured by SunsV_{oc} of LCP SE and UV laser ablated solar cells with Ni-Ag plated front side contacts after a consecutive row of annealing steps for 2 min. in N_2 atmosphere [73].

[19] Cell: 221_MDN_LCP182

After the consecutive annealing the solar cell shows a reduced *pFF* and V_{oc} values of about 58.3% and 612 mV, respectively. Additionally, the dark IV curve in subplot b) in Fig. 74shows a hump feature in the mid voltage regime of 200-400 mV, which makes it impossible to fit a conventional 2-diode model curve to the data (orange triangles). This hump is also visible in the SunsV_{oc} curve in in subplot d) in Fig. 74, which causes a reduction of the maximum power point (MPP) and, therefore, a parallel decrease of the *pFF* and *FF*. The *FF* breakdown is visible in the flattened light IV curve in subplot a) in Fig. 74 for the measurement after annealing (orange triangles).Typically, *pFF* breakdowns correlate with shunting effects. However, ohmic shunts are included in the 2-diode model and would show a stronger impact even in lower voltage regimes. Furthermore, the non-linearity in the dark IV characteristic in forward and reverse direction after annealing in subplot c) in Fig. 74shows that the increased current results not from an ohmic shunt.

The dark IV curve in subplot c) in Fig. 74 reveals a hump feature in the mid-voltage region after the consecutive annealing row. This hump feature in the mid-voltage region is the reason why the *pFF* is much more sensitive on annealing induced non-linear shunting effects than the V_{oc}. In comparison the relative difference in the dark JV curve before and after the annealing row is in the higher voltage region around V_{oc} rather small compared to the mid-voltage region around the maximum power point, which determines the *pFF*. Therefore, the effects such as the shown correlation between the internal series resistance and the *pFF* and V_{oc} in Fig. 70 in section 5.3.4 are much more pronounced in the *pFF*.

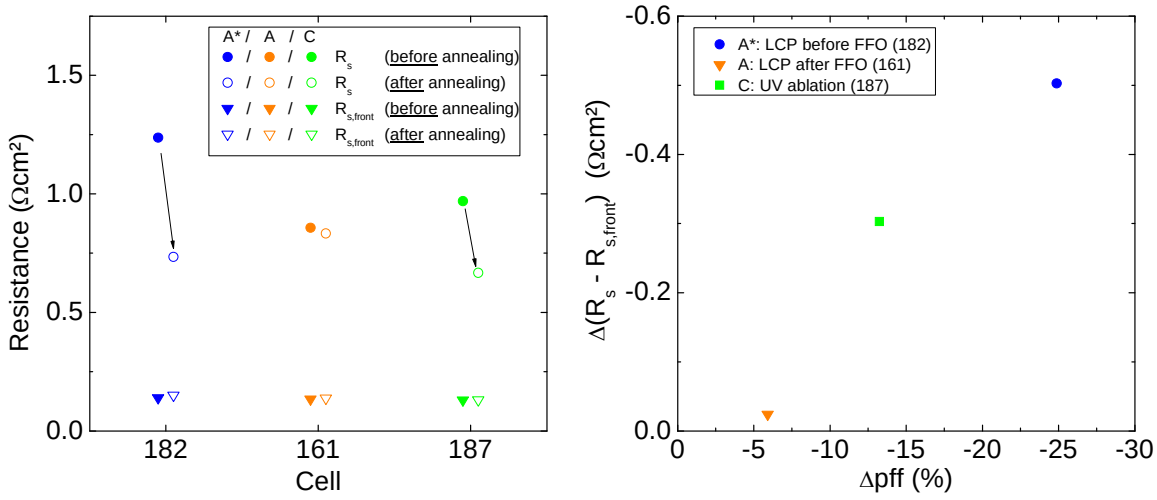

Fig. 73
Measured internal series resistance R_s-$R_{s,front}$ and pseudo fill factor *pFF* before and after the consecutive annealing row.

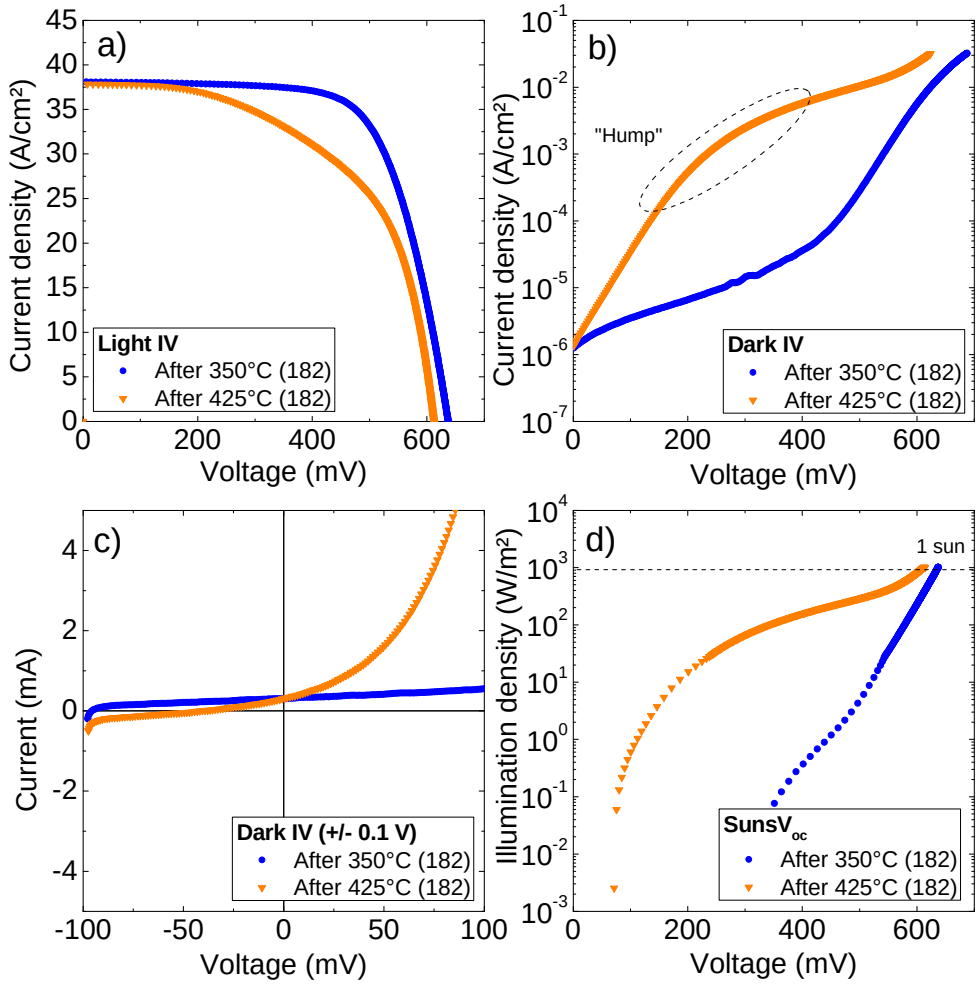

Fig. 74
Measured electrical characteristics of a LCP-SE solar cell of group A* (cell: 182) before and after the consecutive row of annealing steps (see Fig. 72); a) Light IV characteristic, b) Dark IV characteristic , c) Dark IV characteristic in reverse and forward direction in linear scale d) SunsV$_{oc}$ characteristic.

Despite the increased recombination current in forward direction, the solar cells show after the consecutive annealing row an increased breakdown current in reverse direction. However, the reverse current is only increased for high reverse voltages. In Fig. 75 the measured reverse current density J_{rev} at -1 V and -12 V (left plot) is compared before (solid symbols) and after (open symbols) the consecutive temper row. For small reverse voltages at -1 V (circles) the breakdown current density J_{rev} stays the same and only for high reverse voltages at -12 V (triangles) the breakdown current density J_{rev} increases significantly. Furthermore, the increase in the breakdown current also correlates with the decrease in the *pFF* (right plot in Fig. 75).

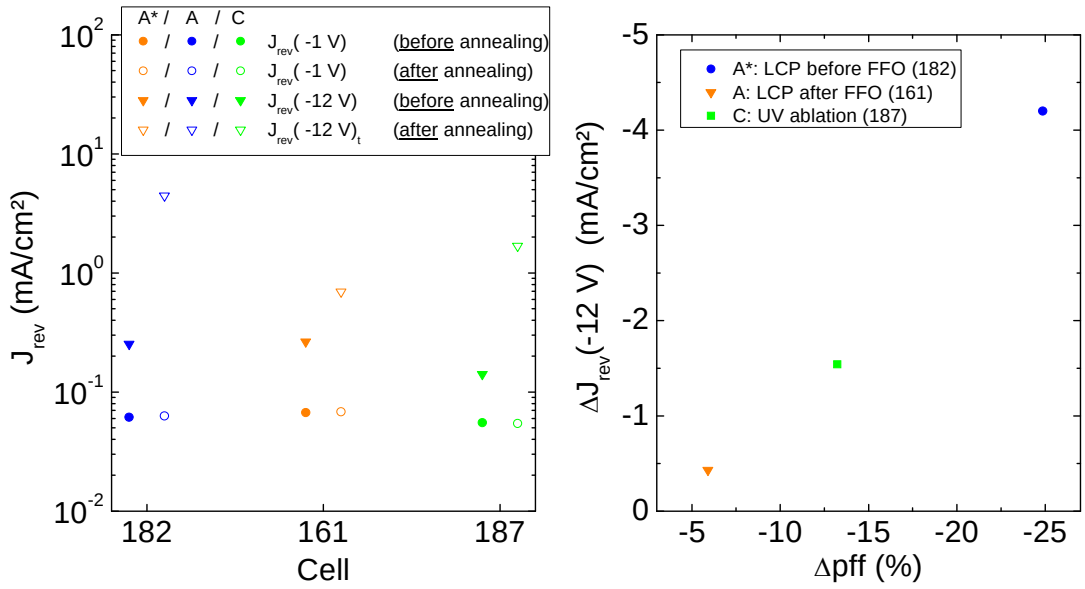

Fig. 75
Measured reverse current density J_{rev} at different reverse voltage (-1 V / -12 V) before and after the consecutive annealing row (left plot) and the correlation of the reverse breakdown current density J_{rev}(-12 V) and the *pFF* for three different solar cells of process group A*(182), A (161) and C (187).

6.2 Hypotheses

The previous section discussed the global electrical characteristics of annealing induced non-linear shunting of Ni plated solar cells with a previous SiN_x structuring process. The main electrical features of the annealed solar cells were:

a. Non-ohmic shunting characteristic
b. "Hump" feature in the dark IV curve in the voltage range 200-500 mV and no conventional 2-diode model characteristic
c. Decreased *pFF*, V_{oc} and J_{sc}
d. Annealing induced *pFF* breakdown shows correlation to:
    1. Internal series resistance R_s-$R_{s,front}$
    2. Reverse breakdown current at high reverse voltages J_{rev}(-12 V)

There are different phenomena causing a) non-ohmic shunting characteristics and b) hump features in the dark IV characteristic. One example is the formation of local Schottky contacts or locally increased space charge recombination [5], which show a diode like behavior causing non-ohmic characteristics [164]. Furthermore, the influence of the series resistance on balancing currents compensating the increased recombination at the local features can leads to a hump in the dark IV. The locally increased recombination causing the hump feature in the dark IV also explains c) the reduced *pFF*, V_{oc} and J_{sc}. The correlation d) of the annealing induced *pFF* breakdown and the internal series resistance indicates a connection between the silicidation induced lowering of the contact resistance and the increased recombination. The lowered reverse breakdown current is a result of local modifications of the pn-junction

diode. Low reverse breakdown currents are extensively analyzed for multi crystalline silicon solar cells, where they are caused by local defect rich structures such as metal precipitates [114] or crystal defects [165].

Comparing the global characteristics of the annealing induced non-linear shunting to similar effects in in the literature, the following hypotheses of the physical origin of the annealing induced *pFF* breakdown are stated:

I. The *pFF* breakdown is a consequence of locally deep Ni silicide formation, which penetrates into the space charge region or even contacts the p-type base (Schottky shunting).
II. The annealing induced non-linear shunting can be prevented by emitter doping depths at the contact openings (i.e. selective emitter) larger than the maximum silicidation depths
III. Large *pFF* variations after annealing between similar processed solar cells result from inhomogeneous silicide growth due to a strong influence of interface oxides or crystal defects on the silicide formation.

The following sections will focus on the evaluation of local characterization methods and micro structure analysis in order to proof the hypothesis of local Ni silicidation induced shunting.

6.3 Local shunting characteristic

The global electrical characteristic of solar cells with annealing induced non-ohmic shunting effects showed that the behavior of the solar cells is affected in forward and reverse direction. Therefore, local characterization techniques in both voltage directions have to be investigated. Within this work various measurement techniques were evaluated: Dark Lock-In Thermography (DLIT) in forward/reverse direction, Illuminated Lock-In Thermography (ILIT) in forward/reverse direction, forward/reverse biased Electroluminescence (EL / ReB-EL), Photoluminescence (PL) and local beam induced current (LBIC). The DLIT, ILIT and EL/ReB-EL measurement setups contact the solar cells via contact bars at the busbar positions. Therefore, the emission from or the illumination of the busbar regions of the solar cell is partially shaded by the contacting bars. This effect has to be taken into account for the interpretation of these measurements shown in this section. In order to avoid misinterpretations due to the contact bar shading, only emission phenomena in the regions between the busbars are discussed in this section.

Fig. 76 shows DLIT measurements under -12 V reverse voltage for two exemplary Ni-Ag plated solar cells with and without selective emitter (group A/C from section 5.1) after each step of the consecutive annealing row. The reverse DLIT measurements demonstrate a correlation of the *pFF* decrease and an increase of local heat signals after each annealing step.

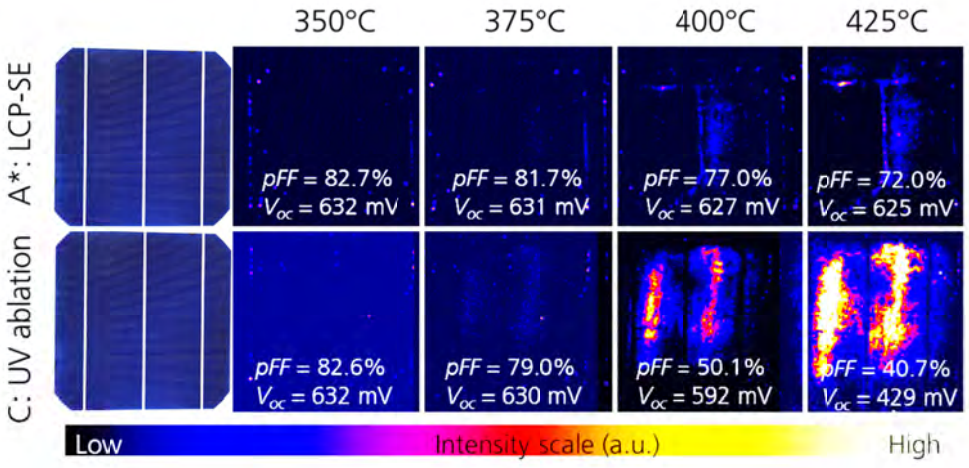

Fig. 76
Photography of the measured solar cell (first column) and DLIT measurements of two exemplary cells with plated Ni-Ag contacts. The front side features either a selective emitter by LCP-SE of group A* (cell: 198) or a UV laser ablated contact openings on a homogenous emitter of group C (cell: 022) under -12V reverse voltage after consecutive annealing steps. The image sequences have the same intensity scale.

The local heat signal is induced by series resistance related heat losses of local current flows. In reverse direction the local current flow equals local breakdown spots of the pn-junction. This measurement confirms the correlation of the *pFF* breakdown and the increase of the reverse breakdown current J_{rev} and illustrates that the breakdown occurs not homogenously over the cell and not at the wafer edges but within the active cell area. However, the low resolution of the DLIT measurements in Fig. 76 does not allow an exact localization of the local breakdown spots. Especially, the differentiation if the spots are located within in the laser structured area or not is not possible.

The LCP-SE solar cell (cell: 198) from Fig. 76 was characterized using DLIT, ILIT, LBIC, EL and PL at different bias voltages. All measurements are summarized in Fig. 77. It becomes obvious that the local features of the reverse voltage DLIT images correlate with local features in other imaging techniques. In the most measurements of Fig. 77 a “J” shaped structure is visible. By comparing the characteristics of this structure in each measurement, different physical attributes of this feature can be determined.

The “J” feature is located between two busbars and is not visible in the optical appearance of the solar cell or correlates with characteristic features in optical microscope measurements. This feature only becomes visible with electrical imaging techniques. Furthermore, the shape of this feature is not similar for all cells. Most cells showed cloud shaped features between the busbars such as the UV ablated cell in Fig. 76 or the cloud shaped structure on the right side of the “J” in the DLIT images in Fig.

77. Although, the shape of the structures varied from cell to cell, the imaging characteristics stayed the same as shown in Fig. 77.

In V_{oc} conditions the “J” appears as region with low signal count rate in PL images. The low PL signal intensity correlates with a low fraction of radiative recombination due to a low minority carrier concentration in these regions. The decreased minority carrier density is a consequence of increased non-radiative recombination channels, such as increased SRH recombination. This shows that under V_{oc} conditions the annealing induced features are areas with increased recombination rates.

In forward bias at +0.5 V the “J” appears as region of high signal intensity in the DLIT and ILIT image and low signal intensity in the EL image. In the DLIT image the cell is not illuminated and the current induced heat signal is a consequence of extracted thermally generated currents, which equal recombination currents. Thus, areas of high DLIT signal can be related to either regions of high recombination currents, regions of high series resistances or ohmic shunted regions. The ILIT measurements image the same features as in DLIT, but operate under real working conditions with 1 sun illumination of the solar cell.

In J_{sc} conditions (0 V) the LBIC measurement was performed at various wavelengths, which mostly did not show the characteristic “J” feature. This is in agreement with the fact the J_{sc} of the solar cell does not significantly change before and after annealing. However, the shown LBIC measurement at 405 nm, which is mostly sensitive to recombination effects on the front side, shows a slightly decrease of the spectral response signal in the “J” region, which is in agreement with the reduced PL signal due to increased recombination rates in this region.

For low reverse bias at -0.5 V the DLIT image is dominated by noise effects and does not show the characteristic “J” feature. This confirms the finding from the global characteristics that the appearing shunts are not ohmic ones, which would lead to the same DLIT result as for +0.5 V. Furthermore, the results of Fig. 75 showed that the reverse current at low reverse voltages is not significantly increased due to the annealing.

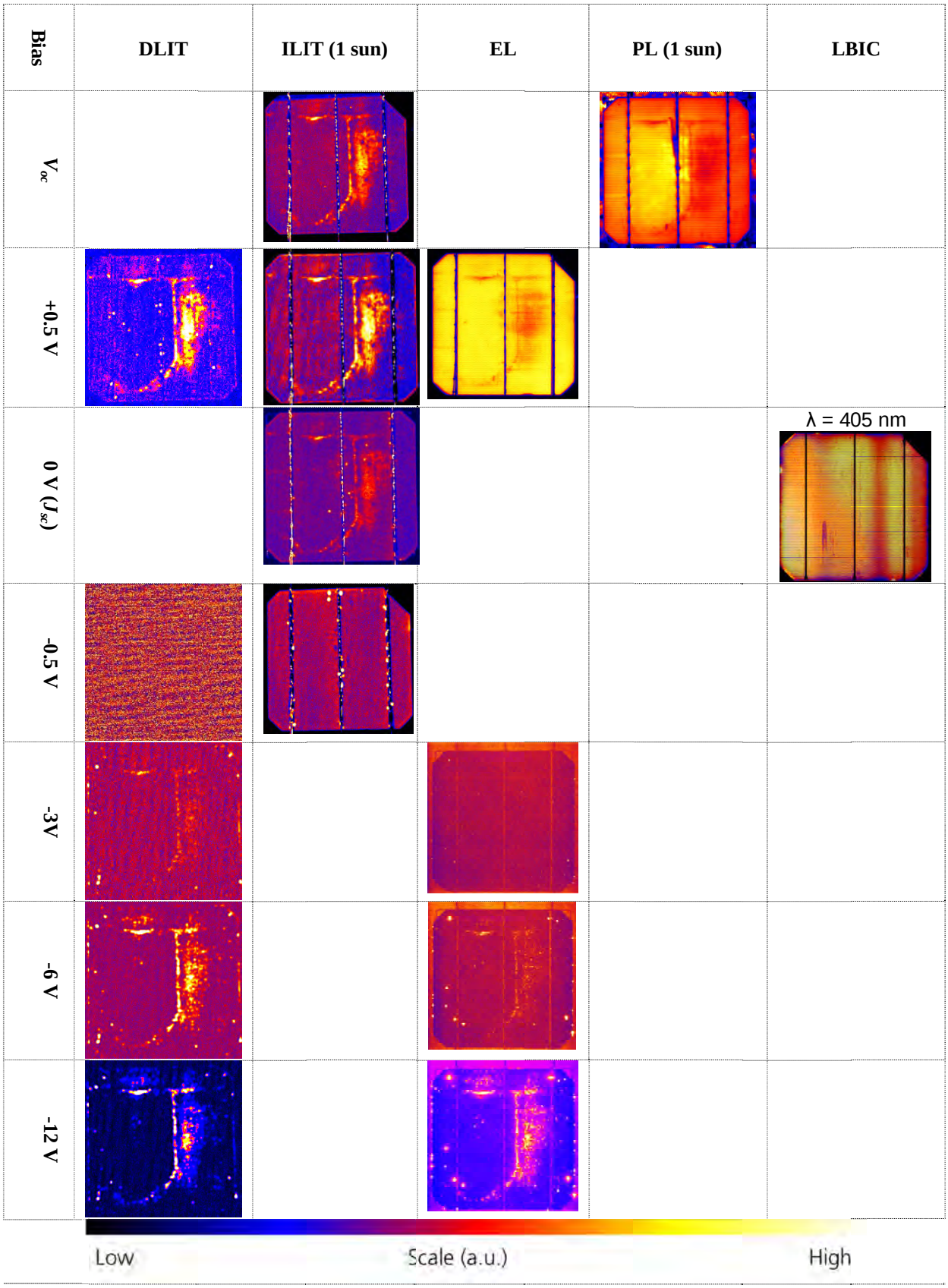

Fig. 77
Summary of different imaging characterization techniques applied on a LCP-SE solar cell (198) with Ni-Ag front side contacts after the consecutive annealing row shown in Fig. 76. The SunsV_{oc} characterization of this solar cell after the consecutive annealing row resulted in *pFF* = 72% and V_{oc} = 625 mV. The scale of each image is in arbitrary units with values corresponding to high signal intensity or count rates in each measurement.

High reverse voltages lead to high signal intensities of the “J” feature in the DLIT and ReB-EL image. The DLIT signal is a consequence of local breakdown currents at the pn-junction. The appearance of the “J” feature in the ReB-EL image is not trivial. The signal is at -3 V not visible and starts to appear at higher reverse voltages. On the one hand the ReB-EL dynamic confirms that the features are not correlated to ohmic shunted regions, which would not be visible in this image. On the other hand the used camera and filter combination show that these features emit under high reverse voltages photons with energies larger than the band gap energy. However, the used setup allows no further spectral information of these features.

The comparison of the different measurement techniques in Fig. 77 demonstrates that the appearance of the pFF breakdown correlated features is present under different voltage conditions and in almost all imaging techniques. Especially, the similarities of the DLIT measurements and the ReB-EL images at high reverse voltages shows that these methods are equally suited to locate the pFF breakdown correlated features. The ReB-EL method has in this context some advantages due to higher spatial resolution and lower measuring times. Therefore, in the following section it will be used to track down the exact locations of the *pFF* breakdown correlated features.

DLIT and ReB-EL imaging allow a more detailed look on the emission characteristic of the analyzed feature. Previous publications [109, 114] demonstrated that the emission intensity-bias voltage dependency shows different characteristics for different physical origins. This analysis is mostly used in order to characterize different breakdown spots in multi crystalline silicon (mc-Si) solar cells. The emission intensity-bias voltage dependency of the different breakdown types is shown in Fig. 25 in the “Fundamentals” chapter 2. In Fig. 78 the emission intensity-bias voltage dependency of the *pFF* breakdown related features is presented. The intensity-voltage characteristic is similar to the one of type II breakdowns after Kwapil [114]. This breakdown type is caused by metal precipitates in mc-Si solar cells. For low reverse voltages the emission intensity is almost negligible and after a threshold voltage between -(4-10) V the intensity increases linear with the reverse voltage square. The linear-quadratic dependency can be found in both measurements DLIT and ReB-EL. This behavior is consistent with the fact that the reverse breakdown current (as shown in Fig. 75) is not increased for low reverse voltages but only in the higher voltage regime. Furthermore, the ReB-EL measurements allowed a more precise localization of the *pFF* breakdown correlated features near the laser structured areas. These features showed a spatial correlation to the grid structure of the laser openings.

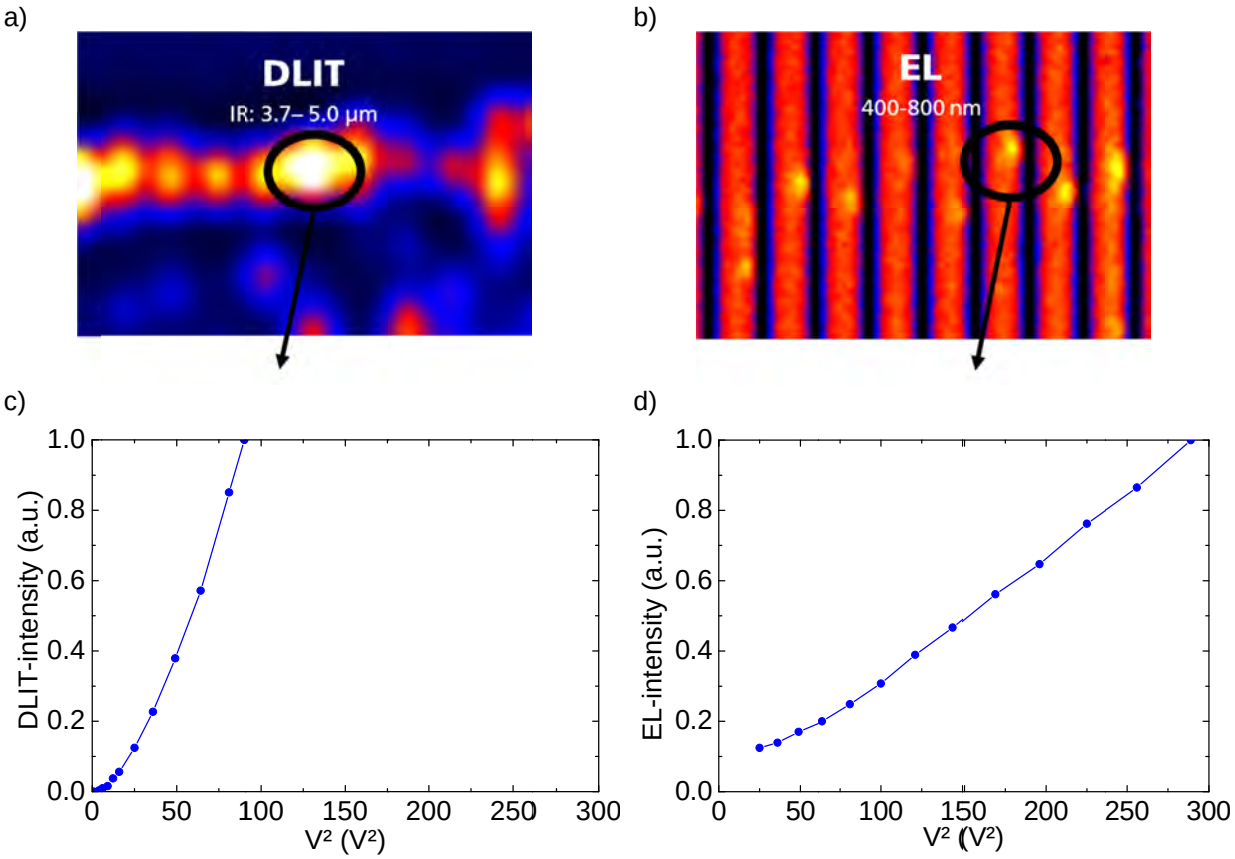

Fig. 78
a) Emissivity corrected [109] DLIT image, c) DLIT intensity-voltage characteristic, b) ReB-EL image and d) ReB-EL intensity-voltage characteristic of the *pFF* breakdown correlated features. The dark stripes in the EL image equal the positions of the front side contact fingers. Both intensity-voltage characteristics are normalized to the value of maximum intensity.

The combination of SunsV_{oc} measurements and ReB-EL measurements at higher reverse voltages makes it possible to distinguish between the impacts of the different fabrication processes on the solar cell performance. Fig. 79 shows the comparison of four exemplary solar cells with either an annealing step directly after the laser structuring without plated metal on the front side (first row in Fig. 79) or laser structured solar cells with plated front side contacts, which are annealed after the plating (second row in Fig. 79). All solar cells show a small number of local spots of high intensity, which do not show any correlation to low *pFF* values and which will be discussed in the next section. Furthermore, two different anneal temperatures were used in order to analyze the influence of different temperature regimes. The solar cells annealed at 275°C for 10 min. do not show any influence on the *pFF* independently of the presence of plated Ni. However, the solar cells annealed at 450°C for 10 min. show a massive *pFF* decrease in the presence of plated Ni front side contacts but only a slightly decrease after annealing without plated Ni on the front side.

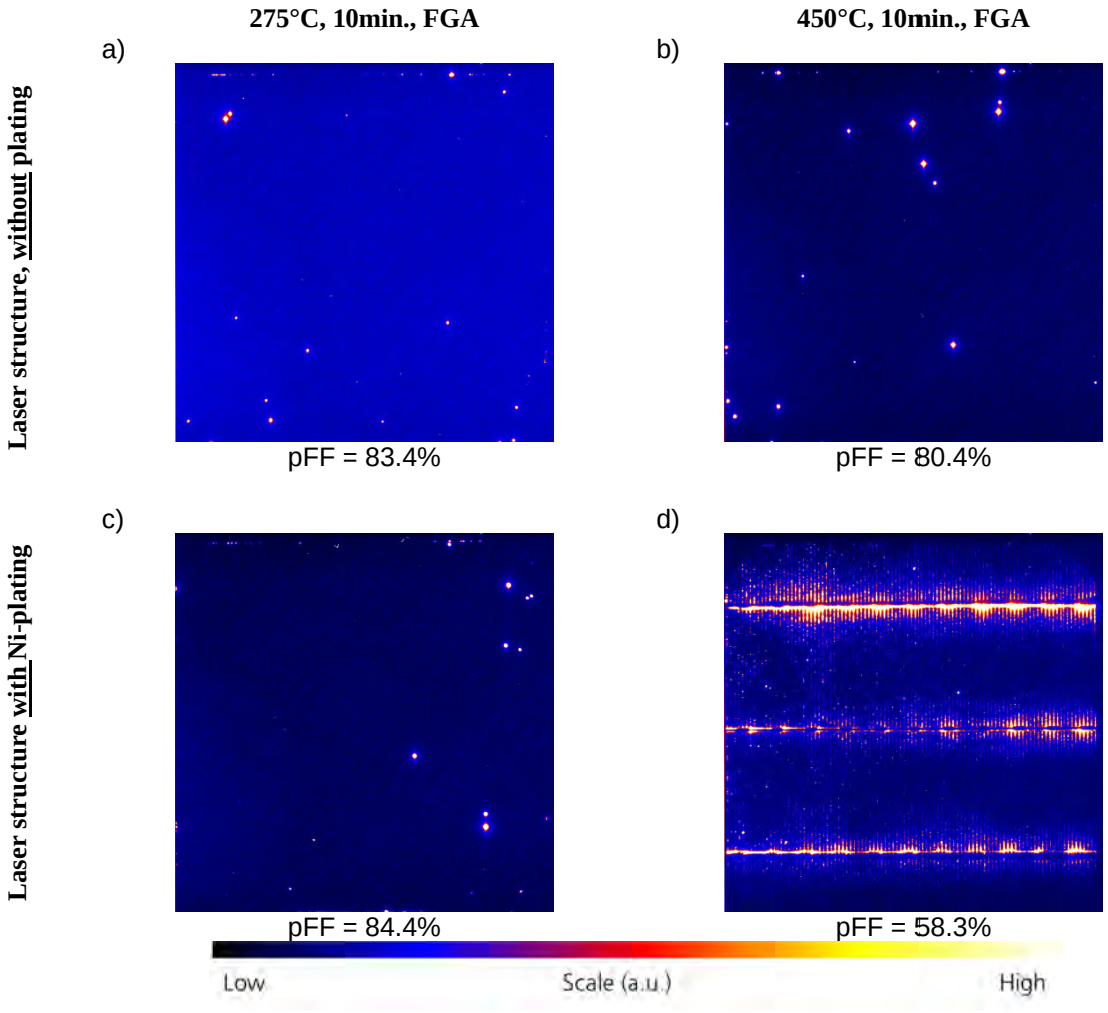

Fig. 79
Suns V_{oc} and ReB-EL (-12V) measurements of laser structured solar cells with and without Ni plated front side contacts characterized after either an annealing process at 275° or 450°C for 10 min. under forming gas atmosphere (FGA). The Ni layer of the plated solar cells was etched back after the annealing process in order to avoid shading of the EL emission due to the metal layer. All measurements feature the same intensity scale.

Furthermore, the results in Fig. 79 show again a correlation between high *pFF* breakdowns and local ReB-EL features. The ReB-EL features of the plated solar cell annealed at 450°C (right bottom image in Fig. 79) are mostly located around the busbar and not in between the busbars as in Fig. 76. This is a result of the local contacting with contact rails along the busbars and the missing front side metal fingers, which leads to an emitter sheet resistance induced voltage difference between the applied voltage and the local voltage for regions far away of the contact rails. Therefore, only regions around the busbar are biased at -12 V and with increasing distance to the contacting rails the local bias of the solar cell decreases, which leads to significantly lower EL emission between the busbars.

The correlation of the annealing induced *pFF* breakdown and the presence of plated Ni on the front side supports the hypothesis of Ni silicide induced shunting. However, the slightly *pFF* decrease after annealing at 450°C without Ni plated contacts shows that also the annealing at higher temperatures itself has a detrimental impact on the solar cell performance in this experiment.

6.4 Microscopic shunting characteristic

6.4.1 Local micro structures

The previous section showed that ReB-EL measurements can be used to roughly locate *pFF* breakdown correlated features on the solar cell. However, the conventional EL imaging system makes it difficult to locate these features on a µm or nm-scale in order to perform further microscopic or element specific characterization techniques such as SEM, TEM or EDX. Therefore, a confocal EL setup was used in order to perform µ-ReB-EL measurements with a much higher resolution compared to the conventional imaging system. The used system was set up by Paul Gundel [94] and Friedemann Heinz and the measurements were performed by Matthias Breitwieser.

Non-pFF correlated features

The ReB-EL measurements at high reverse voltages (-12V) always showed a small amount of local spots with high emission intensity, without any correlation to the *pFF* level (bright spots in Fig. 79 a-c). The application of µ-ReB-EL and µ-PL measurements allowed a localization of these spots on the nm-scale. The µ-ReB-EL images were used as guide for SEM measurements in order to find these spots and perform SEM measurements of the local cross section after milling with a focused ion beam (FIB). The imaging results are presented in Fig. 80. The spot located with µ-ReB-EL shows a particle at the emission location in the SEM measurement. EDX analysis showed that this particle contains large amounts of aluminum. Local alloying of Al and silicon could create an overcompensation of the n-type emitter and create a locally highly doped p-type area around the particle. This Al alloying creates a pn-junction between two highly doped n- and p-type areas, which shows an early breakdown characteristic. The correlation of local Al contaminations with high intensity ReB-EL emission was previously published by Lausch et al. [117], who also showed that the appearance of these pre-breakdown spots show no correlation to decreased *pFF* values of Al-BSF solar cells.

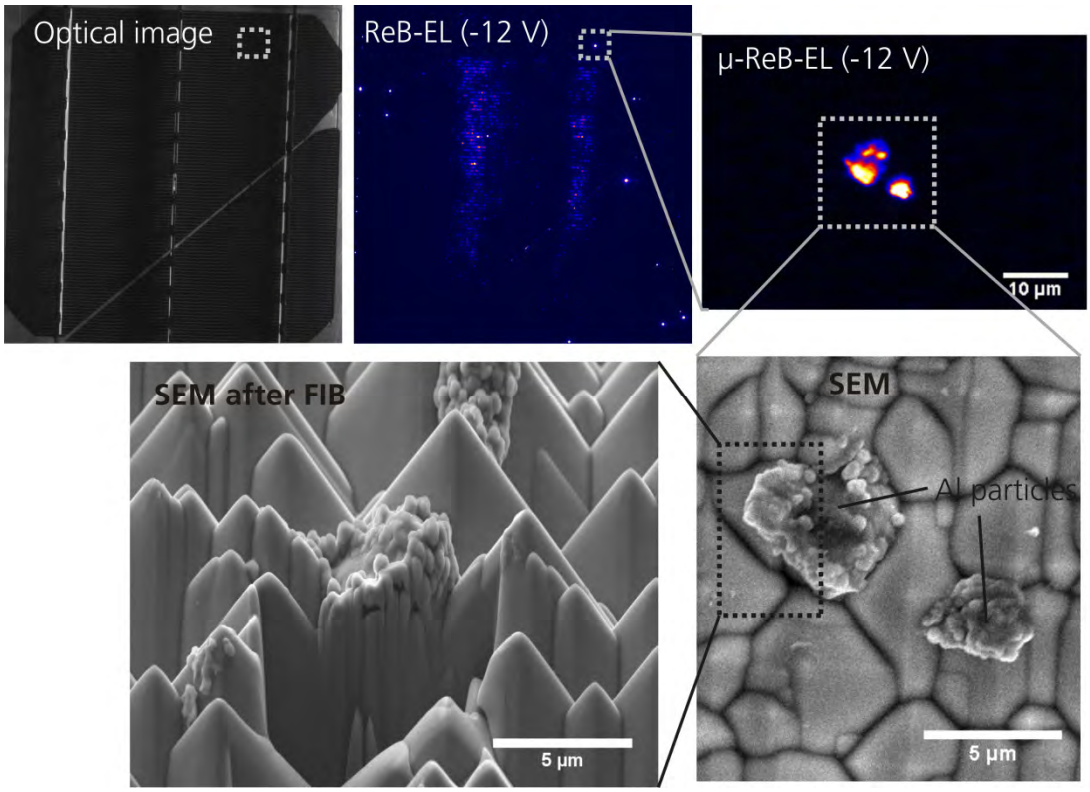

Fig. 80
Micro characterization of non-*pFF* correlated features due to Al particle contamination with high ReB-EL emission intensity by optical imaging (top left), ReB-EL (top center), µ-ReB-EL (top right), top view SEM (bottom right) and side view SEM (bottom left) under an angle of approximately 45° to the wafer surface of the same location after local cross section preparation by FIB of a LCP laser structured and Ni-Ag plated solar cell[20] of process group A (see Fig. 53).

Furthermore, the work of Lausch et al. showed that the in his investigation the Al particle contamination was present before SiN_x coating and rear side Al-screen printing. This shows that the contamination is not necessarily a result of the rear side Al-screen printing process but can also be induced by surface contaminations before the SiN_x passivation. The prepared local cross section by FIB also verifies that the Al is a contamination on the front side and is not coming from the rear side via micro cracks due to the screen printed Al paste.

pFF breakdown correlated features

In contrast to the Al particle realated ReB-EL features, the *pFF* breakdown related ReB-EL features such as the “J” feature in Fig. 80 only occurred in the presence of Ni and high annealing conditions. The ReB-EL measurements of Fig. 78 in the previous section already showed a spatial correlation to the laser opening structure. However, the limited resolution allowed no information if these features are located at the edge

[20] The solar cell features a crack in the downright corner visible in the optical image due to handling before characterization. The crack was not present during fabrication and is not process induced.

of the opening, within the opening or if these features correlate with the position of characteristic surface morphologies. µ-ReB-EL measurements were performed in order to analyze the exact location of the *pFF* breakdown related ReB-EL features in comparison to the laser structured areas. To avoid any shading effects during the µ-ReB-EL measurement the front side metal fingers were locally etched back in Piranha etch (H_2SO_4 : H_2O_2 : H_2O = 1:1:4). The Piranha etch showed in previous experiments by Andrew Mondon a selective etch effect on the plated Ni-Ag finger. The Piranha etch demonstrated for etching times of about 10 min no significant etching of the Ni silicide. The partly etched solar cell was then characterized by spatially corresponding optical microscope, µ-PL and µ-ReB-EL measurements. Fig. 81 illustrates the µ-localization procedure of the *pFF* breakdown correlated features. The lifetime related image of the µ-PL measurement can be used to locate the front side laser openings and relate the µ-ReB-EL signals to specific locations within the laser structured areas. Furthermore, the combination of these two measurements can be used as guide for the location of the *pFF* breakdown correlated features in the SEM measurements. The SEM allows a high resolution image of these areas and by focused ion beam preparation it is possible to analyze local cross sections of these areas. The spatial correspondence between the optical and electro-optical measurements could be ensured by relative coordinates of the structure of interest to characteristic shading structures visible in µ-PL (spatially correspondent to µ-ReB-EL) and electron beam induced current (EBIC) measurements (spatially correspondent to SEM). The shading structures were local particle contaminations of the sample, which appear as shaded structures in µ-PL and EBIC measurements. The detection method is described in more detail in [166].

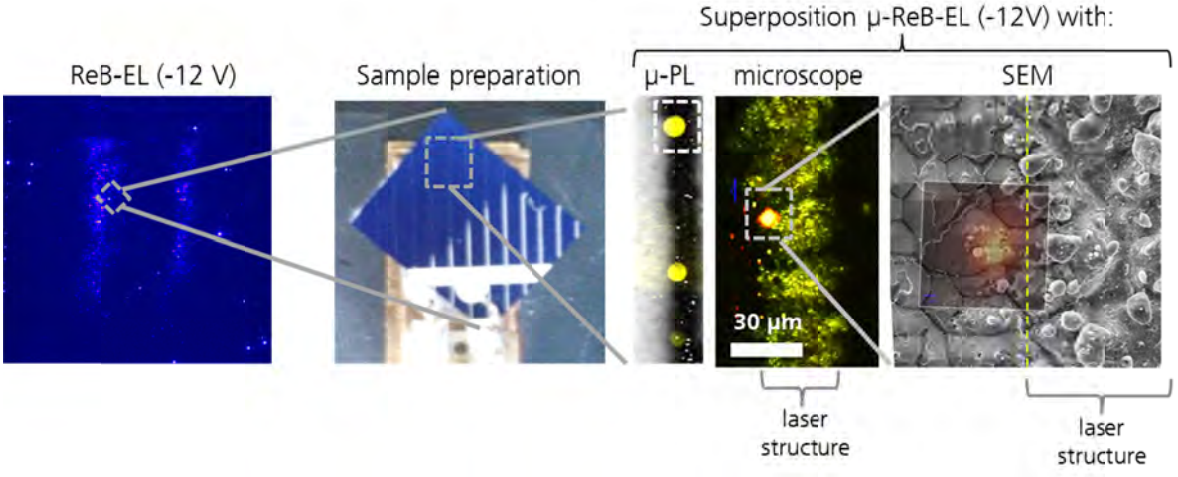

Fig. 81
µ-localization procedure of *pFF* breakdown correlated features on samples with partially etched back front side contacts.

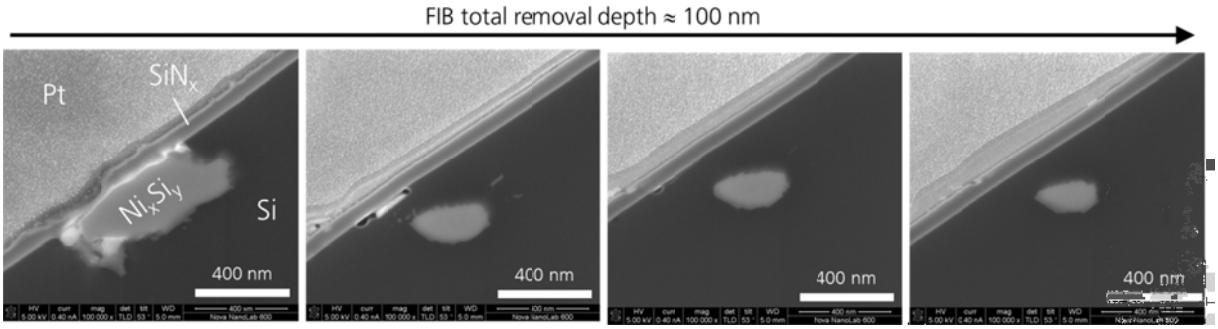

Fig. 82
SEM images at a cross section of a region with high ReB-EL intensities. The four images were taken at the same position after consecutive FIB cross section removals with a total removal depth of about 100 nm.

The top view SEM images at regions of high ReB-EL intensity revealed no characteristic structure, topography or contrast feature. Therefore, local cross sections were prepared by focused ion beam (FIB) in order to perform advanced SEM and transmission electron microscopy (TEM) measurements in this region. One FIB cross section of a region with high ReB-EL intensity was prepared by Horst Blumtritt and later on analyzed by TEM and STEM by Angelika Hähnel at the Max Planck Institute of Microstructure Physics Halle using a LCP-SE sample of group A (see Fig. 53) after the consecutive annealing row (see Fig. 72). The FIB preparation revealed in the region of interest two characteristic structures. The first structure was a locally deep Ni-silicide, which is shown in Fig. 82. The consecutive FIB removal revealed that the silicide structure shows a parallel growth to the surface with a dimension of about 100 nm along the cross section direction. It is most likely that the LCP-SE laser process created a cavity in this region, which was filled with Ni during the plating process and silicided during the annealing steps. The cavity starts in the left image of Fig. 82 where the SiNx layer is locally ablated and the Ni silicide is in contact with the local SiNx opening. The second structure was a micro crack, which was found nearby. The prepared cross section lamella with the micro crack is shown in Fig. 83. Nano-EDX measurements revealed that the crack was at some point filled with Ni, which is most likely also locally silicided during the annealing process.

Different publications [113-115] showed that defect rich structures in mc-Si such as metal precipitates can cause a similar DLIT and ReB-EL emission characteristic (type II) as shown in Fig. 78 in the previous section. The type II breakdown emission is a result of interband [167] or intraband [116] emission after a Zener tunneling or thermionic emission at a Schottky contact in reverse bias [168]. Therefore, the found defect structures (deep metal precipitate, micro crack) are assumed to be the origin of the *pFF* breakdown correlated features.

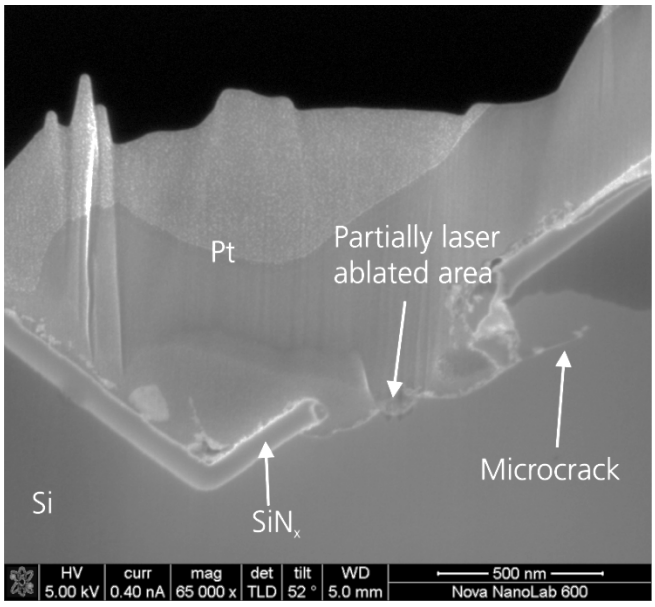

Fig. 83
Cross section lamella prepared by FIB, showing a micro crack at a locally LCP-SE processed area with high ReB-EL intensity.

6.4.2 Local pn-junction characteristic

The previous section showed that local defect structures such as deep Ni silicides or silicided micro cracks are the most likely origin of the *pFF* breakdown correlated features in the ReB-EL measurements. The impact of these structures becomes relevant if they reach the space charge region of the pn-junction and where they create local breakdown spots, which lead to the electrical degradation of the solar cell. However, the silicide induced non-linear shunting should be preventable by a large distance of the space charge region to the metalized surface due to a deep local diffusion underneath the front side contacts as in the case of a selective emitter design. Hence, the question arises why the LCP-SE solar cells in Fig. 72 do not show a significant better performance stability against annealing induced shunting in comparison to the homogenous emitter solar cells with UV ablated local contact openings. Therefore, the characterization of the local pn-junction of both cell designs becomes relevant in order to point out the weak spot of the fabricated selective emitter design.

There are only a few methods to characterize the local doping profile on a sub-µm level both in depth and lateral homogeneity. Two suitable methods for this problem are electron beam induced current (EBIC) [169, 170] and secondary electron dopant contrast imaging (SEMDCI) [171-173]. Both characterization techniques can be performed at cross sections or in top view with samples in a scanning electron microscope (SEM).

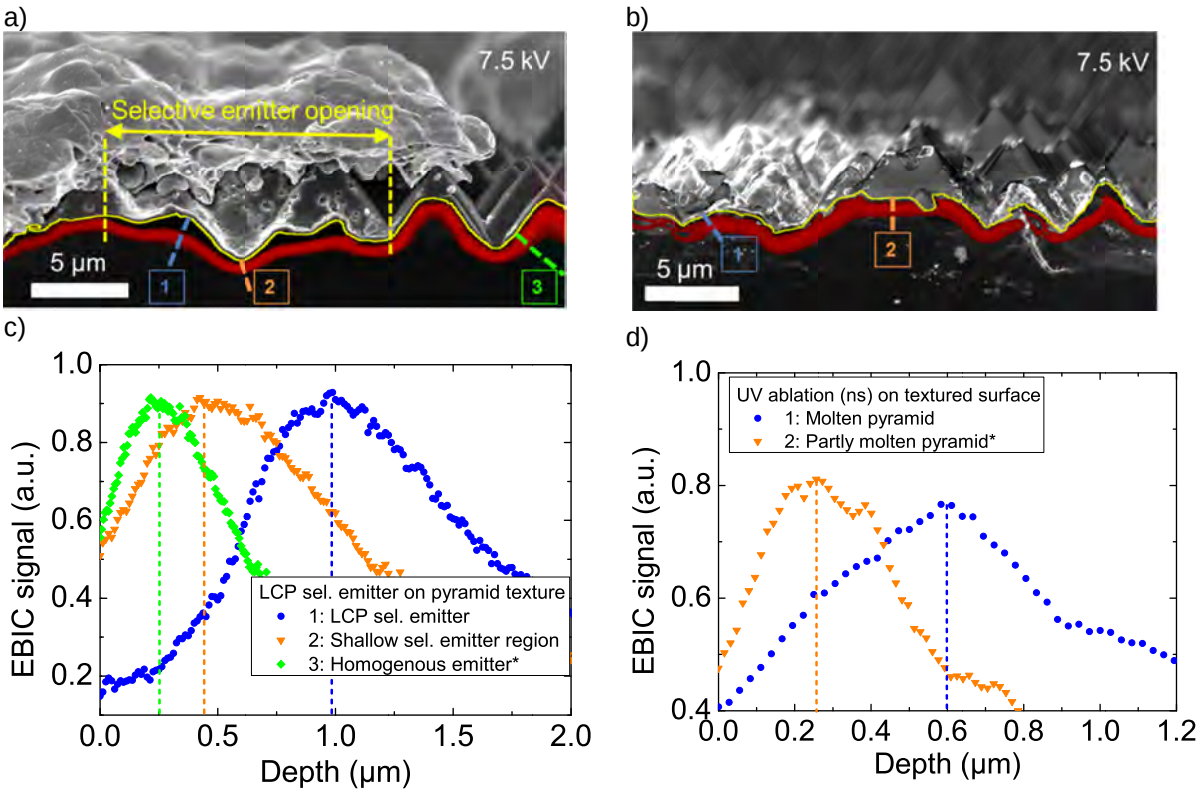

Fig. 84
Superposition of EBIC & SEM cross section measurements within a) LCP-SE and b) UV ablated front side openings on the processed solar cells. For better illustration the EBIC signal and the surface edge of the cross section are colorized red and yellow (solid line), respectively. The graphs show line scans on the marked positions (dashed lines) for the c) LCP SE and d) UV ablated solar cell. All data marked with * are corrected with a correction factor *cos(54.75°)* due to the angle of the cross section to the pyramid surface normal. [73]

EBIC is widely used in the field of semiconductors to analyze pn-junction profiles, local recombination parameters and charge collection probabilities (see [170] for a review of all applications).In this work EBIC is used to analyze local pn-junction inhomogeneities within the laser opened areas. EBIC was preferred to SEMDCI due to a better signal to noise ratio and lower requirements on the sample preparation for the fabricated n-type laser doped samples.

EBIC is based on the local current generation by the SEM electron beam and the imaging of the measured current response of the solar cell. Therefore, the EBIC image depends on local recombination parameters as well as local generation parameters. The measurable local EBIC signal $I(\vec{x})$ is in general given by a product of the locally generated current $I_{gen}(\vec{x})$ and the carrier collection probability $\varphi(\vec{x})$ of the minority carriers [174] within the local excitation volume $V(\vec{x})$ at the electron beam position $\vec{x}$ shown in Eq. (37).

$$I(\vec{x}) = \frac{1}{V(\vec{x})} \int_{V(\vec{x})} I_{gen}(\vec{r})\varphi(\vec{r})\, d\vec{r} \qquad (37)$$

The EBIC signal shows a maximum at the points of the highest carrier collection probability. Assuming a homogenous generation and a small excitation volume, the maximum is located at the pn-junction. However, there are different effects which move the EBIC signal away from the pn-junction location [175].

EBIC is mostly performed on planar samples due to the fact that the locally measured current is not only a function of the local collection probability but also of the local generation. Therefore, the EBIC image can be influenced by topographical features as well. This effect is discussed in the appendix. Furthermore, the signal can be influenced by local recombination inhomogeneities, SEM parameters and the sample preparation itself. Most of these effects such as enhanced recombination within the laser affected zone would move the EBIC maximum away from the metallurgical pn-junction into the high lifetime base region.

The discussed sample and measurement related influence factors make the quantitative interpretation of the measurement results more difficult for the characterized laser openings, which have a random melting topography. Therefore, the EBIC maximum depth within molten regions will only be interpreted as upper limit of the pn-junction depth. Fig. 84 shows EBIC measurements of cleaved cross sections of the laser openings from LCP SE and UV laser ablated solar cells. The data at pyramid topographies in Fig. 84 are corrected with a factor *cos(54.75°)*. This correction is caused by the fact that the measured depth at the cross section shows the doping depth under an angle of 54.75° to the normal of the pyramid surface. Therefore, the measured junction depth has to be corrected for the case of a pyramid texture by the known opening angle of the alkaline etched pyramids. All corrected data is marked in the figures.

The UV laser ablated solar cells show a corrected depth of the EBIC maximum in line scan 2 in Fig. 84 d) at around 200-350 nm, which is in the range of the applied thermal emitter diffusion recipe. Therefore, the EBIC maximum can be interpreted in this case as pn-junction location. The EBIC maximum in line scan 1 in Fig. 84 d) is located at a much deeper position at about 600 nm. The interpretation of this deeper location is not trivial and could be caused either by a drive-in of the emitter doping during the pyramid melting or as discussed above by uncertainties of the method itself. It has to be noted that the apparent shallow region right beside line scan 2 in Fig. 84 b) is most

likely caused by a surface change due to or after the cleavage of the sample. The SEM image in this region is hard to interpret but it looks like the measurement in this area is disturbed by a dust particle, a remaining SiN_x particle or a silicon breakout in this region. Therefore, this region was not taken into account in this study.

In the case of the LCP SE openings the interpretation of the EBIC data is much more difficult due to the melting induced change in topography. Assuming that most of the generation and recombination related effects on the EBIC signal cause a drift of the signal maximum into the substrate, the interpretation can only be limited on the estimation of an upper limit of the pn-junction depth. Therefore, the deeper EBIC maximum in line scan 1 (LCP-SE) in Fig. 84 correlates most likely to a deeper pn-junction due to the local laser doping but cannot be distinguished from other effects. In contrast to this deep EBIC maximum, line scan 2 (LCP-SE) shows a shallow EBIC maximum in the range of 400 nm, which is only slightly deeper than the depth measured for line scan 3 (LCP-SE) at a non-laser doped position, where the homogenous thermally diffused emitter is the only doping. Therefore, line scan 2 (LCP-SE) in Fig. 84 c) shows that there are shallow doped regions within the laser doped opening. These shallow regions could be the reason why even solar cells with selective emitter doping show annealing induced non-linear shunting effects for higher annealing temperatures.

In order to further analyze the doping inhomogeneities of the LCP SE process, EBIC test structures on planar samples were fabricated. The planar samples allow distinguishing between intrinsic doping inhomogeneities of the LCP process itself and inhomogeneities caused by the topography of the random pyramid texture. Fig. 85 shows EBIC measurements of LCP SE n-type laser doping on a planar p-type Si wafer with PECVD SiN_x passivation (without an additional thermally diffused emitter). In this case the doping profiles within the cross sections in Fig. 85 perpendicular b) and along a) the LCP doped line show homogenous depths of the EBIC maxima. In first approximation the EBIC maximum correlates for these samples with the location of the metallurgical pn-junction. Therefore, the measurements in Fig. 85 show that even a local laser intensity distribution due to multimode waveguide properties of the liquid jet does not necessarily cause an intrinsic doping depth inhomogeneity within the locally melted region. Furthermore, the analysis of a variety of samples with n-type LCP doping showed that for the relevant process parameter range in laser pulse energy, and spatial laser pulse distance the EBIC profile was in every case homogenous within the opening on planar samples.

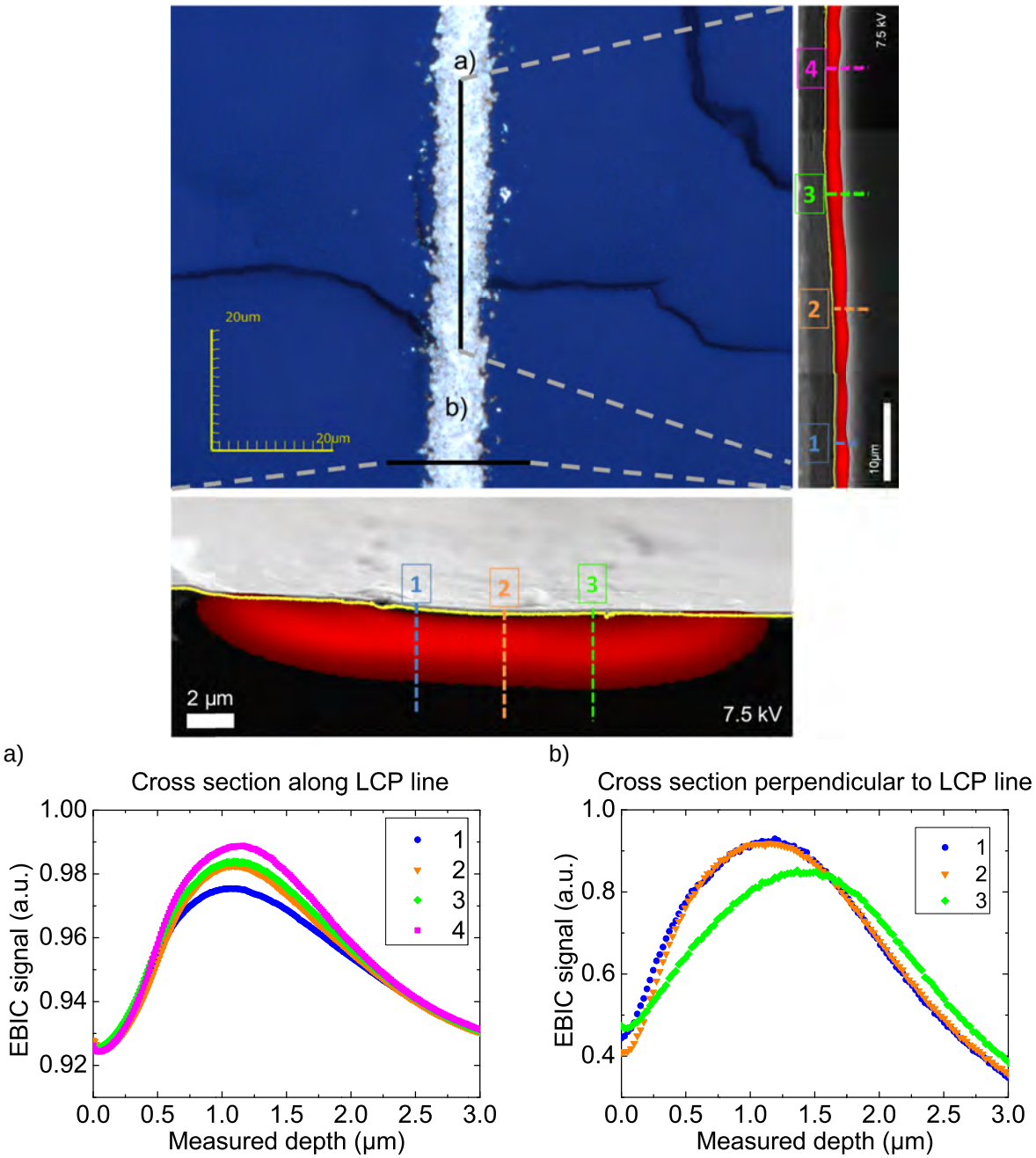

Fig. 85
Confocal microscope image and SEM+EBIC measurements at a cross section along and perpendicular to a LCP SE doped planar sample. For better illustration the EBIC signal and the surface edge of the cross section are colorized red and yellow (solid line), respectively. The graphs a) and b) show EBIC line scans on the marked positions.

Hence, the inhomogeneous doping profile in Fig. 84 seems to be a consequence of a detrimental impact of the pyramid textured topography on the laser process homogeneity. One possible explanation could be interference effects at the pyramid texture, which are already known for the case of UV laser ablation of passivation layers [176].

The microscopic characterization of the non-linear shunted solar cells showed that the annealing induced *pFF* breakdown comes along with the growth of local deep Ni silicides with a broad depth distribution. Furthermore, the local pn-junction profiling showed that the performed local phosphorus doping process by LCP showed an inhomogeneous depth distribution with local shallowly doped regions on a textured surface. These shallow regions could be one reason why the performed LCP-SE process could not prevent the annealing induced shunting. The next section will analyze the relevant process characteristics of local laser doped selective emitter regions in order to prevent annealing induced degradation of Ni plated solar cells.

6.5 Influence of doping and structuring process

The previous section showed that an insufficiently deep selective emitter doping process underneath the local contact openings lead to the same silicide induced shunting problematic as for the case of undoped UV laser ablated contact openings. There are different possible breakdown spots of the LCP locally doped contact openings, which are illustrated in Fig. 86. One possibility is an overall insufficient doping depth (see left schematic in Fig. 86). Alternative possibilities are the problem of shallowly doped regions at the edge of the opening (see center schematic in Fig. 86) or local shallowly doped regions caused by an inhomogeneous doping depth (see right schematic in Fig. 86).

The presented experiment in Fig. 87 aims to distinguish between the possible breakdown locations and find the dominant processing parameters of the local doping process in order to avoid any annealing induced performance limitations. The findings from this experiment should provide the key requirements of a suitable selective emitter doping process, which sets no limitations on the following plating and annealing processes, especially on the used temperature profiles. The presented results are a limited selection of a more detailed experiment performed in collaboration with a supervised master thesis of Wilhelm Hördt [96].

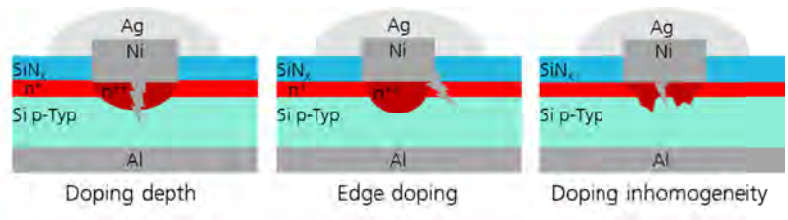

Fig. 86
Possible breakdown spots of locally doped LCP openings. Please note that for illustration reasons the texture was not included in the schematic.

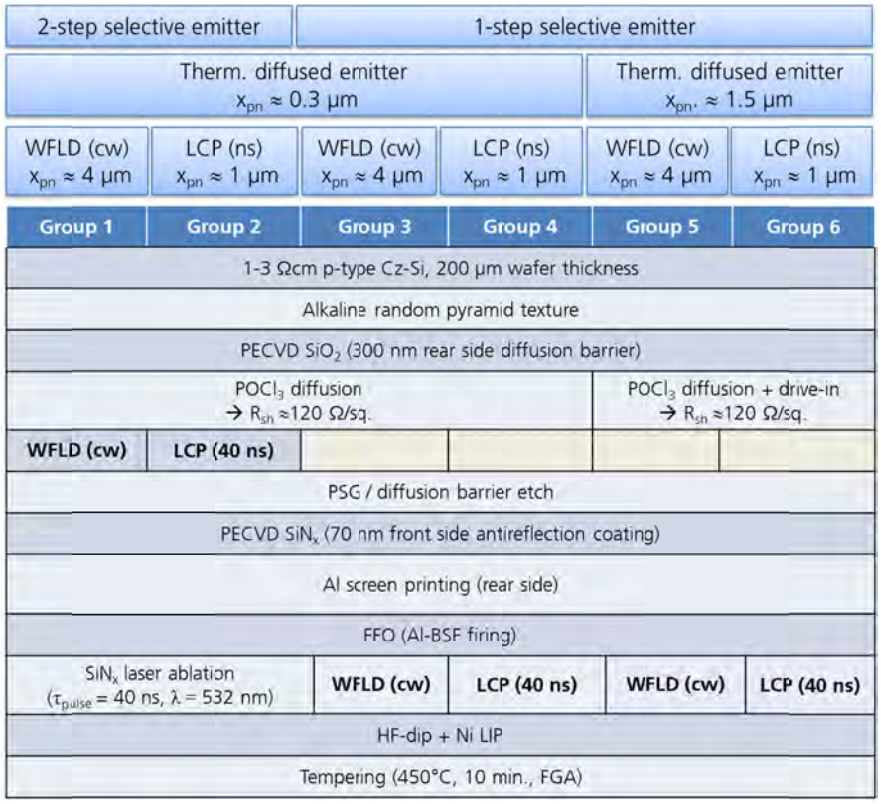

Fig. 87
Processing scheme of fabricated Al-BSF solar cells with 2-step and 1-step laser doped selective emitter processes and plated Ni front side contacts.

The experiment is split up in six different processing groups. All groups result in four 5x5cm² Al-BSF solar cells with Ni plated front side contacts on a large 156x156 mm² (pseudo square) p-type Cz-Si wafer. The wafer is textured with alkaline etched random pyramid structures. After the texturing the rear side is protected by a 300 nm PECVD SiO_x diffusion barrier in order to perform a one-side $POCl_3$ diffusion process aiming a 120 Ω/sq. homogenous emitter with a depth of about 0.3 µm or 1.5 µm for groups 1-4 and 5 & 6, respectively. At this point the wafer groups either get a 2 step selective emitter process (group 1 & 2) by LCP-SE or Wet Film Laser Doping (WFLD) or a 1-step selective emitter later on (group 3-6). The laser processes are described in more detail in the following paragraph. After the thermal diffusion -with or without a subsequent laser doping- the front side phosphorus silicate glass (PSG) and the rear side diffusion barrier are etched back and the front side is passivated with a PECVD SiN_x antireflection coating. The rear side is fully Al-screen printed with a subsequent FFO firing process. The front side contact openings are either performed by an undoped SiN_x laser ablation process (group 1& 2: λ = 532nm, 40 ns laser pulse length) or the open & dope LCP-SE or WFLD process.

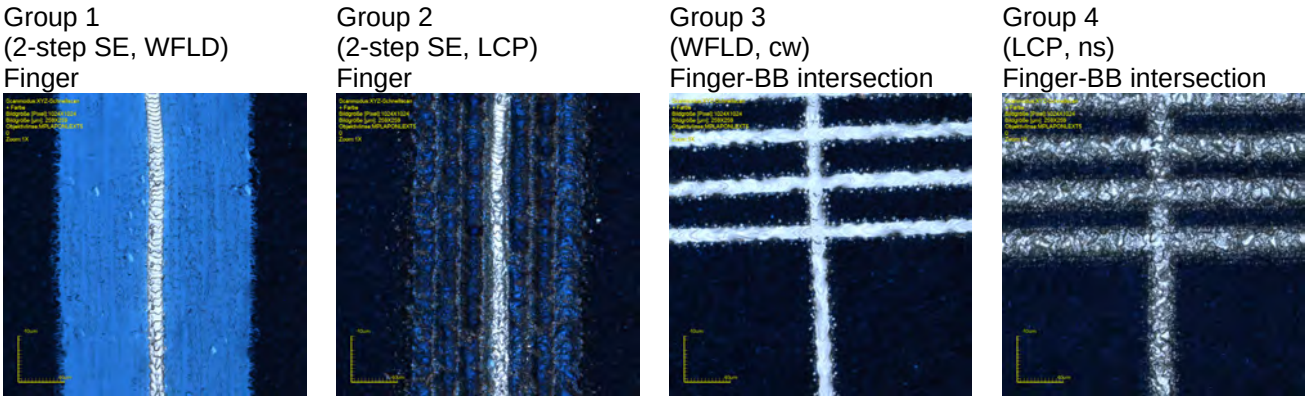

Fig. 88
Microscope images of the 2- and 1-step laser processed front side contact structures before Ni-plating

After the laser structuring the front side Ni contacts were plated in a light induced plating step (LIP) and annealed at 450°C for 10 min. in a forming gas atmosphere (FGA) with a delay between plating and annealing of maximum 10 min. The choice of the annealing conditions is a consequence of earlier experiments which showed on the one hand good adhesion of the plated and annealed contacts (Mondon et al. [100]) and on the other hand the solar cells annealed at this conditions showed a significant decrease in the *pFF*. Therefore, the high peak temperature sets the highest requirement on the local doping underneath the plated Ni contacts. Furthermore, these high annealing processes could be interesting for next generation cell designs such as PERC or PERL solar cells featuring laser structured rear side contacts such as laser fired contacts (LFC), which can be improved by a subsequent annealing process in this higher temperature regime. Therefore, these higher temperature profiles could also be interesting for Co-annealing of the front and rear side contacts for PERC/PERL solar cells with plated front side contacts.

Fig. 88 shows the comparison of the 1-step and 2-step selective emitter (SE) processed structures. The 2-step SE features a 140 µm wide doped finger structure, with locally contact opening of the SiN_x passivation performed by an undoped laser ablation process with an opening width of about 10 µm. The first local doping process in group 1 is a WFLD process developed by Christian Geisler using a spin-on film of 42.5% H_3PO_4 on the wafer and a subsequent laser doping by a galvanometric mirror scanner system, which guides a green (532 nm) continuous wave (cw) laser spot with a laser power of 15 W with a velocity of 5 m/s over the sample. The cw-WFLD process leads to a complete planarization of the doped area and deep pn-junction depths of about 4 µm as shown in Fig. 89. The LCP laser doping process for the 2-step SE used a 85% H_3PO_4 liquid jet, a stainless steel nozzle with 50 µm diameter and a green (532 nm)

pulsed (40 ns) laser system with a pulse energy of 40 µJ (before the optical head) and a spatial laser pulse distance of 1 µm, resulting in a shallow groove topography with a doping depth of about 1 µm. The solar cells of group 2 showed a significant amount of parasitic Ni-plating within the laser doped but not laser opened areas due to an increased pin hole density of the PECVD SiN_x in these areas. The 1-step selective emitter open and dope process by LCP (group 4 & 6) and WFLD (group 3 & 5) featured an opening width of 10-20 µm. The busbar (BB) structure was processed for the 1-step SE as non-overlapping line structure with a line distance of 40 µm and for the 2-step SE as overlapping lines for the doping process and non-overlapping lines with a line distance of 40 µm for the opening process.

Summarizing the features of the processing groups in order to allow the determination of the dominant breakdown location of the three possibilities shown in Fig. 86:

a. Laser doping depth: 1 µm (pulsed laser: LCP) vs. 4 µm (cw-laser: WFLD)

b. Decoupling of the local doping and opening process: 1-step SE vs. 2-step SE

c. Different thermally diffused emitter depths: 0.3 µm vs. 1.5 µm

The three processing schemes allow the analysis of the impact of different design parameters of the local laser doping on the annealing induced shunting risk. The two laser doping depths allow an analysis of the influence of the doping depth. The decoupling of the local doping and the local opening process allows the determination of possibly shallow doped regions in the edge area of the 1-step SE process. Finally, the application of two different thermally diffused emitter depths for the 1-step SE process should reveal if possible inhomogeneities of the local laser doping process can be compensated by a sufficiently deep thermally diffused emitter before the local laser doping.

The measured *pFF* by SunsV_{oc} of the fabricated solar cells of group 1-6 was after Ni plating (without annealing) in the range of 82-85% independently of the processing group. Fig. 90 presents the measured *pFF* after plating and annealing of the fabricated solar cells. It can be seen that the most dominant process parameter for the *pFF* stability is the used laser doping process. All groups featuring a deep local WFLD doping show a good *pFF* level of about 80% after the annealing. The LCP processed groups 2, 3 and 4 on the other hand, show a significant *pFF* decrease down to 40-55% after annealing.

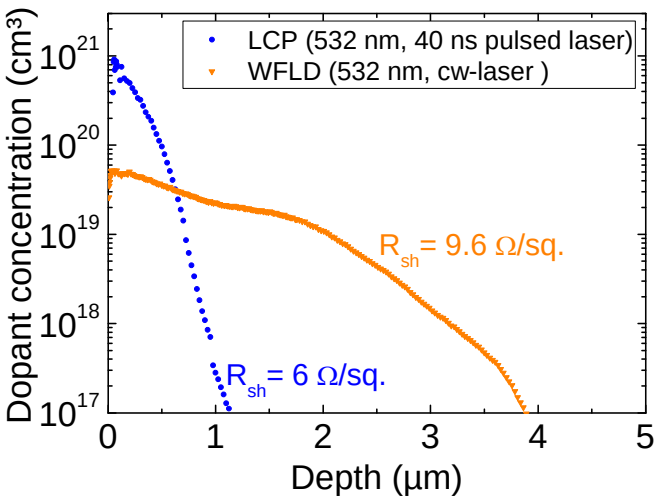

Fig. 89
Measured phosphorus concentration profile of a laser doped box of overlapping lines (same line distance as for the BB of the fabricated solar cells) by electrochemical capacitance voltage technique (ECV).

The previous sections showed that the *pFF* breakdown is most likely a consequence of Ni silicide growth into the space charge region. Therefore, it has to be analyzed if the *pFF*-stability of the WFLD processing groups is a consequence of a sufficiently deep laser doping or the absence of grown Ni silicides. In order to characterize the silicide growth within the laser opened areas, ion polished cross sections were prepared and analyzed by SEM measurements. Fig. 91 shows exemplary SEM measurements of silicide areas along the ion polished cross sections. The cross section analysis revealed different characteristics of the silicidation characteristic on the laser processed solar cells. The different contrast ratios within the silicide areas in Fig. 91 a) demonstrate that for the applied processing conditions the formation of different Ni-silicide phases takes place. Especially, for the applied annealing conditions of 450°C for 10 min. it is known from the literature [101, 103] that the formation of Ni_2Si and NiSi are the most likely silicide phases. The plated Ni layer on top of the laser structured regions acts as Ni source for the initial Ni_2Si formation, which leads later on to the transition to a silicon rich NiSi silicide. The NiSi formation starts at the silicide-silicon interface [103] and shows a reaction limited growth rate in contrast to a specimen diffusion limited growth rate of the Ni_2Si phase [101]. The lighter areas within the silicide region in Fig. 91 a) is assumed to be the Ni-rich Ni_2Si phase and the darker shaded area the Si-rich NiSi phase.

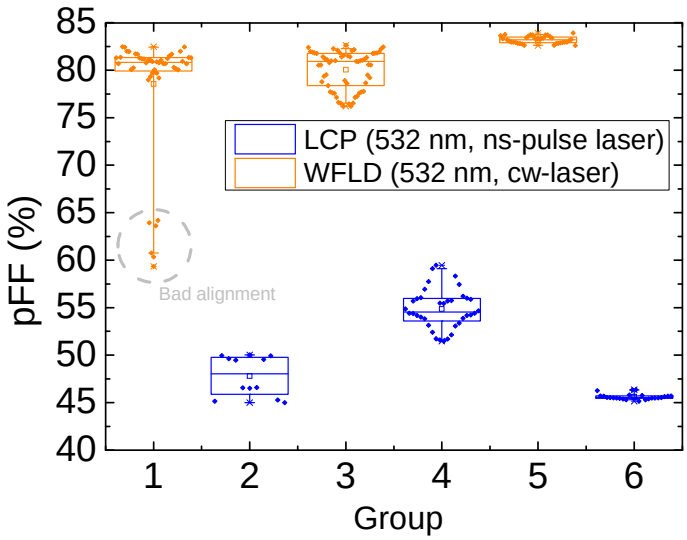

Fig. 90
Measured *pFF* after annealing for each processing group.

The cross section b) in Fig. 91 reveals that for thick Ni layers -as in the case for plating- the formation of the silicide can lead to a gap between the Ni-silicide and the remaining Ni layer. The formation of voids at the interface was already shown by Mondon et al. [100], who showed that the void formation can be detrimental for the adhesion of plated metal contacts. The void formation could be avoided either by a full consumption of the Ni layer during silicidation or an etch back of the remaining Ni after silicidation in combination with subsequent Ni/Cu/Ag plating steps after the etch back.

The applied LCP process for the initial laser doping of the 2-step SE of group 2 featured rather high laser pulse energies. Therefore, the cross sections in Fig. 91 c) and d) revealed some cavity or micro crack structures either due to Si melt flow during the process or micro crack formation during the cool down. Especially, the cross section in c) shows a deep cavity structure with an almost homogenous silicide growth along the edge. This enhanced silicide growth at defect rich silicon interfaces is already known in the literature [177-179] and leads to unintentionally local deep Ni-silicide penetration in MOS devices. These silicide induced breakdowns are called Ni encroachment effects and could be correlated to the growth of deep NiSi spikes especially at defect rich interfaces [177]. However, in the case of d) it is at this stage not evident if the high crack density in the silicide area was present before silicidation or if it is a consequence of crack formation due to different heat expansion coefficients of Si and Ni-silicide during the cool down after annealing.

a) Different silicide phases
Group 1: 2-step SE, WFLD (cw)

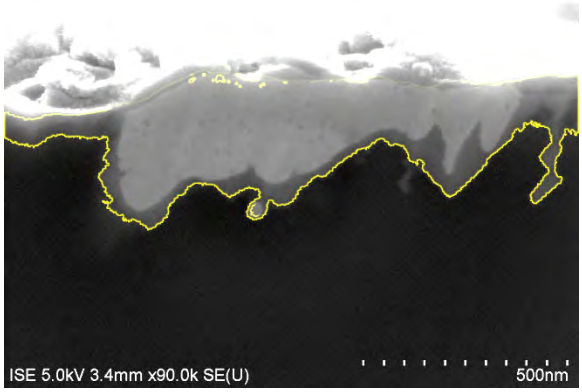

b) Gap between silicide areas and remaining Ni metal
Group 2: 2-step SE, LCP (ns)

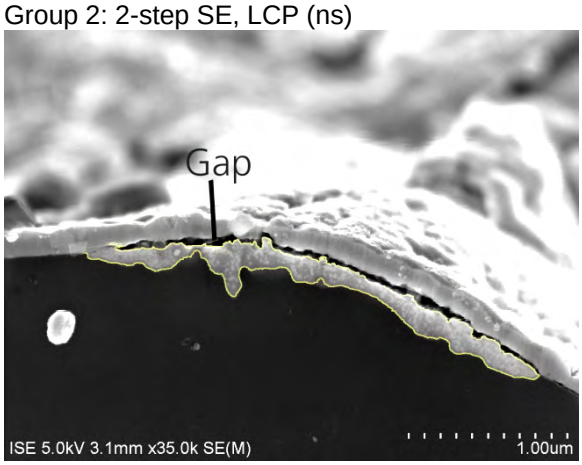

c) Enhanced silicidation along micro cracks
Group 2: 2-step SE, LCP (ns)

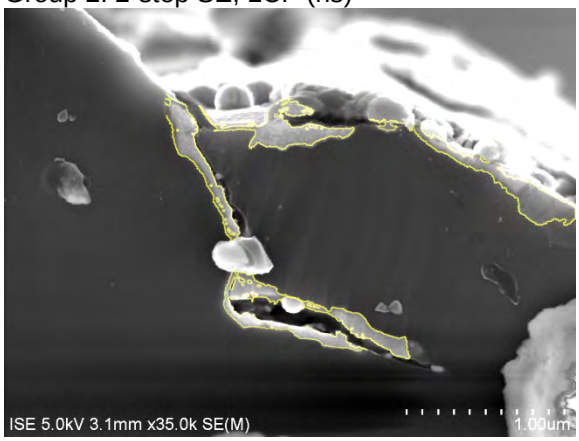

d) Micro cracks in silicide region
Group 2: 2-step SE, LCP (ns)

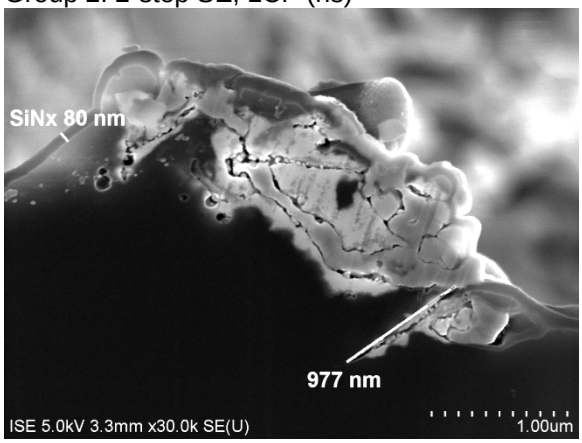

e) Low silicide growth for 1-step WFLD SE
Group 3: 1-step SE, WFLD (cw)

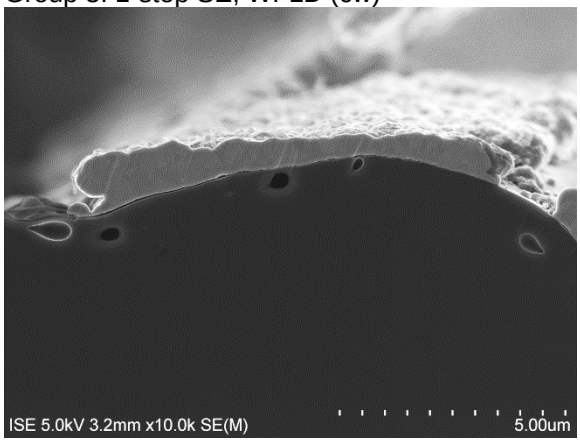

f) Shallow silicidation for 1-step WFLD SE
Group 3: 1-step SE, WFLD (cw)

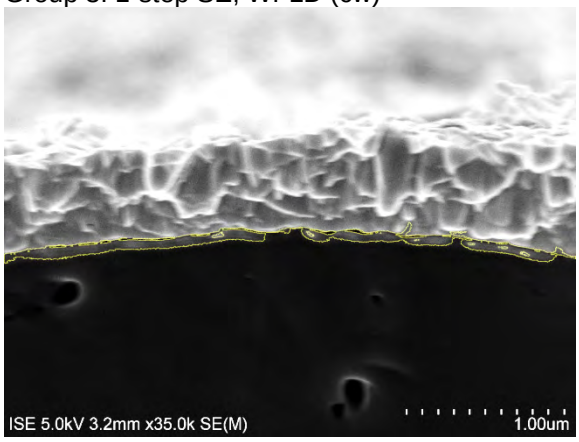

Fig. 91
Exemplary SEM measurements of ion polished cross sections within the laser opened front side contact structures of the different processing groups. For better illustration the silicide areas in a), b), d) and e) have yellow contour lines. Please note the different image scales.

In contrast to the other groups the 1-step SE group with the cw-WLFD process showed a significantly reduced amount of Ni silicide regions (Fig. 91 e)). Furthermore, the

silicide depths appeared to be much shallower as shown in Fig. 91 f). The shallower silicide depths must not be necessarily a problem in terms of adhesion but this finding shows that may be interface oxide layers prevent or reduce the Ni silicide growth for the applied laser– pretreatment – plating – annealing process sequence.

In summary the analyzed samples of group 1, 2, 4 and 6 showed a large amount of Ni silicide regions within the laser opened areas. Independently of the laser doping process all 2-step SE samples showed different silicide phases with a broad depth distribution. Local silicide depths of up to 1 µm could be observed. The presence of Ni-silicide for the *pFF* stable group 1 and the pFF instable group 6 shows that a pn-junction depth of more than 1.5 µm and not more than 4 µm is sufficient to provide a *pFF* performance stability even for high annealing processes. In this context, the combination of the 1 µm LCP doping depth with the 1.5 µm thermally diffused emitter in group 6 shows that 1.5 µm doping depth is not sufficient to provide *pFF* stability if a high annealing process is implemented in the processing chain.

Within group 1 there are some cells, which showed a decrease in the *pFF* even with a deep 2-step SE by WFLD (cw). However, the combination of confocal microscope and ReB-EL measurements revealed that the laser doped areas and the SiN_x opening by pulsed laser ablation showed a bad alignment for these cells (see Fig. 92). This lead to a high amount of finger structures where the laser openings are located besides the laser doped areas on the shallow thermally diffused emitter. These fingers are visible as bright structure in the ReB-EL image in Fig. 92. The laser structured areas also appear as breakdown spots in the ReB-EL measurements of the LCP laser doped solar cells of group 2 (2-step SE) and 4&6 (1-step SE).

µ-ReB-EL measurements shown in Fig. 93 confirmed that the laser structured areas are the origins of the ReB-EL luminescence. Beside the local breakdown spots along the laser opened line, there are also local breakdown spots outside of the laser opening but within the laser doped area. This can be explained by significant parasitic plating in the laser doped areas for all LCP doped samples. The strong topography after the applied LCP process leads to high pin hole densities of the PECVD SiN_x layer in these areas.

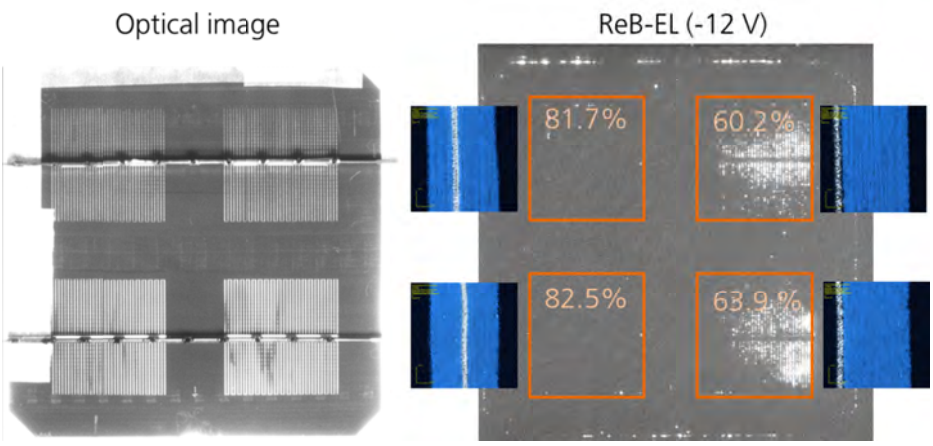

Fig. 92
Optical and ReB-EL image of a wafer with four 5x5 cm² solar cells from group 1 processed with a 2-step SE by WFLD (cw) after Ni plating and annealing. The orange box in the right image marks the solar cell edges, the number in the box gives the according measured *pFF* and the image on the side is a corresponding microscope image of an exemplary WFLD laser doped and ns-pulse laser opened finger structure.

One additional aspect of the ReB-EL emission at parasitic plated regions is the fact that regions outside of the laser doped areas with large amounts of parasitic plating do not show significant ReB-EL emission in this experiment. One example is the horizontal structure in form of a dashed line below the lower two cells in the optical image of Fig. 92. Handling induced SiN_x damages/openings induces a large amount of parasitic plating in these areas. However, the ReB-EL image does not show any significant emission in this region. The experience from different experiments shows that parasitic plating does not necessarily lead to annealing induced shunting in these regions but indeed some parasitic plated regions do show silicide structures. An exemplary parasitic plating induced silicide structure is shown in the SEM cross section analysis of Fig. 94. One possible explanation for the sensitivity of annealing induced shunting in parasitic plated areas might be that on the one hand the opening geometry of the SiN_x in these regions. Small pin hole shaped SiN_x openings could lead to low amounts of Ni at the interface and only shallow silicidation. On the other hand large SiN_x damaging such as scratches could not only lead to a large SiN_x opening in this region but also to damaged peaks at the pyramid textures and thus, to open pn junctions at the damaged surfaces.

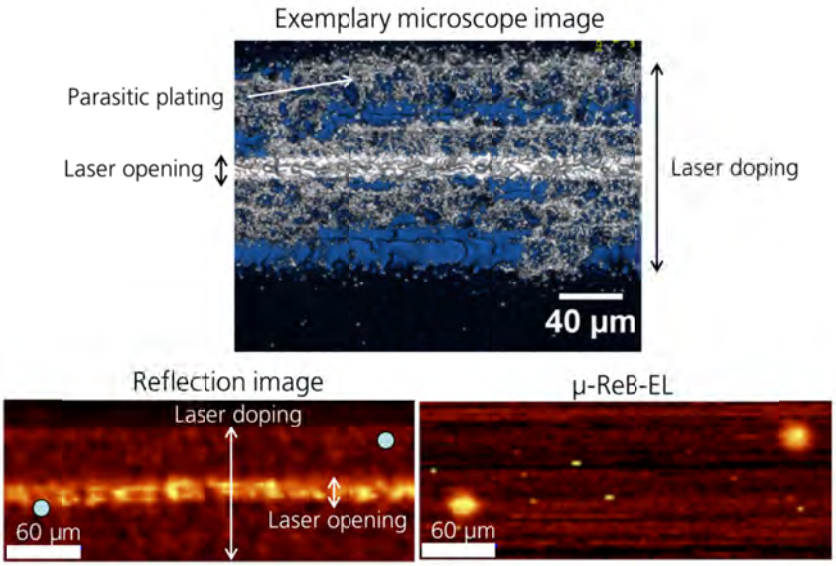

Fig. 93
Spatially corresponding optical (laser reflection) and µ-ReB-EL image of wafer 4001 of group 2 with a 2-step SE by LCP laser doping and an exemplary microscope image at another position. The breakdown spots of the µ-ReB-EL measurement are marked in the reflection image as grey circles.

In conclusion the results of the experiment shown in Fig. 87 led to three findings in the analysis of annealing induced non-linear shunting of Ni plated solar cells. First of all the most dominant cell design parameter on the *pFF* performance stability, especially for high annealing processes, is the pn-junction depth at the contact opening. The applied annealing process of 450°C for 10 min. in FGA induced even on solar cells with a thermally diffused emitter depth of 1.5 µm a significant *pFF* performance breakdown. The required pn-junction depth to assure a performance stability for the applied annealing process is somewhere in between 1.5 and 4 µm. The WFLD laser doped solar cells with a pn-junction depth of 4 µm were the only solar cells, which showed significant *pFF* stability independent of the thermally diffused pn-junction depth. In this context especially the 2-step WFLD SE proved to assure *pFF* stability in combination with a large amount of Ni silicide structures. The second finding of this experiment was the correlation of silicide growth and local defect structures in silicon, such as micro cracks. The laser processed regions with Ni silicide showed partially micro cracks, which either enhanced the silicide growth due to Ni encroachment or are generated during the cool down due to thermally expansion induced stress in the Ni – Ni silicide – silicon system. The last finding results under the assumption that ReB-EL emission reflects the origins of *pFF* breakdown regions; the ReB-EL measurements of the fabricated solar cells with large amounts of parasitic plating revealed that parasitic plated structures can be regions of local breakdowns but not necessarily.

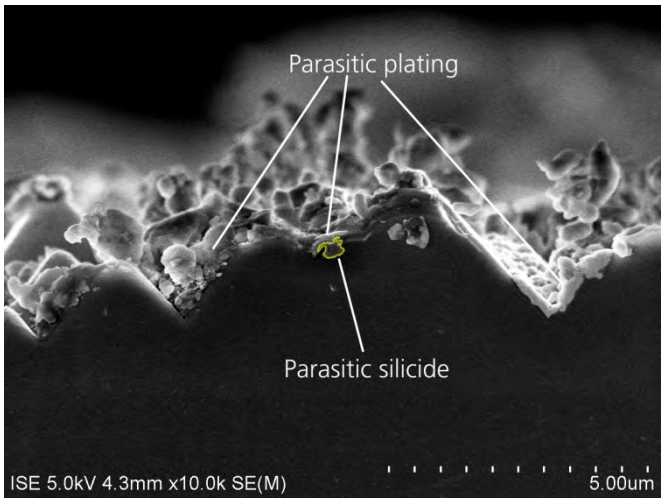

Fig. 94
Ion polished cross section at a parasitic plated area after annealing at 450°C for 10 min. in a forming gas atmosphere. For better illustration the silicide area has a yellow contour line.

6.6 Conclusion

The experiments in chapter 6 focused on the analysis of annealing induced non-linear shunting of Ni plated silicon solar cells. In this context three different aspects were analyzed: the change of the global electrical characteristics of the solar cells before and after annealing, the local characteristics in different imaging characterization techniques and the micro-structure of the localized breakdown spots.

The performed experiment showed that the combination of Ni plated front side contacts and a subsequent annealing process in the range of 300-450°C in forming gas or N_2 atmospheres leads to a degradation of the electrical performance of the solar cells. The contact annealing of the solar cells resulted in a deviation of the current-voltage characteristic from the conventional two diode model. The annealed solar cells showed a “hump” feature in the mid-voltage regime of 200-400 mV, which was visible as increased recombination current in the dark IV curve and the pseudo dark IV curve measured by SunsV_{oc}. This effect decreased the pseudo fill factor *pFF* and in consequence the solar cell efficiency, too. The electrical characteristic of this annealing induced degradation showed some similarities to a shunt phenomenon. However, the shunt revealed in this case a non-linear or non-ohmic electrical characteristic. The appearance of the annealing induced *pFF* breakdowns due to non-linear shunting correlated with a decrease of the internal series resistance R_s-$R_{s,front}$ and a decrease of the reverse breakdown voltage.

The application of different imaging characterization techniques in order to characterize the non-linear shunting effect reveals the appearance of characteristic local features correlating with annealing induced *pFF* breakdowns. The main finding

of the local imaging characterization was the correlation of recombination active structures in DLIT measurements under forward bias and the appearance of the same local features in reverse biased DLIT as well as reverse biased electroluminescence (ReB-EL). The application of ReB-EL under reverse voltages in the range of -6 to -15 V proved to be the most suitable characterization technique in terms of sensitivity of annealing induced local breakdown spots and spatial resolution. The high spatial resolution compared to DLIT allowed a localization of the annealing induced *pFF* breakdown features along the laser structured front side contact openings. The ReB-EL (as well as the DLIT) signal intensity-voltage characteristic shows many similarities to type-II breakdowns known from the characterization of multi crystalline silicon solar cells in the literature. Kwapil [114], Kasemann [109] and Bothe et al. [115] showed that the physical origin of type-II ReB-EL emission is due to internal field emission with trap-assisted tunneling or trap-assisted avalanche breakdowns, which show a strong correlation with defect rich areas with high recombination activity, such as metal precipitates.

The application of a sequence of ReB-EL, µ-ReB-EL, µ-Pl, SEM, FIB and TEM characterizations allowed a localization and characterization of the annealing induced *pFF* breakdown features on a µm- and nm-scale. The characterized cross section lamella of a region of intensive breakdown illumination revealed two characteristic structures. One side of the cross section showed a deep silicide structure which had a depth of about 200-300 nm and a dimension of at least 100 nm parallel to the textured surface. This deep silicide structure introduces a region of high recombination activity into the emitter and could possibly penetrate the space charge region of the pn-junction. The other facet of the cross section lamella exposed a micro crack within the emitter region. Both structures are regions of high recombination activity and could both explain the electrical degradation as well as the early breakdown illumination. However, the close proximity of both structures allowed no distinction between their position and the location of the breakdown emission in the µ-EL measurement.

EBIC characterizations at cross sections of locally LCP-SE laser doped contact openings demonstrated that the applied laser doping parameters resulted in an inhomogeneous doping depth within the contact opening on a textured surface. The analyzed cross section revealed locally shallow doping depth within the LCP-SE laser doped contact opening. These locally shallow doping depths are the most likely explanation why the additional laser doping did not prevent the electrical degradation

due to the detrimental impact of highly recombinative structures such as cracks or deep Ni silicides.

The introduction of a homogenously deep laser doping underneath the front side contact openings by a 2-step or 1-step laser doping process proved to ensure a *pFF* stability even for annealing processes with high peak temperature (450°C) and long plateau durations (10 min.). The performed experiment showed that for the applied laser opening and annealing processes even a pn-junction depth of 1.5 µm at the contact opening of the Ni plated contact is not sufficient to prevent a *pFF* breakdown. However, the application of a 1-step or 2 step local laser doping process with a depth of about 4 µm demonstrated *pFF* stability even in the presence of a high Ni silicide growth rate.

In conclusion the three stated hypotheses of section 6.2 where experimentally confirmed and showed that the main reason of the electrical degradation of Ni plated solar cells after an annealing step is the formation of locally deep Ni silicides, which partly correlate with local defect structures. Furthermore, the main aspect to prevent the silicide induced *pFF* breakdown is a locally deep doping underneath the contact openings. The required doping depth is mostly influenced by the applied annealing process but also by other aspects such as the time between plating and annealing due to the possible growth of interface oxides at the contact opening. Therefore, the findings of this chapter demonstrate that the application of a selective emitter design for silicon solar cells with Ni-Cu-Ag or Ni-Ag plated contacts is not necessarily beneficial in terms of maximum cell efficiency but enables a significant degree of freedom for the development of silicidation process sequences for performance stable silicon solar cells.

7 Summary and outlook

7.1 Summary

The aim of this work was the development and characterization of industrially feasible low-cost structuring and doping processes for high efficiency silicon solar cell designs. The main focus was the development and integration of laser chemical processes (LCP) for silicon solar cells. Furthermore, the fabricated solar cells were characterized and advanced loss analyses were performed in order to determine relevant process influences on the solar cell efficiency. LCP was applied for the fabrication of local boron doping structures as local back surface field (LBSF) for p-type silicon solar cells (chapter 3). The second application area of LCP was the fabrication of locally phosphorus doped structures for selective emitter designs with plated metal contacts. In this context, the LCP highly doped regions underneath the plated contacts were evaluated by solar cells simulations (chapter 4), solar cell fabrication (chapter 5) and solar cell characterization (chapter 6).

LCP local boron doping process

Laser chemical processing (LCP) is based on the idea to couple a laser spot into a liquid jet, which allows local laser structuring of thin layer systems (i.e. passivation layers of solar cells) in combination with local laser doping using the liquid jet as dopant source. Therefore, the development of a LCP local boron doping process requires a suitable liquid boron doping source. After a screening of potential liquids the most promising liquid boron source was an aqueous solution of 4.4 M $NaBH_4$ in 14 M NaOH. The prepared test structures revealed a high amount of boron in the laser doped areas with a surface doping concentration of up to 10^{20} cm^{-3} and doping depths in the range of 1 µm. This local boron laser doping process was successfully implemented as p-type LBSF into a fabrication scheme of a high efficiency silicon solar cell. The first proof of concept in a passivated emitter an rear locally diffused solar cell design (PERL) resulted in a cell efficiency of 20.9% using FZ-Si wafers with a base resistivity of 0.5 Ωcm. The published results [119, 120] developed within this thesis were at the time of publication the first successful examples for the implementation of an industrially feasible laser doped boron LBSF structure in a high efficiency silicon solar cell.

After the successful proof-of-concept the boron LCP process was further evaluated by fabricating LBSF structures for PERL solar cells with varying base resistivities. The LCP-PERL solar cells were compared to similar cells with a doping free LCP structuring process for the rear side openings and solar cells with a well-optimized

LFC LBSF process. The increase of the base resistivity (ρ_{Base} = 0.5 – 9 Ωcm) correlated for the LCP-PERL and LCP-PERC solar cells with a cell efficiency decrease. The application of electrical, electro-optical and optical characterization techniques in combination with analytical and numerical simulations was used in order to identify the limiting loss mechanisms in the fabricated solar cells.

The cell efficiency limitation of the LCP-PERL solar cells was caused by a decrease in the open circuit voltage for increasing base resistivities. The loss analysis allowed the elimination of possible explanations for the V_{oc} losses such as local Schottky contacts due to non-homogenously doped contact openings. The simulation and measurement results indicate that the most likely explanation is a laser processing induced local lifetime reduction around the LBSF structures. The local lifetime reduction is most likely a consequence of laser induced damage during the laser doping process due to non-optimized processing parameters.

Besides the V_{oc} limitation the LCP-PERL solar cells demonstrated slightly lower fill factors than the LFC reference solar cells. However, the series resistance analysis revealed that the FF limitation of the LCP-PERL solar cells was not a result of large contact resistances but of slightly larger spreading resistances. The increased spreading resistance of the LCP solar cells resulted from a slight disadvantage of the line contact design of the LCP-PERL solar cells compared to the point contact design of the LFC reference solar cells for same contact fractions. However, the series resistance analysis showed that the main cell efficiency limitation of the LCP-PERL solar cells is neither induced due to high spreading resistance nor an increased contact resistance as in the case of the LCP-PERC solar cells. The low series resistances of the LCP-PERL solar cells proofed that the formation of an ohmic rear side contact by the LCP boron doping was successful.

In conclusion the developed LCP boron doping process could be successfully implemented in high efficiency p-type PERL solar cells resulting in ohmic contact properties at the LBSF contact. The advanced loss analysis revealed a recombination induced limitation of the open circuit voltage due to increased recombination around the laser doped areas. Therefore, further process optimizations are necessary at this stage in order to improve the recombination properties of the developed boron LCP laser doping process.

Theoretical considerations on selective emitter solar cells

The starting point for the development of a LCP phosphorus doping process for selective emitter designs with plated metal contacts was a 2D numerical solar cell

simulation in order to analyze the influence of the selective emitter design on the electrical performance. The performed simulations evaluated the impact and the critical design parameters of an additional highly doped region underneath the emitter metal contacts. The focus was the analysis of two main aspects of the highly doped region of the selective emitter design: the influence of possible contact resistivity and saturation current density improvements on the cell efficiency. In this context four different solar cell designs were simulated. The results revealed a strong dependency of possible cell efficiency improvements due to a selective emitter on the overall solar cell design.

The modeling of the emitter contact resistivity revealed that beside the theoretical improvement of ρ_{cont} for high doping concentrations, the metallization scheme itself strongly influences the emitter contact resistance. Screen printed Ag contacts show in this context a significantly higher sensitivity on the doping concentration than plated Ni contacts. The solar cell simulations demonstrated that in the case of state-of-the-art metal finger widths the emitter contact resistivity becomes a limiting factor if $\rho_{cont} >> 10^{-3}\,\Omega\text{cm}^2$. Therefore, an additional highly doped region only becomes beneficial for the total series resistance if the contact resistivity of the applied metallization scheme on a homogenous emitter design would be much larger than this value.

The saturation current density (J_{01}) analysis of a selective emitter design aimed to quantify the cell efficiency improvements due to a highly doped region underneath the emitter metal contacts. The simulation results demonstrated the strong correlation of possible cell efficiency benefits due to a selective emitter and the overall solar cell design. The improvement of $J_{01,cont}$ due to a highly doped region underneath the metal contacts has rather small impact on the cell efficiency assuming state-of-the-art Al-BSF solar cells. Only for large contact widths or for cell designs aiming for cell efficiencies $\eta > 21\%$ with lowly doped emitter profiles, the introduction of an additional high doping profile in the contact area becomes significantly beneficial.

The simulation results demonstrated that under the constraints of industrial feasibility the interaction between the cell design, the metallization scheme, the thermally diffused homogenous emitter and the applied selective emitter process decides whether or not the introduction of a selective emitter is beneficial in terms of maximum cell efficiency. Regarding state-of-the-art processing technologies, it is in many cases more beneficial to reduce the contact width (e.g. plated Ni-Cu contacts) and improve the homogenous emitter diffusion (e.g. lowly doped emitter profile) than introducing a

selective emitter by highly doped regions underneath the contacts. The introduction of a selective emitter design is in industrially feasible cell designs mostly beneficial at the point when the applied metallization scheme limits the cell efficiency due to large ρ_{cont} or if the highly doped region prevents shunting related cell efficiency limitations. LCP selective emitter doping for plated Si solar cells

The experiment described in chapter 5 aimed to develop an evolutionary improvement of the Al-BSF solar cell design. In this context three cell design improvements were analyzed: the introduction of a lowly doped thermally diffused homogenous emitter, narrow Ni-Ag or Ni-Cu-Ag plated front side contacts and the introduction of a selective emitter design by an additional highly doped contact opening by LCP-SE. The fabricated solar cells showed a significant cell efficiency benefit compared to a fully screen printed reference group and reached maximum cell efficiencies of up to 19%.

The introduction of the lightly doped emitter proved to be beneficial in terms of short circuit current density J_{sc} and open circuit voltage V_{oc} improvements. The J_{sc} improvement is caused by better quantum efficiencies in the lower wavelength regime due to decreased Auger recombination. Furthermore, the better recombination properties of the lightly doped emitter lead to a lower saturation current density in the passivated regions $J_{01,pas}$, resulting in higher V_{oc}.

The introduction of Ni plated front side contacts allowed the introduction of the lightly doped emitter in the first place due to a low contact resistivity even for reduced surface doping densities. The *FF* analysis indicated that cells with low *FF* were mostly limited by contact resistance losses due to small contact opening widths or in the case of LCP-SE processing before FFO firing, by interface insulating layers. The series resistance analysis also indicates that the contact resistance becomes very low in the case of successful silicidation of the Ni-Si interface during an annealing step. Furthermore, the narrow finger widths of the plated contacts result in an increased J_{sc} due to lower front side contact shading compared to the fabricated screen printed Ag contacts.

The introduction of the selective emitter did not show any significant improvement in terms of maximum cell efficiency. This finding is in agreement with the simulation results of chapter 4. The cases of significant improvements in V_{oc} or R_s of the LCP-SE solar cells could be explained by mostly contact geometry related effects. The low impact of a selective emitter on the cell efficiency is caused by a low sensitivity of the Al-BSF design on contact recombination improvements. Furthermore, the contact

resistivity improvement was for plated Ni contact negligible because the applied thermally diffused emitter already featured a rather high surface doping concentration of about $2 \cdot 10^{20}$ cm^{-3}. In contrast to screen printed contacts, which react very sensitive on surface doping reductions, plated Ni contacts are not limited by high contact resistivities in this regime. The contact resistivity becomes even less problematic after the silicidation of the Ni-Si interface.

The fabricated solar cells with plated Ni-Ag or Ni-Cu-Ag front side contacts showed a correlation between the measured pseudo fill factor *pFF* and the internal series resistance R_s-$R_{s,front}$. This finding supported the hypothesis that the contact interface features for some cells still insulating layers, which improves the V_{oc} and the *pFF* of the solar cell but also increases the contact resistance. The solar cells in this experiment faced the problem that the improvement of the contact resistance due to annealing induced silicidation came along with a reduced *pFF* most likely caused by silicidation induced shunting in the space charge region.

Annealing induced non-linear shunting of Ni plated solar cells

The experiments in chapter 6 focused on the analysis of annealing induced non-linear shunting of Ni plated silicon solar cells. Annealing processes become relevant for Ni plated solar cells in order to increase the contact adhesion by the formation of a Ni-silicide at the contact interface. The annealing induced non-linear shunts were analyzed under three different aspects: the change of the global electrical characteristics of the solar cells before and after annealing, the local characteristics in different imaging characterization techniques and the micro-structure of the localized breakdown spots.

The performed experiment showed that the combination of Ni plated front side contacts and a subsequent annealing process in the range of 300-450°C in forming gas or N_2 atmospheres leads to a degradation of the electrical performance of the solar cells. The contact annealing of the solar cells results in a deviation of the current-voltage characteristic from the conventional two diode model. The annealed solar cells show a “hump” feature in the mid-voltage regime of 200-400 mV, which is visible as increased recombination current in the dark IV curve and the pseudo dark IV curve measured by SunsV_{oc}. This effect decreases the pseudo fill factor *pFF* and in consequence the solar cell efficiency, too. The electrical characteristic of this annealing induced degradation shows some similarities to a shunt phenomenon. However, the shunt shows in this case a non-linear or non-ohmic electrical characteristic. The appearance of the annealing induced *pFF* breakdowns due to non-

linear shunting correlates with a decrease of the internal series resistance R_s-$R_{s,front}$ and a decrease of the reverse breakdown voltage.

The application of different imaging characterization techniques in order to characterize the non-linear shunting effect reveals the appearance of characteristic local features correlating with annealing induced *pFF* breakdowns. The main finding of the local imaging characterization was the correlation of recombination active structures in DLIT measurements under forward bias and the appearance of the same local features in reverse biased DLIT as well as reverse biased electroluminescence (ReB-EL). The application of ReB-EL under reverse voltages in the range of -6 to -15 V proved to be the most suitable characterization technique in terms of sensitivity of annealing induced local breakdown spots and spatial resolution. The high spatial resolution compared to DLIT allowed a localization of the annealing induced *pFF* breakdown features along the laser structured front side contact openings. The ReB-EL (as well as the DLIT) signal intensity-voltage characteristic shows many similarities to type-II breakdowns known from the characterization of multi crystalline silicon solar cells, where the emission is a consequence of internal field emission with trap-assisted tunneling or trap-assisted avalanche breakdowns at defect rich areas with high recombination activity such as metal precipitates.

The application of a sequence of ReB-EL, µ-ReB-EL, µ-Pl, SEM, FIB and TEM characterizations allowed a localization and characterization of the annealing induced *pFF* breakdown features on a µm- and nm-scale. The characterized cross section lamella of a region of intensive breakdown illumination revealed two characteristic structures. One side of the cross section showed a deep silicide structure which had a depth of about 200-300 nm and a dimension of at least 100 nm parallel to the textured surface. This deep silicide structure introduces a region of high recombination activity into the emitter and could possibly penetrate the space charge region of the pn-junction. The other facet of the cross section lamella exposed a micro crack within the emitter region. Both structures are regions of high recombination activity and could both explain the electrical degradation as well as the early breakdown illumination. However, the close proximity of both structures allowed no distinction between their position and the location of the breakdown emission in the µ-EL measurement.

EBIC characterizations at cross sections of locally LCP-SE laser doped contact openings demonstrated that the applied laser doping parameters resulted in an inhomogeneous doping depth within the contact opening on a textured surface. The analyzed cross section revealed locally shallow doping depths within the LCP-SE laser

doped contact opening. These locally shallow doping depths are the most likely explanation why the additional laser doping did not prevent the electrical degradation due to highly recombinative structures such as deep Ni silicides.

The introduction of a homogenously deep laser doping underneath the front side contact openings by a 2-step or 1-step laser doping process proved to ensure a *pFF* stability even for annealing processes with high peak temperature (450°C) and long plateau durations (10 min.). The performed experiment showed that for the applied laser opening and annealing processes even a pn-junction depth of 1.5 µm at the contact opening of the Ni plated contact is not sufficient to prevent *pFF* breakdowns. However, the application of a 1-step or 2 step local laser doping process with a depth of about 4 µm demonstrated *pFF* stability even in the presence of a high Ni silicide growth rate.

In conclusion the analysis confirmed that the main reason of the electrical degradation of Ni plated solar cells after an annealing step is the formation of locally deep Ni silicides, which partly correlate with local defect structures. Furthermore, the main aspect to prevent the silicide induced *pFF* breakdown is a locally deep doping underneath the contact openings. The required doping depth is determined by the maximum silicide depths and has to ensure a sufficient distance between the silicide or defect structures and the space charge region. However, the silicide depth depends on various technological influence parameters such as the applied annealing process, the Ni layer thickness, the interface conditions (e.g. interface oxides between Ni and Si) and the applied passivation layer structuring process (e.g. laser structuring, mask & etch, etc.). Therefore, the findings of this chapter demonstrate that the application of a selective emitter design for silicon solar cells with Ni-Cu-Ag or Ni-Ag plated contacts is not necessarily beneficial in terms of maximum cell efficiency but enables a significant degree of freedom for the development of silicidation process sequences for performance stable silicon solar cells.

7.2 Outlook

The combination of solar cell fabrication, characterization and simulation in this work allowed the determination of the limiting factors of the developed laser doping processes by LCP. These findings can be used in order to further optimize the processes and to evaluate which application areas are suitable for the developed laser doping processes.

The evaluation of the LCP boron doping process revealed two critical aspects, which have to be overcome in future optimizations. On the one hand the laser process has to

be optimized in terms of laser damage. This can be achieved by laser parameter optimizations such as the application of lower pulse energies or larger laser pulse durations. Furthermore, new passivation schemes could be evaluated, which show lower laser ablation thresholds such as silicon rich amorphous layer systems (a-Si, SiriON [180], etc.) or layer systems such as Al_2O_3-SiN_x in contrast to thermally grown SiO_2 layers, which were used in this work. On the other hand some technological hurdles have to be overcome, which are mostly attributed to the liquid boron precursor. The high silicon etch rate of the strong alkaline boron source can be problematic especially for long processing times (> 5-10 min). Furthermore, the applied boron precursor demonstrated water induced precipitation effects due to pH lowering, which caused plugging problems in the pipe and nozzle system.

New application areas for the LCP boron doping process could be the formation of highly doped regions for selective emitter designs in n-type Si solar cell concepts such as the PANDA cell [181] by ECN Solar Energy and Yingli Solar or n-type PERT [182] solar cells. Furthermore, the local structuring and doping would be perfectly suitable for back contact back junction (BC BJ) silicon solar cells [11, 125]. A recent publication of Dahlinger et al. [183] demonstrated that a similar boron laser doping process is suitable for the formation of the boron doped emitter in an interdigitated doping structure.

The evaluation of the n-type LCP process as selective emitter doping for plated Ni contacts revealed that the laser structured passivation openings are perfectly suited for Ni-Cu plating metallization processes. However, the laser parameters used in this work could not prevent the electrical performance degradation during a subsequent annealing induced silicidation. Therefore, the laser process has to be optimized for this application area in terms of a homogenous and deep doping depth in order to reduce the probability of silicidation induced shunts. The increase of the doping depth can be realized by either longer laser pulse durations up to continuous wave laser systems or increased absorption depths in Si by increasing the laser wavelength.

The LCP phosphorus doping and structuring process provides narrow doping structures with high phosphorus content in combination with the possibility of simultaneously structuring of thin layer systems. Therefore, new application areas could be local doping structures in advanced cell concepts such as BC BJ solar cells or electrical insulation structures for cell concepts such as metal wrap through solar cells or n-type solar cells.

The characterization methods and findings developed in this work about annealing induced shunting of Ni plated solar cells will help to develop new process integrations of plated contacts in industrially feasible solar cell concepts. Furthermore, they pave the way for a deeper knowledge of the process interactions along the back-end solar cell fabrication process.

Zusammenfassung

Das Ziel dieser Arbeit bestand darin, industriell umsetzbare lokale Dotier- und Strukturierprozesse für hocheffiziente Siliciumsolarzellenkonzepte zu entwickeln und zu charakterisieren. Der Fokus lag dabei auf der Prozessentwicklung und Prozessintegration von laserchemischen Prozessen (LCP) für Siliciumsolarzellen. Des Weiteren wurden mittels LCP hergestellte Solarzellen charakterisiert, wobei mit Hilfe von detaillierten Verlustanalysen die relevanten Prozesseinflüsse auf den späteren Solarzellenwirkungsgrad bestimmt wurden. LCP wurde im Rahmen dieser Arbeit in Kapitel 3 verwendet um lokale Bordotierungen als lokale Back Surface Field Strukturen (LBSF) für p-Type Solarzellen zu erzeugen. Das zweite Anwendungsfeld für LCP war die Herstellung von lokalen Phosphordotierungen für selektive Emitterstrukturen mit galvanisierten Kontakten. Die mittels LCP hergestellten hochdotierten Bereiche unterhalb der galvanisch aufgebrachten Metallkontakte wurden dabei mit Hilfe von Solarzellensimulationen, der Herstellung von Solarzellen und einer ausführlichen Charakterisierung evaluiert.

Lokaler LCP Bordotierprozess

Laser Chemical Processing (LCP) basiert auf der Idee einen Laserstrahl in einen Flüssigkeitsstrahl einzukoppeln. Dabei kann der Laser eingesetzt werden um dünne Schichten auf Siliciumproben zu strukturieren, Silicium lokal und oberflächlich aufzuschmelzen und den Flüssigkeitsstrahl als Dotierquellen einzusetzen um Atome wie Phosphor oder Bor lokal in die Schmelze einzubringen. Daher wird für die Herstellung einer lokalen Bordotierung mittels LCP eine flüssige Borquelle benötigt, die alle LCP spezifischen Anforderungen erfüllt. Zu Beginn der Arbeit mussten daher geeignete Borquellen gesucht und evaluiert werden. Aus den untersuchten Quellen stellte sich eine wässrige 4,4 M NaBH4 Lösung in 14 M NaOH als die geeignetste heraus. Die damit hergestellten Teststrukturen wiesen Oberflächenborkonzentrationen von bis zu 10^{20} cm^{-3} und Dotiertiefen im Bereich 1 µm auf. Der damit entwickelte lokale Bordotierprozess wurde in einem ersten erfolgreichen Test eingesetzt um LBSF Strukturen für passivierte und lokal dotierte (PERL) Solarzellen zu erzeugen. Die hergestellten Solarzellen auf FZ-Si Substraten mit einem spezifischen Basiswiderstand von 0,5 Ωcm erreichten im Maximum Wirkungsgrade bis zu 20,9%. Die im Rahmen dieser Arbeit entwickelten Ergebnisse waren zum Zeitpunkt der Veröffentlichung [119, 120] die erste erfolgreiche Implementierung eines industriell umsetzbaren Laserdotierverfahrens zur Erzeugung von Bordotierten LBSF Strukturen auf Solarzellenebene.

Nach dem ersten erfolgreichen Test wurden weitere Untersuchen der entwickelten LCP-LBSF Strukturen durchgeführt. In einem anschließenden Experiment wurde untersucht, inwiefern der Wirkungsgrad von Solarzellen mit LCP-LBSF von dem spezifischen Basiswiderstand abhängig ist. Dafür wurden LCP-PERL Solarzellen auf Siliciumsubstraten mit variierendem spezifischen Basiswiderstand (ρ_{Base} = 0.5 – 9 Ωcm) hergestellt. Zum Vergleich wurden Solarzellen mit gleichem Design, aber mit undotierten LCP Rückseitenkontaktstrukturen hergestellt (LCP-PERC), sowie Solarzellen mit einem etablierten LBSF Prozess (LFC). Der Anstieg von ρ_{Base} resultierte bei den LCP-PERL und LCP-PERC Solarzellen in einem reduzierten Solarzellenwirkungsgrad. Die Anwendung elektrischer, elektro-optischer und optischer Charakterisierungsmethoden in Kombination mit analytischen und numerischen Simulationen erlaubte es die limitierenden Verlustquellen der hergestellten Solarzellen zu identifizieren.

Die Wirkungsgradlimitierung der LCP-PERL Solarzellen war im Wesentlichen eine Konsequenz von sinkenden Leerlaufspannungen (V_{oc}) für ansteigende spezifische Basiswiderstände. Die Verlustanalyse der Solarzellen erlaubte es mögliche Erklärungen für den V_{oc} Verlust auszuschließen, z.B. lokale Schottkykontakte auf Grund von LCP-LBSF Dotierinhomogenitäten. Die Simulations- und Messergebnisse deuten darauf hin, dass die wahrscheinlichste Erklärung lokale Bereiche um die LBSF Region sind, mit sehr niedrigen Ladungsträgerlebensdauern. Die Reduzierung der Ladungsträgerlebensdauern ist dabei eine Konsequenz von laserinduzierten Schädigungen durch nicht optimale Prozessparameterwahl.

Neben der V_{oc}-Limitierung wiesen die LCP-PERL Solarzellen im Vergleich zu den LFC-Referenzen teilweise reduzierte Füllfaktoren auf. Die Serienwiderstandsanalyse zeigte jedoch, dass die LCP-PERL Solarzellen nicht durch zu hohe Kontaktwiderstände begrenzt waren (wie z.B. die LCP-PERC Solarzellen), sondern nur leicht erhöhte Spreading Resistances aufwiesen. Der erhöhte Spreading Resistance der LCP-PERL Solarzellen ist verursacht durch intrinsische Nachteile bei gleichen Kontaktflächenanteilen des Linienkontaktdesigns zum Punktkontaktdesign der LFC Solarzellen. Jedoch zeigte die Verlustanalyse, dass die LCP-PERL Solarzellen insgesamt nicht Serienwiderstands limitiert waren. Insbesondere die niedrigen Kontaktwiderstände beweisen, dass die eingebrachte Bordotierung der LCP-LBSF Strukturen zu einer erfolgreichen Ausbildung ohmscher Kontakte verholfen hat. Im Gegensatz dazu zeigte sich bei den LCP-PERC Solarzellen sowohl im *FF* als auch im

V_{oc} eine Limitierung auf Grund der Ausbildung von Schottkykontakten bei den undotierten Rückseitenkontakten.

Zusammenfassend konnte gezeigt werden, dass der entwickelte lokale Bor-LCP Dotierprozess erfolgreich in die Prozesskette zur Herstellung von hocheffizienten Siliciumsolarzellen integriert werden konnte. Die Bor-LCP LBSF Strukturen sorgten für die erfolgreiche Ausbildung von ohmschen Kontakten mit niedrigen Kontaktwiderständen. Allerdings zeigt sich beim Übergang auf hohe spezifische Basiswiderstände eine Wirkungsgradlimitierung auf Grund von laserinduzierter Schädigung. Die durchgeführten Verlustanalysen der hergestellten Solarzellen konnten die dominierenden Verlustquellen identifizieren und erlauben es zukünftig gezielt den Bor-LCP Prozess hinsichtlich Laserschädigung zu optimieren.

Theoretische Überlegungen bzgl. Solarzellen mit selektiven Emitterstrukturen

2D Solarzellensimulationen von selektiven Emitterdesigns bildeten den Ausgangspunkt für die Weiterentwicklung von lokalen Phosphor-LCP Dotierungen. Die durchgeführten Simulationen sollen den Einfluss der LCP erzeugten lokalen Hochdotierung unter den Metallkontakten evaluieren und die kritischen Zielparameter identifizieren. Der Fokus lag dabei auf den zwei Hauptaspekten der lokalen Hochdotierung innerhalb des selektiven Emitters: dem Einfluss möglicher Senkungen des spezifischen Kontaktwiderstands und der Emittersättigungsstromdichte auf den Wirkungsgrad der Solarzelle. In diesem Zusammenhang wurden vier verschiedene Solarzellendesigns simuliert. Die Simulationsergebnisse zeigten, dass die möglichen Wirkungsgradvorteile eines selektiven Emitters stark von dem gesamten Solarzellendesign abhängig sind.

Die Modellierung des spezifischen Kontaktwiderstands zeigte, dass neben der Verbesserung von ρ_{cont} durch erhöhte Oberflächendotierkonzentrationen auch die verwendet Metallisierungskonzept eine wesentliche Rolle spielt. Siebgedruckte Ag-Kontakte zeigen in diesem Zusammenhang eine wesentlich höhere Sensibilität auf die darunter liegende Dotierung, als galvanisierte Ni-Kontakte. Die Solarzellensimulationen belegten, dass bei derzeit umsetzbaren Metallfingerbreiten von 50-100 µm der spezifische Kontaktwiderstand erst limitierend wird für $\rho_{cont} >> 10^{-3}$ Ωcm². Daher wird der Serienwiderstandseinfluss des selektiven Emitterdesigns erst sichtbar, wenn der spezifische Kontaktwiderstand andernfalls über diesem Wert liegen würde.

Um die mögliche Wirkungsgradverbesserungen durch reduzierte Emittersättigungsstromdichten im hochdotierten Bereich zu quantifizieren, wurden

Modellierungen von $J_{01,cont}$ und Solarzellensimulationen durchgeführt. Die Simulationen zeigten, dass eine Korrelation zwischen den möglichen Wirkungsgradgewinnen durch $J_{01,cont}$ Reduzierungen im hochdotierten Bereich eines selektiven Emitters und dem Solarzellendesign besteht. Nimmt man für die Simulation ein Al-BSF Solarzellendesign zu Grunde, ergeben sich nur vernachlässigbar kleine Verbesserungen in den elektrischen Eigenschaften der Solarzelle. Nur für große Emitterkontaktbreiten oder Solarzellendesigns mit hohem Wirkungsgradpotenzial > 21%, ergeben sich signifikante Wirkungsgradvorteile durch die reduzierten $J_{01,cont}$ im hochdotierten Bereich unter den Kontakten.

Die durchgeführten Simulation veranschaulichen, dass ein Wirkungsgradgewinn durch die Einführung eines hochdotierten Bereichs beim selektiven Emitter stark mit anderen Designaspekten der Solarzelle zusammenhängt. Insbesondere unter den Rahmenbedingungen der industriellen Umsetzbarkeit definiert das Zusammenspiel des Metallisierungskonzepts, dem thermisch diffundierten homogenen Emitter und dem angewandten selektiven Emitterprozess ob die zusätzlich eingebrachte Hochdotierung unter den Kontakten einen signifikanten Wirkungsgradvorteil bringt. Unter Berücksichtigung der heutigen industriell anwendbaren Prozesstechnologien und Solarzellendesigns, ist es in den meisten Fällen vorteilhafter eher die Kontaktbreiten zu reduzieren (z.B. durch galvanisierte Ni-Cu Kontakte) oder die homogene Emitterdotierung zu optimieren (z.B. durch niedrig dotierte Emitterprofile), als einen selektiven Emitter mit lokaler Hochdotierung unter den Kontakten zu implementieren. Die Einführung des selektiven Emitters ist in den meisten Fällen erst dann sinnvoll, wenn z.B. das angewandte Metallisierungskonzept auf Grund von zu hohen spezifischen Kontaktwiderständen die Solarzelle limitierte oder eine toefe Hochdotierung das Auftreten von lokalen Kurzschlüssen (Shunts) verhindern kann.

Selektive Emitterdotierungen mittels LCP für galvanisierte Si Solarzellen

Das in Kapitel 5 beschriebene Experiment analysiert verschiedene evolutionäre Möglichkeiten um den Wirkungsgrad von Al-BSF Solarzellen zu erhöhen. In diesem Zusammenhang wurden drei Designaspekte untersucht: die Einführung eines niedrig dotierten homogenen Emitters, schmale Ni-Ag oder Ni-Cu galvanisierte Emittermetallkontakte und die Einführung eines selektiven Emitters durch LCP erzeugte hochdotierte Bereiche unter den Emittermetallkontakten. Die hergestellten Solarzellen zeigten Wirkungsgraden bis 19% und einen signifikanten Wirkungsgradvorteil im Vergleich zu den parallel hergestellten Al-BSF Referenzsolarzellen mit einem hochdotierten homogenen Emitter und siebgedruckten Ag-Vorderseitenkontakten.

Die Einführung eines niedrig dotierten homogenen Emitters zeigte sich vorteilhaft durch höhere Kurzschlussströme J_{sc} und Leerlaufspannungen V_{oc}. Die höheren Kurzschlussströme waren eine Konsequenz von reduzierten Auger-Rekombinationsverlusten im Emitter, wodurch bessere Quenteneffizienzen im kurzen Wellenlängenbereich erreicht werden können. Die verbesserten Rekombinationseigenschaften des niedrig dotierten Emitters sind auch durch reduzierte Emittersättigungsstromdichten in besseren V_{oc} sichtbar.

Die Anwendung von Ni galvanisierten Vorderseitenkontakten ermöglichte erst die Verwendung eines niedrigdotierten Emitters, da diese im Vergleich zu siebgedruckten Kontakten wesentlich besser spezifische Kontaktwiderstände aufweisen. Die Füllfaktoranalyse zeigte, dass einzelne Solarzellen die niedrige *FF* aufwiesen durch zu kleine Emitterkontaktöffnungsflächen limitiert waren. Des Weiteren zeigten Solarzellen, deren Emitterkontaktöffnung mittels LCP vor dem Al-BSF Feuerschritt durchgeführt wurde, auf Grund von isolierenden Schichten am Kontaktinterface *FF*-Limitierungen. Die Serienwiderstandsanalyse der hergestellten Solarzellen deutete darauf hin, dass im Falle von erfolgreicher Silicidierung am Ni-Si Interface der Kontaktwiderstand der Solarzellen deutlich reduziert wurde. Die schmale Fingerbreite der galvanisierten Kontakte im Vergleich zu siebgedruckten Kontakten führte auf Grund der geringeren Abschattung auch zu größeren Kurzschlussströmen.

Die Einführung des selektiven Emitters führte in diesem Experiment zu keiner signifikanten Steigerung des maximalen Wirkungsgrads. Dieses Ergebnis bestätigt die Simulationsergebnisse aus Kapitel 4. Die Fälle von verbesserten V_{oc} und Serienwiderständen (R_s) bei Solarzellen mit LCP-SE konnten i.d.R. auf kontaktgeometrische Ursachen zurückgeführt werden. Der geringe Einfluss des selektiven Emitters auf den Solarzellenwirkungsgrad kommt von einer geringen Empfindlichkeit des Al-BSF Designs auf Kontaktrekombinationsverbesserungen. Des Weiteren war der Einfluss der lokalen Hochdotierung auf den spezifischen Kontaktwiderstand der galvanisierten Ni-Kontakte vernachlässigbar, da auch der thermisch diffundierte Emitter schon eine Oberflächendotierkonzentration von ca. $2 \cdot 10^{20}$ cm^{-3} aufwies. Im Gegensatz zu siebgedruckten Kontakten, ergeben sich bei Ni galvanisierten Kontakten keine Kontaktwiderstandslimitierungen in diesem Bereich. Insbesondere nach erfolgreicher Silizidierung der Ni-Si Grenzfläche ist eine Kontaktwiderstandslimitierung bei dieser Oberflächendotierkonzentration noch geringer ausgeprägt.

Die hergestellten Solarzellen mit Ni-Ag bzw. Ni-Cu galvanisierten Vorderseitenkontakten wiesen eine Korrelation zwischen dem gemessen pseudo-FF (*pFF*) und dem internen Serienwiderstand (R_s-$R_{s,front}$) auf. Diese Erkenntnis unterstützt die Hypothese, dass bei einige Solarzellen innerhalb der Kontaktöffnungen noch isolierende Schichten and der Ni-Si Grenzfläche aufwiesen. Dadurch ergeben sich erhöhte V_{oc} und *pFF* Werte, allerdings gleichzeitig auch erhöhte Kontaktwiderstände. Die Solarzellen in diesem Experiment wiesen das Problem auf, dass Kontaktwiderstandsverbesserungen durch Wärmeinduzierte Silicidierung gleichzeitig zu massiven Einbrüchen im *pFF* führten.

Wärme induzierte nicht-lineare Kurzschlüsse von Ni galvanisierten Solarzellen

Das in Kapitel 6 beschriebene Experiment hatte zum Ziel nicht-lineare lokale Kurzschlüsse zu untersuchen, die bei Wärmebehandlungsschritten von Ni galvanisierten Siliciumsolarzellen entstehen. Wärmebehandlungsschritte sind bei Ni galvanisierten Solarzellen wichtig, um die Kontakthaftung durch Bildung eines Ni-Silizids zu erhöhen. Die während der Wärmebehandlung erzeugten nicht-linearen Kurzschlüsse wurden unter drei Aspekte analysiert: die Veränderung der elektrischen Kennlinien der Solarzelle durch Wärmebehandlungen, lokale Veränderung der Solarzelle sichtbar gemacht in unterschiedlichen optischen Charakterisierungsverfahren und die Mikrostruktur der lokalen Verlustzentren.

Die durchgeführten Experimente zeigten, dass die Kombination von Ni galvanisierten Kontakten und einem anschließenden Wärmebehandlungsschritt bei 300-450°C in einer Formiergas- oder N_2-Atmosphäre zu einer Degradierung der elektrischen Eigenschaften der Solarzelle führen kann. Die Konsequenz ist eine Abweichung der elektrischen Kennlinien vom klassischen 2-Dioden Verhalten. Die wärmebehandelten Solarzellen wiesen einen Buckel bei 200-400 mV in der Dunkel-JV bzw. pseudo-Dunkel-JV Kurve auf, der einem erhöhten Rekombinationsstrom entspricht. Die Veränderung der elektrischen Eigenschaften hatte eine signifikante Reduzierung des *pFF* und damit auch des Solarzellenwirkungsgrads zur Folge. Die elektrische Charakteristik der Wärme induzierten Degradation zeigte einige Ähnlichkeiten mit Kurzschlussphänomenen. Allerdings zeigte sich hierbei ein nicht-lineares Kurzschlussverhalten mit einer nicht-ohmschen Charakteristik. Das Auftreten der nicht-linearen Kurzschlüsse korrelierte mit einem Einbruch des pFF, einer Reduzierung des internen Serienwiderstands R_s-$R_{s,front}$ und einer Reduzierung der Durchbruchsspannung in Rückswärtsrichtung.

Zur lokalen Charakterisierung der nicht-linearen Kurzschlüsse wurden unterschiedliche bildgebender Charakterisierungsverfahren eingesetzt. Es zeigte sich, dass die Wärme induzierte elektrische Degradierung mit dem Auftreten lokaler Strukturen in der optischen Charakterisierung korrelierte. Die auftretenden Strukturen wurden in unterschiedlichen bildgebenden Messverfahren sichtbar, unter anderem in Dark Lock-in Thermographie (DLIT) unter Vorwärts und Rückwärtsspannung und Elektrolumineszenz unter Rückwärtsspannung (ReB-EL). Die Anwendung von ReB-EL bei -6 bis -15 V stellte sich auf Grund einer hohen Messauflösung und einer hohen Sensibilität auf die Wärme induzierten Strukturen als besonders geeignet heraus. Die hohe räumliche Auflösung im Vergleich zum verfügbaren DLIT Aufbau erlaubte eine genaue Lokalisierung der Strukturen. Die Strukturen befanden sich dabei immer entlang oder innerhalb der laserstrukturierten Emitterkontaktöffnungen. Die Intensitäts-Spannungs-Abhängigkeit der Strukturen in DLIT und ReB-EL Messungen zeigten viele Gemeinsamkeiten zu Typ II Durchbrüchen bei multikristallinen Si Solarzellen. Type II Durchbrüche sind dort eine Konsequenz von Diodendurchbrüchen auf Grund von interner Feldemission in Kombination mit Störstellen unterstützten Tunnelprozessen oder Störstellen unterstützten Avalanche Durchbrüchen an defektreichen Strukturen mit hoher Rekombinationsaktivität wie z.B. Metallpräzipitate.

Die Anwendung einer Messsequenz von ReB-EL, µ-ReB-EL, µ-Pl, SEM, FIB und TEM Messungen erlaubte eine Lokalisation und Charakterisierung der *pFF* Einbruch korrelierten Strukturen auf einer µm- bzw. nm-Skala. Die charakterisierte Querschnittslamelle einer Region mit intensiver Durchbruchsstrahlung in µ-ReB-EL offenbarte zwei charakteristische Strukturen. Eine Seite der Querschnittslamelle zeigte eine tiefe Ni-Silizid Struktur mit einer Tiefe von ca. 200-300 nm und einer Ausbreitung von mind. 100 nm parallel zur Oberflächentextur. Diese tiefe Silizid Struktur erzeugt eine sehr hochrekombinative Region im Emitter und könnte sogar die Raumladungszone oder den pn-Übergang durchstoßen. Die andere Seite der Lamelle zeigte einen Mikroriss innerhalb der Emitterregion. Beide Strukturen entsprechen Regionen mit hoher Rekombinationsaktivität und könnten beide ursächlich für die Durchbruchsstrahlung sein. Die Nähe von wenigen 100 nm erlaubt jedoch keine Unterscheidung bezüglich ihrer Position und der Durchbruchsstrahlung in der µ-EL Messung.

Elektronenstrahl induzierte Strommessungen (EBIC) an Querschnitten von LCP hochdotierten selektiven Emitterstrukturen zeigten, dass der verwendete LCP-

Laserdotierprozess bei den untersuchten Proben in Kapitel 5 und 6 zu einer inhomogenen Dotiertiefe geführt hat. Die Dotiertiefeninhomogenität war nur sichtbar auf texturierten Proben. Die lokal flachen Dotiertiefen in Kombination mit den tiefen Ni-Silizidstrukturen war mit aller Wahrscheinlichkeit die Hauptursache, warum die eingebrachte Hochdotierung mittels LCP die lokalen Kurzschlüsse nicht vollständig verhindern konnte.

Die Einführung einer sehr tiefen homogenen Laserdotierung unterhalb der Ni-Kontakte erwies sich als Möglichkeit eine *pFF*-Stabilität auch bei sehr extremen Wärmebehandlungsschritten (z.B. 10 min bei 450°C) zu gewährleisten. Innerhalb eines durchgeführten Experiments zeigte sich allerdings auch, dass selbst Emittertiefen von 1,5 µm nicht ausreichten um bei 450°C (10 min) eine *pFF*-Stabilität zu gewährleisten. Nur Solarzellen mit laserdotierten 4 µm tiefen Emitterstrukturen (selektiver Emitter) unterhalb der Ni-Kontakte konnten nach der Wärmebehandlung bei 450°C (10 min) eine *pFF*-Stabilität garantieren, selbst bei erfolgreicher Ni-Silizidbildung.

Zusammenfassend konnte gezeigt werden, dass die Ursache für die elektrische Degradierung von Ni galvanisierten Solarzellen nach Wärmebehandlungsschritten in der Ausbildung von lokal tiefen Siliziden liegt, die teilweise mit lokalen Kristalldefektstrukturen korrelieren. Des Weiteren konnte gezeigt werden, dass eine ausreichend tiefe Dotierung unterhalb der Kontakte auch nach der Silizidausbildung die elektrische Stabilität der Solarzelle gewährleisten kann. Die nötige Dotiertiefe ist dabei definiert über die maximale Silizidtiefe und muss an jedem Punkt der Zelle einen ausreichenden Abstand zwischen der Raumladungszone und den Silizid- oder Defektstrukturen gewährleisten. Die Silizidtiefe hängt jedoch von zahlreichen rechnologischen Parametern ab, wie z.B. dem angewandten Wärmebehandlungsprozess, der Ni-Schichtdicke, den Grenzflächeneigenschaften (z.B. Grenzflächenoxide zwischen Ni und Si) und dem angewandten Strukturierungsprozess für die die Kontaktöffnungsstrukturen der Passivierungsschicht (z.B. Laserstrukturierung, Mask & Etch, etc.). Die Ergebnisse dieses Kapitels zeigen daher, dass der Vorteil eines selektiven Emitters bei Ni-Cu oder Ni-Ag galvanisierten Kontakten nicht zwangsläufig in der Erhöhung des maximal möglichen Wirkungsgrads liegt, sondern in einer signifikanten Steigerung des Freiheitsgrads bei den nachfolgenden Silizidierungsschritten. Mit Hilfe der selektiven Emitterstruktur kann dabei auch bei lokal tiefen Silizidstrukturen immer noch eine Stabilität der elektrischen Eigenschaften gewährleistet werden.

Bibliography

1. Fraunhofer Institute for Solar Energy Systems ISE. *Photovoltaics Report*. 2013 October 2013]; Available from: http://www.ise.fraunhofer.de/de/downloads/pdf-files/aktuelles/photovoltaics-report-in-englischer-sprache-04-2013.pdf.
2. Wirth, H. *Aktuelle Fakten zur Photovoltaik in Deutschland*. 2013 [cited 2013 October]; Available from: http://www.ise.fraunhofer.de/de/veroeffentlichungen/veroeffentlichungen-pdf-dateien/studien-und-konzeptpapiere/aktuelle-fakten-zur-photovoltaik-in-deutschland.pdf.
3. Robinson, S.J., A.G. Aberle and M.A. Green, *Departures from the principle of superposition in silicon solar cells.* Journal of Applied Physics, 1994. **76**(12): p. 7920-30.
4. Beier, J., *Untersuchung zur Anwendbarkeit des Superpositionsprinzips bei Silizium-Solarzellen*, in *Fakultät für Physik*. 1992, Universität Freiburg: Freiburg. p. 158.
5. McIntosh, K.R., *Lumps, humps and bumps: Three detrimental effects in the current-voltage curve of silicon solar cells*, in *Centre for Photovoltaic Engineering*. 2001, University of New South Wales: Sydney, Australia. p. 180.
6. Fossum, J.G., *Physical operation of back-surface-field silicon solar cells.* IEEE Transactions on Electron Devices, 1977. **ED-24**(4): p. 322-5.
7. Metz, A., D. Adler, S. Bagus, H. Blanke, M. Bothar, E. Brouwer, S. Dauwe, K. Dressler, R. Droessler, T. Droste, M. Fiedler, Y. Gassenbauer, T. Grahl, N. Hermert, W. Kuzminski, A. Lachowicz, T. Lauinger, N. Lenck, M. Manole, M. Martini, R. Messmer, C. Meyer, J. Moschner, K. Ramspeck, P. Roth, R. Schönfelder, B. Schum, J. Sticksel, K. Vaas, M. Volk and K. Wangemann, *Industrial high performance crystalline silicon solar cells and modules based on rear surface passivation technology.* Solar Energy Materials and Solar Cells, 2013(0).
8. Blakers, A.W., A. Wang, A.M. Milne, J. Zhao and M.A. Green, *22.8% efficient silicon solar cell.* Applied Physics Letters, 1989. **55**(13): p. 1363-5.
9. Zhao, J., A. Wang, P.P. Altermatt, S.R. Wenham and M.A. Green, *24% efficient perl silicon solar cell: recent improvements in high efficiency silicon cell research.* Solar Energy Materials and Solar Cells, 1996. **41/42**: p. 87-99.
10. Van Kerschaver, E. and G. Beaucarne, *Back-contact solar cells: a review.* Progress in Photovoltaics: Research and Applications, 2005((online)): p. in press.
11. De Ceuster, D., P. Cousins, D. Rose, D. Vicente, P. Tipones and W. Mulligan. *Low Cost, high volume production of >22% efficiency silicon solar cells*. in *Proc. 22nd European Photovoltaic Solar Energy Conference*. 2007. Milan, Italy.
12. Sinton, R.A. and A. Cuevas. *A quasi-steady-state open-circuit voltage method for solar cell characterization*. in *Proceedings of the 16th European Photovoltaic Solar Energy Conference*. 2000. Glasgow, UK: James & James, London, UK, 2000.
13. Cuevas, A. and F. Recart, *Capacitive effects in quasi-steady-state voltage and lifetime measurements of silicon devices.* Journal of Applied Physics, 2005. **98**: p. 074507.
14. Clemmer, J.D., B.L. Gilliland, R.A. Bartsch and R.A. Holwerda, *Substituent Effects on the Electron-Transfer Reactivity of Hydroquinones with Laccase Blue Copper.* Biochimica Et Biophysica Acta, 1979. **568**(2): p. 307-320.
15. Greulich, J., M. Glatthaar and S. Rein, *Fill factor analysis of solar cells' current–voltage curves.* Progress in Photovoltaics: Research and Applications, 2010. **18**(7): p. 511-5.
16. Harder, N.-P., A.B. Sproul, T. Brammer and A.G. Aberle, *Effects of sheet resistance and contact shading on the characterization of solar cells by open-circuit voltage measurements.* Journal of Applied Physics, 2003. **94**(4): p. 2473-9.
17. Roth, T., J. Hohl-Ebinger, D. Grote, E. Schmich, W. Warta, S.W. Glunz and R.A. Sinton, *Illumination-induced errors associated with suns-VOC measurements of silicon solar cells.* Review of Scientific Instruments, 2009. **80**(033106): p. 1-7.

18. Bivour, M., C. Reichel, M. Hermle and S.W. Glunz *Improving the a-Si:H(p) rear emitter contact of n-type silicon solar cells.* Solar Energy Materials & Solar Cells, 2012. **106**: p. 11-16.
19. Sze, S.M., *Physics of Semiconductor Devices*. 2nd ed. 1981, New York: John Wiley & Sons.
20. Schroder, D.K., *Semiconductor material and device characterization*. 2. ed. Vol. 1. 1998: John Wiley & Sons, Inc.
21. Andrews, J.M. and Lepselte.Mp, *Reverse Current-Voltage Characteristics of Metal-Silicide Schottky Diodes.* Solid-State Electronics, 1970. **13**(7): p. 1011-&.
22. Bucher, E., S. Schulz, M.C. Lux-Steiner, P. Munz, U. Gubler and F. Greuter, *Work function and barrier heights of transition metal silicides.* Applied Physics A, 1986. **40**(2): p. 71-77.
23. Chang, Y.J. and J.L. Erskine, *Diffusion Layers and the Schottky-Barrier Height in Nickel Silicide-Silicon Interfaces.* Physical Review B, 1983. **28**(10): p. 5766-5773.
24. Haynes, W.M., *CRC Handbook of Chemistry and Physics*. 93rd ed, ed. W.M. Haynes. Vol. 93rd. 2012: Taylor & Francis.
25. Card, H.C., *Aluminum-silicon Schottky barriers and ohmic contacts in integrated circuits.* IEEE Transactions on Electron Devices, 1976. **ED-23**(6): p. 538-44.
26. Schubert, G., *Thick film metallisation of crystalline silicon solar cells* 2006, Universität Konstanz: Konstanz. p. 142.
27. Yu, A.Y.C., *Electron tunneling and contact resistance of metal-silicon contact barriers.* Solid-State Electronics, 1970. **13**: p. 239-47.
28. Ng, K.K. and R. Liu, *On the calculation of specific contact resistivity on (100) Si.* Transactions on Electron Devices, 1990. **37**(6): p. 1535-7.
29. Schroder, D.K. and D.L. Meier, *Solar cell contact resistance - a review.* IEEE Transactions on Electron Devices, 1984. **ED-31**(5): p. 637-47.
30. Michl, B., D. Impera, M. Bivour, W. Warta and M.C. Schubert, *Suns-PLI as a powerful tool for spatially resolved fill factor analysis of solar cells.* Progress in Photovoltaics: Research and Applications, 2012: p. n/a-n/a.
31. Schenk, A., *Finite-temperature full random-phase approximation model of band gap narrowing for silicon device simulation.* Journal of Applied Physics, 1998. **84**(7): p. 3684-95.
32. Glunz, S.W., J. Nekarda, H. Mäckel and A. Cuevas. *Analyzing back contacts of silicon solar cells by suns-voc-measurements at high illumination densities*. in *Proceedings of the 22nd European Photovoltaic Solar Energy Conference* 2007. Milan, Italy.
33. Sproul, A.B. and M.A. Green, *Intrinsic carrier concentration and minority-carrier mobility of silicon from 77 to 300 K.* Journal of Applied Physics, 1993. **73**(3): p. 1214-25.
34. Wang, S. and D. Macdonald, *Temperature dependence of Auger recombination in highly injected crystalline silicon.* Journal of Applied Physics, 2012. **112**(11): p. 113708-4.
35. Wagner, L.F., R.W. Young and A. Sugerman, *A Note on the Correlation between the Schottky-Diode Barrier Height and the Ideality Factor as Determined from Iv Measurements.* IEEE Electron Device Letters, 1983. **4**(9): p. 320-322.
36. Shannon, J.M., *Control of Schottky-Barrier Height Using Highly Doped Surface-Layers.* Solid-State Electronics, 1976. **19**(6): p. 537-543.
37. Basterfield, J., J.M. Shannon and A. Gill, *Nature of Barrier Height Variations in Alloyed Al-Si Schottky-Barrier Diodes.* Solid-State Electronics, 1975. **18**(3): p. 290-&.
38. Wittmer, M. and J. Freeouf, *Ideal Schottky diodes on passivated silicon.* Physical Review Letters, 1992. **69**(18): p. 2701-2704.
39. Hahn, G. *Status of selective emitter technology*. in *Proc. 25th European Photovoltaic Solar Energy Conference*. 2010. Valencia, Spain.
40. Bartsch, J., A. Mondon, K. Bayer, C. Schetter, M. Horteis and S.W. Glunz, *Quick Determination of Copper-Metallization Long-Term Impact on Silicon Solar Cells.* Journal of the Electrochemical Society, 2010. **157**(10): p. H942-H946.
41. Nair, J., S. Strand, N. Frank, J. Knauft, H. Wesch, P.R. Galle and H. Bartsch, *Apoptosis and age-dependant induction of nuclear and mitochondrial etheno-DNA adducts in Long-Evans Cinnamon (LEC) rats: enhanced DNA damage by dietary curcumin upon copper accumulation.* Carcinogenesis, 2005. **26**(7): p. 1307-1315.

42. Langer, R., R. Bartsch and G. Nagel, *Irradiation behavior of submerged arc welding materials with different copper content.* Effects of Radiation on Materials: 19th International Symposium, 2000. **1366**: p. 235-244.
43. Esturo-Breton, A., F. Binaie, M. Breselge, T. Frieß, M. Geiger, E. Holbig, J. Isenberg, S. Keller, T. Kühn, J. Maier, A. Münzer, R. Schlosser, A. Schmid, C. Voyer, P. Winter, K. Bayer, J. Krümberg, S. Henze, I. Melnyk, M. Schmidt, S. Klingbeil, F. Walter, R. Kopecek, K. Peter and P. Fath. *Crystalline Si solar cells with selective emitter for industrial mass production* in *Proceedings of the 24th European Photovoltaic Solar Energy Conference*. 2009. Hamburg, Germany.
44. Eisele, S.J., T.C. Röder, J.R. Köhler and J.H. Werner, *18,9% efficient full area laser doped silicon solar cell.* Applied Physics Letters, 2009. **95**(133501): p. 1-3.
45. Jäger, U., M. Okanovic, M. Hörteis, A. Grohe and R. Preu. *Selective emitter by laser doping from phosphosilicate glass*. in *Proceedings of the 24th European Photovoltaic Solar Energy Conference*. 2009. Hamburg, Germany.
46. Jager, U., S. Mack, C. Wufka, A. Wolf, D. Biro and R. Preu, *Benefit of Selective Emitters for p-Type Silicon Solar Cells With Passivated Surfaces.* Photovoltaics, IEEE Journal of, 2012. **PP**(99): p. 1-7.
47. Tjahjono, B., S. Wang, A. Sugianto, Z. Hameiri, N. Borojevic, A. Ho-Baillie and S. Wenham. *Application of laser-doped contact structure on multicrystalline solar cells*. in *Proceedings of the 23rd European Photovoltaic Solar Energy Conference*. 2008. Valencia, Spain.
48. Hallam, B., S. Wenham, H. Lee, E. Lee, H. Lee, J. Kim, J. Shin, K. Cho and J. Kim, *Record Efficiency on Large Area P-Type Czochralski Silicon Substrates.* Japanese Journal of Applied Physics, 2012. **51**(10).
49. D. Kyeong, S.-H. Cho, J.-K. Lim, K. Lee, M.-I. Hwang, W.J. Lee and E.C. Cho. *Approaching 20%-Efficient Selective-Emitter Solar Cells with Copper Front Contacts on Industrial 156 mm Cz Si Wafers*. in *Proceedings of the 27th European Photovoltaic Solar Energy Conference and Exhibition*. 2012. Frankfurt, Germany.
50. Wang, Z.J., P.Y. Han, H.Y. Lu, H.Q. Qian, L.P. Chen, Q.L. Meng, N. Tang, F. Gao, Y.F. Jiang, J.Q. Wu, W.J. Wu, H.D. Zhu, J.J. Ji, Z.R. Shi, A. Sugianto, L. Mai, B. Hallam and S. Wenham, *Advanced PERC and PERL production cells with 20.3% record efficiency for standard commercial p-type silicon wafers.* Progress in Photovoltaics, 2012. **20**(3): p. 260-268.
51. Nair, J., H. Sone, M. Nagao, A. Barbin and H. Bartsch, *Copper-dependent formation of miscoding etheno-DNA adducts in the liver of Long Evans cinnamon (LEC) rats developing hereditary hepatitis and hepatocellular carcinoma.* Cancer Research, 1996. **56**(6): p. 1267-1271.
52. Schneiderlöchner, E., R. Preu, R. Lüdemann and S.W. Glunz, *Laser-fired rear contacts for crystalline silicon solar cells.* Progress in Photovoltaics: Research and Applications, 2002. **10**: p. 29-34.
53. Agostinelli, G., P. Choulat, H.F.W. Dekkers, E. Vermariën and G. Beaucarne. *Rear surface passivation for industrial solar cells on thin substrates*. in *Proc. 4th World Conference on Photovoltaic Energy Conversion*. 2006. Waikoloa, Hawaii, USA.
54. Suwito, D., U. Jäger, J. Benick, S. Janz, M. Hermle, R. Preu and S.W. Glunz. *Industrially feasible rear side concept for n-type silicon solar cells approaching 700 mV of V_{oc}*. in *Proceedings of the 25th European Photovoltaic Solar Energy Conference and Exhibition*. 2010. Valencia, Spain.
55. Kim, J.S., A.J. Bessire, R.A. Bartsch, R.A. Holwerda and B.P. Czech, *Redox Reactivity of Azathiaferrocenophane Complexes with Copper(Ii) and Palladium(Ii) (Vol 484, Pg 47, 1994).* Journal of Organometallic Chemistry, 1995. **494**(1-2): p. C25-C25.
56. Mai, L., Z. Hameiri, B.S. Tjahjono, R.S. Wenham, A. Sugianto and M.B. Edwards. *Rear junction laser doped solar cells on CZ n-type silicon*. in *Proceedings of the 34th IEEE Photovoltaic Specialists Conference*. 2009. Philadelphia, Pennsylvania, USA.

57. Kim, J.S., A.J. Bessire, R.A. Bartsch, R.A. Holwerda and B.P. Czech, *Redox Reactivity of Azathiaferrocenophane Complexes with Copper(Ii) and Palladium(Ii).* Journal of Organometallic Chemistry, 1994. **484**(1-2): p. 47-51.
58. Tjahjono, B.S., *Laser doped selective emitter solar cells* in *Faculty of Engineering*. 2010, University of New South Wales, Australia: Sydney.
59. Bovatsek, J.M., A. Sugianto, B. Hallam, B. Tjahjono, S. Wenham and R.S. Patel. *High-speed fabrication of laser doping selective emitter solar cells using 532nm continous wave (cw) and modelocked quasi-cw laser source*. in *Proceedings of the 26th European Photovoltaic Solar Energy Conference and Exhibition*. 2011. Hamburg, Germany.
60. Nekarda, J.-F., *Laser Fired Contacts (LFC) : Charakterisierung, Optimierung und Modellierung eines Verfahrens zur lokalen Rückseitenkontaktierung dielektrisch passivierter Silizium-Solarzellen*. 2013, Universität Konstanz: Konstanz.
61. Böckelmann, R., *Optimierung und Charakterisierung lasergestützter Kontaktierungsprozesse für kristalline Siliziumsolarzellen*, in *Fakultät für Physik*. 2013, Rheinische Friedrich-Wilhelms-Universität Bonn: Bonn.
62. Richerzhagen, B., *Entwicklung und Konstruktion eines Systems zur Übertragung von Laserenergie für die Laserzahnbehandlung*, in *Département de Microtechnique*. 1994, École Polytechnique Fédérale de Lausanne: Lausanne. p. 102.
63. Fell, A. and F. Granek, *Influence of pulse duration on the doping quality in laser chemical processing (LCP)—a simulative approach.* Applied Physics A: Materials Science & Processing, 2012: p. 1-6.
64. Fell, A., S. Hopman and F. Granek. *Investigation on the influence of the intensity profile on the doping quality in laser chemical processing (LCP)*. in *Proceedings of the 25th European Photovoltaic Solar Energy Conference and Exhibition*. 2010. Valencia, Spain.
65. Willeke, G.P. and D. Kray. *A new route towards 50 µm thin crystalline silicon wafer solar cells*. in *Proceedings of the 17th European Photovoltaic Solar Energy Conference*. 2001. Munich, Germany: WIP-Munich and ETA-Florence.
66. Kray, D., A. Fell, S. Hopman, K. Mayer, G. Willeke and S.W. Glunz, *Laser Chemical Processing (LCP) - A versatile tool for microstructuring applications.* Applied Physics A, 2008.
67. Kray, D., S. Hopman, A. Spiegel, B. Richerzhagen and G.P. Willeke, *Study on the edge isolation of industrial silicon solar cells with waterjet-guided laser.* Solar Energy Materials and Solar Cells, 2007. **91**(17): p. 1638-44.
68. Kray, D., A. Fell, S. Hopman, K. Mayer, M. Mesec, S.W. Glunz and G.P. Willeke. *Progress in laser chemical processing (LCP) for innovative solar cell microstructuring and wafering applications*. in *Proceedings of the 22nd European Photovoltaic Solar Energy Conference* 2007.
69. Hopman, S., A. Fell, K. Mayer, M. Mesec, G.P. Willeke and D. Kray. *First results of wafering with laser chemical processing*. in *Proceedings of the 23rd European Photovoltaic Solar Energy Conference*. 2008. Valencia, Spain.
70. Rodofili, A., S. Hopman, A. Fell, K. Mayer, M. Mesec, F. Granek and S.W. Glunz. *Characterization of doping via laser chemical processing (LCP)*. in *Proceedings of the 24th European Photovoltaic Solar Energy Conference*. 2009. Hamburg, Germany.
71. Rodofili, A., A. Fell, S. Hopman, K. Mayer, G.P. Willeke, D. Kray and S.W. Glunz. *Local p-type back surface fields via laser chemical processing (LCP): first experiments*. in *Proceedings of the 23rd European Photovoltaic Solar Energy Conference*. 2008. Valencia, Spain.
72. Kray, D., M. Alemán, A. Fell, S. Hopman, K. Mayer, M. Mesec, R. Müller, G.P. Willeke, S.W. Glunz, B. Bitnar, D.-H. Neuhaus, R. Lüdemann, T. Schlenker, D. Manz, A. Bentzen, E. Sauar, A. Pauchard and B. Richerzhagen. *Laser-doped silicon solar cells by laser chemical processing (LCP) exceeding 20% efficiency*. in *Proc. 33rd IEEE Photovoltaic Specialists Conference*. 2008. San Diego, USA.
73. Kluska, S., C. Fleischmann, A. Büchler, W. Hördt, C. Geisler, S. Hopman and M. Glatthaar, *Micro characterization of laser structured solar cells with plated Ni–Ag contacts.* Solar Energy Materials and Solar Cells, 2014. **120, Part A**: p. 323-331.

74. Hopman, S., A. Fell, M. Mesec, S. Kluska, C. Fleischmann, F. Granek and S.W. Glunz *Influence of concentration of phosphorus dopant liquid and pulse distance on parameters of LCP selective emitters for silicon solar cells*. in *Proceedings of the 25th European Photovoltaic Solar Energy Conference and Exhibition*. 2010. Valencia, Spain.
75. Hopman, S., A. Fell, K. Mayer, C. Fleischmann, K. Drew, D. Kray and F. Granek. *Study on laser parameters for silicon solar cells with LCP selective emitters*. in *Proceedings of the 24th European Photovoltaic Solar Energy Conference*. 2009. Hamburg, Germany.
76. Hopman, S., A. Fell, K. Mayer, M. Aleman, M. Mesec, R. Müller, D. Kray and G.P. Willeke. *Characterization of laser doped silicon wafers with laser chemical processing*. in *Proceedings of the 22nd European Photovoltaic Solar Energy Conference* 2007. Milan, Italy.
77. Zhao, Y.P., H.N. Yang, G.C. Wang and T.M. Lu, *Diffraction from diffusion-barrier-induced mound structures in epitaxial growth fronts.* Physical Review B, 1998. **57**(3): p. 1922-1934.
78. Kray, D., N. Bay, G. Cimiotti, S. Kleinschmidt, N. Kösterke, A. Lösel, M. Sailer, A. Träger, H. Kühnlein, H. Nussbaumer, C. Fleischmann and F. Granek. *Industrial LCP selective emitter solar cells with plated contacts*. in *Proceedings of the 35th IEEE Photovoltaic Specialists Conference*. 2010. Honolulu, Hawaii USA.
79. Späth, W., *Verfahren zur galvanischen Abscheidung einer Metallschicht auf der Oberfläche eines Halbleiterkörpers*, in *Patentschrift 23 48 182*. 1979, Siemens AG: Germany.
80. Durkee, L.F., *Method of plating by means of light*, in *US Patent No. 4 144 139*. 1979, Solarex Corporation, Rockville, Md.: USA.
81. Grenon, L.A., *Verfahren zum Elektroplattieren*, in *Offenlegungsschrift 30 06 716*. 1980, Motorola, Inc., Schaumburg, Ill. (USA): Germany.
82. Grenon, L.A. *Photoelectrolytic plating on silicon solar cells*. in *Proceedings of the Symposium on Materials and New Processing Technologies for Photovoltaics, Pennington, NJ, Electrochemical Society, Inc., 1981*. 1980. Hollywood, Florida, USA.
83. Grenon, L.A., *Electroplating method*, in *US Patent No. 4 251 327*. 1981, Motorola, Inc., Schaumburg, Ill.: USA.
84. Maczka, T., T. Zabinski and J. Kluska, *Discovering Rules for Production Speed Prediction in Fasteners Manufacturing.* Intelligent Systems in Technical and Medical Diagnostics, 2014. **230**: p. 199-209.
85. Bartsch, J., A. Mondon, B.-J. Godejohann, M. Hörteis and S.W. Glunz *Advanced front side metallization for crystalline silicon solar cells based on a fully plated contact*. in *Proceedings of the 25th European Photovoltaic Solar Energy Conference and Exhibition*. 2010. Valencia, Spain.
86. Bartsch, J., V. Radtke, C. Savio and S.W. Glunz *Progress in understanding the current paths and deposition mechanisms of light-induced plating and implications for the process*. in *Proceedings of the 24th European Photovoltaic Solar Energy Conference*. 2009. Hamburg, Germany.
87. Bartsch, J., V. RAdtke, C. Schetter and S.W. Glunz *Electrochemical methods to analyse the light-induced plating process.* Journal of Applied Electrochemistry, 2010. **40**(4): p. 757-65.
88. Radtke, V., J. Bartsch, S. Greil, C. Schetter, R. Bergander and S.W. Glunz. *Understanding the electrochemical mechanisms of light induced plating by means of voltammetric techniques*. in *Proceedings of the 23rd European Photovoltaic Solar Energy Conference*. 2008. Valencia, Spain.
89. Mette, A., *New concepts for front side metallization of industrial silicon solar cells*, in *Fakultät für Angewandte Wissenschaften*. 2007, Albert-Ludwigs-Universität Freiburg: Freiburg. p. 231.
90. Istratov, A.A. and E.R. Weber, *Electrical properties and recombination activity of copper, nickel and cobalt in silicon.* Applied Physics A (Materials Science Processing), 1998. **A66**(2): p. 123-36.
91. Istratov, A.A. and E.R. Weber, *Physics of copper in silicon.* Journal of the Electrochemical Society, 2002. **149**(1): p. G21-30.

92. Macdonald, D., *Impact of nickel contamination on carrier recombination in n- and p-type crystalline silicon wafers.* Applied Physics A (Materials Science Processing), 2005. **81**(8): p. 1619-25.
93. Weber, E.R., *Transition metals in silicon.* Applied Physics A (Solids and Surfaces), 1983. **A30**(1): p. 1-22.
94. Lindroos, J., D.P. Fenning, D.J. Backlund, E. Verlage, A. Gorgulla, S.K. Estreicher, H. Savin and T. Buonassisi, *Nickel: A very fast diffuser in silicon.* Journal of Applied Physics, 2013. **113**(20).
95. Bartsch, J., A. Mondon, K. Bayer, C. Schetter, M. Hörteis and S.W. Glunz *Quick determination of copper-metallization long-term impact on silicon solar cells.* Journal of the Electrochemical Society, 2010. **157**(10): p. H942-6.
96. Ono, H., T. Nakano and T. Ohta, *Diffusion Barrier Effects of Transition-Metals for Cu/M/Si Multilayers (M=Cr, Ti, Nb, Mo, Ta, W).* Applied Physics Letters, 1994. **64**(12): p. 1511-1513.
97. Wang, S.Q., I. Raaijmakers, B.J. Burrow, S. Suthar, S. Redkar and K.B. Kim, *Reactively Sputtered Tin as a Diffusion Barrier between Cu and Si.* Journal of Applied Physics, 1990. **68**(10): p. 5176-5187.
98. Wang, M.T., Y.C. Lin and M.C. Chen, *Barrier properties of very thin Ta and TaN layers against copper diffusion.* Journal of the Electrochemical Society, 1998. **145**(7): p. 2538-2545.
99. Pinnel, M.R. and J.E. Bennett, *Qualitative Observations on Diffusion of Copper and Gold through a Nickel Barrier.* Metallurgical Transactions a-Physical Metallurgy and Materials Science, 1976. **7**(5): p. 629-635.
100. Mondon, A., M.N. Jawaid, J. Bartsch, M. Glatthaar and S.W. Glunz *Microstructure Analysis of the Interface Situation and Adhesion of Thermally Formed Nickel Silicide for Plated Nickel-Copper Contacts on Silicon Solar Cells.* 2013.
101. Coe, D.J. and E.H. Rhoderick, *Silicide formation in Ni-Si Schottky barrier diodes.* Journal of Physics D: Applied Physics, 1976. **9**(6): p. 965.
102. Chen, L.J., *Silicide Technology for Integrated Circuits (Processing)*. Vol. 5. 2004: Iet.
103. Christensen, M., V. Eyert, C. Freeman, E. Wimmer, A. Jain, J. Blatchford, D. Riley and J. Shaw, *Formation of nickel-platinum silicides on a silicon substrate: Structure, phase stability, and diffusion from ab initio computations.* Journal of Applied Physics, 2013. **114**(3): p. 033533.
104. Lee, P.S., D. Mangelinck, K.L. Pey, J. Ding, J.Y. Dai, C.S. Ho and A. See, *On the Ni-Si phase transformation with/without native oxide.* Microelectronic Engineering, 2000. **51-2**: p. 583-594.
105. Giesecke, J., M. The, M. Kasemann and W. Warta, *Spatially resolved characterization of silicon as-cut wafers with photoluminescence imaging.* Progress in Photovoltaics: Research and Applications, 2008. **published online**.
106. Giesecke, J.A., M. Kasemann, M.C. Schubert, P. Würfel and W. Warta, *Separation of local bulk and surface recombination in crystalline silicon from luminescence reabsorption.* Progress in Photovoltaics: Research and Applications, 2010. **18**(1): p. 10-9.
107. Glatthaar, M., J. Haunschild, M. Kasemann, J. Giesecke, W. Warta and S. Rein, *Spatially resolved determination of dark saturation current and series resistance of silicon solar cells.* Physica Status Solidi RRL, 2010. **4**(1): p. 13-15.
108. Haunschild, J., M. Glatthaar, M. Kasemann, S. Rein and E.R. Weber, *Fast series resistance imaging for silicon solar cells using electroluminescence.* Physica Status Solidi RRL, 2009. **published online**.
109. Kasemann, M., *What photons tell us about solar cells*. 2010, Albert-Ludwigs Universität Freiburg: Freiburg.
110. Kasemann, M., D. Grote, B. Walter, W. Kwapil, T. Trupke, Y. Augarten, R.A. Bardos, E. Pink, M.D. Abbott and W. Warta, *Luminescence imaging for the detection of shunts on silicon solar cells* Progress in Photovoltaics, 2008.
111. Isenberg, J., S. Riepe, S.W. Glunz and W. Warta, *Imaging method for laterally resolved measurement of minority carrier densities and lifetimes: measurement principle and first applications.* Journal of Applied Physics, 2003. **93**(7): p. 4268-75.

112. Trupke, T., R.A. Bardos, M.C. Schubert and W. Warta, *Photoluminescence imaging of silicon wafers.* Applied Physics Letters, 2006. **89**(4): p. 44107-1-3.
113. Breitenstein, O. and M. Langenkamp, *Lock-in Thermography - Basics and Use for Functional Diagnostics of Electronic Components*. 2003, Berlin/Heidelberg: Springer Verlag.
114. Kwapil, W., *Alternative materials for crystalline silicon solar cells - Risks and implications*. 2010, Universität Konstanz: Konstanz.
115. Derome, J. and A.J. Lindroos, *Copper and nickel mobility in podzolic forest soils subjected to heavy metal and sulphur deposition in western Finland.* Chemosphere, 1998. **36**(4-5): p. 1131-1136.
116. Schneemann, M., T. Kirchartz, R. Carius and U. Rau, *Measurement and modeling of reverse biased electroluminescence in multi-crystalline silicon solar cells.* Journal of Applied Physics, 2013. **114**(13): p. 134509.
117. Lausch, D., K. Petter, R. Bakowskie, C. Czekalla, J. Lenzner, H. von Wenckstern and M. Grundmann, *Identification of pre-breakdown mechanism of silicon solar cells at low reverse voltages.* Applied Physics Letters, 2010. **97**(7).
118. Kluska, S., A. Rodofili, K. Mayer, C. Fleischmann, F. Granek and S.W. Glunz *Analysis of local boron dopings formed with LCP*. in *Proceedings of the 25th European Photovoltaic Solar Energy Conference and Exhibition*. 2010. Valencia, Spain.
119. Kluska, S. and F. Granek, *High-Efficiency Silicon Solar Cells With Boron Local Back Surface Fields Formed by Laser Chemical Processing.* Electron Device Letters, IEEE, 2011. **32**(9): p. 1257-1259.
120. Kluska, S., M.K. Cinkowski, F. Granek and S.W. Glunz. *Boron LCP local back surface fields for high efficiency silicon solar cells*. in *Photovoltaic Specialists Conference (PVSC), 2011 37th IEEE*. 2011.
121. Rauer, M., R. Woehl, K. Rühle, C. Schmiga, M. Hermle, M. Hörteis and D. Biro, *Aluminum alloying in local contact areas on dielectrically passivated rear surfaces of silicon solar cells.* IEEE Electron Device Letters, 2011. **32**(7): p. 916-8.
122. Schmiga, C., M. Rauer, M. Rüdiger, K. Meyer, J. Lossen, H.-J. Krokoszinski, M. Hermle and S.W. Glunz *Aluminium-doped p^+ silicon for rear emitters and back surface fields: results and potentials of industrial n- and p-type solar cells*. in *Proceedings of the 25th European Photovoltaic Solar Energy Conference and Exhibition*. 2010. Valencia, Spain.
123. Woehl, R., R. Keding, M. Rüdiger, H. Gentischer, F. Clement, J. Wilde and D. Biro. *20% efficient screen-printed and aluminium-alloyed back-contact back-junction cells and interconnection scheme of point-shaped metalized cells*. in *Proceedings of the 37th IEEE Photovoltaic Specialists Conference*. 2011. Seattle, Washington, USA.
124. Granek, F., M. Hermle, B. Fleischhauer, A. Grohe, O. Schultz, S.W. Glunz and G. Willeke. *Optimisation of laser-fired aluminium emitters for high efficiency n-type si solar cells*. in *Proceedings of the 21st European Photovoltaic Solar Energy Conference*. 2006. Dresden, Germany.
125. Granek, F., *High-Efficiency Back-Contact Back-Junction Silicon Solar Cells*, in *Fakultät für Angewandte Wissenschaften*. 2009, Albert-Ludwigs-Universität: Freiburg.
126. Zhao, J.H., A. Wang and M.A. Green, *24.7% efficient perl silicon solar cells and other high effeciency solar cell and module research at the university of New South Wales.* Applied Physics Letters: p. 8.
127. Sze, S.M., *Semiconductor devices, Physics and Technology.* . 2 ed. 2001, New York: John Wiley & Sons Inc. .
128. Trumbore, F.A., *Citation Classic - Solid Solubilities of Impurity Elements in Germanium and Silicon.* Current Contents/Engineering Technology & Applied Sciences, 1983(1): p. 16-16.
129. Benick, J., B. Hoex, M.C.M. van de Sanden, W.M.M. Kessels, O. Schultz and S.W. Glunz *High efficiency n-type Si solar cells on Al_2O_3-passivated boron emitters.* Applied Physics Letters, 2008. **92**(253504): p. 253504/1-3.

130. Rüdiger, M., M. Rauer, C. Schmiga and M. Hermle, *Effect of incomplete ionization for the description of highly aluminum-doped silicon.* Journal of Applied Physics, 2011. **110**: p. 024508.
131. Altermatt, P.P., A. Schenk, B. Schmithusen and G. Heiser, *A simulation model for the density of states and for incomplete ionization in crystalline silicon. II. Investigation of Si : As and Si : B and usage in device simulation.* Journal of Applied Physics, 2006. **100**(11).
132. Kluska, S. and F. Granek, *High Efficiency Silicon Solar Cells with Boron Local Back Surface Fields formed by Laser Chemical Processing.* to be published in IEEE Electron Device Letters, DOI: 10.1109/LED.2011.2159699, 2011.
133. McIntosh, K.R. and P.P. Altermatt. *A freeware 1d emitter model for silicon solar cells*. in *Proceedings of the 35th IEEE Photovoltaic Specialists Conference*. 2010. Honolulu, Hawaii, USA.
134. Fell, A., *Modelling and Simulation of Laser Chemical Processing (LCP) for the Manufacturing of Silicon Solar Cells*. 2010, Dissertation thesis: Universität Konstanz.
135. Glunz, S.W., A. Grohe, M. Hermle, E. Schneiderlöchner, J. Dicker, R. Preu, H. Mäckel, D. Macdonald and A. Cuevas. *Analysis of laser-fired local back surface fields using n^+np^+ cell structures*. in *Proceedings of 3rd World Conference on Photovoltaic Energy Conversion*. 2003. Osaka, Japan.
136. Wolf, M. and H. Rauschenbach, *Series resistance effects on solar cell measurements.* Advanced Energy Conversion, 1963. **3**: p. 455-79.
137. Pysch, D., A. Mette and S.W. Glunz, *A review and comparison of different methods to determine the series resistance of solar cells.* Solar Energy Materials & Solar Cells, 2007. **91**: p. 1698-706.
138. Karmalkar, S., P.V. Mohan, H.P. Nair and R. Yeluri, *Compact Models of Spreading Resistances for Electrical/Thermal Design of Devices and ICs.* Electron Devices, IEEE Transactions on, 2007. **54**(7): p. 1734-1743.
139. Saint-Cast, P., M. Rüdiger, A. Wolf, M. Hofmann, J. Rentsch and R. Preu, *Advanced analytical model for the effective recombination velocity of locally contacted surfaces.* Journal of Applied Physics, 2010. **108**: p. 013705.
140. Sinton, R.A. *Possibilities for process-control monitoring of electronic material properties during solar-cell manufacture*. in *Proc. 9th Workshop on Crystalline Silicon Solar Cell Materials and Processes*. 1999. Golden, Colorado, USA.
141. Sentaurus TCAD, release E-2010.12, Synopsis, Zürich, Switzerland.
142. De Rose, R., M. Zanuccoli, P. Magnone, M. Frei, E. Sangiorgi and C. Fiegna, *Understanding the Impact of the Doping Profiles on Selective Emitter Solar Cell by Two-Dimensional Numerical Simulation.* Photovoltaics, IEEE Journal of, 2013. **3**(1): p. 159-167.
143. Greulich, J., Jager, x, U., S. Rein and R. Preu, *A Review and Comparison of One- and Two-Dimensional Simulations of Solar Cells Featuring Selective Emitters.* Photovoltaics, IEEE Journal of, 2012. **2**(4): p. 441-449.
144. Jensen, J.D., P. Moller, T. Bruton, N. Mason, R. Russell, J. Hadley, P. Verhoeven and A. Matthewson, *Electrochemical deposition of buried contacts in high-efficiency crystalline silicon photovoltaic cells.* Journal of the Electrochemical Society, 2003. **150**(1): p. G49-57.
145. Mason, N.B., T.M. Bruton and M.A. Balbuena. *Laser grooved buried grid silicon solar cells from pilot line to 50 MWp manufacture in ten years*. in *PV in Europe - Prom PV Technology to Energy Solutions*. 2002. Rome, Italy.
146. Lee, E., H. Lee, J. Choi, D. Oh, J. Shim, K. Cho, J. Kim, S. Lee, B. Hallam, S.R. Wenham and H. Lee, *Improved LDSE processing for the avoidance of overplating yielding 19.2% efficiency on commercial grade crystalline Si solar cell.* Solar Energy Materials and Solar Cells, 2011. **95**(12): p. 3592-3595.
147. Hörteis, M., *Fine-line printed contacts on crystalline silicon solar cells*, in *Fachbereich Physik*. 2009, Universität Konstanz: Konstanz. p. 229.
148. Schubert, G., *Thick Film Metallisation of Crystalline Silcion Solar Cells Mechanisms, Models and Applications*. 2006, Iniversität Konstanz Fachbereich Physik. p. 141.

149. Kontermann, S., *Characterization and modeling of contacting crystalline silicon solar cells*, in *Fachbereich Physik*. 2009, Universität Konstanz: Konstanz, Germany. p. 156.
150. Hermann, S., T. Dezhdar, N.P. Harder, R. Brendel, M. Seibt and S. Stroj, *Impact of surface topography and laser pulse duration for laser ablation of solar cell front side passivating SiNx layers.* Journal of Applied Physics, 2010. **108**(11).
151. Braun, S., E. Emre, B. Raabe and G. Hahn. *Electroless nickel and copper metallization: contact formation on crystalline silicon and background plating behavior on PECVD SiNx:H layers*. in *Proceedings of the 25th European Photovoltaic Solar Energy Conference and Exhibition*. 2010. Valencia, Spain.
152. Tous, L., R.-P. M., M. Ngamo, J.-L. Hernandez, J. Poortmanns and R. Mertens. *Evaluating Contact Resistance Using Epitaxially Grown Phosphorus Emitters*. in *Proceedings of the 26th European Photovoltaic Solar Energy Conference and Exhibition*. 2011. Hamburg, Germany.
153. Wilking, S., A. Herguth and G. Hahn, *Influence of hydrogen on the regeneration of boron-oxygen related defects in crystalline silicon.* Journal of Applied Physics, 2013. **113**(19).
154. Canali, C., C. Jacoboni, F. Nava, G. Ottaviani and A. Alberigiquaranta, *Electron Drift Velocity in Silicon.* Physical Review B, 1975. **12**(6): p. 2265-2284.
155. Canali, C., G. Majni, R. Minder and G. Ottaviani, *Electron and Hole Drift Velocity-Measurements in Silicon and Their Empirical Relation to Electric-Field and Temperature.* IEEE Transactions on Electron Devices, 1975. **22**(11): p. 1045-1047.
156. Glunz, S.W., S. Sterk, R. Steeman, W. Warta, J. Knobloch and W. Wettling. *Emitter dark saturation currents of high-efficiency solar cells with inverted pyramids*. in *Proceedings of the 13th European Photovoltaic Solar Energy Conference*. 1995. Nice, France: H.S. Stephens & Associates, Bedford, UK, 1995.
157. Altermatt, P.P., J.O. Schumacher, A. Cuevas, S.W. Glunz, R.R. King, G. Heiser and A. Schenk, *Numerical modeling of highly doped Si:P emitters based on Fermi-Dirac statistics and self-consistent material parameters.* Journal of Applied Physics, 2002. **92**(6): p. 3187-97.
158. Fell, A., *A Free and Fast Three-Dimensional/Two-Dimensional Solar Cell Simulator Featuring Conductive Boundary and Quasi-Neutrality Approximations.* Electron Devices, IEEE Transactions on, 2012. **PP**(99): p. 1-6.
159. Klaassen, D.B.M., *A unified mobility model for device simulation. I. Model equations and concentration dependence.* Solid-State Electronics, 1992. **35**(7): p. 953-9.
160. Kimmerle, A., A. Wolf, U. Belledin and B. Biro. *Modelling carrier recombination in highly phosphorus-doped industrial emitters*. in *Proceedings of the 1st International Conference on Silicon Photovoltaics*. 2011. Freiburg, Germany: Elsevier Energy Procedia.
161. Blakers, A.W., *Shading losses of solar-cell metal grids.* Journal of Applied Physics, 1992. **71**(10): p. 5237-41.
162. Rauer, M., A. Mondon, C. Schmiga, J. Bartsch, M. Glatthaar and S.W. Gunz *Nickel-plated front contacts for front and rear emitter silicon solar cells*. in *SiliconPV 2013*. 2013. Hamelin, Germany, to be publshed in Energy Procedia.
163. Mondon, A., J. Bartsch and M. Glatthaar, submitted to Solar Energy Materials and Solar Cells, 2013.
164. Smith, B.L. and Rhoderic.Eh, *Schottky Barriers on P-Type Silicon.* Solid-State Electronics, 1971. **14**(1): p. 71-&.
165. Breitenstein, O., J.P. Rakotoniaina, M.H. Al Rifai and M. Werner, *Shunt types in crystalline silicon solar cells.* Progress in Photovoltaics, 2004. **12**(7): p. 529-538.
166. Büchler, A., S. Kluska, M. Kasemann, M. Breitwieser, A. Hähnel, H. Blumtritt, S. Hopman and M. Glatthaar, *Localization of temperature induced shunts in Ni plated monocrystalline silicon solar cells.* to be published.
167. Kluska-Nawarecka, S., B. Sniezynski, W. Parada, M. Lustofin and D. Wilk-Kolodziejczyk, *The use of LPR (logic of plausible reasoning) to obtain information on innovative casting technologies.* Archives of Civil and Mechanical Engineering, 2014. **14**(1): p. 25-31.
168. Rhoderick, E.H. and R.H. Williams, *Metall-semiconductors contacts*. 1988, Oxford: Claren-don Press (University-Press).

169. Everhart, T.E., O.C. Wells and R.K. Matta, *A novel method of semiconductor device measurements.* Proceedings of the IEEE, 1964. **52**(12): p. 1642-1647.
170. Leamy, H.J., *Charge collection scanning electron microscopy.* Journal of Applied Physics, 1982. **53**(6): p. R51-80.
171. Perovic, D.D., M.R. Castell, A. Howie, C. Lavoie, T. Tiedje and J.S.W. Cole, *Field-Emission Sem Imaging of Compositional and Doping Layer Semiconductor Superlattices.* Ultramicroscopy, 1995. **58**(1): p. 104-113.
172. Hovorka, M., F. Mika, P. Mikulik and L. Frank, *Profiling N-Type Dopants in Silicon.* Materials Transactions, 2010. **51**(2): p. 237-242.
173. Xu, L., K. Weber, S.P. Phang, A. Fell, F. Brink, D. Yan, X. Yang, E. Franklin and H. Chen, *Secondary Electron Microscopy Dopant Contrast Image (SEMDCI) for Laser Doping.* Photovoltaics, IEEE Journal of, 2013. **3**(2): p. 762-768.
174. Donolato, C., *A reciprocity theorem for charge collection.* Applied Physics Letters, 1985. **46**(3): p. 270-2.
175. Kittler, M. and J. Larz, *Evaluation of p-n junction position and channel length in Si devices with resolution of a few nanometers by low-energy EBIC.* Solid State Phenomena, 1998. **63-4**: p. 77-87.
176. Knorz, A., M. Peters, A. Grohe, C. Harmel and R. Preu, *Selective laser ablation of SiN_x layers on textured surfaces for low temperature front side metallizations.* Progress in Photovoltaics: Research and Applications, 2008. **2008**: p. 1-10.
177. Imbert, B., R. Pantel, S. Zoll, M. Gregoire, R. Beneyton, S.d. Medico and O. Thomas, *Nickel silicide encroachment formation and characterization.* Microelectronic Engineering, 2010. **87**(3): p. 245-248.
178. Hoummada, K., D. Mangelinck, B. Gault and M. Cabié, *Nickel segregation on dislocation loops in implanted silicon.* Scripta Materialia, 2011. **64**(5): p. 378-381.
179. Hoummada, K., D. Mangelinck, C. Perrin, P. Gas, V. Carron, P. Holliger and E. Ziegler, *Redistribution of arsenic during the reaction of nickel thin films with silicon at relatively high temperature: Role of agglomeration.* Microelectronic Engineering, 2006. **83**(11-12): p. 2264-2267.
180. Seiffe, J., L. Gautero, M. Hofmann, J. Rentsch, R. Preu, S. Weber and R.A. Eichel, *Surface passivation of crystalline silicon by plasma-enhanced chemical vapor deposition double layers of silicon-rich silicon oxynitride and silicon nitride.* Journal of Applied Physics, 2011. **109**: p. 034105.
181. Burgers, A.R., R.C.G. Naber, A.J. Carr, P.C. Barton, L.J. Geerligs, X. Jingfeng, L. Gaofei, S. Weipeng, A. Haijiao, H. Zhiyan, P.R. Venema and A.H.G. Vlooswijk. *19% efficient n-type Si solar cells made in pilot production*. in *Proceedings of the 25th European Photovoltaic Solar Energy Conference and Exhibition*. 2010. Valencia, Spain.
182. Richter, A., J. Benick, A. Kalio, J. Seiffe, M. Hörteis, M. Hermle and S.W. Glunz. *Towards industrial n-type PERT solar cells: rear passivation and metallization scheme*. in *Proceedings of the 1st International Conference on Silicon Photovoltaics*. 2011. Freiburg, Germany: Elsevier Energy Procedia.
183. Dahlinger, M., B. Bazer-Bachi, T.C. Röder, J.R. Köhler, R. Zapf-Gottwick and J.H. Werner, *22.0% Efficient Laser Doped back Contact Solar Cells.* Energy Procedia, 2013. **38**(0): p. 250-253.

List of constants, symbols and acronyms

Constant	Description	Value	
A*n	Richardson constant (n-type Si)	32	AK^2/cm^2
A*p	Richardson constant (p-type Si)	112	AK^2/cm^2
c	Speed of light	299 792 458	m/s
$E_{Gap,Si}$	Band gap energy Si	1,1242	eV
k_B	Boltzmann constant	$1{,}380\ 650\ 4(24) \cdot 10^{-23}$	J/K
π	Pi	3,141 592 653	
q	Electron elementary charge	$1{,}602\ 176\ 487 \cdot 10^{-19}$	C

Acronym	Description
BC BJ	Back contact back junction
BSF	back surface field
Cz	Czochralski
DLIT	Dark lock-in thermography
EBIC	Electron beam induced current
Ec	Conduction band energy
Ev	valence band energy
FFO	fast firing process
FGA	Forming gas atmosphere
FIB	Focused ion beam
FZ	Float zone
HE	Homogeneous emitter

Acronym	Description
ILIT	Illuminated lock-in thermography
LBIC	Local beam induced current
LBSF	Local back surface field
LCP	Laser chemical processing
LFC	Laser fired contact
LFE	Laser fired emitter
LIP	Light induced plating
LMJ	Laser micro jet
mc	multicrystalline
PECVD	Plasma enhanced chemical vapor deposition
PERC	Passivated emitter and rear solar cell
PERL	Passivated emitter and rear locally diffused solar cell
PL	Photoluminescence
ReB-EL	Reverse biased electroluminescence
SE	Selective emitter
SEM	Secondary electron microscopy
SIMS	Secondary ion mass spectroscopy
TEM	Transmission electron microscopy
WFLD	Wet film laser doping

Symbol	Description	Unit
A	Area	cm^2
ΔE_F	Conduction or valence band - Fermi level difference	eV

Symbol	Description	Unit
E_F	Fermi level	eV
E_g	Band gap	eV
EQE	External quantum efficiency	-
$\Phi_{B,n}$	Barrier height (n-type Si)	eV
$\Phi_{B,p}$	Barrier height (p-type Si)	eV
f_{cont}	Contact fraction	%
FF	Fill factor	%
η	Solar cell efficiency	%
I	Current	A
IQE	Internal quantum efficiency	-
J	Current density	A/cm²
J_{01}, J_{02}, J_{0S}	Saturation current density	A/cm²
J_{rev}	Current density under reverse bias	A/cm²
J_{sc}	Short circuit current density	A/cm²
l	Length	m
n_1, n_2	Ideality factor	-
N_A	Acceptor density	cm^-3
N_d	Donator density	cm^-3
pFF	Pseudo fill factor	%
P_{in}	Illumination power	W
P_{MPP}	Maximum power point	W
ρ_{Base}	Base resistivity	Ωcm
ρ_c	Specific contact resistivity	Ωcm²
R_c	Contact resistance	Ωcm²

Symbol	Description	Unit
R_p	Parallel resistance	Ωcm²
R_s	Series resistance	Ωcm²
R_{sh}	Sheet resistance	Ω/sq.
S	Surface recombination velocity	cm/s
T	Temperature	K
τ	Lifetime	s
V	Voltage	V
V_{oc}	Open circuit voltage	V
W	Wafer thickness	m
w	Width	m
Ψ	Illumination intensity	Suns

List of publications

Articles in peer reviewed journals

S. Kluska, F. Granek, M. Rüdiger, M. Hermle and S. W. Glunz
"Modeling and optimization study of industrial n-type high-efficiency back-contact back-junction silicon solar cells", Solar Energy Materials and Solar Cells, 94(3): p. 568-77 (2010)

S. Kluska and F. Granek
"High-Efficiency Silicon Solar Cells With Boron Local Back Surface Fields Formed by Laser Chemical Processing", IEEE Electron Device Letters, 32(9): p. 1257-1259 (2011)

S. Kluska, C. Fleischmann, A. Büchler, W. Hördt, C. Geisler, S. Hopman and M. Glatthaar
"Micro characterization of laser structured solar cells with plated Ni–Ag contacts", Solar Energy Materials and Solar Cells, 120 (Part A): p. 323-331 (2014)

M. Heinrich, S. Kluska, Z. Hameiri, B. Hoex and A. Aberle
"Extracting physical properties of arbitrarily shaped laser-doped micro-scale areas in semiconductors", Applied Physics Letters 103 (26), 262103 (2013)

A. Büchler, S. Kluska, M. Kasemann, M. Breitwieser, W. Kwapil, A. Hähnel, H. Blumtritt, S. Hopman and M. Glatthaar
"Localization of annealing-induced shunts in Ni plated mono crystalline silicon solar cells", Physica Status Solidi – Rapid Research Letters 8 (5), p. 385-389 (2014)

Contributions to national and international conferences

Oral presentations

S. Kluska, A. Rodofili, K. Mayer, C. Fleischmann, F. Granek and S. W. Glunz
„Analysis of local boron dopings formed with LCP", 25th European Photovoltaic Solar Energy Conference, Valencia, Spain (2010)

S. Kluska
"Charakterisierung von Rückseitensolarzellen", SiliconFOREST 2010, Falkau, Germany (2010)

S. Kluska
"Development and characterization of laser chemical processes for high efficiency silicon solar cells", Stiftungstreffen Reiner Lemoine Stiftung, Berlin, Germany (2010)

S. Kluska, C. Fleischmann, A. Büchler, W. Hördt, C. Geisler, S. Hopman and M. Glatthaar
„Micro characterization of laser structured solar cells with plated Ni–Ag contacts", SiliconPV Conference, Hamelin, Germany (2013)

Poster presentations

S. Hopman, A. Fell, M. Mesec, S. Kluska, C. Fleischmann, F. Granek and S. W. Glunz
"Influence of concentration of phosphorus dopant liquid and pulse distance on parameters of LCP selective emitters for silicon solar cells", 25th European Photovoltaic Solar Energy Conference. Valencia, Spain (2010)

F. Granek, C. Fleischmann, S. Kluska, D. Erath and J. Rentsch
"Screen-printed silicon solar cells with LCP selective emitters", 25th European Photovoltaic Solar Energy Conference. Valencia, Spain (2010)

J. Benick, A. Richter, S. Kluska, B. Steinhauser, D. Suwito, M. Rüdiger, M. Hermle and S. W. Glunz
"Approaches for the Processing of Rear Side Passivated n-Type Solar Cells", (unpublished), 26th European Photovoltaic Solar Energy Conference and Exhibition, Hamburg, Germany (2011)

F. Granek, S. Hopman, S. Kluska, A. Fell, M. Breitwieser, C. Fleischmann, M. Glatthaar, S.W. Glunz
"Progress in laser chemical processing for silicon solar cells", 26th European Photovoltaic Solar Energy Conference and Exhibition, Hamburg, Germany (2011)

S. Kluska, M. K. Cinkowski, F. Granek and S. W. Glunz
„Boron LCP local back surface fields for high efficiency silicon solar cells”, 37th IEEE Photovoltaic Specialists Conference, Seattle, USA (2011)

A. Fell, D. Walter, S. Kluska, E. Franklin, K. Weber
"Determination of injection dependent recombination properties of locally processed surface regions", SiliconPV Conference, Hamelin, Germany (2013)

Other publications

S. Kluska, C. Fleischmann, M. Glatthaar, S. Hopman, M. Lieder, M. Mesec, S. W. Glunz
“Lokale Bordotierung, für hocheffiziente Siliciumsolarzellen”, Fraunhofer ISE Jahresbericht 2011, Freiburg, Germany (2011)

Patents

S. Kluska, F. Granek. Andreas Fell
"Verfahren zur Erzeugung einer Metallstruktur zur lokalen elektrischen Kontaktierung einer Halbleiterstruktur", German patent application: DE201110017292 (2011)

Danksagung

Ich möchte mich an dieser Stelle bei allen bedanken, die zum Gelingen dieser Arbeit beigetragen haben und mich in der ganzen Zeit persönlich und/oder fachlich unterstützt haben.

Meinem akademischen Betreuer Prof. Eicke R. Weber für die Betreuung dieser Arbeit und die anregenden und konstruktiven Diskussionen. Prof. Leonhard Reindl für die Übernahme der Zweitkorrektur dieser Arbeit.

Mein besonderer Dank gilt der Reiner Lemoine-Stiftung, insbesondere Dr. Annegret Jatzkewitz und Anja Lemoine, ohne deren Stipendium diese Doktorarbeit gar nicht möglich gewesen wäre. Hierbei möchte ich der RLS nicht nur für die finanzielle Unterstützung danken, sondern insbesondere auch für die interessanten und angenehmen Stipendiatentreffen, die immer wieder zu neuen Einsichten und Ideen führten und sich dabei nie nach Arbeit angefühlt haben.

Filip Granek für die damalige Aufnahme in seine Gruppe und die wunderbare Zusammenarbeit und Unterstützung. In diesem Zusammenhang möchte ich auch Sybille Hopman danken, die mich in meiner Zeit als Doktorand jederzeit unterstützt hat und auf deren Rat und Hilfe ich mich immer verlassen konnte. Meinem Abteilungsleiter Markus Glatthaar, der durch sein umfangreiches Fachwissen und seine Kreativität mir in vielen Diskussionen neue Pfade aufgezeigt hat und meine Kenntnisse der Solarzellenphysik dadurch stetig hat wachsen lassen. Stefan Glunz, der es durch seine herzliche Art und seine wissenschaftliche Führung schafft, in seinem Bereich SEC optimale Arbeitsbedingungen für das Gelingen einer Doktorarbeit in angenehmer Atmosphäre zu schaffen.

Meinen „Abschlussarbeitern“: Marcin Cinkowski, Frieder Junginger, Simon Kretschmer, Wilhelm Hördt und Andreas Büchler. Die durch ihren unermüdlichen Einsatz und ihre hervorragenden Arbeiten die Zusammenarbeit mit ihnen immer zu einem Vergnügen gemacht haben.

Unseren Hiwis: Phillip Bendix, Stephie Henrich, Niklas Wehkamp und Björn Gerdes. Hierbei sei insbesondere Matthias Breitwieser gedankt, dem ich durch sein Engagement nicht nur die vielen µ-PL/Raman/EL Messungen in dieser Arbeit verdanke, sondern der mir auch durch die Vermittlung seines halben Freundeskreises die besten Hiwis und Abschlussarbeiter Freiburgs beschert hat.

Den vielen Kollegen die mich durch Diskussionen, Messungen, Prozessen oder netten Gesprächen immer wieder unterstützt haben und dadurch das ISE zu einem wunderbaren Arbeitsplatz gestaltet haben (in alphabetischer Reihenfolge):

Jonas Bartsch, Martin Bivour, Andreas Brand, Gisela Cimiotti, Matthias Demant, Arne Fallisch, Andreas Fell, Christoph Fleischmann, Christian Geisler, Johannes Giesecke, Martin Heinrich, Martin Kasemann, Martin Lieder, Sebastian Mack, Kuno Mayer, Matthias Mesec, Bernhard Michl, Henning Nagel, Milan Padilla, Michael Rauer, Christian Reichel, Andreas Rodofili, Elisabeth Schäffer, Birgit Stadel, Robert Woehl, dem kompletten Reinraum- und PV-TEC Team und den vielen netten Leuten aus den Bereichen SEC und PTQ die ich an dieser Stelle vergessen habe.

Im Rahmen dieser Arbeit hatte ich auch das Glück in spannenden Projekten mitarbeiten zu dürfen, die einem immer wieder gezeigt haben, dass das die Kunst darin liegt die wissenschaftlichen Fragestellungen mit den Problemstellungen der realen Welt zu vereinen. In diesem Zusammenhang möchte ich mich bei den Projektpartnern Solarworld Innovations GmbH, Rena GmbH, REC Solar ASA und Synova S.A bedanken. Insbesondere gilt mein Dank: Bernd Bitnar, Daniel Kray und Damian Pysch für die vielen spannenden Diskussionen im Rahmen der Projekttreffen, sowie Klaus Weber und Evan Franklin für die Möglichkeit des Austauschs und der Mitarbeit in ihrer Gruppe im Rahmen einen gemeinsamen Projekts.

Der größte Dank gilt allerdings meinen Eltern. Ihre Liebe, Unterstützung und Zuversicht sorgt überhaupt dafür, dass ich die Ziele in meinem Leben, wie z.B. diese Arbeit, erreichen kann und konnte und ist ein ständiger Ansporn.